Spin-orbit phenomena and interfacial proximity effects in magnetic multilayers

ROWAN-ROBINSON, RICHARD,MATTHEW

Spin-orbit phenomena and interfacial proximity effects in magnetic multilayers

Richard Matthew Rowan-Robinson

A Thesis presented for the degree of
Doctor of Philosophy

Centre of Material Physics
Department of Physics
University of Durham
England

May 2016

Abstract

This thesis examines phenomena originating from the spin-orbit interaction in the context of interfacial effects. Four effects were studied, the anisotropic magnetoresistance, spin-orbit torques, magnetic damping and the Dzyaloshinskii-Moriya interaction.

The anisotropic magnetoresistance (AMR) was studied in Ni, $Ni_{95}V_5$ and $Ni_{95}Cr_5$ thin films. The absolute resistivity change due to AMR reduced with decreasing film thickness. This was explained in terms of enhanced electron-magnon spin-flip scattering in the presence of reduced dimensionality. It was shown that the Campbell, Fert and Jaoul model could be extended to include this generalised thickness dependence.

Spin-orbit torques were investigated in multilayer structures with different magnetic anisotropies. Current-induced magnetisation reversal, due to the spin-Hall effect of Pt, was observed in a symmetric Pt/Co/Pt sample with weak perpendicular magnetic anisotropy. No evidence for the Rashba effect was found in this symmetric structure. A spin Hall angle of 0.13 ± 0.06 was extracted for Pt.

Using x-ray resonant magnetic reflectivity, the interfacial proximity induced magnetism (PIM) in Pt was investigated in Pt/Co/Pt multilayer structures with in-plane magnetic anisotropy and characterised as a function of Au and Ir spacer layers at the Co/Pt interface. The PIM was shown to depend strongly on interface morphology and decayed rapidly with increasing spacer layer thickness.

The magnetic damping and Dzyaloshinkskii-Moriya interaction (DMI) were measured in the same samples to investigate the contribution of the PIM to these effects. It was shown that the magnetic damping was dominated by the *d-d* hybridisation at the Co/Pt interface which reduced as spacer layers of increasing thickness were inserted. It was not clear whether the loss of PIM plays a substantial role in this. The DMI was shown to increase as Au and Ir spacer layers were added, due to the prevention of cancellation of opposite DMI contributions from the Pt interfaces. This rise in DMI was on a different lengthscale than was found for the loss of PIM. The results suggested no correlation between the PIM and DMI.

Contents

Abbreviations

AC	Alternating current
AHE	Anomalous Hall effect
AMR	Anisotropic magnetoresistance
BLS	Brillouin light scattering
CFJ	Campbell, Fert and Jaoul
CIMR	Current induced magnetisation reversal
DC	Direct current
DMI	Dzyaloshinskii-Moriya interaction
EDX	Energy dispersive x-ray
FIB	Focussed ion beam
LCP	Left circularly polarised
MOKE	Magneto-optical Kerr effect
MRAM	Magnetic random access memory
PHE	Planar Hall effect
PIM	Proximity induced magnetism
PMA	Perpendicular magnetic anisotropy
RCP	Right circularly polarised
RF	Radio frequency
RKKY	Ruderman, Kittel, Kasuya and Yosida
SHE	Spin Hall effect
SIA	Structural inversion asymmetry
SOI	Spin-orbit interaction
SOT	Spin-orbit torque
SL	Spacer layer
sSLD	Structural scattering length density
mSLD	Magnetic scattering length density
SQUID-VSM	Superconducting quantum interference device - vibrating sample magnetometry
TEM	Transmission electron microscopy
TR-MOKE	Time-resolved magneto-optical Kerr effect
XRMR	X-ray resonant magnetic reflectivity
XRR	X-ray reflectivity

Declaration

Unless explicitly stated otherwise, the work presented in this thesis is solely that of the author and has not been submitted for examination for any other degree at any University.

The SQUID-VSM measurements in chapter 4 were made with the assistance of Dr Oscar Céspedes at the University of Leeds. The SQUID-VSM measurements and anomalous Hall effect measurements in chapter 5 were made at the University of Leeds with the assistance of Dr Philippa Shepley. The optical lithography was completed with the assistance of Dr Michael Cooke and Miss Sarah Trattles.

Synchrotron experiments were coordinated by the author but involve the work of several team members. The x-ray resonant magnetic reflectivity results presented in chapter 6 and chapter 7 were performed at the XMaS beamline at the ESRF along with Dr. Del Atkinson, Dr. Aidan T Hindmarch, Mr Sinan Azawwi, Dr. Laurence Bouchenoire, Dr Simon Brown and Dr. Thomas P A Hase. Analysis of the x-ray resonant magnetic reflectivity was made by the author, though advice was provided by Dr. Matts Björck and Dr. Thomas P A Hase.

The time-resolved magneto-optical Kerr effect measurements were made at the S. N. Bose National Centre for Basic Science, Kolkata, India. The measurements were made by Mr Arnab Ganguly. However, the author was present for all the measurements used in this thesis. The fits to the magnetisation precession data were made by Mr Arnab Ganguly, except for the Pt/Co/Cu/Pt samples explicitly stated in the text which were analysed by the author. The Brillouin light scattering measurements were made at the Université Paris 13 Nord, Paris, France, by Dr Yves Roussigné. The extraction of the frequency shifts from this data was made by Dr Yves Roussigné.

Acknowledgements

There are many people that I offer my thanks and gratitude to. Firstly, my primary supervisor, Prof. Del Atkinson, for his supervision, wealth of knowledge and insight as well as my secondary supervisor Dr Aidan Hindmarch for his invaluable contribution to my supervision throughout my PhD.

I would like to thank Prof. Anjan Barman and all the members of his group at the S. N. Bose National Centre for Basics Science for their enthusiasm for the collaboration that we shared with their group.

I express my gratitude to all those involved in the Brillouin light scattering measurements at the Université Paris 13, in particular Dr Yves Roussigné and Prof. Andreï Stachkevitch.

For the x-ray resonant magnetic reflectivity measurements, I am grateful to Dr Tom Hase and Dr Matts Björck for their assistance and willingness to help. I'd also like to thank Dr Laurence Bouchenoire and Dr Simon Brown for their technical support on the beamtime runs.

I am grateful to all the people in the University of Leeds Condensed Matter Physics group, in particular Dr Oscar Céspedes, Dr Tom Moore and Dr Philippa Shepley for their help with the SQUID-VSM measurements.

I'd like to thank all the people of room 12 - though it may no longer say so on the door, it will always be room 12 - both occupants from past and present. I am grateful to David Burn, Sarah Dempsey, Samridh Jaiswal, Mustafa Tokaç, Liam Stubbington, Oto-obong Inyang, Jeovani Brandao and Sinan Azzawi. We've had many fruitful discussions, some with more Physics in than others. I am grateful to my partners in crime, Rob Williams and George Wells. As well as all the good friends I've made in the Durham Physics department.

Finally I would extend my utmost gratitude to those closest to me, both my parents, my family, and Rebekah, who have provided me with so much support throughout this process and in particular these last months whilst I have been writing my thesis.

List of publications

Enhanced electron-magnon scattering in ferromagnetic thin films and the breakdown of the Mott two-current model

R. M. Rowan-Robinson, A. T. Hindmarch, D. Atkinson.

Physical Review B, **90**, 104401 (2014)

Evolution of damping in ferromagnetic/nonmagnetic thin film bilayers as a function of nonmagnetic layer thickness

S. Azzawi, A. Ganguly, M. Tokac, **R. M. Rowan-Robinson**, J. Sinha, A. T. Hindmarch, A. Barman, D. Atkinson.

Physical Review B, **93**, 054402 (2016)

Investigating the correspondence of proximity induced magnetism and the Dzyaloshinskii-Moriya interaction at the Co/Pt interface

R. M. Rowan-Robinson, Y. Roussigné, T. P. Hase, A. T. Hindmarch, A. Thiaville, A. Stachkevitch, D. Atkinson.

In preparation

Spin-orbit torque magnetisation switching in a symmetric multilayer with weak perpendicular magnetic anisotropy

R. M. Rowan-Robinson, A. T. Hindmarch, D. Atkinson.

In preparation

Additional co-authored publications not directly related to the content of this thesis

Time-domain detection of current controlled magnetization damping in Pt/$Ni_{81}Fe_{19}$ bilayer and determination of Pt spin Hall angle

A. Ganguly, **R. M. Rowan-Robinson**, A. Haldar, S. Jaiswal, J. Sinha, A. T. Hindmarch, D. Atkinson, A. Barman.

Applied Physics Letters, **105**, 112409 (2014)

Precise control of interface anisotropy during deposition of Co/Pd multilayers

C. W. Barton, T. J. A. Slater, **R. M. Rowan-Robinson**, S. J. Haigh, D. Atkinson, T. Thompson.

Journal of Applied Physics, **116**, 203903 (2014)

Tunable Magnetization Dynamics in Interfacially Modified $Ni_{81}Fe_{19}$/Pt Bilayer Thin Film Microstructures

A. Ganguly, S. Azzawi, S. Saha, J. A. King, **R. M. Rowan-Robinson**, A. T. Hindmarch, J. Sinha, D. Atkinson, A. Barman.

Scientific Reports, **5**, 17596 (2015)

1 Introduction

1.1 Background

The aim of the field of spintronics is to exploit the spin of the electron for applications. With the development of sophisticated thin-film fabrication techniques such as sputtering and molecular beam epitaxy, this has become a reality where synthetic multilayer structures can be fabricated which exhibit magnetic properties dramatically different from their bulk counterparts. The discovery of effects unique to these multilayer structures, such as giant magnetoresistance [1, 2], has led to revolutionary advances in magnetic memory and sensors [3, 4].

A particular goal of spintronics is the realisation of a universal memory which combines high write speed, high storage density and non-volatility. Such schemes can be realised in technologies such as magnetic random access memory (MRAM) [3] and magnetic racetrack memory [5].

Within these technologies, it is required that the magnetisation state of nanoscale magnetic elements can be manipulated, be it single domain elements in MRAM or domain walls in racetrack memory. An important development for these concepts is the ability to manipulate these magnetic elements using spin-polarised currents. Here, a spin current is a flow of spin-angular momentum, that can occur even without the presence of a net charge current [6]. The transfer of this spin-angular momentum to the magnetisation can exert spin-transfer torques [7] or, as investigated in this thesis, spin-orbit torques [8], dependent on the origin of the spin-current. This can allow one to manipulate magnetisation with the use of spin-current alone, allowing one to overcome the difficulties associated with magnetic field confinement when using a magnetic field to write information, and thereby improving the scalability of the devices.

However, the mechanism of this process is complex, and in particular with regard to the spin-orbit torques, the realisation of this requires a thorough understanding of a variety of interfacial and spin-orbit effects. For example, magnetic damping [9], which describes the dissipation of energy from magnetisation precession, will act to counter magnetisation dynamics induced by the spin-orbit torques. Alongside this, the Dzyaloshinskii-Moriya interaction (DMI) [10, 11] is an interfacial effect [12] that can promote chiral spin textures [13] and as discussed later plays a crucial role in the use of spin-orbit torques [14] for the manipulation of magnetic domain walls and magnetic elements.

All these effects, magnetic damping, DMI and spin-orbit torques, are expected to play an important role in determining the viability of these future technologies and are investigated in this thesis. Furthermore, all of these effects originate from the spin-orbit interaction, and the importance of this effect is discussed in the next section.

1.1.1 Spin-orbit interaction phenomena

The relativistic interaction of the electron's spin with its orbital angular momentum gives rise to the spin-orbit interaction (SOI). This subtle effect is responsible for a large number of phenomena both well established and also at the forefront of research in spintronics. Some examples, and by no means a comprehensive list, include: intrinsic magnetic damping [15], magnetostriction [16], anisotropic magnetoresistance [17], anomalous Hall effect [18], spin-Hall effect [19], Rashba effect [20] and the DMI [10, 11]. To help further the understanding of these phenomena, the work in this thesis studies the anisotropic magnetoresistance (AMR) effect, magnetic damping, the DMI and the spin-orbit torques.

In perpendicularly magnetised nanowires, the DMI acts as an effective internal magnetic field that stabilises Néel domain walls that would ordinarily be energetically unfavourable [13, 21]. This has particular importance with regard to the spin-orbit torques. The microscopic origin of the spin-orbit torques is in the spin-Hall and Rashba effects, which originate from the SOI and give rise to spin-currents at the ferromagnet interface which can be used to exert a torque on the magnetisation. These are discussed in detail in chapter 2. With regard to this, the importance of the DMI effect is that the symmetry of the torques due to these spin-currents is such that they can only drive Néel domain walls [13]. However, with this in place, the spin-orbit torques have been shown to be ex-

tremely efficient at driving domain walls in these systems [22]. Furthermore they have been demonstrated capable of inducing magnetisation reversal with the application of an electric current [23, 24]. This removes the need for an external magnetic write field, which dramatically improves scalability and lowers power consumption.

Also investigated in this thesis is the AMR effect, fundamental to which is the SOI, which gives rise to the asymmetry in electrical resistivity with respect to the magnetisation orientation and is discussed in chapter 2. AMR is a well established effect and was discovered by Thompson over 150 years ago [25], and it is testament to its resilience as a research topic that the AMR family of effects is still growing, where in the past decade the discovery of the new ballistic AMR [26], coulomb blockade AMR [27] and interfacial AMR [28] effects has renewed interest in the effect as a research topic. Furthermore, in industry, AMR still finds applications in magnetic-resistive field sensors [29, 30].

Fundamentally, the DMI and Rashba effects are interfacial in their very nature, both requiring the combination of the SOI and structural inversion asymmetry present at an interface. Furthermore, in order for the Rashba and spin Hall effects to exert a torque on a magnetisation, a spin-current needs to diffuse across an interface, which in turn depends on the interfacial spin-mixing conductance [31]. Therefore it is clear that the spin-orbit interaction and its related phenomena are not the only important consideration in the development of these future technologies and the interfaces in these multilayer structures also carry significant importance.

1.1.2 The importance of interfaces

The SOI is likely to play an important role in the future technological developments within spintronics, but when considering layers of material that are only a few atoms thick, and comprised of multiple layers of different materials, the interface can make up a significant proportion of the total volume of the film and have dramatic effects. The interface describes the transition between adjacent layers in the multilayer and has a structure which can influence the properties within the layers themselves. In electron band theory, overlapping bands with different chemical potentials must join at the interface, which modifies the electronic and magnetic properties of the material in this region through hybridisation. Some examples regarding the importance of the interface that relates to these effects are

discussed below.

An early example of the effect that interfaces can have on the observed properties of thin films is the rapidly rising resistivity due to the interfacial contribution to electrical scattering when the film thickness is comparable or less than the electron mean free path. This additional resistivity contribution is known as Fuchs-Sondheimer scattering [32, 33]. Furthermore, the physical structure of the interface can influence the contributions from diffuse and specular interfacial scattering [34], which in turn can modify the magnitude of the AMR effect [35, 36]

The interface also contributes energetically, whereby there is an energy contribution associated with the surface anisotropy constant. This is the origin of perpendicular magnetic anisotropy. As the ferromagnetic film thickness is reduced, the surface contribution can be so strong that the energy cost due to the demagnetisation field associated with out-of-plane magnetisation can be overcome [37]. This has found applications in the latest generation of magnetic hard-disk drives, since perpendicularly magnetised domains have better scalability, allowing much higher storage densities than their longitudinal counterparts.

The interface has a structure that defines the transition between adjacent layers of the multilayer. It has been shown that the physical structure of the interface is crucial for the spin-mixing conductivity and the efficiency of the spin-orbit torques [31]. Furthermore, experiments where the interface has been systematically modified using focused ion beam irradiation have shown it is possible to modify the magnetic damping [38] and also perpendicular magnetic anisotropy [39].

Alongside the physical structure, the way in which the magnetism changes at an interface can also be important, particularly when a ferromagnet is interfaced with a late-*d* transition metal such as Pt or Pd. In these circumstances the ferromagnetism extends past the physical interface and into the non-magnetic layer [40, 41]. This spontaneous polarisation of paramagnetic metals is known as proximity induced magnetism (PIM) and occurs due to the hybridisation of atomic orbitals at the interface. Since the spin-orbit interaction scales with atomic weight, the PIM in Pt results in a magnetic region with a significant SOI at the interface. Within this thesis, this particular interfacial effect is investigated in detail, whereby the effects of the PIM in Pt are studied with regard to magnetic damping and DMI.

This thesis is a study of phenomena arising due to the SOI, with a focus on highlighting where relevant the role of the interface. A greater understanding of the fundamental physics associated with these effects could lead to further improvements and increased efficiency where these phenomena are already found in applications, for example the use of the AMR effect in magneto-resistive field sensors. Alternatively, developments in the understanding of SOTs could pave the way for completely new forms of spin-torque MRAM where switching of magnetic bits is achieved using spin-polarised current.

1.2 Aims and thesis outline

1.2.1 Aim of the thesis

The aim of this thesis is to explore phenomena resulting from the spin-orbit interaction and to develop the understanding of the role of the interfaces in these systems. A detailed understanding of the contribution of interfacial effects in these phenomena may lead to the design of new materials in which the respective spin-orbit phenomena are enhanced. Particular attention is given to the contribution of the interfacial proximity magnetism induced in Pt, for which two chapters are devoted to the study and characterisation of this in various Pt/Co/Pt multilayers, since this would give rise to a polarised interfacial region with a significant spin-orbit interaction, and how this may influence the DMI and magnetic damping.

1.2.2 Thesis outline

Chapter 2 describes the relevant theoretical concepts necessary for the discussion and analysis of the results in this thesis. The phenomena are described and the underlying role of the spin-orbit interaction in each effect is explained.

Chapter 3 introduces the main investigative techniques used to study the interfacial and spin-orbit phenomena in this thesis. This includes a discussion of the origin of the effect being used for the measurement as well as the measurement technique itself and a description of the experimental methodology.

Chapter 4 presents measurements of the AMR effect investigated in Ni, $Ni_{95}V_5$ and

$Ni_{95}Cr_5$ films of various thickness. In conjunction with this, SQUID-VSM is used to characterise the samples magnetically and x-ray reflectivity and transmission electron microscopy are used to characterise them structurally. From the combination of these measurements the contribution of the interfaces to AMR as the film thickness is reduced is investigated.

In chapter 5, SOTs are investigated using a combination of polar and longitudinal magneto-optical Kerr effects as well as the anomalous and planar Hall effects. Measurements of the SOTs made in films with in-plane and out-of-plane magnetic anisotropies are presented. Samples with and without structural inversion asymmetry are fabricated in order to compare the role of the Rashba effect.

In chapter 6 the first series of measurements within this thesis of the PIM in Pt are presented. The induced moment on Pt is characterised using x-ray resonant magnetic reflectivity (XRMR) at the Pt L_3-edge in Pt/Co/Pt multilayers with in-plane magnetic anisotropy. Spacer layers of Au or Ir of increasing thickness are inserted at the top Co/Pt interfaces and the dependence of the induced moment on spacer layer thickness and morphology is investigated.

Chapter 7 presents further XRMR studies of the PIM in Pt within Pt/Co/Pt multilayers, but as a function of the changing magnetic anisotropy of the Co from in-plane magnetic anisotropy to perpendicular magnetic anisotropy with reducing Co thickness. Element specific hysteresis loops measured at the Pt L_3-edge and longitudinal magneto-optical Kerr effect (MOKE) hysteresis loops are used to compare the magnetisation reversal of the proximity polarised Pt with that of the Co as the magnetic anisotropy of the Co layer is changed.

In chapter 8, using the same samples from chapter 6, where the PIM was characterised as a function of Au and Ir spacer layers, time-resolved MOKE measurements are presented from which the magnetic damping is extracted as function of spacer layer thickness. The spacer layer thickness dependence of magnetic damping is compared with that of the induced moment in Pt. Furthermore, Brillouin light scattering was used to extract the interfacial DMI constant for these same multilayers and likewise the results are compared with the spacer layer dependence of the induced moment in Pt.

In chapter 9, the thesis concludes with a summary of the key findings as well as a discussion of further work.

2 Theoretical aspects

This chapter discusses the theoretical concepts that are relevant to the phenomena referred to throughout this thesis. It provides background information and also emphasises the underlying link, which is frequently found at the root of the explanations and is the spin-orbit interaction.

The chapter is broadly split into two halves, each with two sub-sections. The first section addresses magnetic interactions, starting with a brief introduction to the origin of ferromagnetism through a discussion of the exchange interaction arising between electron spins. Following this, the spin-orbit interaction is introduced and the antisymmetric Dzyaloshinskii-Moriya interaction. The second part of this first section discusses the proximity induced magnetisation effect, the study of which forms a significant part of this thesis. The discussion introduces the Stoner criterion, which outlines a fundamental requirement for ferromagnetism, and discusses how ferromagnetic interactions can arise in a Stoner-enhanced paramagnet such as Pt or Pd at the interface with a ferromagnet.

The second half addresses electrical transport phenomena in the presence of the spin-orbit interaction. This includes the anisotropic magnetoresistance effect, which is discussed in detail, and in particular with regard to the model of Campbell, Fert and Jaoul. An explanation of the effect in the context of the spin-orbit interaction is given. In the final section, the role of spin-orbit torques is addressed, both the influence they have on magnetisation dynamics in context of the Landau-Lifshitz-Gilbert equation but also the proposed microscopic origins of the spin Hall and Rashba effects.

2.1 Magnetic moments and interactions

Spin is a fundamental property of the electron. However, in many materials the electron spins are arranged in such a way that there is no net moment. In diamagnetic materials, the

electron sub shells are fully occupied resulting in no net spin or orbital angular momentum. In paramagnetic materials there exists unpaired electrons and a net moment per atom, but no internal interaction between the electrons to cause spontaneous alignment of the moments. The application of an external magnetic field in a paramagnet will cause electrons to align their spin along the field direction due to the Zeeman interaction. In ferromagnets, this field exists inherently within the material and arises due to the *exchange interaction* which causes the spins to spontaneously align parallel to each other.

2.1.1 The exchange interaction

Weak magnetic dipolar interactions can give rise to magnetic ordering, but at room temperature these are easily overcome by thermal fluctuations [42]. In order to explain room temperature ferromagnetism, there must exist another much stronger interaction. This interaction is the *exchange interaction* and it is a quantum mechanical interaction between electrons.

Consider the combined wavefunction of two electrons. They are indistinguishable, hence the overall wavefunction must be either symmetric or anti-symmetric upon particle exchange. However, since electrons are fermions, the Pauli exclusion principle requires that the overall wavefunction is antisymmetric.

The total wavefunction will thus be the sum of the spatial and spin parts for the two electrons. We can therefore write two anti-symmetric wavefunctions that satisfy this criteria

$$\Psi_S = \frac{1}{\sqrt{2}}\Big[\psi_i(\boldsymbol{r}_1)\psi_j(\boldsymbol{r}_2) + \psi_i(\boldsymbol{r}_2)\psi_j(\boldsymbol{r}_1)\Big]\chi_S \tag{2.1.1}$$

$$\Psi_T = \frac{1}{\sqrt{2}}\Big[\psi_i(\boldsymbol{r}_1)\psi_j(\boldsymbol{r}_2) - \psi_i(\boldsymbol{r}_2)\psi_j(\boldsymbol{r}_1)\Big]\chi_T \tag{2.1.2}$$

where Ψ_S is the singlet wavefunction, containing a symmetric spatial component and anti-symmetric spin singlet component χ_S. Ψ_T is the triplet wavefunction, comprised of an anti-symmetric spatial component and symmetric spin triplet component χ_T. For ferromagnetism, Ψ_T must have the lower energy of the two wavefunctions.

The *exchange integral* $\boldsymbol{J}_{ij}$, is related to the energy difference ($\Delta E = E_{\text{Singlet}} - E_{\text{Triplet}}$)

between the states Ψ_S and Ψ_T by,

$$\boldsymbol{J}_{ij} = \int \psi_i^*(\boldsymbol{r}_1)\psi_j^*(\boldsymbol{r}_2)\hat{\mathcal{H}}\psi_i(\boldsymbol{r}_2)\psi_j(\boldsymbol{r}_1)\, d\boldsymbol{r}_1 d\boldsymbol{r}_2 = \frac{\Delta E}{2} \tag{2.1.3}$$

where $\hat{\mathcal{H}}$ is the complete Hamiltonian, which includes the total energy contributions from both electrons. Hence, if $\boldsymbol{J}_{ij} > 0$ then the triplet spin state has the lower energy and parallel spin alignment gives ferromagnetic order. Likewise if $\boldsymbol{J}_{ij} < 0$ then the spin singlet state has lower energy and antiferromagnetic alignment of spins is favoured.

In the Heisenberg model, $\boldsymbol{J}_{ij}$ arises in the exchange Hamiltonian, $\hat{\mathcal{H}}_{\text{ex}}$, for an n-body system of electrons and has the form;

$$\hat{\mathcal{H}}_{\text{ex}} = -2\sum_{i>j}^{n} \boldsymbol{J}_{ij}\hat{\boldsymbol{S}}_i \cdot \hat{\boldsymbol{S}}_j \tag{2.1.4}$$

here, $\boldsymbol{J}_{ij}$ parametrises the type (ferromagnetic or antiferromagnetic) and strength of the exchange coupling. The operators $\hat{\boldsymbol{S}}_i$,$\hat{\boldsymbol{S}}_j$ are the spin momentum operators for each i, j electron.

As shown in equation (2.1.3), $\boldsymbol{J}_{ij}$ is a function of position $\boldsymbol{r}$ and depends on the overlap of the wavefunctions. The Bethe-Slater, curve illustrated in Fig. 2.1, shows calculations of $\boldsymbol{J}_{ij}$ as a function of the ratio a/r_d, where a is the interatomic separation and r_d is the radius of the partially filled d-orbital. The ratio a/r_d roughly parametrises the amount of orbital overlap between atoms for the $3d$-transition metals. The exchange integral correctly predicts the antiferromagnetic coupling of Cr and Mn and rises to a maximum for the ferromagnetic $3d$ elements Fe, Co and Ni. The Bethe-Slater curve demonstrates that the sign of the exchange interaction is dependent on the interatomic and interelectronic spacing [43].

We can understand the exchange interaction in terms of the competition between Coulomb repulsion and kinetic energy. If we consider two electrons occupying the same atom, the triplet state is generally the lower energy state since this requires an antisymmetric spatial component which minimises the Coulomb repulsion. This is the origin of Hund's first rule [42]. In the $4f$ ferromagnets Gd and Dy, the localised orbitals retain their atomic character hence the triplet state is favoured by the same argument. However, there is very little overlap of these orbitals, hence the magnitude of $\boldsymbol{J}_{ij}$ is small. Consequently these ferromagnets have low Curie temperatures.

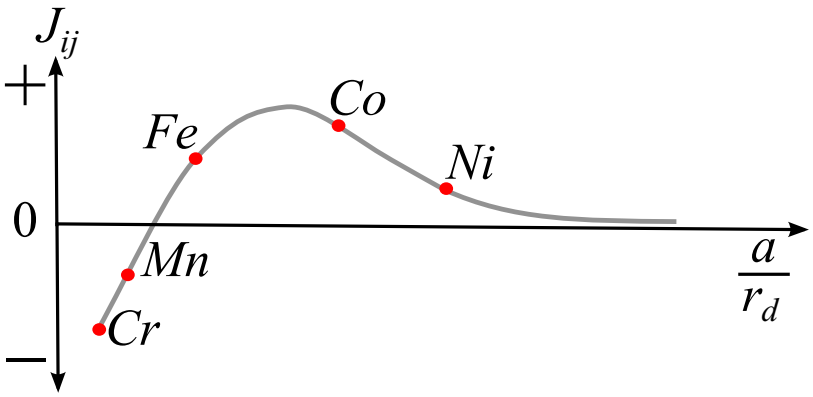

Figure 2.1: Bethe-Slater curve demonstrating how the sign and magnitude of the exchange integral, J_{ij}, depends on the overlap of the atomic d-orbitals. Cr and Mn are antiferromagnets since $J_{ij} < 0$ whilst Fe, Co and Ni are ferromagnets since $J_{ij} > 0$.

In transition metals, the onset of ferromagnetism is dictated by the competition between the energy cost of the Coulomb repulsion when occupying overlapping spatially symmetric orbitals and the higher kinetic energy associated with occupying spatially anti-symmetric orbitals. For the 3d ferromagnets Ni, Fe and Co, there exists a large density of d-states near to the Fermi energy, hence the Coulomb repulsion cost is greater than the kinetic energy gain and for these materials the spin triplet state is favoured.

In the next section the self interaction between electron spin and orbital angular momenta is addressed, namely the spin-orbit interaction.

2.1.2 Spin-orbit interaction

A significant amount of phenomena within the field of magnetism occurs as a direct result of the coupling between the electron spin and orbital angular momenta. The *spin-orbit interaction* (SOI) gives rise to magnetocrystalline anisotropy and provides a mechanism for energy dissipation to the lattice, as is observed in magnetic damping. It also results in spin-dependent scattering which leads to the spin Hall effect, and in ferromagnets the anomalous Hall effect and anisotropic magnetoresistance. Further to this it can give rise to relativistic magnetic fields in the frame of reference of the electron and consequently the Dresselhaus and Rashba fields in systems lacking inversion symmetry.

Semiclassically, the origin of the SOI can be understood by considering an electron orbiting a nucleus. As shown in Fig. 2.2, in the frame of reference of the electron, the electron is stationary and the nucleus orbits it forming a closed current loop. This orbit-

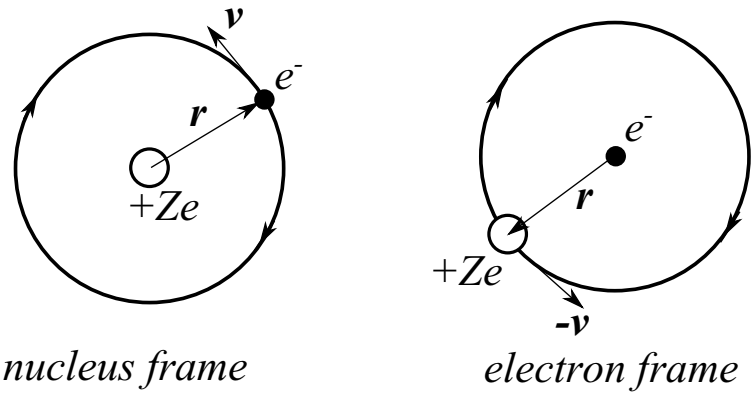

Figure 2.2: In the frame of reference of the nucleus, the electron orbits with velocity $\boldsymbol{v}$. However, in the frame of reference of the electron, it observes a positive nuclei with charge $+Ze$ and velocity $-\boldsymbol{v}$ which forms a closed current loop around it. Consequently the electron experiences a magnetic field due to its orbital angular momentum.

ing positive charge then produces a magnetic field which interacts with the electron spin. Consequently, the orbital motion of the electron is coupled to its spin. For a single electron orbiting a positively charge nucleus, the SOI Hamiltonian is given by;

$$\hat{\mathcal{H}}_{\mathrm{SOI}} = \frac{Ze^2}{2m_{\mathrm{e}}^2 c^2 r^3} \boldsymbol{L} \cdot \boldsymbol{S} \tag{2.1.5}$$

where m_{e} is the electron's mass, Z is the atomic number of the nuclei and r is the radius of the electron orbital. The expectation value $\langle r^{-3} \rangle \propto Z^3$, hence the SOI scales with Z^4 [42], which explains why the SOI is strong in heavy elements such as Pt, Ta and Ir. However, it is important to note that orbital hybridisation also plays a significant role when considering complete crystals rather than single atoms.

When calculating the response of a system to the SOI, it is generally introduced as a perturbation of the form;

$$\hat{\mathcal{H}}_{\mathrm{SOI}} = \lambda \boldsymbol{L} \cdot \boldsymbol{S} \tag{2.1.6}$$

where λ is a constant that is proportional to the strength of the SOI. Here, the SOI is considered a small effect that can be applied after the strong contributions from the crystal field have been calculated. This is known as the $\boldsymbol{L}$-$\boldsymbol{S}$ coupling regime, by which the total angular moment $\boldsymbol{J}$ is computed and the SOI is applied as a small perturbation later. This is valid for the lighter elements, including the transition metals and is the method by which the anisotropic magnetoresistance is evaluated. Since the SOI scales as Z^4, for the

heavy elements the spin orbit coupling is dominant, and must be applied to each electron individually when calculating $\boldsymbol{J}$. This is referred to as the $\boldsymbol{J}$-$\boldsymbol{J}$ coupling regime.

The SOI has consequences for the exchange interaction and can lead to an anisotropic exchange interaction referred to as the Dzyaloshinksii-Moriya interaction (DMI), which is discussed in the next section.

2.1.3 Dzyaloshinskii-Moriya interaction

The exchange interaction acts directly between spins and is extremely short ranged. However, there exists a variety of indirect exchange mechanisms in materials that can lead to magnetic polarisation over larger lengthscales. An example of this, which is also relevant to the explanation of the DMI, is superexchange. This exists in a number of ionic solids, by which the short ranged exchange interaction between two non-neighbouring magnetic ions is mediated by a non-magnetic ion that resides between them. This generally results in antiferromagnet coupling, since in most systems this allows the electrons to explore a greater number of excited states which would be disallowed by the exclusion principle with a ferromagnetic interaction and therefore lowers the total kinetic energy.

In the same manner as superexchange, the SOI can play the role of the non-magnetic ion, mediating an indirect exchange between two ferromagnetic atoms through the ground states and excited states of the non-magnetic heavy metal. This type of exchange interaction is called the Dzyaloshinskii-Moriya interaction. The generalised form for the interaction is;

$$\hat{\mathcal{H}}_{\mathrm{DM}} = \boldsymbol{D}_{ij} \cdot \boldsymbol{S}_i \times \boldsymbol{S}_j \tag{2.1.7}$$

where $\boldsymbol{D}_{ij}$ is the Dzyaloshinkii-Moriya vector, which is non-zero only in the presence of inversion asymmetry and acts orthogonal to the plane of the spins $\boldsymbol{S}_i$ and $\boldsymbol{S}_j$. This is illustrated in Fig. 2.3 a) where the configuration of the two spins results in a DMI vector that points into the page. This antisymmetric interaction was first predicted by Dzyaloshinkii through symmetry arguments [11], later a microscopic model which expresses $\boldsymbol{D}_{ij}$ in terms of hopping integrals and kinetic energy with analogy to superexchange was developed by Moriya [10].

This type of exchange favours spin orientated orthogonal to each other in such a way

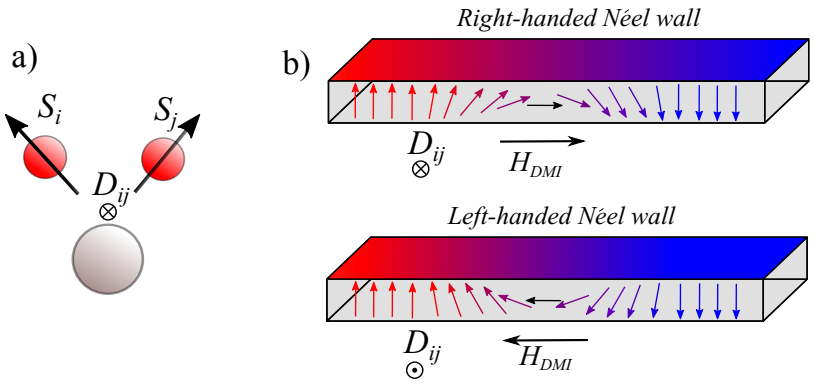

Figure 2.3: a) The DMI energy is minimised for orthogonal alignment of spins $\boldsymbol{S_i}$ and $\boldsymbol{S_j}$ exchange coupled via the strong SOI of a heavy metal ion. b) The DMI vector $\boldsymbol{D_{ij}}$ dictates the sign of the effective magnetic field $\boldsymbol{H}_{\mathrm{DMI}}$ and consequently the chirality of the Néel wall.

that the DMI vector $\boldsymbol{D}_{ij}$ is negative. In this way the DMI gives rise to weak ferromagnetism in antiferromagnetic materials by causing a slight canting of spins away from the anti-parallel configuration.

Dzyaloshinskii-Moriya interaction in ferromagnetic thin films

The inversion asymmetry at an interface can modify the crystal field such that with an appreciable SOI the DMI can have significant effects. This is manifested in perpendicularly magnetised Pt/Co multilayers [13,44], where the interfacial DMI constitutes an effective in-plane magnetic field which stabilises the Néel domain wall configuration which otherwise would be energetically unfavourable [45]. As shown in Fig. 2.3 b), this in-plane field exists only inside the domain wall and acts along the length of the wall. This also induces a specific chirality to the Néel wall which is dependent on the sign of $\boldsymbol{D}_{ij}$ [13,45].

2.2 Proximity induced magnetism in paramagnetic metals

In the previous section, magnetic interactions within ferromagnetic materials were discussed. In this section magnetic interactions are considered that can be induced in a material which is usually paramagnetic but can become magnetised under certain conditions. There are a variety of ways that this can occur, for example, alloying the paramagnet with a ferromagnet [46,47] or forming the paramagnet from nanoparticles [48], but they all originate from local modifications to the density of states and the subsequent satisfaction of the

Stoner criterion.

In this discussion we focus on *proximity induced magnetism* (PIM), and in particular that which occurs in the paramagnetic metals Pt and Pd. Here, the paramagnet can obtain a spontaneous magnetic polarisation at the interface with a ferromagnet that generally exists over a length of the order of 1 nm into the paramagnet.

Microscopically, PIM can be explained using a Hubbard model where the interaction energy between atomic sites is given some degree of spatial dependence [49, 50]. From *ab initio* calculations it was demonstrated that the induced moment can be attributed to orbital hybridisation between the ferromagnet and the paramagnet [51]. An enhanced density of states would then lead to Stoner enhanced paramagnetism in the non-magnetic layer.

In Stoner enhanced paramagnetism, a paramagnet with a large density of states at the Fermi energy, such as Pt or Pd, shows a significantly enhanced magnetic susceptibility. This is due to these materials being very close to satisfying the Stoner criterion. This is an inequality derived by E. C. Stoner [52] that relates the density of states and the exchange interaction with itinerant ferromagnetism. At the interface with a ferromagnet, the orbital hybridisation can result in an enhancement of the density of states such that the paramagnet can satisfy the Stoner criterion and develop ferromagnetism.

2.2.1 The Stoner criterion

The Stoner criterion for itinerant ferromagnetism requires that;

$$I.g(E_{\mathrm{F}}) > 1 \tag{2.2.8}$$

where, I is the exchange integral, which is proportional to the strength of the exchange interaction and $g(E_{\mathrm{F}})$ is the density of states at the Fermi energy.

The criterion can be understood by considering the existence of an internal effective magnetic field inside the Pauli paramagnetic metal.

When a magnetic field is applied to a metal, Pauli paramagnetism arises because the Zeeman energy lifts the degeneracy of the spin $\uparrow$ and spin $\downarrow$ bands, shifting them by $\pm\mu_{\mathrm{B}}\mu_0 H$. This is shown schematically in Fig. 2.4. Occupied spin $\downarrow$ states get pushed above E_{F} and vacant spin $\uparrow$ states get pushed below E_{F}. There is therefore a transfer of

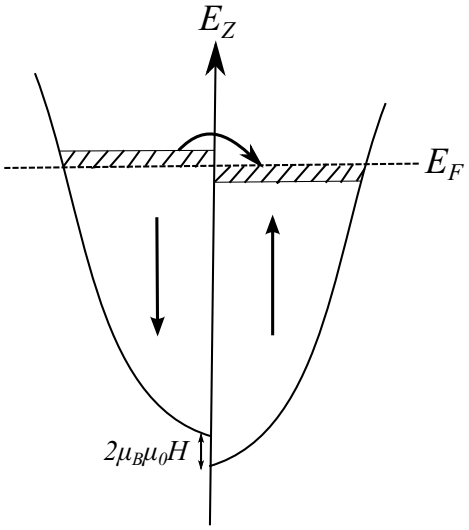

Figure 2.4: Schematic density of states of a metal. Application of a magnetic field causes a small shift in energy of spin ↑ and spin ↓. There then follows a transfer of electrons from spin ↓ states into the lower energy vacant spin ↑ states.

spin ↑ to spin ↓ states, thereby inducing a small polarisation.

The number of electrons that have moved from spin ↑ states to spin ↓ states is given by $n_\uparrow = g(E_\mathrm{F})\mu_\mathrm{B}\mu_0 H$, where $g(E_\mathrm{F})$ is the density of states at the Fermi energy. This gives a magnetisation of;

$$M = \mu_\mathrm{B}(n_\uparrow - n_\downarrow) = 2\mu_\mathrm{B}^2 g(E_\mathrm{F})\mu_0 H \tag{2.2.9}$$

and the Pauli susceptibility as;

$$\chi_P = \frac{M}{H} = 2\mu_\mathrm{B}^2 g(E_\mathrm{F})\mu_0. \tag{2.2.10}$$

In the Stoner model, the exchange interaction is inserted as an internal molecular field, $H_\mathrm{mol} = \lambda M$, where λ is the exchange constant. The magnetisation is therefore given by

$$M = \chi_P(H + H_\mathrm{mol}) = \chi_P(H + \lambda M). \tag{2.2.11}$$

Rearranging this for the susceptibility gives,

$$\chi = \frac{M}{H} = \frac{\chi_P}{(1 - \lambda\chi_P)}. \tag{2.2.12}$$

This is plotted in Fig. 2.5, where it can be seen that metals such as Pt and Pd with a large

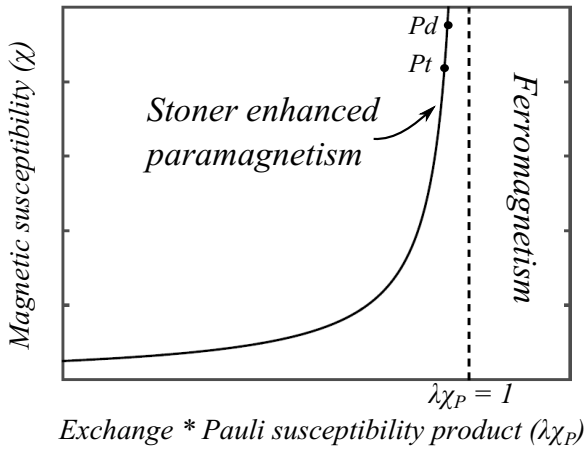

Figure 2.5: Magnetic susceptibility, χ, plotted as a function of $\lambda\chi_P$, demonstrating the dramatic enhancement of χ in materials such as Pt and Pd, where a large g(E_F) results in a large Pauli susceptibility, χ_P.

Pauli susceptibility exhibit a significant enhancement to their magnetic susceptibility. From equation (2.2.10), it can be seen that χ_P depends only on the density of states at E_F, hence material with large g(E_F) can be referred to as Stoner enhanced paramagnets. The equation diverges where $\lambda\chi_P = 1$, above which spontaneous magnetism occurs. Materials such as Pd and Pt are therefore close to the onset of itinerant ferromagnetism.

Now, with $\lambda\chi_P > 1$ as the requirement for itinerant ferromagnetism, where $\chi_P \propto g(E_F)$ and $\lambda \propto I$, this expression leads to the Stoner criterion.

An enhancement of $g(E_F)$ in Pd or Pt can induce a transition into a ferromagnetic phase. This can be achieved through doping with small amounts of ferromagnetic impurities [46, 47], reducing the dimensionality by forming nanoparticles [48] or by the proximity to a ferromagnet in the interfacial region [40].

2.2.2 Proximity induced magnetism in the *5d* elements

In an x-ray magnetic circular dichroism study by Wienke *et al.* [53], it was found that all the 5*d* series of elements take on some form of polarisation when introduced as an impurity within Fe. It can be seen from Fig. 2.6 that the coupling between the impurity and the local moment changes from antiferromagnetic to ferromagnetic between Os and Ir. The reason for this is related to whether spin ↑ or spin ↓ electrons form the majority species from the spin-polarised density of states for the impurity [54]. It can also be seen that there is significant polarisation of Pt, as expected from the Stoner enhanced paramagnetism.

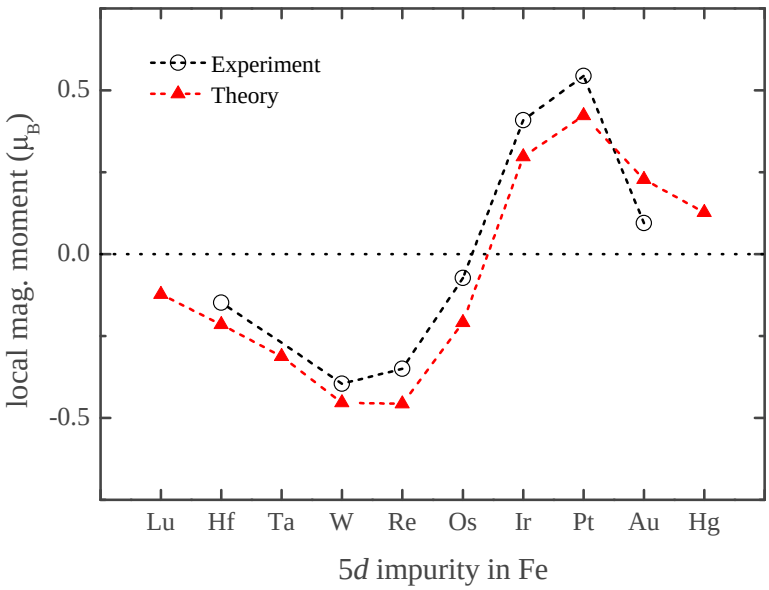

Figure 2.6: Magnitude of proximity induced moment and sign relative to the host Fe ferromagnet for 5*d* transition metal impurities. The measured moments from experiment are sourced from [53] and the theoretical values from [54].

These heavy metal elements, in particular Pt, are used regularly within the field of spintronics due to their significant SOI, which as discussed, gives rise to interesting phenomena such as the DMI. Connections are now beginning to be drawn between the interfacial PIM and these phenomena. In particular work by S. S. P. Parkin [55] has suggested a strong correlation between the DMI and PIM from observations of current-induced domain wall motion within perpendicularly magnetised Pt/Co/Ni/Co structures. However, *ab initio* calculations are in disagreement with this result, finding no link between PIM and DMI [56]. These results are discussed in detail and in the context of the studies of the PIM in Pt presented here in chapters 6 and 8.

In the next section the discussion moves towards magnetotransport phenomena in the presence of the SOI, focussing first on the anisotropic magnetoresistance effect followed by the current-induced spin-orbit torques.

2.3 Anisotropic magnetoresistance

Fundamentally, the *anisotropic magnetoresistance* (AMR) effect is a difference in resistivity that depends on the axis of the magnetisation relative to the current flow. Unlike

ordinary magnetoresistance due to the Lorentz force, AMR depends on the magnetisation orientation and not the magnetic field. Consequently it only occurs in materials with a spontaneous magnetisation. Early evidence for the role of SOI within AMR stemmed from studies of the compositional dependence of AMR using $Ni_{1-x}Fe_x$ alloys, finding maximum AMR for compositions with zero magnetocrystalline anisotropy and zero magnetostriction [57] as well as a minimum in the anomalous Hall effect [16], and indeed an explanation of AMR can be found by applying the spin-orbit perturbation from equation (2.1.6).

However, in order to describe the AMR effect, first it is necessary to discuss the *Mott two-current model* which describes the electrical resistivity of itinerant ferromagnets. The Mott two-current model forms the foundation of the explanation of AMR proposed by Smit [17] as well as that of the additions to the theory made by Campbell, Fert and Jaoul [58]. Both of these developments in the understanding of AMR are discussed in here.

2.3.1 Mott two-current model

Mott developed the two-current model in order to explain the decrease in resistivity that a ferromagnet undergoes when cooled below its Curie temperature [59]. He was able to show that the flow of current in a ferromagnet can be described by the conduction via two separate channels, one populated by spin ↑ electrons and the other by spin ↓ electrons.

Firstly, it is assumed that magnon scattering events can be ignored for a ferromagnet at $T<<T_c$ and therefore the dominant scattering mechanisms are spin conserving. This means that spin ↑ and spin ↓ electrons conduct in parallel channels with negligible cross scattering between the spin states.

Next, by considering the structure of the density of states for a transition metal ferromagnet, as shown in Fig. 2.7 a), it can be seen that itinerant ferromagnets have a significant number of available $3d$ states close to the Fermi energy. The exchange interaction causes significant spin splitting of the $3d$ bands resulting in one spin species having a larger density of states at the Fermi energy, defined as spin ↓. However, for the spin ↑ $3d$ states, the exchange interaction acts to place these states below the Fermi energy, and consequently they are fully occupied.

Due to the large curvature of the d bands, electrons in these states have a large effective

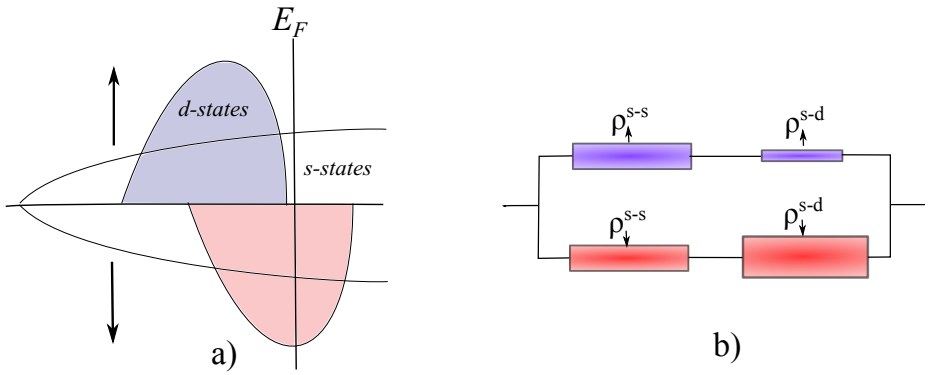

Figure 2.7: a) Schematic density of states for a ferromagnet. b) Schematic parallel resistor model. The size of the resistors reflects the resistivity of the particular scattering pathway.

mass, and the greatest contribution to the resistivity arises from $s \rightarrow d$ scattering events. Therefore, almost all the current is carried by $4s$ electrons. Consequently, since there is an abundance of available resistive $3d$ states for spin $\downarrow$ electrons to scatter into, $\rho_{\downarrow}$ is significantly larger than $\rho_{\uparrow}$. This is portrayed schematically in Fig. 2.7 b) by the relative difference in the size of the resistors.

From the parallel conduction, the total resistivity ρ at T<<T_c can be written as;

$$\rho = \frac{\rho_{\uparrow}\rho_{\downarrow}}{\rho_{\uparrow} + \rho_{\downarrow}}. \tag{2.3.13}$$

Magnon spin-flip scattering in the Mott two-current model

The temperature dependence of the magnon density of states means that for most ferromagnets, spin-flip scattering cannot be disregarded entirely at room temperature. This is observed as a deviation from Matthiesson's rule with rising temperature [60]. Using a Boltzmann analysis, Fert was able to describe the temperature dependence of resistivity in itinerant ferromagnets within the Mott two-current model [60, 61].

By including contributions from electron-magnon scattering, the following expression was obtained;

$$\rho(T) = \frac{\rho_{\uparrow}\rho_{\downarrow} + \rho_{\uparrow\downarrow}(\rho_{\uparrow} + \rho_{\downarrow})}{\rho_{\uparrow} + \rho_{\downarrow} + 4\rho_{\downarrow\uparrow}} \tag{2.3.14}$$

where the inclusion of a *spin-mixing resistivity* term $\rho_{\downarrow\uparrow}$ parametrises the spin-flip electron-magnon scattering. Each resistivity term includes contributions from impurity scattering and the temperature dependence with the form, $\rho_{\sigma} = \rho^0_{\sigma} + \rho^i_{\sigma}(T)$ where $\sigma = \uparrow$ or $\downarrow$. The

residual resistivity ρ_σ^0 is associated with the density of states and in particular how the inclusion of impurities modifies this. This is of particular importance for the Campbell, Fert and Jaoul model, which describes AMR in lightly-doped ferromagnetic films and is discussed later. The intrinsic temperature dependent terms $\rho_\sigma^i(T)$ depend on the host ferromagnet only and are independent of impurities. This particular work was very successful in explaining the temperature dependent resistivity of ferromagnetic films and it was this experimental validation of two-current conduction in ferromagnets that paved the way for the discovery of giant magnetoresistance [1, 2].

Within the Mott two-current model the magnetisation is included implicitly through the exchange split d-bands. However, in this model the conductivity remains isotropic with respect to the magnetisation direction. AMR can be included within this model though by the addition of the SOI, and this is discussed in the next section.

2.3.2 Anisotropic magnetoresistance explained with the spin-orbit interaction

In general, the resistivity anisotropy of the AMR effect is such that the resistance is a maximum when the magnetisation is oriented parallel to the current flow $\rho_\parallel$ and a minimum when the magnetisation is transverse to the current flow $\rho_\perp$, such that the angular dependence of AMR follows a $\sim\cos^2\theta$ relationship. The absolute resistivity change due to AMR, $\Delta\rho$, and the AMR ratio, $\Delta\rho/\rho$, are defined as;

$$\Delta\rho = \rho_\parallel - \rho_\perp \tag{2.3.15}$$

$$\frac{\Delta\rho}{\rho} = \frac{\rho_\parallel - \rho_\perp}{\rho_\perp}. \tag{2.3.16}$$

There are two mechanisms by which a resistivity anisotropy can be obtained, either by an anisotropic scattering potential with isotropic wavefunctions or alternatively an isotropic scattering potential with anisotropic wavefunctions.

Here, the model outlined by Smit [17] is discussed, this considers the latter method to be the explanation. The SOI contributes to mixing of the spin states which gives the required asymmetry in the wavefunction. The mixing of the states allows spin-flip scattering which in turn allows holes to be created in the spin $\uparrow$ d-band, which, as outlined in the Mott

two-current model, was fully occupied prior to the SOI. Consequently, the available holes in the spin ↑ d-band results in an enhancement of $\rho_{\uparrow}^{s-d}$ in Fig. 2.7 b) and it is this term that leads to the AMR effect.

Smit included the SOI perturbation introduced in equation (2.1.6) and computed the resulting perturbed wavefunctions, whilst taking the magnetisation to be along the z-axis. It was found that the spin mixing was weaker for atomic d-orbitals with orientation functions within the xy-plane, which is perpendicular to the magnetisation, and hence inaccessible to an electron travelling along the magnetisation direction.

Essentially, the SOI creates d-states in the fully occupied spin ↑ d-band and removes d-states from the spin ↓ d-band. However, the distribution of the new d-states in the spin ↑ d-band is asymmetric with respect to the magnetisation direction. This results in a transfer of a small resistivity component from $\rho_{\uparrow}^{s-d}$ to $\rho_{\downarrow}^{s-d}$ that can be written as [58];

$$\rho_{\uparrow}^{s-d}(\|) \approx \frac{3}{2}\epsilon^2 \rho_{\downarrow}^{*s-d} \tag{2.3.17}$$

$$\rho_{\uparrow}^{s-d}(\perp) \approx \frac{3}{4}\epsilon^2 \rho_{\downarrow}^{*s-d} \tag{2.3.18}$$

$$\rho_{\downarrow}^{s-d}(\|) \approx \left(1 - \frac{3}{2}\epsilon^2\right)\rho_{\downarrow}^{*s-d} \tag{2.3.19}$$

$$\rho_{\downarrow}^{s-d}(\perp) \approx \left(1 - \frac{3}{4}\epsilon^2\right)\rho_{\downarrow}^{*s-d} \tag{2.3.20}$$

where $\epsilon = \lambda/H_{\text{ex}}$ parametrises the relative strengths of the SOI to the exchange interaction and $\rho_{\downarrow}^{*s-d}$ is the spin ↓ $s \rightarrow d$ scattering resistivity prior to the inclusion of the SOI. Hence by including the SOI, $\rho_{\uparrow}^{s-d}$ undergoes an enhancement, that depends on the magnetisation orientation and differs by approximately a factor of two between ∥ and ⊥ magnetisation directions.

2.3.3 The Campbell, Fert and Jaoul model

There is little in the theoretical framework of AMR developed by Smit [17] that makes quantitative predictions. However, in 1970 Campbell, Fert and Jaoul (CFJ) expanded on this to create the CFJ model [58], a macroscopic theory capable of making predictions of the magnitude of AMR in Nickel films that are doped lightly (<10%) with transition metal impurities. This model is essential to the work in chapter 4 where it was extended to also

explain the thickness dependence of $\Delta\rho$ [62].

The model uses both the Mott two-current model and Smit's model as its basis. First, the following assumptions are made;

1. All of $\rho_\downarrow$ is due to $s \rightarrow d$ scattering. This is because the large density of d-states at the Fermi energy for spin $\downarrow$ electrons means this resistivity contribution is much larger than $s \rightarrow s$ scattering

2. The contributions due to magnon scattering are unaffected by the SOI. Hence the spin-mixing resistivity is the same regardless of the magnetisation orientation.

With these assumptions, the resistivity components from equations (2.3.17-20) can be written in terms of the parallel and perpendicular resistivities,

$$\rho_\uparrow^{\parallel} = \rho_\uparrow^{\perp} + \gamma\rho_\downarrow^{\perp} \tag{2.3.21}$$

$$\rho_\downarrow^{\parallel} = \rho_\downarrow^{\perp} - \gamma\rho_\downarrow^{\perp} \tag{2.3.22}$$

$$\rho_{\downarrow\uparrow}^{\parallel} = \rho_{\downarrow\uparrow}^{\perp}. \tag{2.3.23}$$

Here, $\gamma \approx \frac{3}{4}\epsilon^2$ and is a constant, where $\epsilon = \lambda/H_{\text{ex}}$ as before. The terms $\rho_\sigma^{\parallel} = \rho_\sigma^{s-s} + \rho_\sigma^{s-d}(\parallel)$ and $\rho_\sigma^{\perp} = \rho_\sigma^{s-s} + \rho_\sigma^{s-d}(\perp)$.

These resistivities can then be substituted into equation (2.3.14), to calculate the total longitudinal and transverse resistivities $\rho^{\parallel}$ and $\rho^{\perp}$ within the Mott two-current model. From this, $\Delta\rho$ and $\Delta\rho/\rho$ are found to be;

$$\Delta\rho = \frac{\gamma(\rho_\downarrow - \rho_\uparrow)\rho_\downarrow}{\rho_\uparrow + \rho_\downarrow + 4\rho_{\downarrow\uparrow}} \tag{2.3.24}$$

$$\frac{\Delta\rho}{\rho} = \frac{\gamma(\rho_\downarrow - \rho_\uparrow)\rho_\downarrow}{\rho_\uparrow\rho_\downarrow + \rho_{\downarrow\uparrow}(\rho_\uparrow + \rho_\downarrow)}. \tag{2.3.25}$$

At low temperature, assuming $\rho_{\downarrow\uparrow} << \rho_\sigma$ and $\gamma^2 \approx 0$ equation (2.3.25) simplifies to,

$$\frac{\Delta\rho}{\rho} = (\alpha - 1)\gamma \tag{2.3.26}$$

The parameter α is defined as, $\alpha = \frac{\rho_\downarrow^0}{\rho_\uparrow^0}$ where $\rho_\downarrow^0$ and $\rho_\uparrow^0$ are the residual resistivities for the spin $\downarrow$ and spin $\uparrow$ channels as defined in section 2.3.1. This contribution is related to

the number of available d-states at the Fermi energy, which is modified by doping with impurities.

In general, $\rho^0_\downarrow > \rho^0_\uparrow$ and $\alpha > 1$, hence $\Delta\rho/\rho > 0$ and $\rho^\parallel > \rho^\perp$. From equation (2.3.26) it can be seen that the AMR scales with α. Hence, the AMR is largest when there is the greatest difference in resistivities for spin $\uparrow$ and spin $\downarrow$ channels. It also predicts negative AMR in systems where the conduction is mediated by the minority spin species, such is the case for half metals [63].

The parameter α can be measured by zero-field temperature dependent resistivity measurements [60]. Table 2.1 shows the measured values for different transition metal dopants in Ni. Cr exhibits the lowest value due to a $d\uparrow$ bound state close to the Fermi energy [64], which increases the number of d-states for the spin $\uparrow$ band and therefore enhances $\rho_\uparrow$.

It was mentioned in the AMR discussion that the resistivity anisotropy can arise due to an anisotropic distribution of states or alternatively an anisotropic scattering potential. For the AMR effect, it was considered that the SOI brought about an anisotropic distribution of states. However, the SOI can give rise to anisotropic scattering mechanisms, which in turn can lead to spin-orbit torques. In the final section these concepts are discussed.

2.4 Spin-orbit torques

A generalised definition for *spin-orbit torques* (SOTs) are mechanisms by which the magnetisation can be influenced by the application of a current, where the origin of the mechanism is in the SOI. Generally, heavy metals such as Pt and Ta are used to provide the strong SOI and the SOTs arise at the interface with the ferromagnet under the application of a current. The spin Hall [19, 65] and Rashba effects [20] are generally considered to be the microscopic mechanisms behind the SOTs, but the exact contributions of each mechanism is a highly debated topic [66] and depends on a variety of factors including the choice of heavy metal [14, 67] and ferromagnetic layer thickness [68, 69].

Dopant	Ti	V	Cr	Mn	Fe	Co
$\alpha = \rho^0_\downarrow/\rho^0_\uparrow$	2.4	0.65	0.45	15	20	30

Table 2.1: Measured values of α for different transition metal dopants in Ni. Reproduced from [60].

Before discussing the microscopic origins of the SOTs, it is useful to first consider a phenomenological explanation in the context of the magnetisation dynamics. The time evolution of magnetisation can be described by the Landau-Lifshitz-Gilbert equation [9,70] which explains how the magnetisation is influenced by a number of physical processes that includes the exchange interaction, magnetic anisotropy, magnetostatic contributions as well as magnetic damping. As will be discussed later, the equation can be extended to also include components which arise from SOTs.

2.4.1 Landau-Lifshitz-Gilbert equation

The Landau-Lifshitz-Gilbert (LLG) equation is given by;

$$\frac{d\boldsymbol{M}}{dt} = -\gamma_0 \boldsymbol{M} \times \boldsymbol{H}_{\text{eff}} + \alpha \boldsymbol{M} \times \frac{d\boldsymbol{M}}{dt} \tag{2.4.27}$$

where γ_0 is the gyromagnetic ratio, $\boldsymbol{H}_{\text{eff}}$ is the effective field containing contributions from external, anisotropy and demagnetising fields and α is the magnetic damping parameter.

The $\boldsymbol{M} \times \boldsymbol{H}_{\text{eff}}$ term describes the precession of the magnetisation about the total effective field axis. The $\boldsymbol{M} \times \frac{d\boldsymbol{M}}{dt}$ term was introduced by Gilbert [9] and describes the relaxation of the magnetisation along the field axis due to magnetic damping. Fig. 2.8 shows a schematic of these contributions. The magnetic damping will be discussed first before addressing the contribution of SOTs on the magnetisation dynamics.

2.4.2 Magnetic damping

Magnetic damping describes the energy dissipation from the magnetisation to the thermal bath [71]. It has great importance with regard to spintronics, in particular magnetisation switching speeds [72] and domain wall velocity [73]. With regard to SOTs, systems with a large damping parameter, α, will oppose changes in magnetisation induced by torques, reducing the effective spin-orbit torque efficiency and increasing the current required for magnetisation reversal [69, 74]. However, despite its importance, the microscopic mechanisms of magnetic damping are not clearly understood [15, 75–77].

It common to divide the total damping into intrinsic and extrinsic components. The intrinsic damping originates from the SOI, by which the spin is coupled to the lattice,

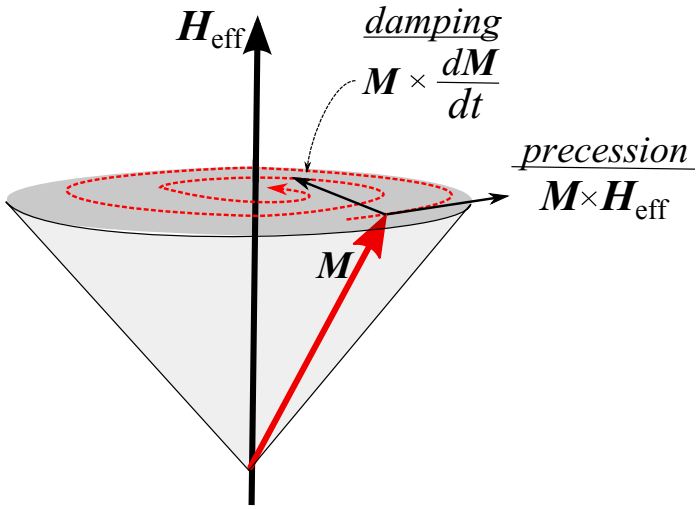

Figure 2.8: Schematic demonstrating the separate components of the LLG equation. An external field $\boldsymbol{H}_{\text{eff}}$ causes the magnetisation to process. Energy is dissipated through magnetic damping and the magnetisation will relax along the field direction.

and is a consequence of the non-spin-conserving nature of the interaction [15, 76]. At the interface between ferromagnets and a normal metal, further intrinsic contributions arise due to interfacial *d*-*d* hybridisation [76, 78] and spin-pumping across the interface [75].

The extrinsic contribution arises from spin-wave scattering at impurities and defects. Again, this can be enhanced at the interface with a normal metal, where topological roughness can provide scattering centres [78]. The microscopic origin of this is thought to be two-magnon scattering [76, 77]. There exist spin-wave modes which are degenerate in energy with the uniform magnetisation precession mode. These degenerate modes have a component of wave-vector parallel to the sample surface. It is thought that scattering with impurities and defects, where the translation symmetry of the surface is broken, provides a mechanism by which these degenerate modes can be accessed and allow for energy dissipation from the precessional mode through pairs of magnons.

The intrinsic and extrinsic components can be separated, since the contribution from two-magnon scattering yields a shift in the precession frequency. Consequently extrinsic damping shows a dependence on the $\boldsymbol{H}_{\text{eff}}$ whereas intrinsic damping is independent of these factors [78, 79].

2.4.3 Spin-orbit torques

Spin-orbit torques enter the LLG equation as effective fields of the form;

$$J\boldsymbol{\sigma} = a\boldsymbol{\sigma} \times \boldsymbol{M} + b\boldsymbol{\sigma} \tag{2.4.28}$$

which relates to the exchange coupling J and the spin accumulation $\boldsymbol{\sigma}$ [80]. The form of $J\boldsymbol{\sigma}$ derives from the fact that only components of spin-current transverse to the magnetisation contribute to magnetisation dynamics [80]. The terms a and b are material parameters, which scale with physical values such as spin-mixing conductivity and ferromagnetic layer thickness and relate the torque to its physical origins.

This term is included in the LLG equation as an additional effective field due to the spin-orbit torque;

$$\frac{d\boldsymbol{M}}{dt} = -\gamma_0 \boldsymbol{M} \times (\boldsymbol{H}_{\text{eff}} + J\boldsymbol{\sigma}) + \alpha \boldsymbol{M} \times \frac{d\boldsymbol{M}}{dt}. \tag{2.4.29}$$

Following the substitution into the LLG equation, it can be seen that two torques develop. A *field-like* torque with the form $\boldsymbol{\Gamma}_{\text{FL}} = b\boldsymbol{M} \times \boldsymbol{\sigma}$ and a *damping-like* torque with the form $\boldsymbol{\Gamma}_{\text{DL}} = a\boldsymbol{M} \times \boldsymbol{\sigma} \times \boldsymbol{M}$.

The behaviour of the torques is summarised in Fig. 2.9. The field-like torque is independent of magnetisation orientation and resembles an internal field $\boldsymbol{H}_{\text{FL}} = b\boldsymbol{\sigma}$. The damping-like torques is similar in action to the torque due to magnetic damping, since it rotates with the magnetisation direction. The effective field therefore takes the form $\boldsymbol{H}_{\text{DL}} = \boldsymbol{\sigma} \times \boldsymbol{M}$. These torques can work in conjunction or against magnetic damping dependent on the direction of the current and external magnetic fields leading to the possibility of electrical manipulation of the effective damping parameter, α [81].

The origin of these torques is greatly debated between two phenomena: the spin Hall and Rashba effects. The consensus would now suggest that both can exist alongside each other, but the magnitude of the effects are highly dependent on the system investigated [66]. In particular the Rashba effect requires structural inversion asymmetry [82, 83]. In the following section, both the spin Hall and Rashba effects are introduced phenomenologically and discussed in terms of their microscopic origins.

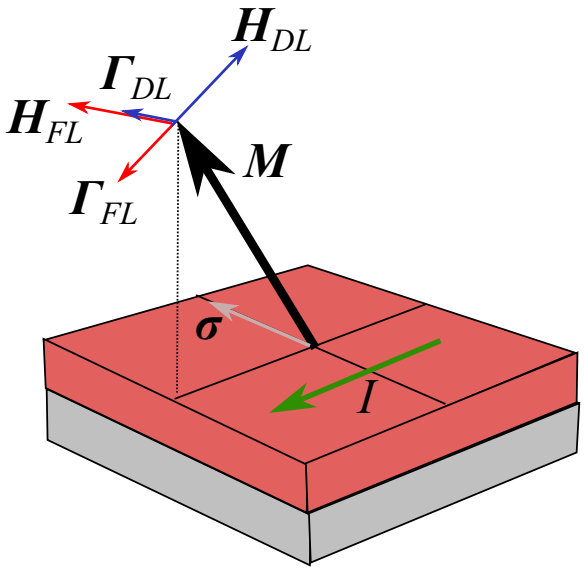

Figure 2.9: Schematic summarising the SOTs and the associated effective fields which can arise as a consequence of the transverse spin polarisation σ.

2.4.4 Spin Hall effect

The SOI can give rise to spin-dependent scattering mechanisms, whereby spin ↑ and spin ↓ electrons obtain opposite transverse velocity components after scattering. This results in a spin accumulation transverse to the current flow and is shown schematically in Fig. 2.10 a). Analogous to the ordinary Hall effect, where opposite charges accumulate on opposite sides of the metal, this effect results in accumulation of opposite spin on either side and consequently it was termed the *spin Hall effect* (SHE) [19].

The mechanisms by which the spin accumulation occurs is the same as that which gives rise to the *anomalous Hall effect* (AHE) in ferromagnets. They can be split into two varieties: extrinsic contributions which originate from spin-dependent scattering from impurities and intrinsic contributions which are inherent to the band structure of the pure crystal.

There exist two varieties of extrinsic contributions: *skew scattering* and *side-jump scattering*, both of which originate from spin-dependent scattering from un-polarised impurities with strong spin-orbit coupling. These are shown schematically in Fig. 2.10 b)-c).

Skew scattering was first proposed by Smit [18] and can be understood through a semi-classical Boltzmann transport treatment. It arises from the inclusion of spin-orbit coupling within the disorder scattering potential which results in different scattering cross-sections

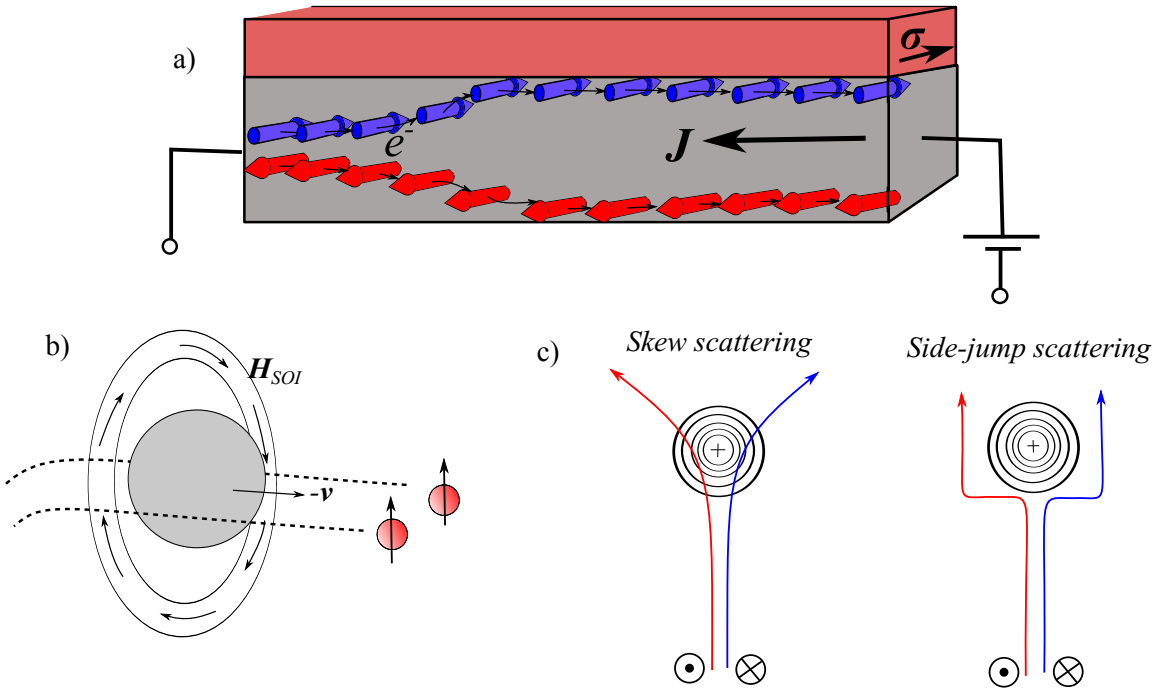

Figure 2.10: a) On the application of a current, spin-dependent scattering mechanisms due to the strong SOI within a heavy metal spatially separate the electrons by their spin. This gives rise to spin accumulation at the interfaces. b) Schematic of the skew scattering mechanism. In the frame of reference of the electron, the effective magnetic field due the SOI from an approaching heavy metal ion scatters spin ↑ electrons in the same direction regardless of which side of the ion they approach. c) Schematics demonstrating the differences between the skew and side-jump mechanisms with a view of the electric potential gradient of the heavy metal.

for spin ↑ and spin ↓ electrons. The electrons are therefore skew scattered dependent on the projection of their spin on the z-component of angular momentum. A pictorial explanation is shown in Fig. 2.10 b), which considering the frame of reference of the electron, then the approaching impurity induces an effective magnetic field due to the SOI. For a spin ↑ electron passing to the left of the impurity, it experiences the effective magnetic field anti-parallel to its spin and consequently is repelled from the impurity where the field is strongest. A spin ↑ electron passing to the right of the impurity experience a magnetic field parallel to its spin and is therefore attracted towards the impurity. Consequently, the spin ↑ electron is deflected left regardless of which side of the impurity it approaches. Likewise, spin ↓ electrons would be scattered to the right.

The side jump mechanism also originates from impurity scattering in the presence of the SOI and was derived by Berger [84]. However, the effect arises due to the difference between the response of a spin ↑ and spin ↓ electron to the gradient of the electric field on approach of the impurity. There is no classical analogy to this effect, and it arises as a

consequence of the Gaussian probability distribution for the position of the electron. The spin-orbit perturbation due to the impurity distorts the probability distribution such that there is a high probability of a spin ↑ electron being spontaneously displaced to the left. Likewise, for a spin ↓ electron the reverse is true. The side-jump mechanism is shown schematically in Fig. 2.10 c).

The intrinsic contribution was first derived by Luttinger and Karplus [85] where they found an anomalous transverse current component developed when they perturbed a system of spin-orbit coupled Bloch states in the presence of an electric field. The origin of the transverse velocity is intrinsic to the band structure and does not require scattering, arising directly from the non-equilibrium spin-dynamics.

These mechanism were developed as part of the theoretical developments in the understanding of the AHE, but it was quickly realised that the same scattering mechanisms could be applied to a non-magnetic material with a strong SOI, which led to the prediction of the SHE by Dyakonov and Perel [65] over 40 years ago.

However, it was 30 years later when Hirsch [19] made similar predictions and proposed devices by which the SHE could be measured that attempts to experimentally verify the existence of the SHE began. Note, that these studies exclusively considered the extrinsic contributions. The prediction of the intrinsic SHE was made by Murakami *et al.* in 2003 [86] and importantly focused on semiconductors, by which the optical activity of these materials could be exploited for the first detection of the SHE [87, 88]. Furthermore, the reciprocal effect, the inverse spin-Hall effect by which a spin-current is converted into a charge current was detected shortly after by Valenzuela *et al.* [89].

Spin-Hall angles in 5*d* elements

The spin-Hall angle, $\theta_{\mathrm{SH}} = j_{\mathrm{s}}/j_{\mathrm{e}}$ is defined as the ratio of spin current j_{s} to injected charge current j_{e} and therefore parametrises the efficiency of the current conversion. Typical values for Pt range between $\theta_{\mathrm{SH}} = 0.02$ and 0.13 [81, 90–94], where the variation between results is largely attributed to the difference in spin-mixing conductivities at the choice of ferromagnet/Pt interface [31]. Ta has a negative spin-Hall angle with typical values in the range of $\theta_{\mathrm{SH}} = -0.02$ and -0.15 [24, 90, 91, 95]. To date, the largest reported spin-Hall angle is for the β-W phase with $\theta_{\mathrm{SH}} \sim -0.3$ [96]. The θ_{SH} scales with the SOI as Z^4, but a

theoretical study by Tanaka *et al.* [97] found that there is also a strong dependence on *d*-electron valency as shown in Fig. 2.11. Interestingly, the form of the data and the change in sign resembles the dependence of proximity induced magnetism shown in Fig. 2.6. However, an investigation into the role of PIM, by measuring the temperature dependence of the spin-Hall effect, suggested that PIM was detrimental to the θ_{SH} [98]. The Z^4 and *d*-orbital valency dependence of θ_{SH} was confirmed experimentally by Wang *et al.* [90] and is shown alongside the theoretical predictions by Tanaka *et al.* in Fig. 2.11.

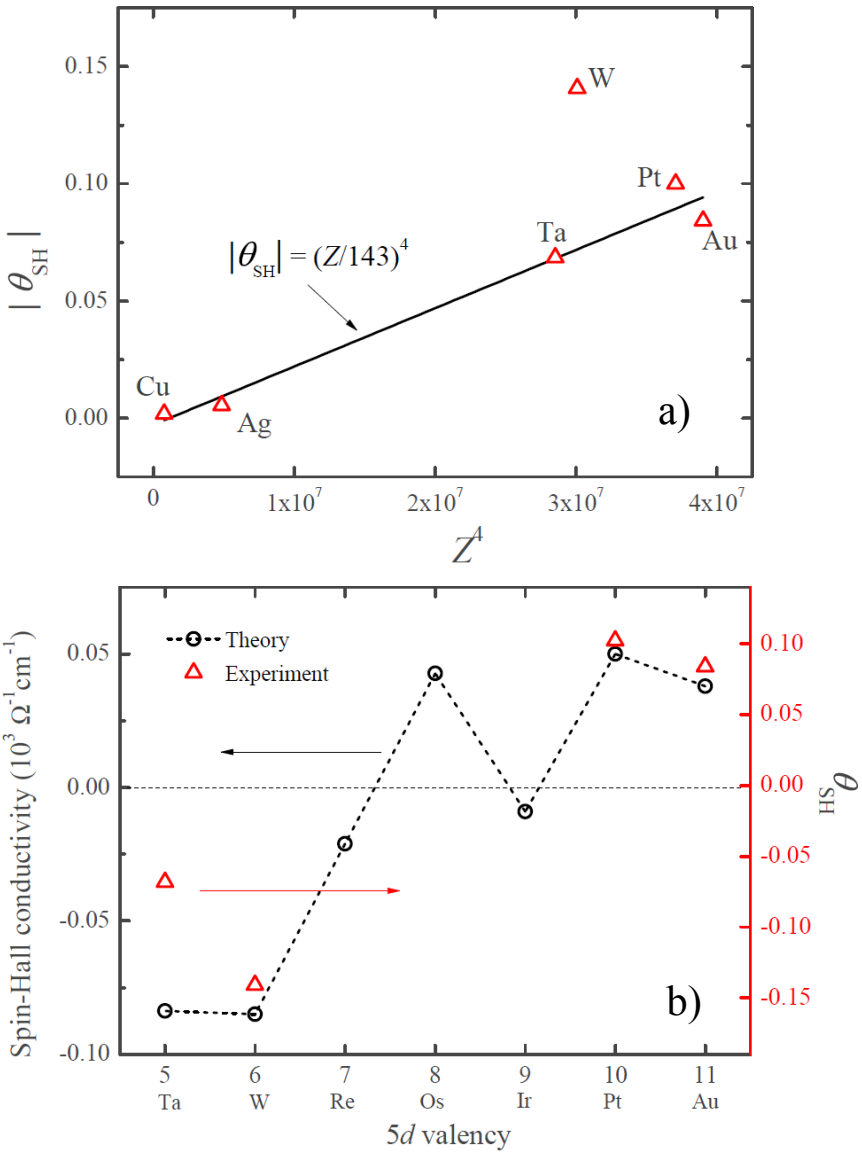

Figure 2.11: a) Dependence of $|\theta_{SH}|$ on atomic weight Z, adapted from Ref. [90]. The linear dependence on Z^4 is representative of scaling with the SOI. b) Dependence of θ_{SH} on electron valency for the 5*d* transition metals. Theoretical predictions of the spin-Hall conductivity are adapted from Ref. [97] and experimentally extracted values of θ_{SH} from Ref. [90].

We now introduce the second microscopic origin of the spin-orbit torques, the Rashba effect.

2.4.5 Rashba effect

The *Rashba effect* occurs when the SOI is present alongside structural inversion asymmetry (SIA). Fundamentally the SIA gives rise to a large crystal field, which acts normal to the surface, which in the frame of reference of the electron and through the SOI transforms into a magnetic field transverse to the current flow.

We can investigate the role of SIA by considering the effects of time and spatial inversion symmetries which are summarised in Table 2.2, where it can be seen that spin degeneracy is direct consequence of the combination of time and spatial inversion symmetry. In a ferromagnet, time inversion symmetry is broken and hence the only requirement on the band structure is that $E_\uparrow(\boldsymbol{k}) = E_\uparrow(-\boldsymbol{k})$ which allows spin $\uparrow$ and spin $\downarrow$ electrons to have different energy for the same $\boldsymbol{k}$. When spatial inversion symmetry is broken, the symmetry requirement is such that $E_\uparrow(\boldsymbol{k}) = E_\downarrow(-\boldsymbol{k})$, hence the spin $\uparrow$ and spin $\downarrow$ bands can move laterally in k-space by equal amounts in the opposite direction. This is shown schematically for a 2D-electron gas in Figs. 2.12 a)-c).

The Rashba Hamiltonian [8];

$$\hat{\mathcal{H}}_{\mathrm{Ra}} = \alpha(\boldsymbol{k} \times \hat{\boldsymbol{z}}) \cdot \boldsymbol{\sigma} \tag{2.4.30}$$

describes how spin-degeneracy is lifted in k-space. Here, α is a material dependent constant that scales with the SOI and $\boldsymbol{\sigma}$ is the spin direction. For a 2D free electron gas, the energy eigenvalues are

$$E_{\pm,k} = \frac{\hbar k^2}{2m_{\mathrm{e}}^*} \pm \alpha|k| \tag{2.4.31}$$

where m_{e}^* is the electron effective mass. This corresponds to the dispersion relation shown schematically in Fig. 2.12 b). Revolving this dispersion relation about $|k| = 0$ results in

Space inversion	$E_\uparrow(\boldsymbol{k}) = E_\uparrow(-\boldsymbol{k})$	$\Rightarrow E_\uparrow(\boldsymbol{k}) = E_\downarrow(\boldsymbol{k})$
Time inversion	$E_\uparrow(\boldsymbol{k}) = E_\downarrow(-\boldsymbol{k})$	

Table 2.2: Summary of symmetry operations and their combined effect.

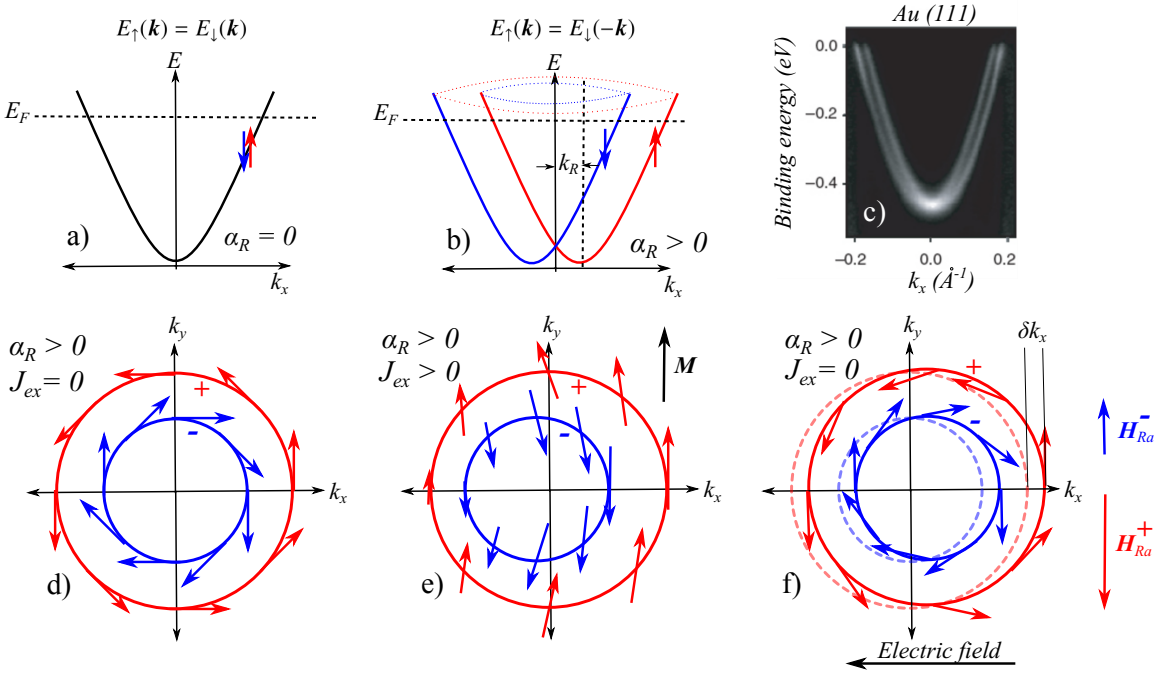

Figure 2.12: Schematics of a 2D electron gas without Rashba spin-orbit coupling ($\alpha_R = 0$) and b) with Rashba spin-orbit coupling ($\alpha_R > 0$). The blue and red dashed lines show the Fermi contours for the spin-split bands. c) Experimentally observed band splitting of the surface states of Au(111) using ARPES [99]. Equilibrium Rashba fields in d) a non-magnetic material and e) in a ferromagnet. f) Non-equilibrium Rashba fields in a non-magnetic material with the application of an electric field along the -x-direction.

the 2D projection of the Fermi contours for k_x and k_y as indicated by the coloured dotted lines. These Fermi contours are shown for a non-magnetic and a ferromagnetic system in Figs.2.12 d) and e) respectively, for both minority (-) an majority (+) electrons.

It can be shown that the spin expectation value is given by [8];

$$\langle \boldsymbol{\sigma} \rangle_{\pm,\boldsymbol{k}} = \langle \psi_{\pm,\boldsymbol{k}} | \boldsymbol{\sigma} | \psi_{\pm,\boldsymbol{k}} \rangle = \frac{1}{|k|} \begin{bmatrix} \pm k_y \\ \mp k_x \\ 0 \end{bmatrix} \tag{2.4.32}$$

where $|\psi_{\pm,\boldsymbol{k}}\rangle$ are the eigenvectors corresponding to equation (2.4.31) for the majority (minority) +(-) electrons with wavevector $\boldsymbol{k}$. In the non-magnetic case, it can be seen that the Rashba fields, given by the arrows in Fig. 2.12 d), cause the spins to align in-the-plane and transverse to the electron momentum. In the case of the ferromagnet, the Rashba fields work against the exchange interaction, causing the spins to cant away from the magnetisation.

The direction of the Rashba field is k-dependent, hence the application of a current can induce a spin polarisation. It is shown for the non-magnetic system in Fig. 2.12 e), that an electric field along the $-x$ direction shifts both majority and minority Fermi contours by an amount δk_x . From equation (2.4.32), the extra component of k_x gives rises to a y-component in the spin direction for all electrons and has the opposite sign for majority and minority electrons. This can be thought of in terms of an effective field H_{Ra}, which produces a spin-polarisation along the y-direction for the minority spin and along the -y direction for the majority spin [100]. Since the majority spin Fermi contour is larger, there results a net spin polarisation along the -y direction [83].

The same argument can be applied to the ferromagnet, in which case the exchange interaction couples the non-equilibrium spin density to the local magnetisation. When a current is applied, conduction electrons precess around the effective magnetic field leading to a torque on the magnetisation [101]. In the literature, this effect is also sometimes referred to as the inverse spin galvanic effect [102] or the Edelstein effect [103].

Further to this, the spins will precess around the effective magnetic field due to the Rashba effect, gaining a component of magnetisation perpendicular to the xy-plane [100]. This can give rise to a damping-like torque, thus making it difficult to distinguish entirely between Rashba and SHE contributions. However, it is generally considered that the SHE contributes primarily to the damping-like torque and the Rashba effect to the field-like torque [66].

3 Experimental techniques

3.1 Introduction

In this chapter, the experimental techniques used to fabricate and investigate the thin films used in this thesis are presented. Sputtering was used exclusively to fabricate the films and is presented first. A variety of investigative techniques were used, including, x-ray reflectivity, magneto-optical Kerr effects and electronic transport measurements. Detailed consideration is given to the explanations of grazing incidence reflectivity and x-ray resonant magnetic reflectivity in order to discuss the concepts necessary to describe the data analysis. For each experimental technique an introduction to the physical principles and the origin of the effect is presented first, followed by a discussion of the experimental methodology associated with the measurement itself.

3.2 Preparation of thin films and microstructures

The inclusion of thin film technologies within magnetic memory and magnetic sensor devices has led to great advances in deposition and lithographic techniques. In particular the sputtering technique has become an industry standard. In this thesis, all samples were fabricated using sputter deposition.

When lithography was used, this process was completed in a class 1000 clean room facility using optical lithography. Depositions were made onto SiO_2 oxidised Silicon substrates. Prior to deposition and lithography, the substrates were diced into appropriate sizes using a diamond scribe and then cleaned in acetone and then isopropan-2-ol using ultrasonic agitation. The chips were then dried with dry nitrogen.

Within this section the process of sputtering is presented first, including DC and RF

magnetron sputtering. Following this a description of the fabrication processing used to make the samples in chapter 5 is given, namely, optical lithography and wire bonding.

3.2.1 The sputtering process

Sputtering is the process by which atoms are ejected from a target material by the bombardment of ions and deposited onto a substrate. The technique finds diverse applications in industry, from the large area deposition of self cleaning hydrophillic coatings on window panes [104] to the fabrication of nanoscale circuits within the semiconductor industry [105].

In the physical realisation, an incident particle impinges on the target surface as shown in Fig. 3.1. This transfers momentum to the surface atoms of the target, which results in a series of collisions which can then result in the ejection of a surface atom. The process is initiated using a working gas. The target is charged as the cathode and the large electric field that then exists between the target and the shielding ionises the working gas producing a plasma. The positively charged ions are then accelerated towards the negatively charged target and initiate the sputtering process. Secondary electrons are also emitted, which play an important role in maintaining the plasma [106].

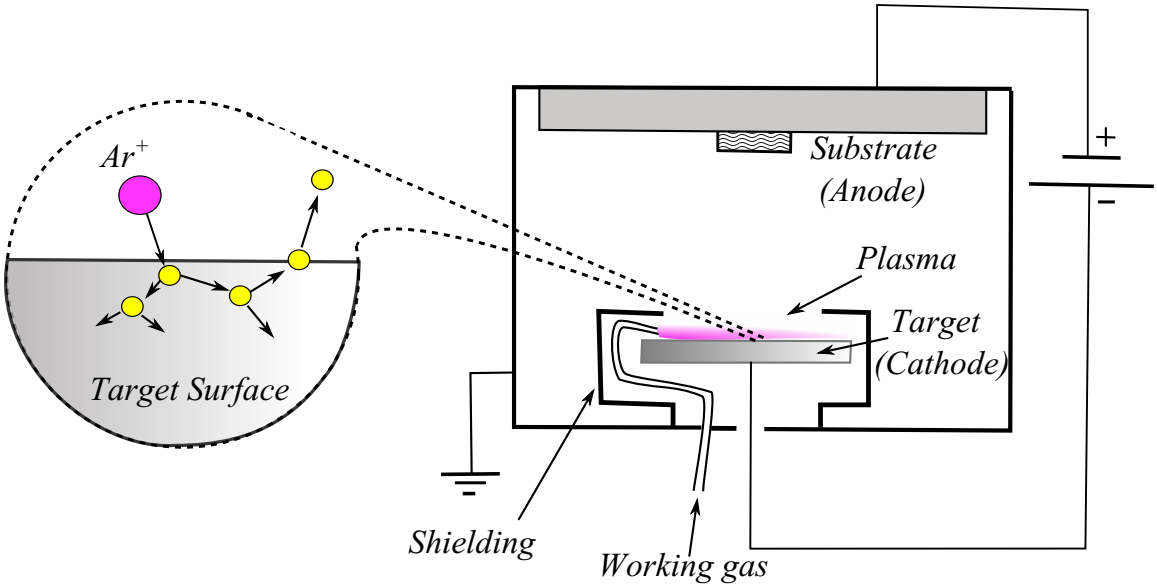

Figure 3.1: Schematic demonstrating the key features of the sputtering system. The voltage can be as large as 600 V in order to ionise the Ar working gas. Collisions between the Ar^+ ions and the target causes the ejection of atoms from the target surface which then condense on the substrate and vacuum chamber walls.

Generally, Ar is used as the working gas, since it is massive enough to impart sufficient momentum to induce sputtering and it is inert, preventing chemical reaction with the deposited film. However, reactive gases such as oxygen can be used in order to deposit oxide films through the process of reactive sputtering.

DC and RF magnetron sputtering

Magnetron sputtering was developed to overcome the high working gas pressures required to induce sputtering [106]. This results in low deposition rates since the ejected atoms from the target undergo multiple collisions with the Ar^+ on en-route to the substrate [107].

For magnetron sputtering, an arrangement of permanent magnets are positioned behind the target, such that the stray field shown in Fig. 3.2 is produced. The magnetic field is largely parallel to the target surface and perpendicular to the electric field and hence the plasma becomes trapped in an epicyclic path close to the target surface due to the Lorentz force. This assists ionisation in the vicinity of the target by promoting electron collisions through the localisation of the plasma, which then allows for lower working gas pressures. Simultaneously this also increases the deposition rate due to the increase in the number of ions. However, due to the epicyclic path of the plasma, a racetrack erosion profile in the target is signature of magnetron sputtering, which reduces the efficiency of target utilisation.

Within this description so far the electric field has been static with the target negatively biased. This configuration is referred to as DC magnetron sputtering. However, if the target is an insulator it will rapidly develop a net positive charge and the sputtering process will

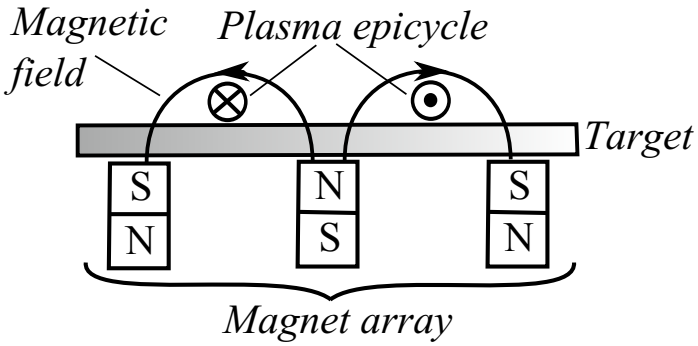

Figure 3.2: Typical magnet array used to produce the confining magnetic field used for magnetron sputtering. If the target is a ferromagnet, stronger permanent magnets are required in order to over the flux closure due to the formation of magnetic domains in the ferromagnet.

cease. In this case an RF source is used which alternates the polarity of the substrate and the target. The sputtering is sustained by periodic neutralisation of the insulator target through electron collisions when the target becomes the anode. Furthermore, at high frequency (>50 kHz), the heavy Ar^+ ions cannot follow the switching and hence there is no sputtering of the substrate for the short period it is charged as the cathode. For RF sputtering, it is necessary to use an impedance matching network to optimise the power discharge to the target and sustain the plasma.

Shadow mask deposition

When measuring fundamental properties such as resistivity and magnetisation it is useful to have a well defined geometry to use in the volume calculation. One way that this can be achieved is by sputtering through a mask. Here, the substrate was fixed behind a mask in contact mode and the deposition took place through the pattern cut into the mask. The masks were made from 1 mm thick sheet brass. Shadowing can occur close to the edges of the mask since fewer trajectories are able to arrive at the substrate. This shadowing produces a graded edge to the deposition pattern with a thickness variation, but the effect can be minimised by chamfering the mask edges, which is demonstrated in Fig 3.3.

Specifics of the sputtering system used in this thesis

A Mantis Qprep500 sputtering system [108] was used in this work and is shown in Fig. 3.4, where some of the key features are indicated. The sputtering system operates in ultra-high vacuum (UHV) with a base pressure of the order 1×10^{-9} Torr. It can be seen in Fig. 3.4 a) that the system is split into two chambers: the load lock and the main chamber.

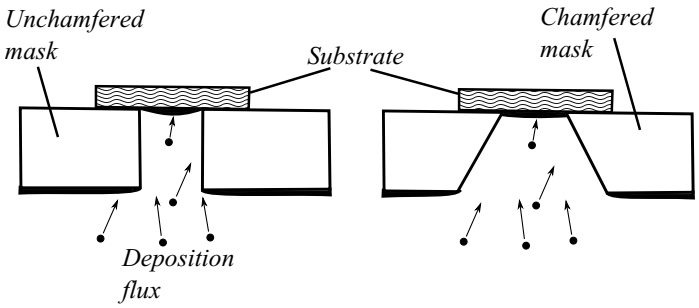

Figure 3.3: Schematics comparing the deposition through an unchamfered and a chamfered mask. The unchamfered mask produces a variable deposition thickness close to the mask edge.

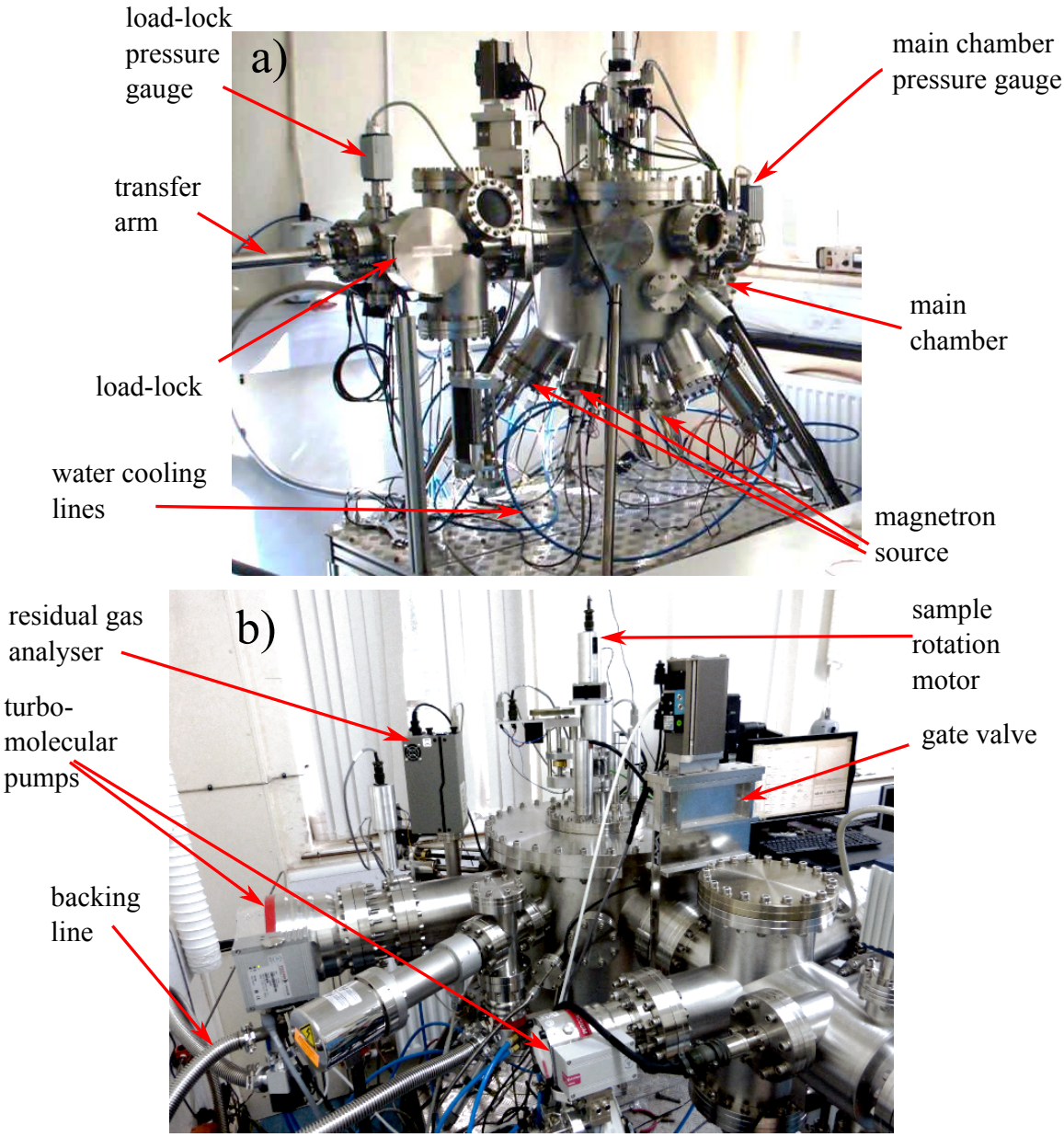

Figure 3.4: a) Front view and b) back view of the Mantis Qprep500 sputtering system, where the key features discussed in the main text are labelled.

The chambers are separated by a gate valve and the load-lock allows for samples to be loaded into the system without having to vent the main chamber. For both chambers, turbo molecular pumps are used to create the vacuum, see Fig. 3.4 b). These are connected by backing lines to oil-less scroll pumps. In the initial pump-down of the system, these are used to reach a working pressure of 10 mTorr, below which the turbo-molecular pumps can be activated. The turbo-molecular pumps are likely to stall if operated at a higher pressure since the mean free path of the gas molecules would be less than the spacing between the

rotary blades, which results in a pressure accumulation at the rear of the pump.

When the chambers are vented, dry nitrogen gas is used to bring the chambers back to atmospheric pressure. This minimises the adsorption of water vapour onto the chamber walls. The chambers are separated by a gate valve, which can be opened without significant contamination to the main chamber vacuum once the load-lock has reached a pressure of below 5×10^{-7} Torr. This was confirmed using a residual gas analyser attached to the main chamber. The samples were transferred into the main chamber using the transfer arm.

Within the main chamber there are five magnetron sources. To power these, there are two DC supplies and one RF supply, which are switched between sources using relay circuits. The magnetron sources and turbo-molecular pumps are water cooled and each source has an individual Argon gas line, for which the flow rate is controlled using a mass-flow controller. Whilst deposition occurs, the sample is rotated to ensure a uniform deposition and to prevent any induced magnetic anisotropy due to the stray magnetic fields of the magnetron sources, although this may not be completely removed [109].

In the next section, sample micro-processing methods that were used to pattern the samples are discussed.

3.2.2 Optical lithography

For the studies in chapter 5 it was necessary to pattern devices with micrometre dimensions in order to obtain the high current densities ($\sim10^{10}$ Am^{-1}) necessary for the spin-orbit torque measurements. This was achieved using optical lithography.

Optical lithography is a multistage process summarised in Fig. 3.5. Starting with a clean Si/SiO_2 substrate, a single layer of S1813 positive photoresist with thickness 1.5 μm was spin-coated onto the sample. A positive photoresist will weaken after exposure whereas negative photoresist would harden. This was baked onto the substrate using a hotplate at a temperature of 100 °C. Following this the mask was aligned with the substrate using an EVG 620 mask aligner and exposed to UV light. Between the mask features, where the UV light exposed the photoresist, the photoresist undergoes a chemical change by which the polymer bonds are broken, making the exposed resist more soluble. The sample was then placed in the developer MF319, where the exposed regions dissolve from the substrate and the unexposed regions remain. Following this stage a reactive ion etch can be used to

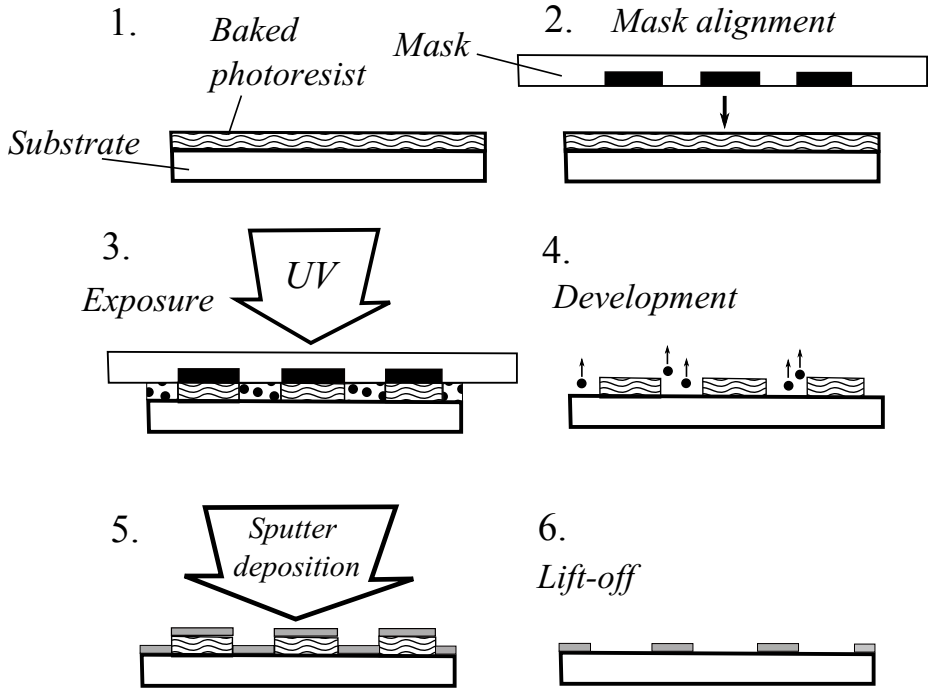

Figure 3.5: Schematic demonstrating the processing stages used in optical lithography. Each stage is described in the main text.

ensure complete removal of photoresist from the channels.

With sputter deposition, the whole patterned sample was coated in the deposited material. Then in the lift-off stage, acetone was used to remove all of the resist, which in turn lifts-off any sputtered material which was not bonded directly to the substrate. This leaves the mask design patterned in the selected material on the substrate.

Once the micro-structures have been patterned, a second stage of lithography was used to pattern Ti/Au contacts which extend out to macroscopic contact pads to which wires could be bonded.

Wire bonding of microstructures

In order to pass current through the microstructures, electrical connections need to be made between the contact pads of the microstructure and the chip carrier. In this thesis, an FEK delvotek 5330 wire bonder was used. A 100 μm Au wire was bonded to the Ti/Au contact pads. The size of the pads is limited by the minimum bond size requirement of ~50 μm. The wire-bonder used the wedge bonding method, which combines ultrasonic and force to create a localised weld to the sample surface. Once a bond to the sample was formed, the wire was then unspooled a little and a second bond was made to the chip carrier. Once

bonded, the chip carrier could then simply be placed into a larger sample socket that was wired to a break out box.

The rest of this chapter is devoted to presenting the experimental techniques used in this thesis, starting with grazing incidence x-ray reflectivity. This forms a significant portion of the work presented in this thesis and hence included is an overview of the theory of reflectivity necessary to understand the data analysis presented in the experimental chapters in this thesis.

3.3 X-ray reflectivity

In the classical picture of x-ray scattering with atoms, the interaction of the electric field from an incident plane-wave x-ray causes the electrons to oscillate [110]. An oscillating electron then becomes a source, re-radiating the x-ray at the same energy as a spherical wave. This elastic process is referred to as Thomson scattering.

The interaction of x-rays with matter can be used to gain detailed insight into sample structure. There exists a variety of different x-ray scattering techniques, but within this thesis the primary technique used is grazing incidence x-ray reflectivity (XRR).

XRR is an established experimental technique that can be used to obtain sub-nanometer resolution of interfaces and layers thicknesses. In chapter 4 it is used to structurally characterise Ni films thin films. In chapters 6 and 7 it is used as part of a hybrid technique, x-ray resonant magnetic reflectivity (XRMR), to characterise the interfacial proximity induced magnetism induced in Pt/Co/Pt multilayers.

In the following sections we briefly introduce the general theory behind x-ray scattering and the measurement geometry. Derivations are not included since the purpose of this chapter is only to introduce the important equations and concepts used in the fitting procedure for the XRR analysis. However, detailed discussions of the XRR technique and analysis can be found in Ref. [110, 111].

3.3.1 Principles of specular reflectivity

We start by defining the scattering geometry shown in Fig. 3.6. For grazing incidence reflectivity, the wave vector transfer q_z between the incident and reflected x-ray is suffi-

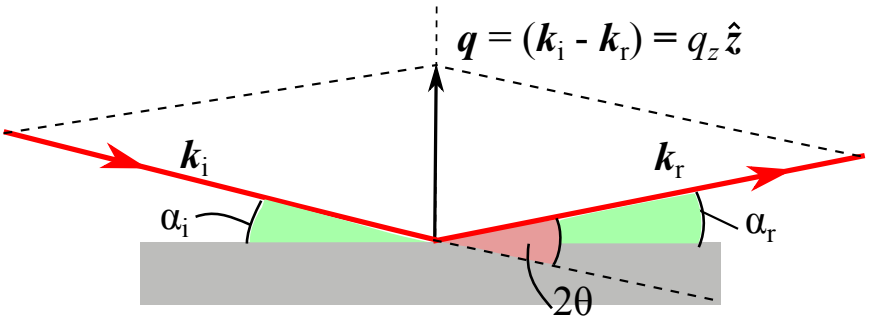

Figure 3.6: An incoming x-ray is scattered from the sample surface. Under the specular condition $\alpha_i = \alpha_r$. The wavevector transfer $\boldsymbol{q}$ is therefore directed along the surface normal. The angle 2θ defines the angular position of the detector relative to the incoming x-ray for which the specular condition is satisfied.

ciently small that the lengthscales probed are much larger than the lattice spacing and the technique is therefore sensitive only to electron density variations [112]. Furthermore, the condition for specular reflectivity is such that the incidence angle is equal to the exit angle, consequently the total wave vector transfer $\boldsymbol{q} = q_z\hat{\boldsymbol{z}}$. XRR is therefore sensitive to the mean electron density $\rho_e(z)$ variation along the surface normal direction and yields information about layer thickness, interfacial width and electron density [112].

The following expressions for the reflectivity are derived within the *Born approximation* (sometimes referred to as the *kinematic approximation*) which neglects multiple scattering events. This greatly simplifies the problem, since within this approximation the scattered x-rays from two electrons which are separated by a distance $\boldsymbol{r}$ differ only by a phase factor $e^{i\boldsymbol{q}_z\cdot\boldsymbol{r}}$.

Here, the total reflectivity of a perfectly smooth infinitely thick slab of material is given by the Fresnel reflectance [111],

$$R_F(q_z) = \frac{(4\pi r_e \rho_e)^2}{q_z^4} \tag{3.3.1}$$

where, ρ_e is the electron density and r_e is the Thomson scattering length or the classical radius of the electron $r_e = 2.818\times10^{-5}$Å. The reflected intensity decays as $q_z^{-4} \propto \alpha_i^{-4}$. Note that this diverges for $q_z \to 0$ since the Born approximation disregards multiple scattering events, which are significant around the critical angle [111].

The general expression for the reflectance is related to the Fourier transform of the

derivative of the electron density [112, 113].

$$R(q_z) = R_F(q_z)\left|\int \frac{d\rho_e(z)}{dz}\exp(iq_z z)\,dz\right|^2 \tag{3.3.2}$$

Importantly here, in order to model an interface, the electron density must vary over the z-direction. For the smooth surface, the electron density $\rho_e(z)$ falls to zero following a step function. However, we now consider that the slab has a finite interface width σ between the surface and vacuum. There are two contributions to σ: topographical roughness σ_{top} and intermixing σ_{int}. In Fig. 3.7 it can be seen that these contributions to the interface width give rise to the same distribution in electron density along the z-direction and are therefore indistinguishable with specular XRR. The interface width is defined as;

$$\sigma = \sqrt{\sigma_{top}^2 + \sigma_{int}^2}. \tag{3.3.3}$$

In general, an error function is used to incorporate a finite width σ to this interface as shown in Fig. 3.7 c). This is used to model the electron density profile across the interface [113] and when substituted into equation (3.3.2) yields,

$$R(q_z) = R_F(q_z)\left|\int \frac{d}{dz}\left(\mathrm{erf}\left(\frac{z}{\sqrt{2}\sigma}\right)\right)\exp(iq_z z)dz\right|^2. \tag{3.3.4}$$

The differential of an error function is a Gaussian distribution,

$$\frac{d}{dz}\left(\mathrm{erf}\left(\frac{z}{\sqrt{2}\sigma}\right)\right) = \frac{1}{\sqrt{2\pi\sigma^2}}\exp\left(\frac{1}{2}\left(\frac{z}{\sigma}\right)^2\right) \tag{3.3.5}$$

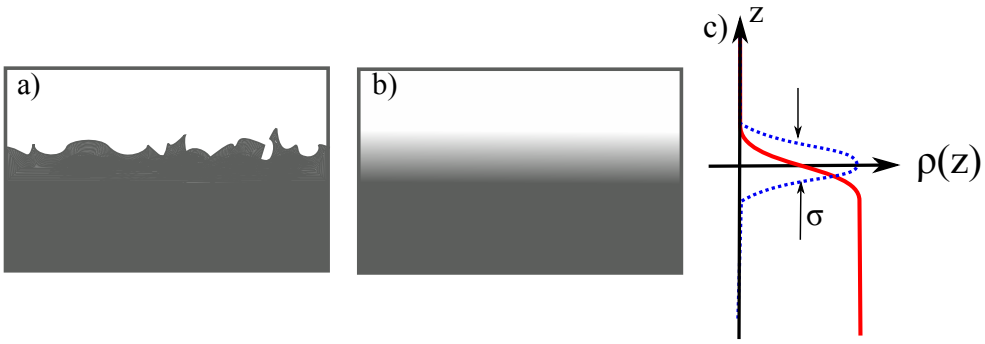

Figure 3.7: Schematic representations comparing a) a topographically rough interface and b) a intermixed interface. c) If the interface width σ is the same, both the topographically rough and intermixed profiles can give rise to the same electron density profiles.

and the Fourier transform of this Gaussian distribution is,

$$\exp\left(-\frac{1}{2}q_z^2\sigma^2\right) \tag{3.3.6}$$

Therefore, the Fresnel reflectance is modified by the finite interface width such that,

$$R(q_z) = R_{\mathrm{F}}(q_z)\exp(-q_z^2\sigma^2). \tag{3.3.7}$$

where $\exp(-q_z^2\sigma^2)$ is the Debye-Waller factor [112]. The finite interface width causes the reflectivity to fall faster than q_z^{-4} with an exponential factor that is related to the interface width.

We next progress to the treatment of multilayers for which the scattering from multiple interfaces must be considered.

3.3.2 Optical treatment of x-ray reflectivity and Parratt's recursive formalism

In order to treat the reflectivity of a multilayer, a phenomenological optical approach is considered where the x-ray reflectivity is treated in terms of the Fresnel coefficients and the refractive index of the material, $n = c/v$ where v is the velocity of light in the medium. For x-rays, the refractive index as can be redefined as [110];

$$n = 1 - \delta + i\beta \tag{3.3.8}$$

where δ and β represent the absorptive and dispersive components respectively [110]. They are both related to the electron density $\rho_{\mathrm{e}}(z)$ and have a strong dependence on x-ray energy, which will be discussed later in reference to x-ray resonant magnetic reflectivity. However, for most mediums n is close to unity with $n \approx 1 - 1 \times 10^{-5}$ [113].

The reflection of x-rays from interfaces can be discussed in terms of Snell's law, given by;

$$n_0\cos(\alpha_{\mathrm{i}}) = n_1\cos(\alpha_{\mathrm{t}}) \tag{3.3.9}$$

where α_{t} is the angle of the transmitted beam with respect to the interfacial plane between

the two mediums. The critical angle α_c, below which total external reflection occurs, can be found by setting $\alpha_t = 0$ and using the second order expansion of cosine, yielding,

$$\alpha_c = \sqrt{2(1 - n_1)} = \sqrt{2\delta}. \tag{3.3.10}$$

In the optical treatment of x-rays, the scattering of x-rays by electrons is not considered directly, instead the total reflectivity is found by addressing how x-rays are reflected or transmitted across the interface between media with different refractive indexes. This is governed by the Fresnel coefficients for reflectivity and can be found for each interface of the multilayer using,

$$r_{\mathrm{j,j+1}} = \frac{q_{\mathrm{z,j}} - q_{\mathrm{z,j+1}}}{q_{\mathrm{z,j}} + q_{\mathrm{z,j+1}}} \tag{3.3.11}$$

where $q_{z,j}$ is the transfer wave-vector at the j^{th} interface.

Within a multilayer we must consider the contributions of transmitted and reflected x-rays from various interfaces and their interference. Parratt's recursive formalism addresses this [114] by calculating the total Fresnel reflectivity coefficient of a multilayer in a recursive manner. Parratt's formalism for perfectly smooth interfaces is given by

$$r_{\mathrm{j}} = \frac{r_{\mathrm{j+1}} e^{id_{\mathrm{j}} q_{\mathrm{z,j}}} + r_{\mathrm{j,j+1}}}{1 + r_{\mathrm{j+1}} r_{\mathrm{j,j+1}} e^{id_{\mathrm{j}} q_{\mathrm{z,j}}}} \tag{3.3.12}$$

where $e^{id_{\mathrm{j}} q_{\mathrm{z,j}}}$ is the phase factor mentioned earlier and $\boldsymbol{r}$ has been replaced with the layer thickness d_{j}. The reflectivity amplitude is calculated from the substrate up, as shown in Fig. 3.8. The substrate is assumed to be infinitely thick, for which the reflectivity amplitude for $r_{\mathrm{N}} = 0$. The reflected intensity is then given by $I_{\mathrm{ref}} = R_0 I_0 = |r_0|^2 I_0$

A finite interface width σ can be included by incorporating the Debye-Waller factor derived previously, such that the

$$R_{\mathrm{j},\sigma} = \left| r_{\mathrm{j}} \times \exp\left(-\frac{1}{2} q_{\mathrm{z}}^2 \sigma_{\mathrm{j}}^2 \right) \right|^2 \tag{3.3.13}$$

Alternatively, the material can be cut into sub-nanometer slices and the interface modelled as small concentration gradients between subsequent slices. This is computationally expensive, but particularly useful for modelling ultra-thin layers with thickness comparable to the interface width and was used in chapter 6.

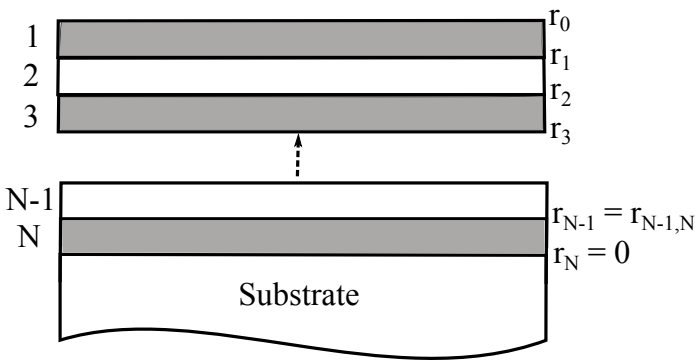

Figure 3.8: Demonstration of the interface and layer label notation used in the Parratt recursive formalism. The Fresnel reflectivity for the substrate interface is r_N. The recursive formalism is applied from the substrate working upwards in steps of N-1 to the surface interface r_0.

Example XRR spectra simulated using the Parratt recursive formalism for smooth Co thin films of different thickness are shown in Fig. 3.9 a). Interference of x-rays reflected from the substrate and surface gives rise to Kiessig fringes and the spacing of these fringes is inversely proportional to the total film thickness. They occur when the requirement for constructive interference is satisfied, which is given by,

$$d \sin \alpha_t = m\lambda \tag{3.3.14}$$

and is analogous to Bragg's law for diffraction from atomic planes [115] but instead for multilayer interfaces.

Fig. 3.9 b) shows the effect of incorporating a finite interface width σ between the Co and the substrate. The Debye-Waller factor causes the intensity to vanish more rapidly and hence the intensity is lower at high incidence angles compared to the case with a smooth interface. The interface also alters the transmission, which results in greater interference effects and deeper Kiessig minima.

In summary, grazing incidence x-ray reflectivity is sensitive to interfacial structure and layer thickness. By simulating the reflectivity these parameters can be extracted with sub-nanometer resolution. From the best fit simulation, the electron density profile through the sample is representative of the cross-sectional structural profile through the sample, making XRR an extremely powerful technique. The next section discusses the XRR measurements.

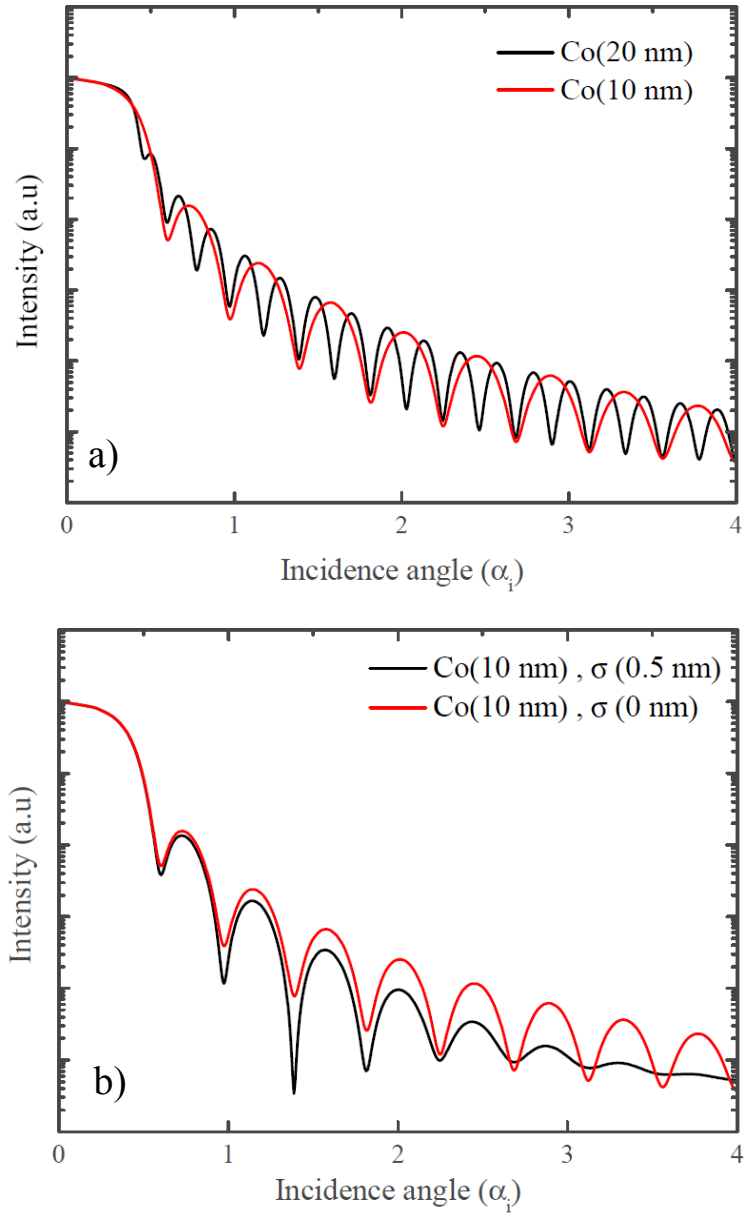

Figure 3.9: Simulated reflectivity using the Parratt recursive formalism for a) Co(20 nm) and Co(10 nm) films with smooth surface interfaces and b) Co(10 nm) films with the inclusion of a finite interface width σ.

3.3.3 Grazing incidence reflectivity experimental method

The XRR measurements presented in chapter 4 were made using a Bede D1 reflectometer with a monochromated Cu-K_α source. A schematic of the system is shown in Fig 3.10. Within the x-ray tube, electrons are accelerated from a filament towards a water cooled Cu target through a 40 kV voltage. This results in bremsstrahlung radiation as well as characteristic Cu-K_α and Cu-K_β emission lines. The majority of the bremsstrahlung radiation was

removed at the primary source slits. A channel cut Si crystal was used to select the Cu-K_α line exclusively by using the Bragg reflections from the (111) plane of Si. It also produced a 2.8 mm lateral offset in the beam. The secondary source slits conditioned the beam to a 0.5 mm beam width and a divergence of approximately 0.01°.

The sample was mounted onto a six axis diffractometer and the beam was incident on the sample at an angle θ. The normal component of the x-ray transfer vector q_z was varied by varying the incidence angle θ and the two variables are interchangeable using the relation $q_z = (4\pi/\lambda)\sin\theta$ [112]. The resulting intensity was measured at the detector, which was mounted at an angle 2θ to obtain the specular condition.

To measure the XRR, coupled $\theta - 2\theta$ scans were made and the intensity variation of the specular reflection as a function of the detector angle was measured. In conjunction with the specular XRR a second scan where the θ rotation was given a systematic offset of 0.1° was also made. This measures the diffuse off-specular scattering and can be subtracted from the specular XRR to obtain the true-specular reflectivity necessary to obtain the true distribution and form the Kiessig fringes for the extraction of the out-of-plane structural properties of the film.

The XRR spectra were fitted using the Parratt recursive formalism described in section 3.3.2 to extract the layer thicknesses, relative electron densities and interface widths. The fitting procedure used a genetic evolution algorithm employed within the freely available GenX software. Further detail on the software and the algorithm can be found at Ref. [116].

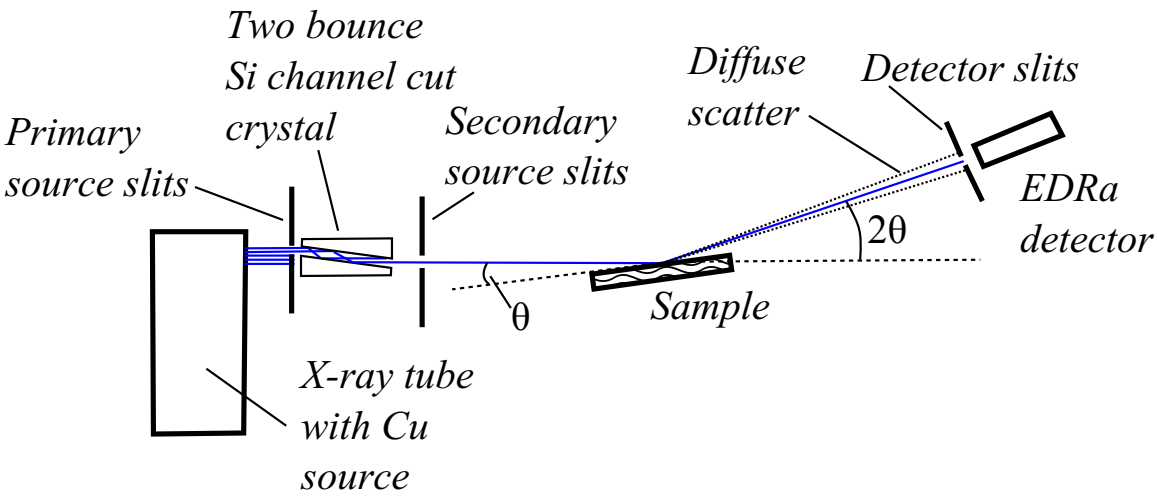

Figure 3.10: Plan view of the XRR measurement setup employed within the Bede D1 reflectivity system.

3.4 X-ray resonant magnetic reflectivity

Grazing incidence x-ray reflectivity is sensitive to the physical sample structure and can be used to obtain the cross-sectional profile of samples. By tuning the x-rays to a resonant energy of electronic transitions and using circularly polarised light, the magnetic circular dichroic properties of x-rays can also be exploited [112, 113, 117]. The measurements can then be used to extract the magnetic cross-sectional profile and since it is resonant, this is also element specific [40]. This technique is referred to as x-ray resonant magnetic reflectivity (XRMR) and was used extensively to study interfacial proximity induced magnetism in chapters 6 and 7.

In this section the effect of resonant scattering on the refractive index and the origin of the circular dichroic effect are discussed, including how this can be incorporated into Parratt's recursive formalism for the analysis of XRMR data.

3.4.1 Resonant enhancement of scattering lengths

When discussing x-ray reflectivity the refractive index can be written in the form $n = 1 - \delta + i\beta$, where δ and β are absorptive and dispersive terms, which depend on the electron density, but are also dependent on the x-ray energy. In fact the total refractive index is given by [110];

$$n = 1 - \frac{\lambda^2 \rho_{at} r_e}{2\pi}\Big\{f_0 + f'(E) + if''(E)\Big\} \tag{3.4.15}$$

with

$$\delta = \frac{\lambda^2 \rho_{at} r_e}{2\pi}\left(f_0 + f'(E)\right) \tag{3.4.16}$$

$$\beta = -\frac{\lambda^2 \rho_{at} r_e}{2\pi} f''(E) \tag{3.4.17}$$

where λ is the x-ray wavelength, ρ_{at} is the atomic density and r_e is the Thomson radius. The terms f_0, f' and f'' are the charge scattering lengths specific to the material. For grazing incidence reflectivity, the energy independent charge scattering length $f_0 \simeq Z$, where Z is the atomic number of the element. Note that the product of the atomic density ρ_{at} and the atomic number Z yields the electron density ρ_e which relates this to the analysis of re-

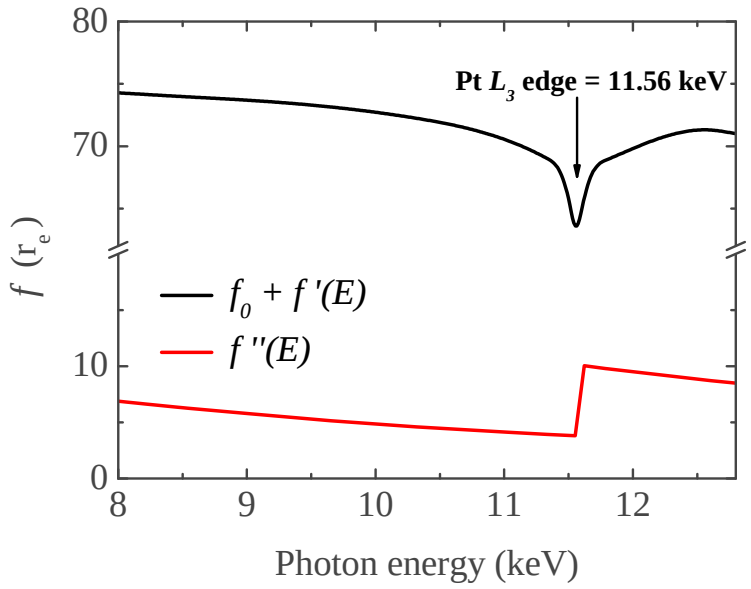

Figure 3.11: Calculated energy dependence of the real and imaginary components of the scattering length for Pt. Data reproduced from the NIST scattering length database [118].

flectivity within the Born approximation presented in section 3.3.1. The anomalous charge scattering lengths, $f'(E)$ and $f''(E)$, have weak energy dependence, except at the resonant energy where they are associated with strong absorption. This is shown in Fig. 3.11 where the energy dependence of the real and imaginary parts of the scattering lengths for Pt are plotted as a function of energy about the Pt L_3-edge.

From equation (3.4.15), it can be seen that the refractive index, and consequently the reflectivity, depend on the product of the total scattering length and atomic density ρ_{at}. This product is referred to as the structural scattering length density (sSLD). The sSLD is specific to the material and consequently sSLD profiles can be formulated which are representative of the cross-sectional structure of the sample. Simulated sSLD profiles for a Pt/Co/Pt trilayer structure are shown in Fig. 3.12, where a dip occurs in the Co layer due to the significantly reduced scattering length relative to Pt, even though the atomic density of hcp Co is higher. Between Figs. 3.12 a) and b), it can be seen that the real/imaginary parts of the sSLD profile are suppressed/enhanced when the x-ray energy is tuned to the resonant edge of the Pt or Co respectively. This reflects the enhancement in absorption at the resonant energy and the resulting change in scattering length shown in Fig. 3.11.

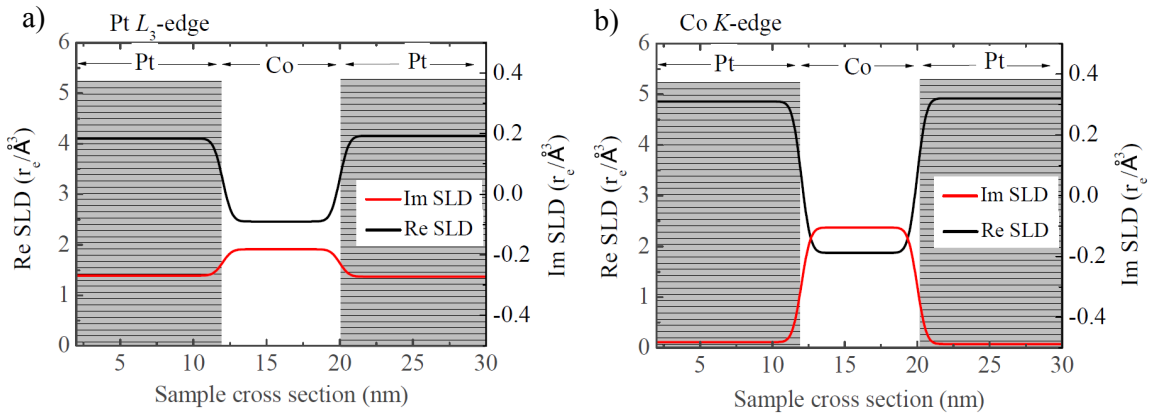

Figure 3.12: Example sSLD profiles for a Pt (12 nm)/Co (8 nm)/Pt (12 nm) film with 0.5 nm topographical roughness applied to the Pt/Co and Co/Pt interfaces, simulated at a) the Pt L_3-edge and b) the Co K-edge.

Resonant magnetic scattering

In analogy to the resonant charge scattering lengths f' and f'', resonant magnetic scattering lengths m' and m'' can also be included in the description of the refractive index. The complete expression for the total scattering length, within the dipole approximation becomes [119],

$$f(E) = (\hat{\epsilon}_s \cdot \hat{\epsilon}_i)F^0(E) - i(\hat{\epsilon}_s \times \hat{\epsilon}_i) \cdot \hat{m}F^1(E). \tag{3.4.18}$$

Here, $\hat{\epsilon}_i$ and $\hat{\epsilon}_s$ are unit vectors describing the polarisation state of the incident and scattered x-rays respectively. F^0 is the total charge scattering length, comprised of both real $f_0+f'(E)$ and imaginary $f''(E)$ parts. F^1 is the equivalent total magnetic scattering length, containing analogous real m' and imaginary m'' components. The refractive index now depends on the direction of the magnetisation and the polarisation axis of the beam and becomes $n^{\pm} = 1-\delta^{\pm}+i\beta^{\pm}$ with $\delta^{\pm}((f_0+f'), \mp m')$ and $\beta^{\pm}(f'', \mp m'')$, where the $\pm$ reflects either a reversal of the magnetisation or the light helicity [119]. This representation can then be incorporated into the Parratt recursive formalism whereby reversing the magnetisation or x-ray helicity results in a change in the XRR simulated intensity.

The magnetic density is defined as the product of the interfacial moment μ and atomic density ρ_{at}. From this the real and imaginary magnetic scattering length densities (mSLD) are defined as the product of the magnetic density and the magnetic scattering factors, m' and m''. In analogy to the sSLD profiles shown in Fig. 3.12, an mSLD profile can be simulated which is representative of the distribution of magnetised resonant atoms throughout

the sample.

In the next section a phenomenological description of the origin of the circular dichroic effect, which gives rise to the variation in reflectivity under the reversal of magnetisation or helicity is presented.

3.4.2 The resonant circular dichroic effect

The circular dichroic effect refers to the change in absorption which is dependent on the relative alignment of the sample magnetisation and polarisation of the x-rays. In a simplified picture the effect can be explained as a two step process [120], starting with a spin-orbit split core state. It can be seen in Fig. 3.13 that the degeneracy of the $2p$ states is lifted by the spin-orbit interaction and split into the $2p_{3/2}$ and $2p_{1/2}$ states, where the spin and orbital angular momentum couple parallel and anti-parallel respectively. When the electron is excited by a photon, conservation of momentum couples the photon momentum to the spin and orbital momentum of the electron [119]. The first step then is that the circularly polarised x-rays become a source of spin-polarisation, preferentially exciting electrons with momentum collinear to their own [113]. In this way the x-ray helicity can be used to choose which spin-species is predominantly excited. However, in ferromagnets there also exists an asymmetry in the number of available states at the Fermi energy (E_{F}) between spin $\uparrow$ and spin $\downarrow$ states. This second step gives rises to a difference in absorption for right circularly polarised (RCP) and left circularly polarised (LCP) light, since the Pauli exclusion principle only allows excitations to vacant states.

The effect is dependent on the transitions from the spin-split core states to the valence states above E_{F}. Consequently F^1 in equation (3.4.18) is small unless the x-ray energy is close to a resonant energy. Within this expression, only the imaginary component m'' contributes to absorption and can be measured directly using x-ray magnetic circular dichroism (XMCD). However, when measuring XRMR, the magnetic sensitivity arises through the combination of absorption and re-emission, which then depends on both m' and m'' and hence these factors cannot be isolated independently. For this reason absolute values for magnetic moments cannot be extracted using XRMR alone. The F^1 term is linear in magnetisation, hence by measuring the scattering intensity under positive/negative magnetisation or LCP/RCP helicity, the magnetic contribution to scattering can be isolated [121].

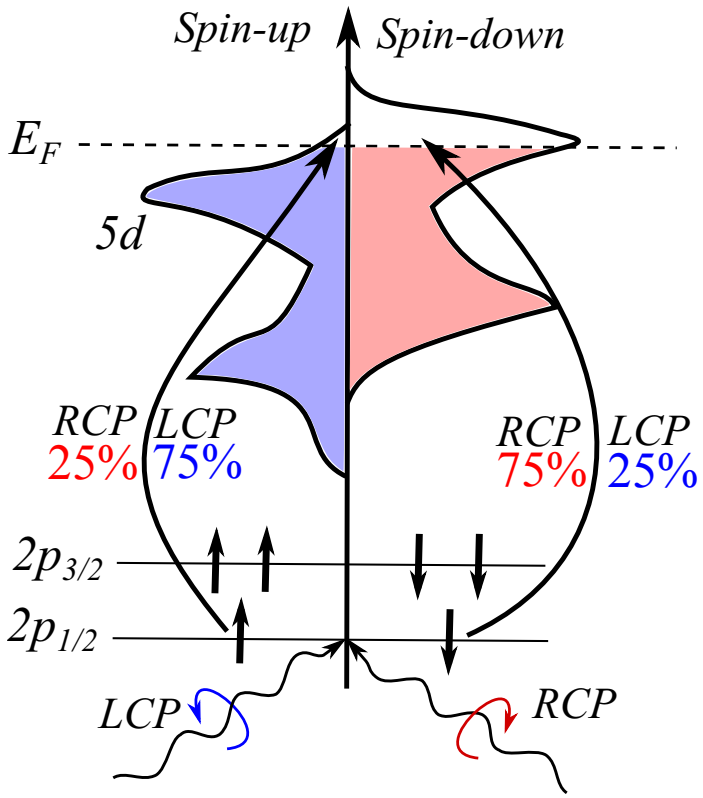

Figure 3.13: Since the $2p_{1/2}$ is a spin-orbit split state, the spin and orbital angular momentA are coupled and consequently a RCP x-ray is more likely to excite a spin ↓ electron (75%) to the valence states than a spin ↑ electron (25%). Conversely, an LCP x-ray is more likely to excite a spin ↑ electron to the valence states. In ferromagnets this results in a difference in transition rates between RCP x-rays and LCP x-rays since there is a difference in the number of available 5*d* states for the allowed spin-coherent transitions around E_F.

3.4.3 Spin-asymmetry measurements and element specific hysteresis loops

The XRMR experimental setup is identical to the XRR measurement demonstrated in section 3.3.3. The principle difference is that circularly polarised x-rays were used, the x-ray energy was tuned to a resonant edge and the difference in scattering intensity under positive/negative magnetic saturation or alternatively RCP/LCP x-rays was determined.

For the measurements in this thesis, the circularly polarised x-rays were obtained using a diamond phase plate. Close to the Bragg condition, a perfect crystal of a birefringent material can behave as a phase retarder and convert linearly polarised light into circularly polarised light and vice versa when the phase retardation is equal to $\pm\pi/2$ [122].

For the XRMR measurement, the magnetic reflectivity is contained in the difference in

intensity between positive/negative magnetic saturation respectively or alternatively RCP/LCP x-rays. For the purpose of the measurement, the spin-asymmetry ratio is defined;

$$R_{\mathrm{a}} = \frac{I^{+} - I^{-}}{I^{+} + I^{-}} \tag{3.4.19}$$

which is the difference in scattering intensities normalised to the total scattering intensity. Here, $I^{\pm}$ are the reflected intensities at positive/negative magnetic saturation respectively or alternatively LCP/RCP helicity polarity respectively. Generally, it was faster to reverse the magnetisation with fixed helicity, and consequently this method of measuring R_{a} was used throughout this thesis. R_{a} was then measured as a function of the x-ray incidence angle and some example data for a Pt/Co/Pt trilayer structure measured at the Pt L_3-edge is shown in Fig. 3.14. Note that the peaks in R_{a} coincide with the Kiessig minima, this is because R_{a} contains the normalisation to the total scattered intensity. This data can be fitted in order to obtain the distribution of magnetic moments associated with the resonant elements throughout the cross-section of the sample. For this, the magnetic reflectivity package included within the GenX software [116] was used, which employs a modified Parratt recursive formalism, whereby the resonant magnetic scattering terms outlined in the previous section are included in the definition of the refractive index.

The XRMR technique can also be used to obtain element specific hysteresis loops. Here, instead of reversing the magnetisation, the helicity was flipped and R_{a} was measured as a function of the applied magnetic field swept in-plane along the scattering vector. This is demonstrated in the inset of Fig. 3.14. Under positive magnetic saturation, flipping the light helicity and calculating $\mathrm{R_a}$ at point 1 in angular space on the schematic yields a large positive value for $\mathrm{R_a}$. When the magnetic field was swept, at some point the magnetisation reversed and the value of $\mathrm{R_a}$ switched from that at point 1 to that at point 2. Therefore, $\mathrm{R_a}$ is sensitive to the magnetisation direction with respect to the light helicity and since the magnetic scattering factors are only sensitive to the resonant elements, this was a hysteresis loop specific to the proximity polarised Pt.

The interaction of light and magnetism is not restricted to the x-ray region of the electromagnetic spectrum and in the next section the magneto-optical Kerr effect is introduced, which occurs in the visible part of the spectrum.

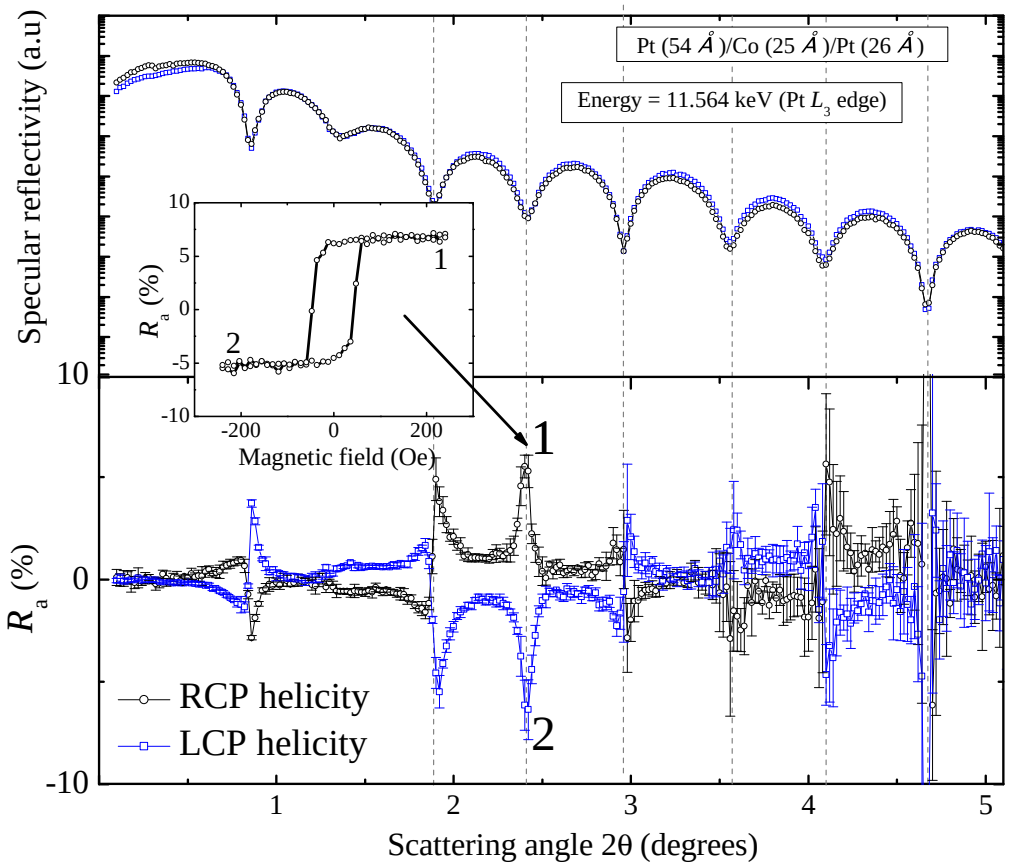

Figure 3.14: A typical measurement of the specular reflectivity (top) and angular dependence of R_a (bottom). The R_a distribution was obtained by reversing the magnetisation at each x-ray incidence angle θ and measuring the spin asymmetry R_a. Reversing the light helicity caused a reflection in the x-axis. An element specific hysteresis loop for Pt is shown in the inset. This was measured at $2\theta = 2.4°$, which combines the high count statistic at low angle with a large change in R_a between the points 1 and 2.

3.5 Magneto-optical Kerr magnetometry

The origin of the magneto-optical Kerr effect (MOKE) is closely related to that which causes the polarisation dependence in XMCD and XRMR measurements in the x-ray part of the electromagnetic spectrum. The MOKE occurs in the optical region and the excitations originate from the conduction bands rather than the low lying core states [112].

The interaction of polarised light with magnetisation was first observed by Faraday in 1845 [123], by which it was observed that the plane of polarisation of light underwent a rotation when transmitted through a magnetic material. Thirty years later, Kerr demonstrated that a similar effect arose when light was reflected from a magnetic surface [124].

Throughout this thesis MOKE magnetometery was used as a measurement tool to measure magnetisation reversal behaviour.

3.5.1 Interaction of polarised light and magnetisation

For MOKE magnetometry linearly polarised light is used, which itself can be expressed as the sum of LCP and RCP components. The angle of the polarisation axis of the linear polarisation is dependent on the phase difference between the LCP and RCP contribution. The MOKE arises due to the difference in the effective refractive index experienced by LCP and RCP light within a magnetised medium. This phenomena is referred to as circular birefringement.

The consequence of this is that, after reflection from a magnetic surface, a phase difference develops between the LCP and RCP light, which results in a rotation of the linear polarisation axis. This rotation is referred to as the Kerr rotation. Alongside this, it is usual that some degree of ellipticity also develops after reflection as a consequence of the material exhibiting a degree of circular dichroism.

The origin of the circular birefringence, and therefore the MOKE, is due to the combination of the exchange interaction and the spin-orbit interaction in ferromagnetic materials. The effective refractive index for LCP and RCP has a dependence on the magnetisation of the film and hence the Kerr rotation can be used to probe the magnetic state of the sample. However, a detailed understanding of the origin of the birefringence requires a thorough discussion of dielectric tensor theory, which can be found in Ref. [125]. Dependent on the choice of measurement geometry the MOKE is sensitive to different components of magnetisation with respect to the plane of the sample. These geometries are discussed in the next section.

3.5.2 Longitudinal, transverse and polar Kerr effects

There are three measurement geometries for the MOKE: longitudinal, transverse and polar, which are summarised in Fig. 3.15 and characterised by the relative directions of the magnetisation M and scattering vector k. The Kerr rotation only occurs if there is a component of magnetisation along the scattering vector. The longitudinal MOKE is therefore sensitive

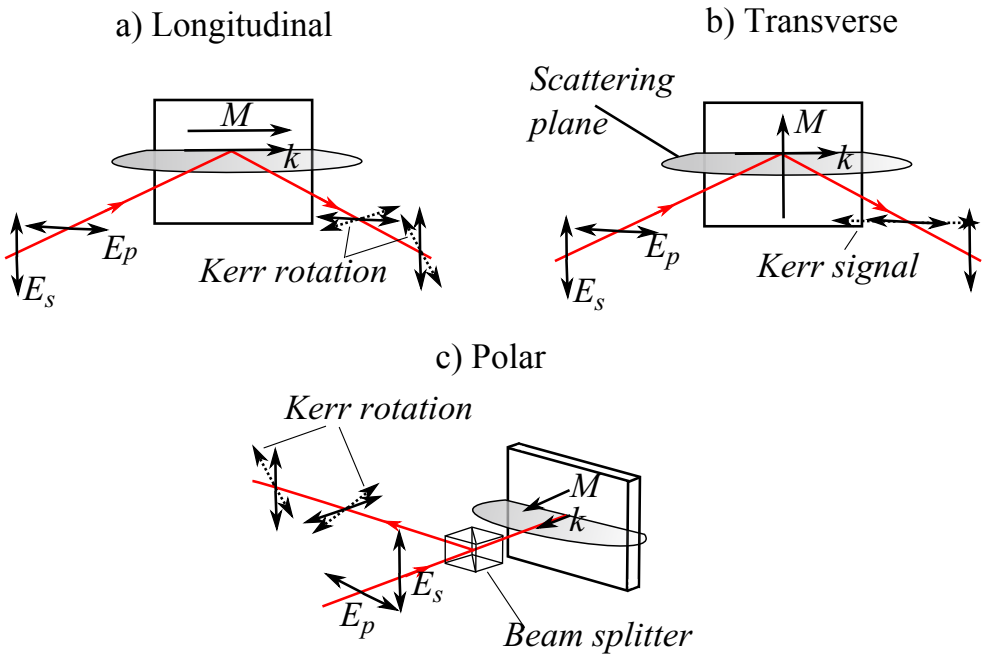

Figure 3.15: The scattering geometries for a) longitudinal, b) transverse and c) polar MOKE experiments.

to in-plane magnetisation whilst the polar MOKE is sensitive to out-of-plane magnetisation components. The transverse MOKE is unique in that it only occurs with *p*-polarised light. It does not result in a Kerr rotation, since no component of M lies along the scattering vector k, but instead it gives rise to a magnetisation dependent intensity variation. Only the longitudinal and polar MOKE were used in this thesis. The polar MOKE has the largest effect and is generally an order of magnitude larger than the longitudinal MOKE.

3.5.3 Optical penetration depth

Typically, in a metallic film the MOKE is sensitive only to the magnetisation of the top 5-20 nm. This is because the effect is limited by the penetration depth of the light into the sample. The penetration depth is given by;

$$\lambda_{\mathrm{MOKE}} = \frac{1}{2k\beta} \tag{3.5.20}$$

where k is the wavevector of the incident light and β is a constant which represents the absorptive component of the refractive index. At the depth given by λ_{MOKE} the laser intensity is attenuated by 1/e of its original value. For film thicknesses below λ_{MOKE} the Kerr

rotation is proportional to the total magnetic moment of the sample, and hence is proportional to the sample thickness. However, extracting absolute magnetic moments from the MOKE is challenging since it is significantly affected by reflections that occur at the ferromagnet/substrate interface. For film thicknesses above λ_{MOKE}, the Kerr rotation is limited by the absorptive component.

3.5.4 Magneto-optical measurements of micro-structures

In this thesis, both longitudinal and polar MOKE were used. The experimental setup used for these measurements are shown in Fig. 3.16 and Fig. 3.17 respectively. For the longitudinal MOKE the laser was incident on the sample at an angle of approximately 45°, whereas for the polar MOKE the light was incident at 90°. The polar MOKE measurement requires an additional beam splitter to separate the incident and reflected light from the sample and two additional lenses to re-focus the light onto the photodiode. The following discussion applies to both MOKE setups.

For MOKE measurements both the in/out attenuator and in/out beamsplitter were placed out of the beam. A diode laser with a wavelength of 658 nm was used for all MOKE measurement in this thesis. This passed through a beam expander, then a Glan-Taylor polarising prism, which was set to ensure p-polarised light was incident on the sample. The first lens focused the laser spot to ~ 5 μm onto the sample. The reflected light was then focused onto the photodiode, passing through a $\lambda/4$ wave plate and an analysing polariser. The purpose of the $\lambda/4$ wave plate was to remove any induced ellipticity in the reflected light. The analyser was set to extinction and then offset to between $2-6°$, which was variable dependent on the reflectivity of the sample. The Kerr rotation was then measured as a change of intensity at the photodiode due the rotation of the polarisation axis of the reflected light relative to the polarisation axis of the analyser. The photodiode voltage was passed to a Melles-Griot large dynamic range amplifier that enables the amplification of small signals superimposed onto large offsets, which is typical for the Kerr voltage.

The hysteresis loops obtained using these MOKE set ups were averaged over many field cycles. Here the magnetic field was driven by a Kepco BOP 50-5M power supply which was in turn driven by a signal generator operating at 23 Hz. This oscillating magnetic field would cause the sample to cycle through the hysteresis loop, which would produce an

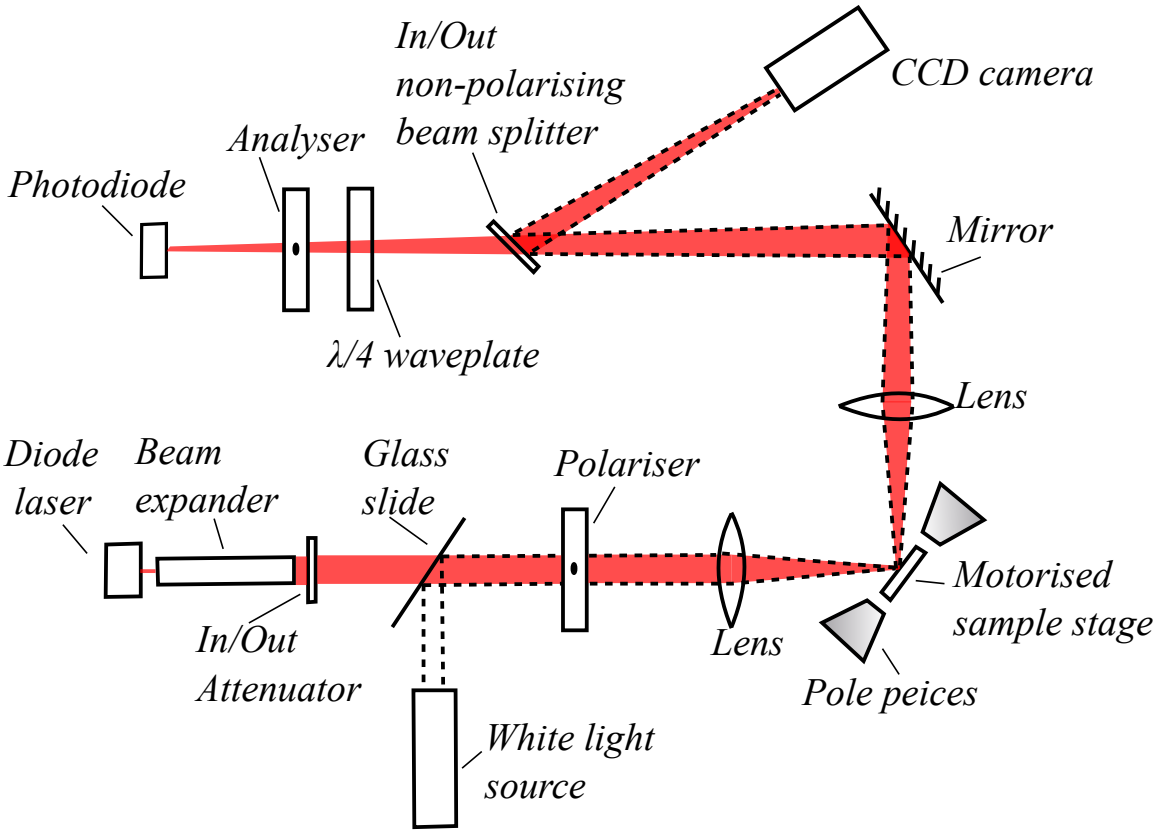

Figure 3.16: The experimental setup for the longitudinal MOKE measurements.

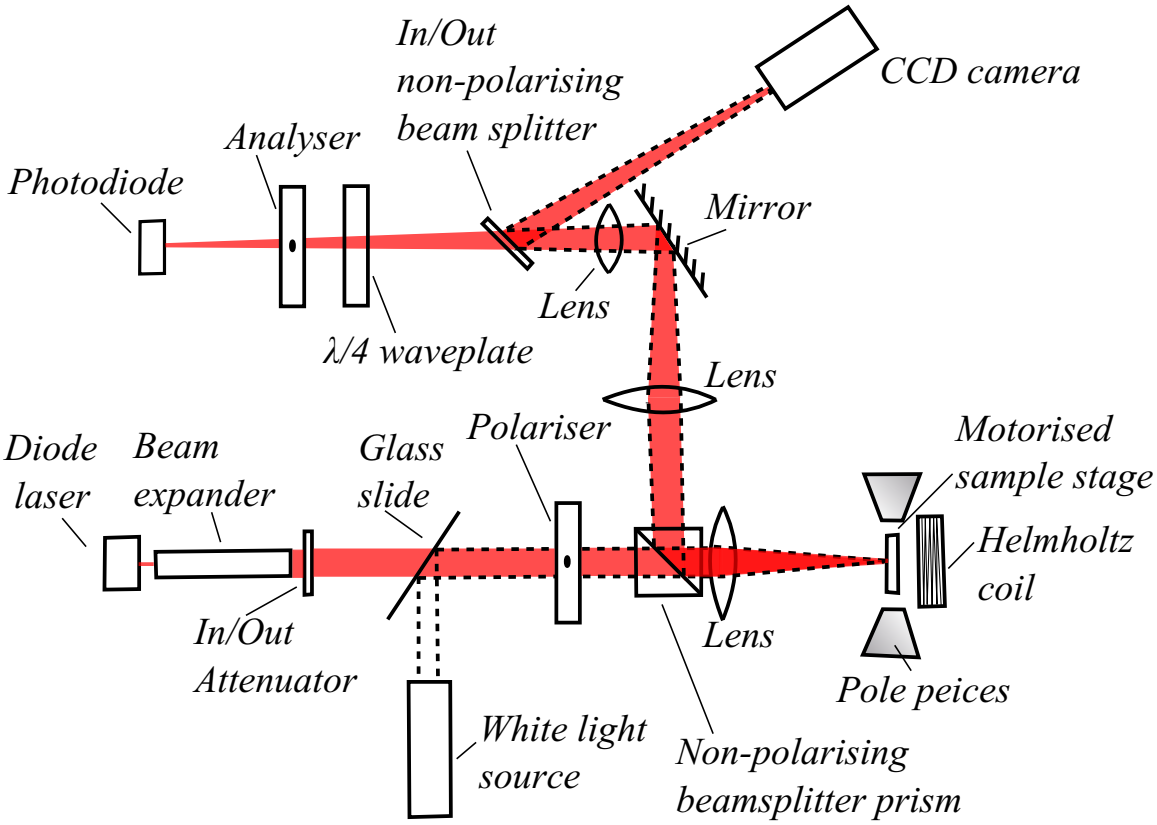

Figure 3.17: The experimental setup for the polar MOKE measurements.

oscillating Kerr voltage, which was measured by an oscilloscope and time-averaged over many hundreds of field cycles, and therefore provides a very effective way to efficiently enhance the signal to noise ratio.

White light was used to image the sample for the purpose of aligning microstructures with the laser spot. For this, the in/out attenuator and in/out beamsplitter were placed into the beam. The white light follows the same beam path as the laser beam. The attenuator reduced the laser light intensity such that it did not saturate the CCD camera. The in/out beamsplitter then reflected the light onto a CCD camera, where both the attenuated laser spot and sample surface were imaged. Here, a motorised *xy* translation stage with 1 μm step resolution was used to position the laser spot onto the microstructure to be measured. This configuration was also used to focus the laser spot to achieve maximum central intensity, whilst minimising the higher order modes.

3.5.5 Time-resolved magneto-optical Kerr effect

Measurements of the MOKE were also made within the time-domain using time-resolved magneto-optical Kerr effect (TR-MOKE) measurements. The measurements presented in this thesis were made at the S.N. Bose institute for Basic Sciences, Kolkata, India and publications made using this specific TR-MOKE system can be found at Refs. [79, 81].

TR-MOKE is a pump-probe technique with picosecond resolution and can be used to measure the magnetisation precession about an external magnetic field in order to investigate the magnetisation dynamics of a sample. The experimental set-up is significantly more complex than the MOKE experiments presented in the previous section and is shown in Fig. 3.18.

However, the key features of the experiment can be summarised as follows. A 100 fs pulsed Ti-sapphire laser with a wavelength of 800 nm was split into two beams, which were termed the pump and probe beams. The pump beam passed through a second harmonic generator (SHG), which halved the wavelength to 400 nm. This beam had a high power of 17.0 mJ/cm^2 and when incident on the sample caused the film to demagnetise, recover and then initialised the magnetisation precession about the external in-plane magnetic field. The probe beam had a power of 2.1 mJ/cm^2 and was directed to a retro-reflector mounted on a variable delay stage. The polar component of the magnetisation precession about the

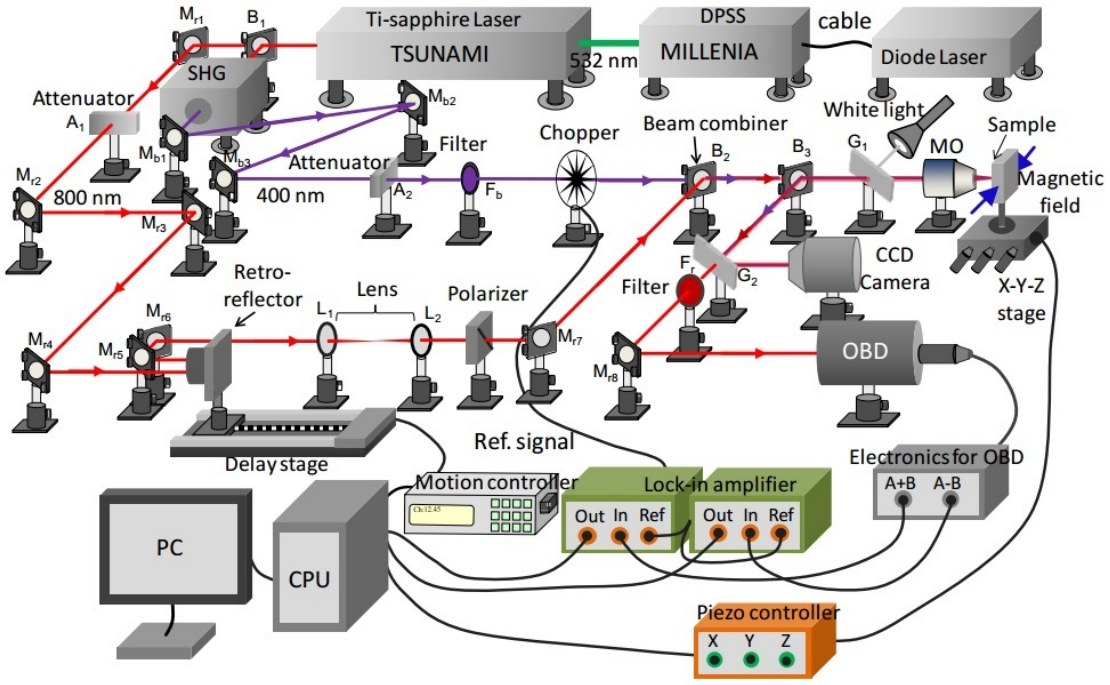

Figure 3.18: Schematic of the TR-MOKE experimental set-up. The polar MOKE configuration was used to study the out-of-plane component of the magnetisation precession with temporal resolution after demagnetisation caused by pump beam pulse. Figure reproduced from Ref. [126]

in-plane applied magnetic field was then measured using an optical bridge detector (OBD).

The delay stage was calibrated such that the extension in probe beam path resulted in a known time delay between the arrival of the probe beam at the sample relative to the pump beam, which was of the order of picoseconds. Temporal resolution was then obtained through the repeated sampling of the magnetisation state at different time delays between the pump and probe beams, therefore developing an ensemble representation of the magnetisation precession.

3.6 Brillouin light scattering spectroscopy

Brillouin light scattering (BLS) spectroscopy is a technique by which spin-wave modes can be investigated through their inelastic scattering with photons. This inelastic scattering results in a frequency shift of the reflected light, which can be measured using a tandem Fabry-Pérot interferometer.

Within this thesis, all BLS measurements were made at the Université Paris 13. Here, a brief overview of the particular BLS measurement applied to obtain the results used in

chapter 8 is presented. For a detailed discussion of the BLS technique the reader is referred to reference [127]. Published work using the BLS system used by the Université Paris 13 group can be found at Refs. [12, 128].

The backscattering geometry was used for all measurements and is shown in Fig. 3.19 a). Here, the magnetic field was applied in the plane of the film and transverse to the incident light scattering vector. This probes the Damon-Eshbach surface propagation spin-wave mode.

Linearly polarised laser light was incident on the sample and the backscattered light was collected by an objective lens and directed to the Fabry-Pérot interferometer, where it was combined with a reference beam. The reference beam originates directly from the laser without scattering from the sample and hence provides the reference frequency. The frequency spectrum was then analysed by comparing the interference between the back-scattered and reference beams inside the Fabry-Pérot interferometer. An example of a BLS spectrum is shown in Fig. 3.19 b). Most light is scattered elastically through Rayleigh scattering, but at higher frequency, stokes and anti-stokes lines occur due to phonon and magnon scattering events. The phonon lines can be removed by including a polarisation analyser before the Fabry-Pérot interferometer. From the frequency of the magnon line the energy of the magnon excitation can be calculated.

Laser light of wavelength λ = 532 nm was used. The spin-wave mode probed by the

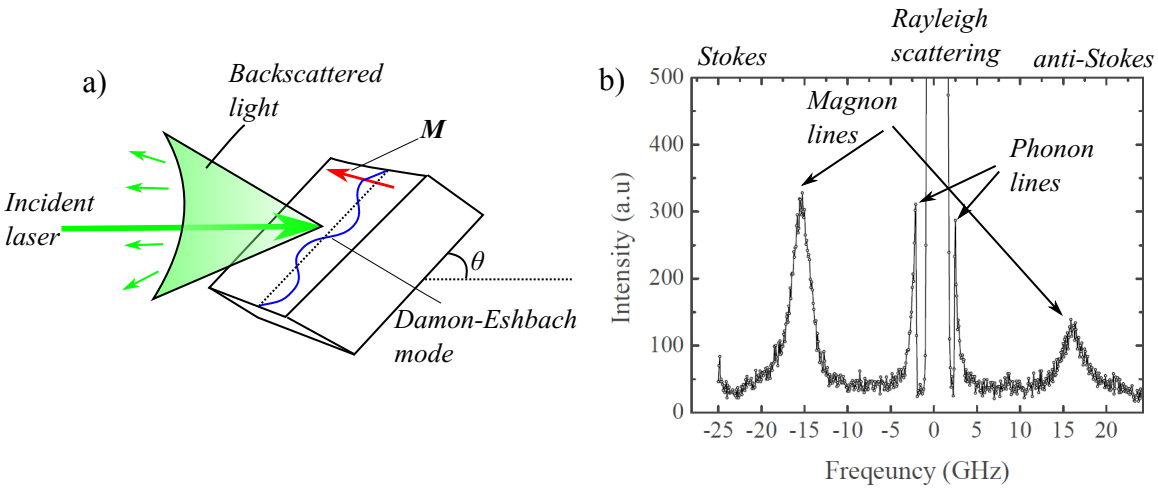

Figure 3.19: a) Schematic of the scattering geometry used to measure the Damon-Eshbach surface spin-wave mode. b) Example of a BLS spectrum measured from a Pt (54 Å)/Co (25 Å)/Ir (10 Å)/Pt (26 Å) multilayer.

laser is related to the angle of incidence θ by;

$$k_{sw} = \frac{4\pi}{\lambda} \sin\theta \tag{3.6.21}$$

and hence spin-wave numbers between 0-20 μm^{-1} could be investigated by rotating the sample about the planar axis. From this the spin-wave dispersion relation can be obtained.

In the final section, the methodology applied to the electronic transport measurements used in this thesis is discussed.

3.7 Electronic transport measurements

In this thesis all transport measurements were made using the four-probe method, whereby the voltage was measured independently from the applied current. For the transport measurements, two geometries were used, which were termed the longitudinal and transverse geometries. Here, the voltage was measured either along the current flow (longitudinal) or in the Hall geometry (transverse) and are shown schematically in Fig. 3.20. In this thesis, the longitudinal geometry was used primarily, where it formed the basis of chapter 4 for the anisotropic magnetoresistance measurements. However, the transverse geometry was used to an extent in chapter 5 in conjunction with MOKE measurements to elucidate on the nature of spin-orbit torques.

Both geometries utilise four-probes, which has the advantage that it discounts any contributions from contact or lead resistances. A constant current was applied using a Keithley 2400 current source, which was independent of the voltage measured across the samples. The voltage was measured between the voltage probes using a Keithley nanovoltmeter. The input impedance of this was greater than 10 GΩ, hence the nanovoltmeter draws negligible

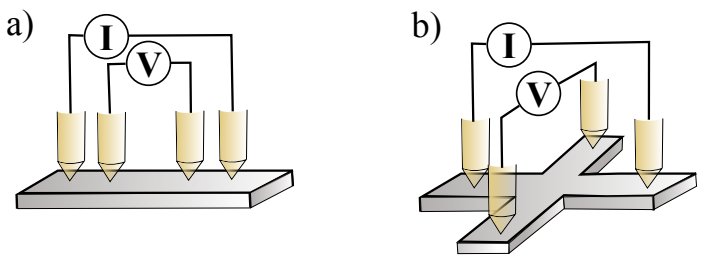

Figure 3.20: Schematic representations of the measurement geometry for a) longitudinal and b) transverse resistivity measurements.

current. The voltage drop was therefore due to the resistance across the film between the voltage probes only. The measured voltage is proportional to the gap between the voltage probes, hence the space between the voltage probes was maximised in order to improve the measurement sensitivity.

3.7.1 Four-probe magnetoresistance measurements

Magnetoresistance measurements form the basis of chapter 4, in which the anisotropic magnetoresistance (AMR) was measured in the longitudinal geometry. A detailed discussion of the AMR effect is given in chapter 2, but crucially the resistance is maximum for when measured in-plane and along the magnetisation direction $\rho_{\parallel}$ and minimum when measured transverse to the magnetisation direction $\rho_{\perp}$.

The sample geometry was defined as 18 mm $\times$ 3 mm using shadow mask deposition, in order to induce a large aspect ratio and to reduce the error within the resistivity calculations. There are two fundamental AMR measurements: change in resistivity as a function of applied magnetic field magnitude at a fixed angle and change in resistivity as a function of fixed magnetic field magnitude but varying angle. These are termed field-sweeps and angular-sweeps respectively.

The experimental setup for these measurements can be described as follows. The sample was mounted on a rotation stage between an electromagnet and electrical contact was made using gold-plated phosphor bronze spring loaded pins. The separation between the voltage pins was 7 mm. Dependent on the size of the measured voltage and the contribution of Joule heating in the specific sample, a current of between 0.1 – 2 mA was applied to the sample. The electromagnet was capable of applying magnetic fields of up to 1 kOe and was powered by a Kepco BOP 50-5M power supply. The true field at the sample was measured using a calibrated Hall probe. Rotation of the sample varied the direction of the magnetic field with respect to the current flow within the plane of the film. Software developed by the author and written in the Visual Basic 6.0 programming language was used to perform the angular or field sweeps by measuring the resistivity as the sample stage rotated or as the magnitude of the magnetic field was varied respectively.

Hall effect measurements

In the transverse configuration the voltage probes are sensitive to the Hall voltage. If the magnetisation change was out-of-plane then the anomalous Hall effect (AHE) was measured. For in-plane magnetisation rotation, the planar Hall effect (PHE) was measured.

Measurements of both the anomalous and planar Hall effect are included in chapter 5. For the PHE the voltage change has its origin in the AMR effect whereas the AHE originates from the same spin-dependent scattering mechanisms which give rise to the spin-Hall effect in non-magnetic materials.

In this thesis, these measurements were performed simultaneously alongside the MOKE measurements, but the same principle as the longitudinal resistivity measurements applied, by which the change in resistivity was measured as a function of applied magnetic field at various angles between the magnetic field and current flow. The electromagnet associated with the MOKE system could apply in-plane magnetic fields of up to 300 Oe and was powered by a Kepco BOP 50-5M power supply.

4 Understanding the thickness dependence of the anisotropic magnetoresistance effect

4.1 Introduction

Although the existence of the anisotropic magnetoresistance (AMR) effect in ferromagnets has been known since the experiments of Thompson over 150 years ago [25] and a theoretical framework, developed by J. Smit, has existed since 1952 [17], the phenomena continues to demonstrate many subtleties that are not clearly understood. The origin is known to arise from the spin-orbit interaction, but the microscopic details arising from extrinsic factors such as interface structure, film composition and texture are not well accounted for in current theories and can have a dramatic effect on the AMR observed.

Consequently, over 150 years after its discovery, AMR is still the focus of a large number of experimental [34, 35, 129–131], and theoretical studies [132, 133] including the addition of new members to the AMR family of effects, such as, ballistic AMR [26], interfacial AMR [28], Coulomb blockade AMR [27], crystalline contributions to AMR [134] and negative AMR in half metals [63]

The use of AMR in magnetic read heads [30] in the 1990s, and the application of AMR in magneto-resistive field sensors [29, 135], resulted in intensive research aimed at maximising the AMR ratio ($\Delta\rho/\rho$) and the field sensitivity. The AMR ratio is defined as the absolute resistivity difference between longitudinal and transverse resistivities $\Delta\rho$, divided by the sample resistivity ρ. This is the figure of merit for technological applications, where higher values indicate enhanced response.

From several studies, one particular outstanding problem relating to AMR that became apparent, was the unexplained thickness dependence, in which the absolute resistivity

change $\Delta\rho$, reduces as film thickness is decreased [62,115,136]. This problem has attracted limited attention since the thickness dependence of $\Delta\rho/\rho$ was supposedly explained by the rising sample resistivity due to the size effect [32, 33]. Furthermore, the thickness dependence of $\Delta\rho$ is subtle, where it is constant over a range of thicknesses [16, 137], before falling dramatically for ultrathin ferromagnetic films [62].

Theoretical studies by Dieny et al [36] and Rijks et al [138] made an attempt to address the thickness dependence of $\Delta\rho$ by considering the effects of perfect specular or perfect diffuse scattering from the film interfaces. Both found that for perfect diffuse scattering from interfaces, $\Delta\rho$ should be enhanced with reducing film thickness. They argued that, similar to the AMR effect itself, the contribution of diffuse scattering to the resistivity is greater for an electron travelling parallel to the magnetisation than one travelling transverse to it. This theoretical development is in direct contradiction with the reduction in $\Delta\rho$ that is observed experimentally [62, 115, 136], demonstrating the need for a more complete understanding of the contribution of interfacial scattering to AMR.

In this chapter, the thickness dependence of $\Delta\rho$ was investigated and explained in terms of enhanced electron-magnon spin-flip scattering with reducing film thickness [62]. Fundamental to this understanding is the Campbell, Fert and Jaoul (CFJ) model [58], which was successful in quantitatively explaining the AMR in a variety of Ni-based alloys, and was explained in chapter 2. A series of pure Ni, $Ni_{95}Cr_5$ and $Ni_{95}V_5$ films of varying thickness were sputter deposited and characterised structurally using grazing incidence x-ray reflectivity (XRR), transmission electron microscopy (TEM) and energy dispersive x-ray spectroscopy (EDX). Magnetoresistance measurements were made on the Ni, $Ni_{95}Cr_5$ and $Ni_{95}V_5$ films to extract the AMR as function of film thickness. Complementary to the AMR measurements, magnetisation measurements were made to extract the spin-wave stiffness, D, to inform on magnon density, in order to give insight into any changes in the contribution of electron-magnon scattering. Furthermore, a thickness dependent electron-magnon scattering term was added to the CFJ model and was able to reproduce the experimental results with reasonable parameters.

In the following sections, details of the sample structure and the differences in sample morphology for films of different thickness are discussed before reporting the AMR results and the subsequent analysis and interpretations.

4.2 Structural characterisation of the thin films

4.2.1 Description of the samples investigated

A series of Ni, $Ni_{95}Cr_5$ and $Ni_{95}V_5$ films with different thickness varying between 3-17 nm, were sputter deposited onto SiO_2 substrates with a base pressure of order 5×10^{-8} Torr. No capping layers were deposited in order to remove the need for current shunting corrections. However, a native oxide formed on the films which was characterised using XRR. Deposition was performed through a 18 mm x 3 mm mask to create a well defined geometry for the resistivity measurements. A dopant concentration of $x = 5$ at.% was used for both $Ni_{100-x}Cr_x$ and $Ni_{100-x}V_x$ alloys, and was achieved by co-sputtering two targets simultaneously. When co-sputtering the Ni with V or Cr, the deposition rates were adjusted in order to obtain the required dopant concentration. From these samples, the film thickness, native oxide thickness and interface widths were obtained using XRR.

Alongside these, three sister samples of Ni films with thickness 15 nm, 6 nm and 4 nm were sputter deposited onto 10 nm thick silicon nitride windows for the TEM analysis to study the film morphology at different thicknesses and in particular to determine the onset of film discontinuities. EDX was also used to investigate the oxygen content in these pure Ni films, as a result of the surface oxide.

4.2.2 Grazing incidence reflectivity characterisation of the native oxide and interface roughness

The XRR measurements of the Ni, $Ni_{95}V_5$ and $Ni_{95}Cr_5$ films were made using the Bede D1 system described in chapter 3. Fits were made using the GenX software [116] which uses a modified Parratt recursive formalism, also described in chapter 3. Structural information was obtained by simulating the distribution and shape of the Kiessig fringes which occur due to interference between refracted waves at the film interfaces. Since the spacing of these fringes is inversely proportional to the thickness of the film, this technique works best for mid-range thickness films (10-30 nm) for which the fringes are well resolved and numerous within the θ scan range to produce robust and reliable fits. Consequently, XRR was not used to characterise the thinnest films in this study. The XRR from Ni, $Ni_{95}V_5$

and $Ni_{95}Cr_5$ films and the best fit simulations to the true specular reflectivity are shown in Fig. 4.1.

The parameters obtained from the best fits are shown in Table 4.1. The surface region is referred to as the native oxide of the thin film and is associated with a pronounced deficit in electron density. This arises due to oxidation, surface roughness and a reduction in nearest neighbour interactions. For the purpose of the simulation this surface region is given the composition of NiO, which is a reasonable approximation since all the films comprised predominantly of Ni. The electron density was allowed to fluctuate significantly for this layer since it is unlikely to have the bulk NiO electron density. This is reflected in the best fitting parameters, where the native oxide electron density is consistently lower than that for bulk NiO. There is an indication from the higher electron density from the Ni(12 nm) to the Ni(17 nm) that as the Ni thickness increases the electron density of the native oxide begins to approach that of bulk NiO, suggesting thicker films form oxides with improved structure.

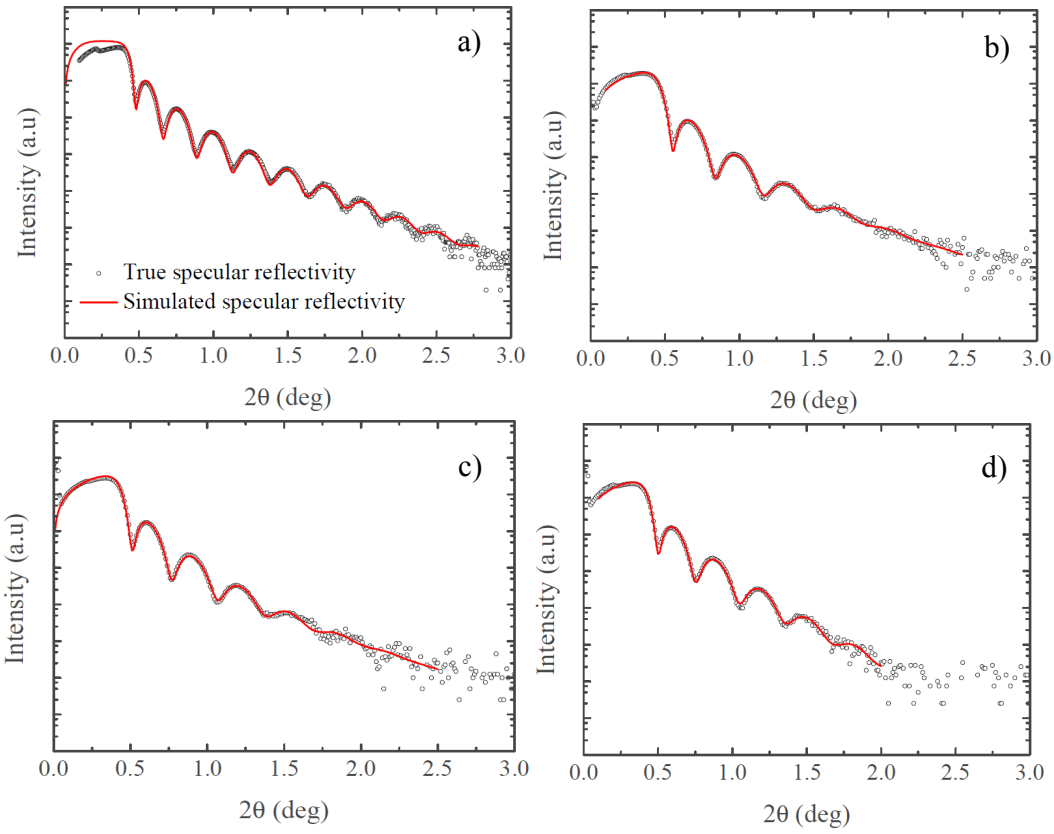

Figure 4.1: Grazing incidence specular XRR for a) Ni (17 nm), b) Ni (12 nm) c) $Ni_{95}V_5$ (12 nm) and d) $Ni_{95}Cr_5$ (12 nm) films and simulated best fits (solid lines). Nominal sample thicknesses are quoted in the brackets.

Sample	Layer	Thickness (*nm*)	Interface width (*nm*)	Electron density (*% of bulk value*)
Ni(17 nm)	Native oxide	0.7 ± 0.3	0.5 ± 0.3	83 ± 10
	Ni	16.2 ± 0.7	0.5 ± 0.3	100 ± 3
	SiO_2	∞	0.6 ± 0.1	100
Ni (12 nm)	Native oxide	0.5 ± 0.5	0.5 ± 0.1	68 ± 7
	Ni	11.7 ± 0.6	1.2 ± 0.3	107 ± 2
	SiO_2	∞	1.0 ± 0.1	100
$Ni_{95}V_5$ (12 nm)	Native oxide	0.5 ± 0.5	0.4 ± 0.1	45 ± 12
	$Ni_{95}V_5$	13.3 ± 0.7	1.1 ± 0.2	97 ± 4
	SiO_2	∞	1.0 ± 0.1	100
$Ni_{95}Cr_5$ (12 nm)	Native oxide	0.3 ± 0.3	0.9 ± 0.1	45 ± 3
	$Ni_{95}Cr_5$	13.5 ± 0.1	0.6 ± 0.1	93 ± 1
	SiO_2	∞	1.0 ± 0.1	100

Table 4.1: Extracted parameters from the best fits to the XRR data shown in Fig. 4.1 for the Ni (17 nm), Ni (12 nm), $Ni_{95}V_5$ (12 nm) and $Ni_{95}Cr_5$ (12 nm) films.

The thickness of the native oxide is smaller than the error margin and comparable to the interface width. The simulations use error functions to model the electron density across interfaces, hence for sub-nanometer layers like this, there is significant overlap of the error functions for the top and bottom interfaces resulting in a large uncertainty in the layer thickness. However, the native oxide thicknesses modelled and the interface widths are not unreasonable and indicate that it has not formed a continuous layer. There is also reasonable consistency between the native oxide layer thicknesses modelled, where it is below 1 nm for all films. This demonstrates that the introduction of a small amount of Cr and V does not cause the native oxide to change significantly.

The true film thicknesses extracted from the XRR fitting of the thicker films was used to calculate the conversion factor to transform nominal thicknesses to true thickness for the thinner films, for which XRR was not reliable. The true thickness obtained from XRR is used throughout the rest of this chapter. There is a typical roughness of approximately 1 nm for all the ferromagnetic layers. This indicates that the addition of impurities of V or Cr in concentrations up to 5 at.% does not greatly influence the structure of the Ni.

The specular XRR gives depth sensitive structural information. In the next section, TEM and EDX were used to gain further insight into the contribution of the native oxide.

4.2.3 Contribution of the native oxide to the film as measured through energy dispersive x-ray spectroscopy

In an electron microscope, for EDX measurements, the primary electron beam is used to eject electrons from the core shells of atoms within the sample. Outer shell electrons transition to fill the newly created holes and emit x-rays of frequency characteristic of the energy associated with the transitions of that element. Here, it was used to gain insight into the contribution of the surface oxide to the Ni films by measuring the relative proportions of oxygen and nickel atoms in the sample.

The EDX measurements were made in association with Dr B. G. Mendis on the three samples of Ni (15 nm), Ni (6nm) and Ni (4 nm) deposited onto silicon nitride windows, using a beam operation voltage of 200 kV. The EDX spectra are shown in Fig. 4.2, and the Ni-L_α, Ni-L_γ and O-K_α absorption peaks have been labelled. Each spectrum was measured for the same duration for the three different Ni films. The intensity of both Ni peaks diminish as film thickness is reduced. This is to be expected since the absolute intensity of the peaks is proportional to the number Ni atoms. The O-K_α peak remains consistent in magnitude between the samples, suggesting that the native oxide formed is of approximately the same thickness regardless of Ni thickness. This is consistent with the atmospheric oxidation being a self limiting reaction, forming a passivating layer [139].

The peaks in the EDX spectrum were fitted with Gaussian distributions in order to extract the peak heights and to separate the Ni-L_γ and Ni-L_α nested peaks. The total fitted distributions are shown as the solid lines in Fig. 4.2 a).

In Fig. 4.2 b)-d) the fitted double Gaussian distributions for the Ni-L_α and Ni-L_γ absorption peaks are shown separately for each Ni film. This has been used to determine the heights of the two absorption peaks. It can be seen that the intensity of the Ni-L_γ absorption peak reduces alongside the Ni-L_α absorption peak with reducing thickness. Since the peaks originate from atomic emission, and are therefore independent of crystal morphology and texture, within experimental error, the peak positions are the same between samples.

The peak heights extracted from the Gaussian fits to the EDX spectra are shown in Fig. 4.3. With reducing Ni thickness, the reduction in intensity of Ni-L_α absorption peak intensity is faster than the linear dependence that would be expected, since the number of

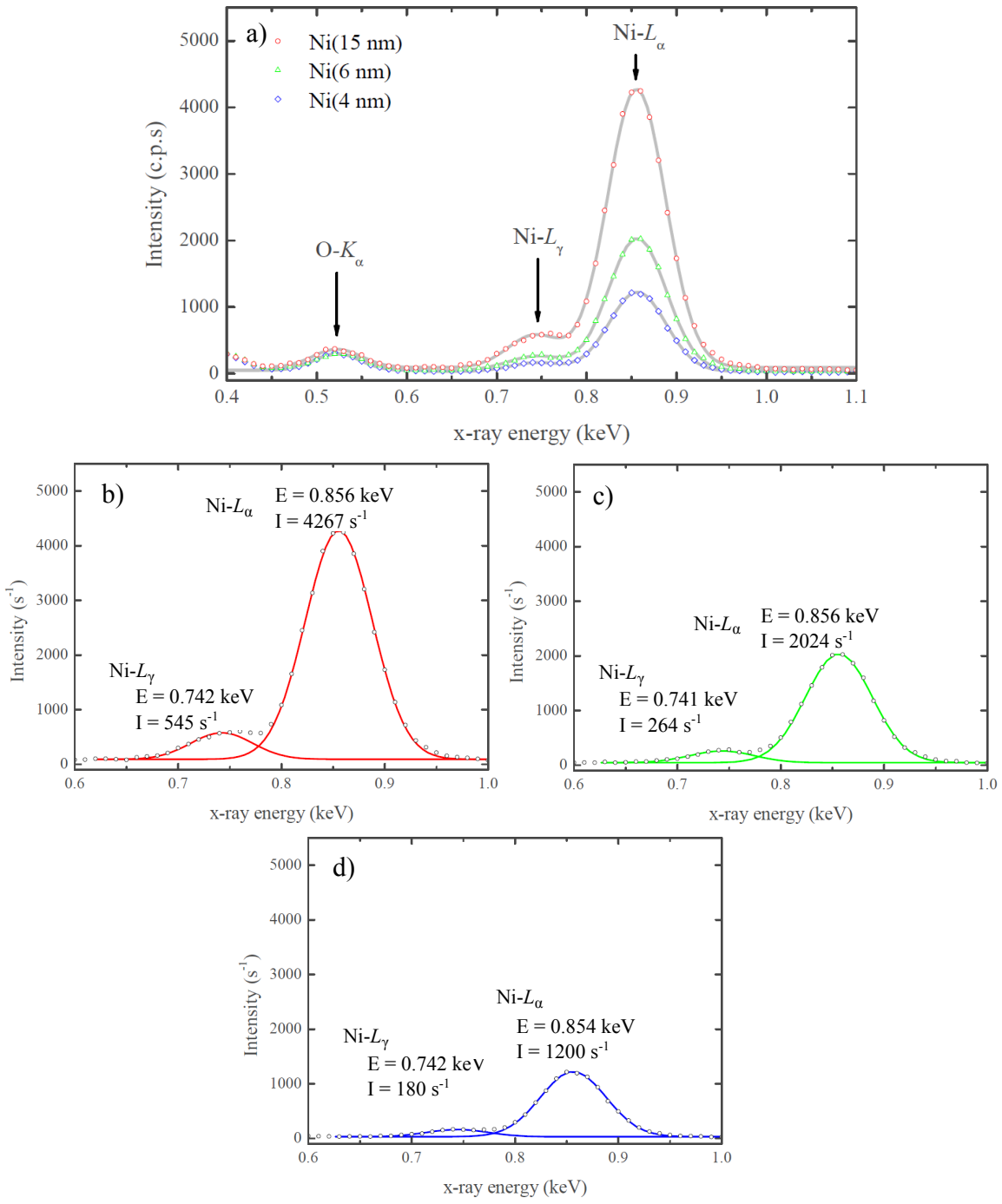

.

Figure 4.2: a) EDX spectra for the three Ni films of different thickness showing the Ni-L_α, Ni-L_γ and O-K_α absorption peaks. The O-K_α peak is approximately the same height for all three thicknesses of Ni. The solid line shows the total distribution fitted using three Gaussian functions. b)-d) Magnified view of the EDX spectra in the energy range of the Ni absorption peaks, showing the Ni-L_α and Ni-L_γ peaks for Ni films of thickness b) 15 nm, c) 6 nm and d) 4 nm. The solid lines show the two fitted Gaussians used to determine the individual peak heights of the Ni-L_α and Ni-L_γ peaks.

Ni atoms is proportional to the film thickness.

The O-K_α peak height is approximately the same when compared between samples, though there is a weak linear dependence on Ni film thickness, which is observable in the magnified scale in the inset. This reinforces the statement from the XRR analysis that thicker Ni films form higher quality oxides, since stoichiometric oxides would have the maximum oxygen content and therefore a stronger O-K_α intensity.

The XRR indicated that the native oxide was approximately 1 nm in thickness for all films. As a crude estimate, this would give ratios of 1/4 = 0.25, 1/6 = 0.16 and 1/15 = 0.07 for the ratio of O-K_α to Ni-L_α peak heights for the Ni (4 nm), Ni (6 nm) and Ni (15 nm) films respectively. It can be seen in Fig 4.4 that there is excellent agreement between these predicted ratios and those observed from the EDX spectra, providing further evidence that the oxide thickness is constant between the Ni films of different thickness and approximately 1 nm in thickness.

The ratio of peak height intensities for Ni-L_α to Ni-L_γ were also compared. The value of 7.0 $\pm$ 0.5 is constant with thickness, as would be expected, since both peaks arise from Ni absorption and is also within the expected range of 4.5-18 [140].

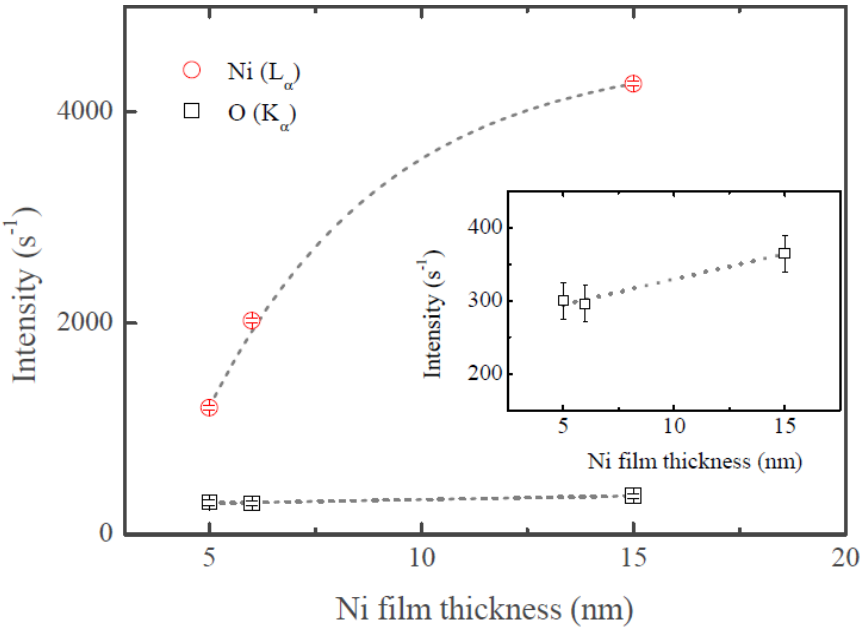

Figure 4.3: EDX peak height intensities for Ni-L_α and O-K_α lines as a function of Ni film thickness. The dashed lines are linear and exponential fits included as a guide to the eye for the O-K_α and Ni-L_α intensities respectively. The inset shows a magnified view of the O-K_α absorption peak height intensity and linear fit.

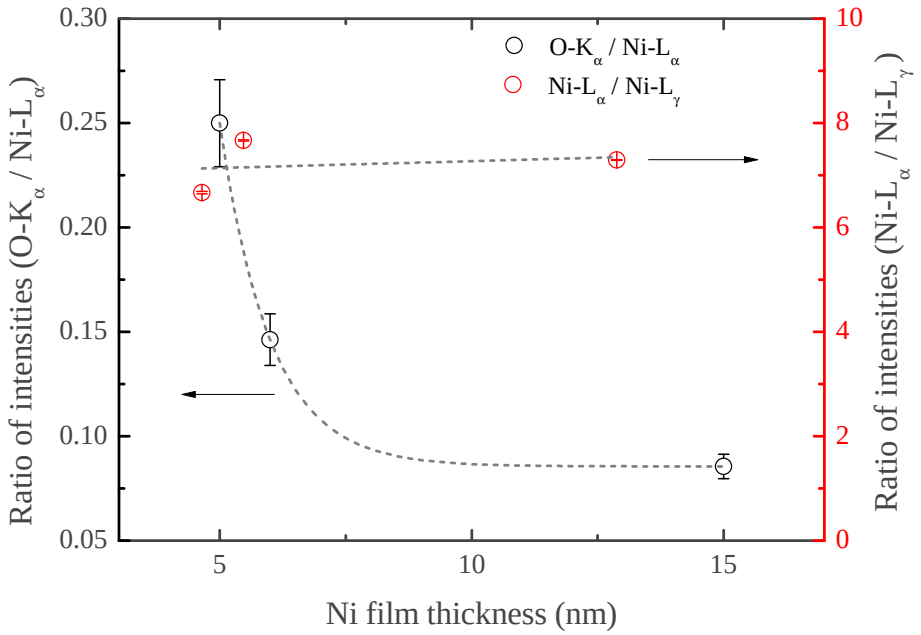

Figure 4.4: Ratios of the peak height intensities for the O-K_α to Ni-L_α lines and the Ni-L_γ to Ni-L_α lines. The dashed lines are linear and exponential fits included as a guide to the eye for the O-K_α/Ni-L_α and Ni-L_γ/Ni-L_α ratios respectively.

Following the compositional analysis of the films using EDX and the depth dependent analysis using XRR, the discussion now moves to the in-plane morphological structure characterised using transmission electron microscopy (TEM) techniques in order to complete the structural analysis of the films.

4.2.4 Morphological structure of the films using transmission electron microscopy

TEM uses electron diffraction to obtain interference patterns with atomic resolution that are representative of the crystal structure. The electron beam is passed through the sample, hence the sample substrate and film needs to be thin enough to allow complete transmittance. This was why three samples were deposited onto 10 nm thick silicon nitride windows and all TEM analysis was completed on these samples only. The samples should be nominally identical to those deposited onto SiO_2 substrates, as both substrates are amorphous and Si based. However, the use of different substrates may modify the sample growth. TEM imaging in this section was completed with the assistance of Dr B. G Mendis.

Grain structure of the Ni films

Bright-field and dark-field imaging can be used to investigate the grain structure of the films. When using bright-field imaging, the sample surface is orthogonal to the beam and an aperture is used so that only the direct beam can pass. The electron beam is then attenuated by the film. Diffraction contrast arises between grains with crystal planes that are orientated such that the transmitted beam is diffracted away from the detector. Discontinuities and pinholes tend to appear bright since they direct transmission through the aperture.

When using dark-field imaging the sample is tilted such that the diffracted beams reach the detector. For these images, the condition was such that the angle of tilt corresponded to that which would allow diffracted beams from (111) and (200) textures to reach the detector and appear bright. These atomic planes are associated with the face-centred cubic structure as expected for Ni.

Fig. 4.5 shows a comparison of bright-field and-dark field images for the same region of the 15 nm film. Diffraction contrast can be seen between the images, in which grains which were dark in the bright-field image are bright in the dark-field image. Some example crystallites in the image have been circled.

A high resolution bright-field TEM image of the 15 nm film is shown in Fig. 4.6. The lattice planes can be seen clearly and the orientation of the planes changes between grains, which is indicative of the polycrystalline nature of the film. It can be seen that the grains are all between 5-10 nm in the plane, which is consistent with that found for Ni films of similar thickness in the literature [141].

The diffraction patterns for the Ni (15 nm), Ni (6 nm) and Ni (4 nm) films are shown in Fig. 4.7. For all films the patterns form rings rather than spots. This again confirms the polycrystalline nature of the films. The expression;

$$R = \frac{\lambda L}{d_{hkl}} \tag{4.2.1}$$

can be used to identify the rings, where R is the ring radius, λ is the electron wavelength, L is the camera length of the electron microscope and d_{hkl} is the spacing of the lattice planes allowing for the texture to be identified. The values of d_{hkl} can be found from the

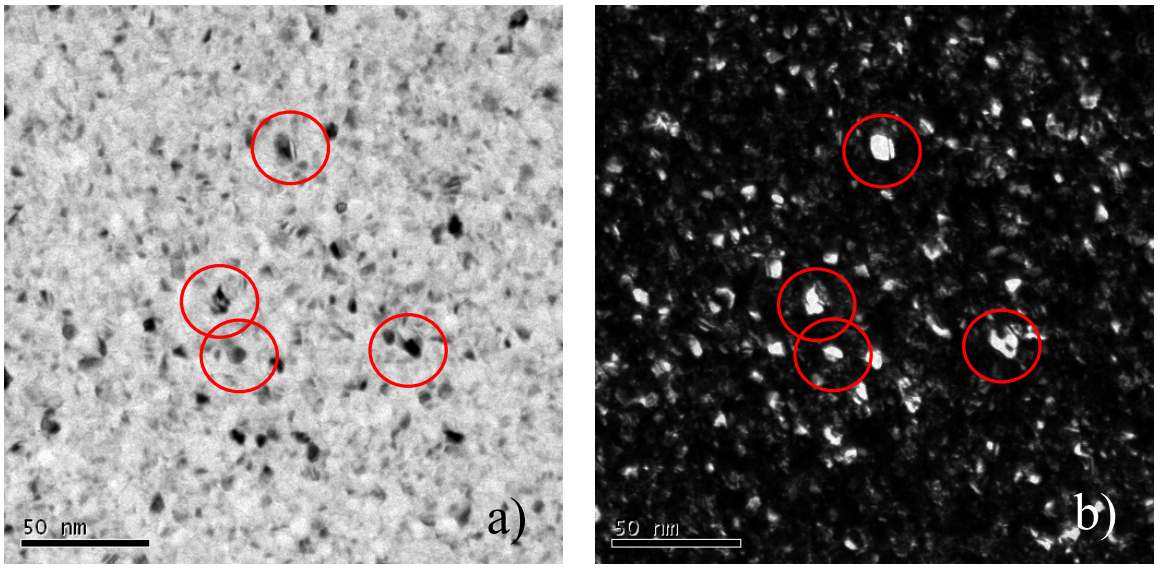

Figure 4.5: a) Bright-field TEM image of the 15 nm Ni film. b) Dark-field image taken in the same location. The circled areas show good examples of diffraction contrast between the two images.

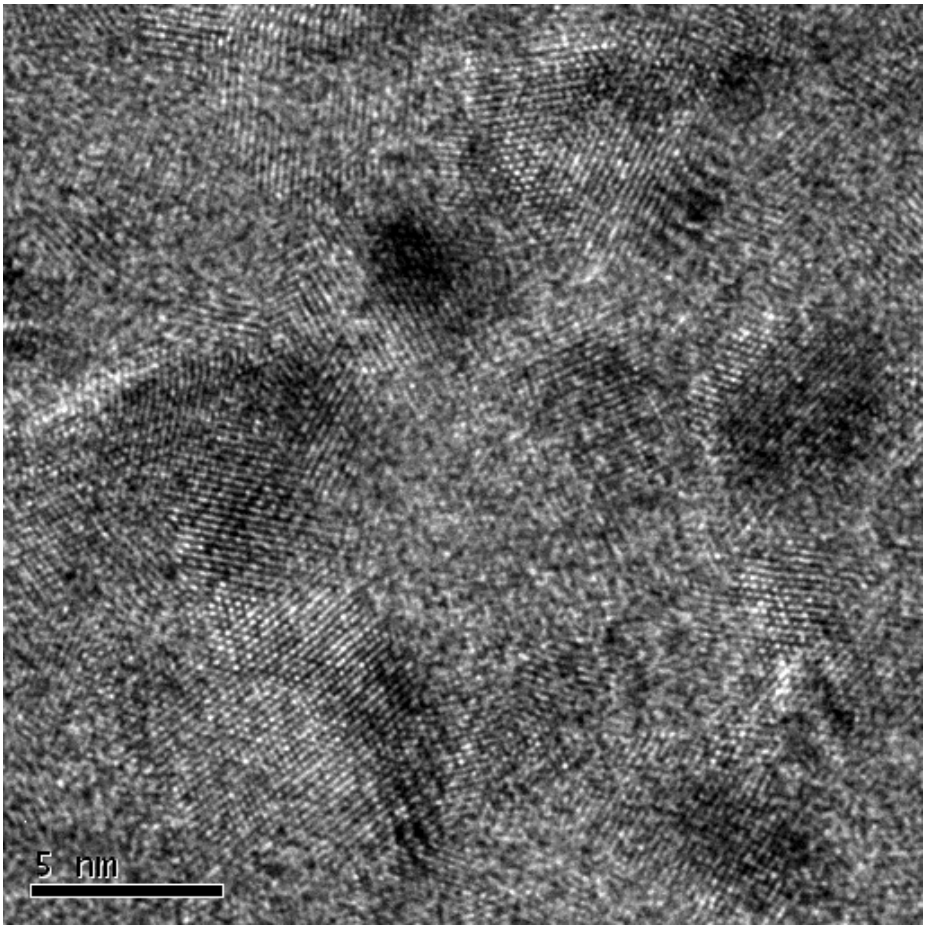

Figure 4.6: High resolution TEM image of the 15 nm Ni film. The atom columns are visible and individual crystallites can be identified as the regions where the atom columns are orientated along uniform planes in the same direction.

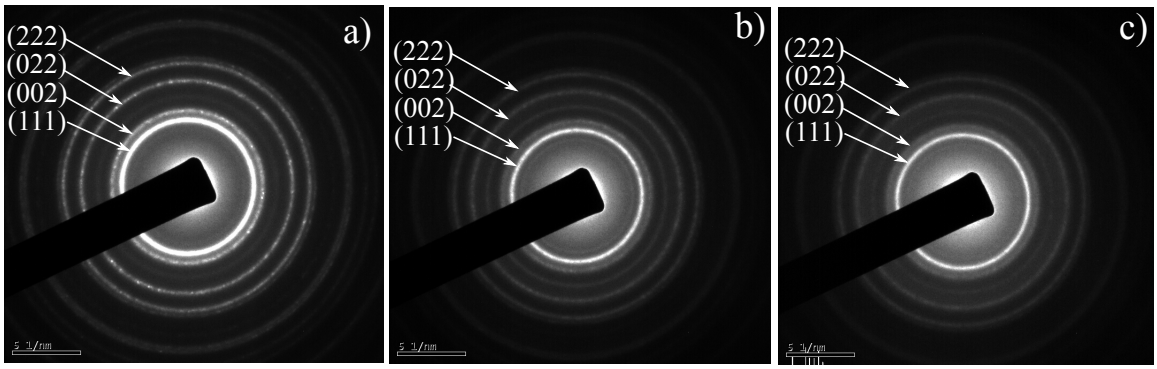

Figure 4.7: Electron diffraction patterns for a) Ni (15 nm), b) Ni (6 nm) and c) Ni (4 nm) films. Each diffraction ring has been labelled with the corresponding Miller indices.

corresponding Miller indices using

$$d_{hkl} = \left[\frac{a^2}{h^2 + k^2 + l^2} \right]^{\frac{1}{2}} \tag{4.2.2}$$

where a is the lattice parameter of Ni and h, k and l are the Miller indices for lattice plane. The (111), (002), (022) and (222) rings have been identified on the diffraction patterns. The intensity of the (111) ring is brightest for all three films, indicating that the grains are primarily orientated with (111) texture out of the film plane.

There is no change in the radius of the rings over the three Ni film thicknesses. However, all rings have a radius that is 9.5% smaller than the value expected from the calculation using the bulk lattice parameter of Ni of 3.52 Å. This indicates a constant strain that is independent of thickness, in the thickness range of 4-15 nm, and results in an expansion of the lattice parameter to (3.85 ± 0.02) Å.

With reduced film thickness, in particular below 5 nm, the structural integrity of the film can become compromised. This is important with regard to the electrical properties of the films where the onset of discontinuities will be accompanied by a dramatic rise in resistivity. This structural change was investigated using Fresnel contrast.

Identifying the onset of film discontinuities with reducing film thickness

The images in Fig. 4.8 were made using bright-field imaging with Fresnel contrast. For Fresnel contrast, the beam is slightly defocused to enhance the contrast from grain boundaries. In Fig. 4.8 a) for the 15 nm film, contrast between grains with different crystalline

orientation can be seen. The onset of discontinuities between these grains can be seen in Fig. 4.8 b) for the 6 nm film, where bright contrast appears between the crystallites. On further reducing the film thickness, it can be seen in Fig. 4.8 c) that these bright segments become more pronounced indicating further discontinuities in the film.

To summarise, XRR revealed that there was a native oxide of approximately 1 nm thickness for all films and that the introduction of small amounts of V and Cr impurities does little to modify the interfacial roughness of the Ni. EDX confirmed that the oxide was self passivating and that there was little variation in oxygen content between the films.

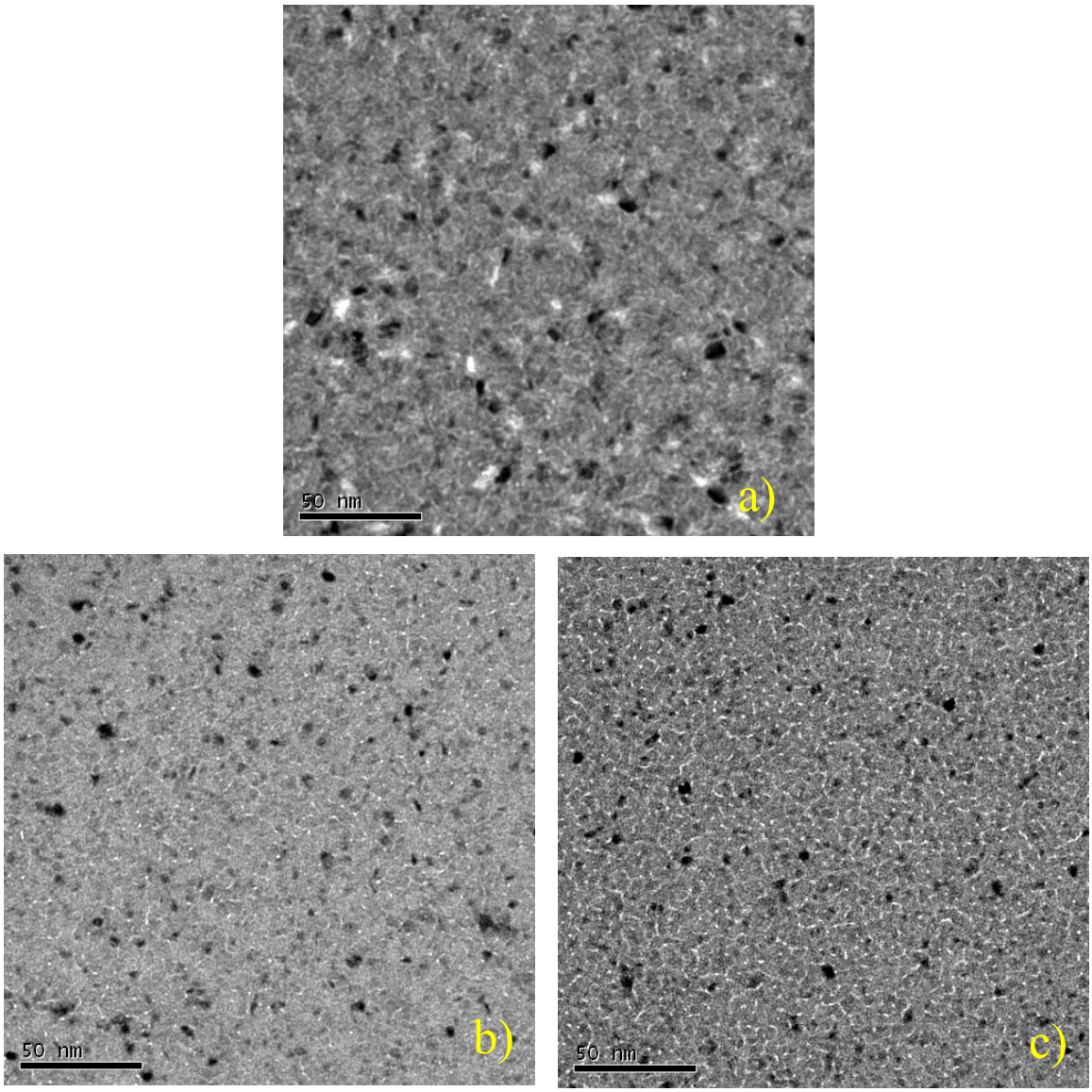

Figure 4.8: Bright-field TEM images with Fresnel contrast of a) 15 nm, b) 6 nm and c) 4 nm Ni films. The bright regions between the grains indicate the formation of discontinuities, which first appear in the 6 nm film and become more prevalent in the 4 nm film.

From the TEM analysis it was identified that the films were predominantly (111) textured and had undergone an average lattice expansion of 9.5%. Importantly, from the Fresnel contrast, the onset of discontinuities was established to be at 6 nm for the Ni films. The chapter now proceeds to present and explain the measured thickness dependence of AMR in the Ni, $Ni_{95}V_5$ and $Ni_{95}Cr_5$ thin films.

4.3 Thickness dependence of AMR in doped Ni thin films

The thickness dependence of $\Delta\rho$ was measured in the Ni, $Ni_{95}V_5$ and $Ni_{95}Cr_5$ thin films. By including the dopants, the electronic structure of the Ni was modified and the thickness dependence of the AMR could be investigated with reference to the CFJ model.

The CFJ model was described in chapter 2 and can be used to make quantitative predictions of $\Delta\rho$ in Ni films doped with small concentrations of transition metals [58]. In this chapter the CFJ model was modified with a new thickness dependence to gain theoretical insight into the unexplained thickness dependence of $\Delta\rho$.

Doping the Ni with Cr or V reduced the value of α. Referring to chapter 2, α parametrises the spin-dependent resistivity channels from the Mott-two-current model [59]. A larger value of α means a greater difference between spin $\uparrow$ channel resistivity $\rho^0_\uparrow$ and spin $\downarrow$ channel resistivity $\rho^0_\downarrow$, and therefore a greater $\Delta\rho$. Some values for α for transition metal impurities in Ni are quoted in Table 4.2.

4.3.1 AMR measured through the angular resistivity dependence

AMR was measured using a standard four-probe technique in the longitudinal geometry, as outlined in chapter 3. The sample was rotated through 180° in a saturating in-plane magnetic field and the resulting distribution of resistivities was fitted with

$$\rho = \rho_\perp + \Delta\rho \cos^2(\theta + \theta_c), \tag{4.3.3}$$

Dopant	Ti	V	Cr	Mn	Fe	Co
$\alpha = \rho^0_\downarrow/\rho^0_\uparrow$	2.4	0.65	0.45	15	20	30

Table 4.2: Measured values of α for different transition metal dopants in Ni. Reproduced from Ref. [60]

to extract the AMR. Here, θ is the angle between the magnetic field and the current and θ_c is a small constant correction angle (typically $\sim 2°$) required due to offsets in the sample alignment with respect to the magnetic field. Measurements of the angular dependence of the resistivity and best fits with equation (4.3.3) for different thicknesses of Ni, $Ni_{95}V_5$ and $Ni_{95}Cr_5$ thin films are shown in Fig. 4.9 a)-c).

It can be seen that the magnitude of $\Delta\rho$ is much smaller for the V doped and smaller still for the Cr doped films in comparison to the pure Ni films. This is consistent with the expectations of the CFJ model based on the quoted values of α in Table 4.2, where α is smallest for Ni films doped with Cr.

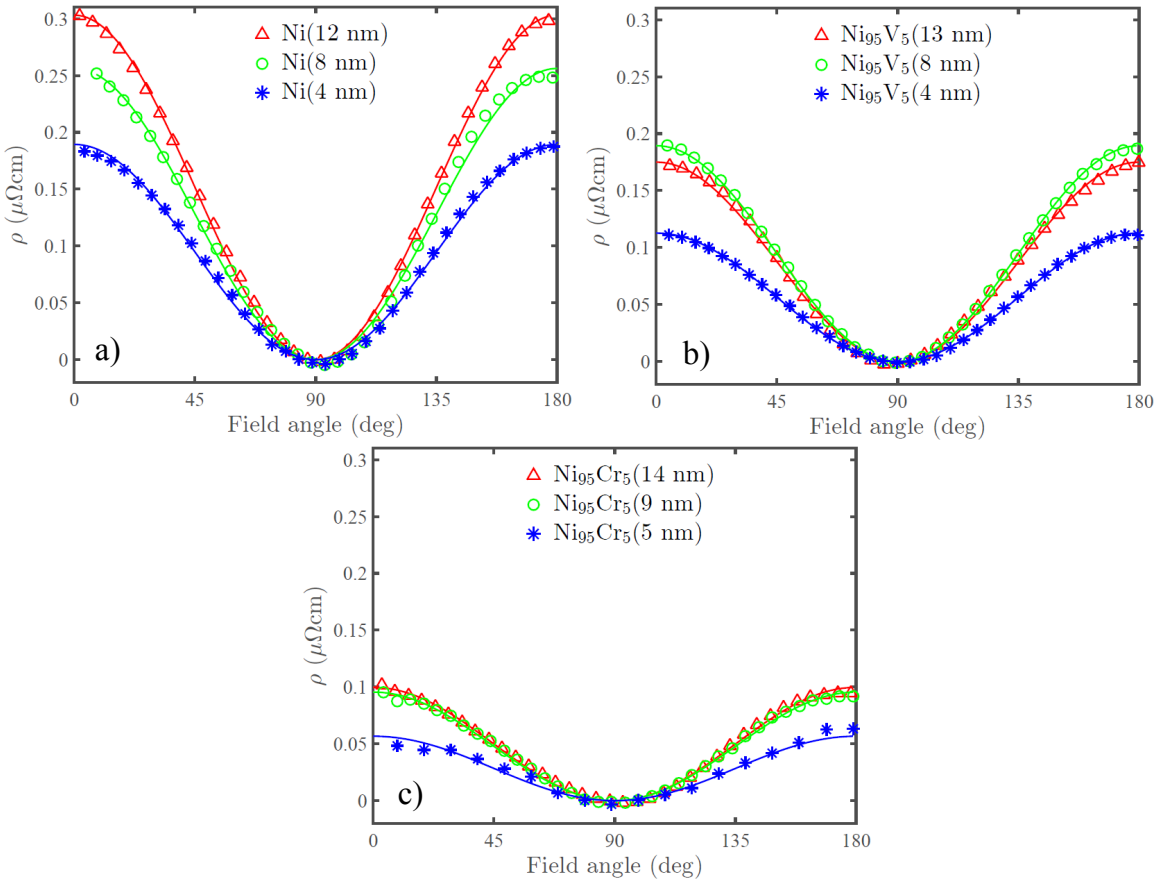

Figure 4.9: Variation of ρ as a function of the in-plane angle between the applied magnetic field and the current flow for a) Ni films, b) $Ni_{95}V_5$ film, and c) $Ni_{95}Cr_5$ films of different thickness. The solid lines show the best fit with equation (4.3.3). The transverse resistivity $\rho_\perp$ has been subtracted from the data and the fits so that $\Delta\rho$ can be compared more easily between samples with different electrical resistivities. The θ_c offset has also been applied to centre the data about 90°.

4.3.2 Thickness dependence of $\Delta\rho$ in doped Ni thin films

The variation of $\Delta\rho$ and $\Delta\rho/\rho$ with film thickness is shown for the Ni, $Ni_{95}V_5$ and $Ni_{95}Cr_5$ films in Fig. 4.10 a) and b) respectively. $\Delta\rho$ begins to fall quite dramatically when the film thickness is below 6 nm. Above this, it is roughly constant, saturating at $\Delta\rho$ = (0.30 ± 0.02) $\mu\Omega$cm for the Ni films, $\Delta\rho$ = (0.18 ± 0.01) $\mu\Omega$cm for the $Ni_{95}V_5$ films and $\Delta\rho$ = (0.10 ± 0.01) $\mu\Omega$cm for the $Ni_{95}Cr_5$ films. This is termed the saturation $\Delta\rho$. For thicknesses below 6 nm, the reduction in $\Delta\rho$ is very rapid.

The drop of $\Delta\rho$ for film thicknesses below 6 nm coincides with the onset of discontinuities in the films as found from the TEM analysis. This suggests that sample morphology is likely to be very important in determining the magnitude of $\Delta\rho$ within this thickness range.

The work of L. Bogart found the saturation of $\Delta\rho$ for evaporated $Ni_{81}Fe_{19}$ films occurred for films above 18 nm in thickness [115] and Thanh *et al.* found the saturation of $\Delta\rho$ occurred above 10 nm $Ni_{81}Fe_{19}$ thickness in sputtered Ta/$Ni_{81}Fe_{19}$/IrMn/Ta multilayers [136]. In this study it is considered that this variation occurs due to the difference in sample deposition environment and the resulting transformations in film structure. However, the structural analysis of the $Ni_{81}Fe_{19}$ films used by L. Bogart found comparable roughness, grain size and native oxide thicknesses with the films used in this study. There is no data in either study regarding the onset of film discontinuities though, which may play an important role. The work of Thanh *et al.* is further complicated by the need for current shunting corrections due to the Ta layers, making the true saturation of $\Delta\rho$ due to

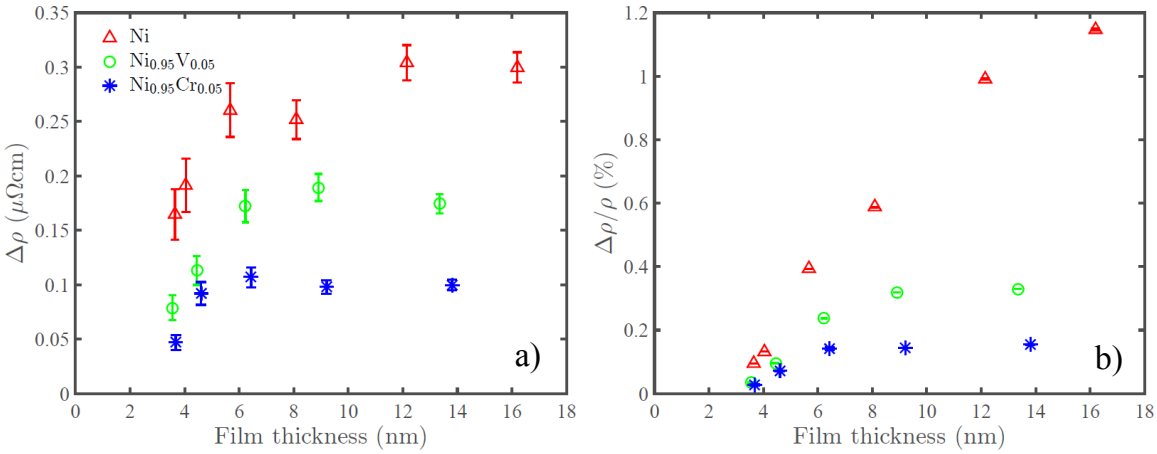

Figure 4.10: a) The dependence of $\Delta\rho$ on film thickness for sputtered Ni, $Ni_{95}V_5$ and $Ni_{95}Cr_5$ films. b) Likewise, $\Delta\rho/\rho$ as a function of film thickness for Ni, $Ni_{95}V_5$ and $Ni_{95}Cr_5$ films.

the $Ni_{81}Fe_{19}$ thickness dependence more challenging to identify.

The drop in $\Delta\rho/\rho$ with reducing thickness onsets earlier and is less dramatic. This is because the effects of the rising resistivity due to the size effect are apparent at greater thickness. This thickness is related to the mean free path in the material, which for Ni is approximately 2-4 nm at room temperature [142].

The thickness at which $\Delta\rho$ begins to fall is independent of the dopant used. This can be seen clearly in Fig. 4.11 where $\Delta\rho$ has been normalised to the saturation values of $\Delta\rho$ in Fig. 4.10 for each sample series, and referred to as $\Delta\rho_{norm}$. The universal scaling is quite clear and demonstrates that the thickness dependence is not arising due to the dopant but is inherent to the reduced dimensionality of the films, whether that be due to the encroaching interfaces or the consequence of the poorer film quality at low thickness.

4.4 Correlations between electrical resistivity and $\Delta\rho$

In thin films, where the thickness is comparable to the mean free path of the electron in that material, the resistivity, ρ, is not a constant and instead rises dramatically due to diffuse scattering at the interfaces as the thickness is reduced. This contribution was derived by Fuchs and Sondheimer [33] using a Boltzmann equation approach where the interfaces are

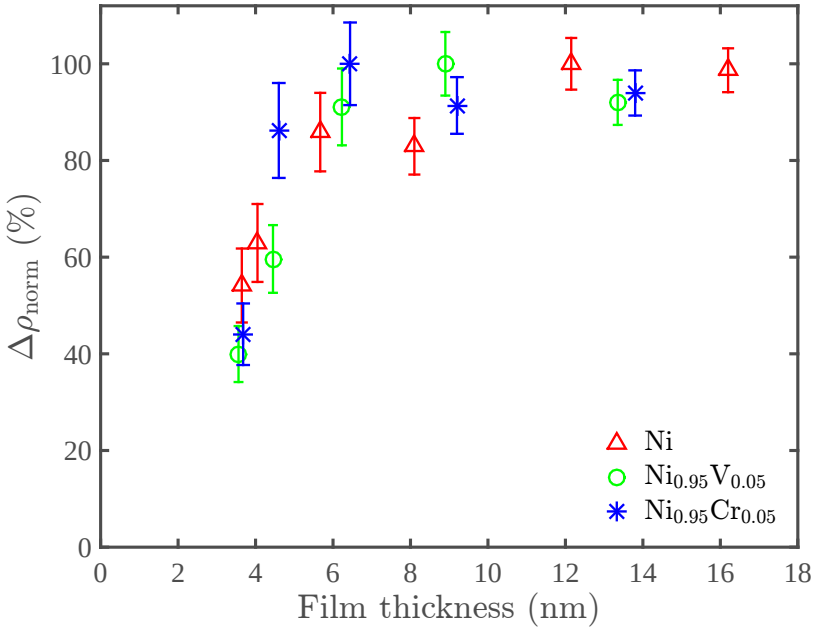

Figure 4.11: The dependence of $\Delta\rho_{norm}$ on film thickness for sputtered Ni, $Ni_{95}V_5$ and $Ni_{95}Cr_5$ film.

incorporated into the boundary conditions of the problem. In the limiting case that $t < l_0$, the resistivity in the presence of interface scattering is given by

$$\rho = \frac{4l_0\rho_0}{3}\frac{1}{[\ln(l_0/t) + 0.423]}, \tag{4.4.4}$$

where l_0 is the electron mean free path. For films where $t > l_0$ this simplifies to

$$\rho = \rho_0\left[1 + \frac{3}{8}(l_0/t)\right]. \tag{4.4.5}$$

The transverse resistivity, $\rho_\perp$, is plotted as a function of film thickness in Fig. 4.12 with fits obtained using equation (4.4.5) for the limiting case where $t > l_0$. The fits have been made to the data above 5 nm, since equation (4.4.5) applies to the films thicker than the l_0, which for Ni should be approximately 2-4 nm at room temperature [142]. The derived values for l_0 and ρ_0 are shown in Table 4.3. The values for l_0 are consistently large for all three data series, in particular for the Ni films, which brings into question the validity of the application of the Fuchs-Sondheimer theory to this data. Furthermore, no fit could be obtained using equation (4.4.4) for the low thickness region where $t < l_0$. It is likely that this is because of the onset of discontinuities in the film results in a resistivity that rises faster than can be accounted for from interfacial scattering alone.

Below 6 nm there is a distinct change in slope of the data, which is due to the onset of film discontinuities. A plot of $\Delta\rho_{\text{norm}}$ against $\rho_\perp$ is shown in Fig. 4.13 and importantly there is a correlation which suggests that the origin of the rapid rise in resistivity is the same as that which causes the fall in $\Delta\rho$. A linear fit has been made to the data which from the slope of (-0.24 ± 0.09) $\mu\Omega^{-1}\text{cm}^{-1}$ gives an empirical relationship between the loss of $\Delta\rho$ and the rise in resistance.

	l_0 (nm)	ρ_0 $(\mu\Omega cm)$
Ni	120 ± 5	7 ± 5
$Ni_{95}V_5$	18 ± 4	45 ± 5
$Ni_{95}Cr_5$	17 ± 2	50 ± 5

Table 4.3: Extracted values of l_0 and ρ_0 from best fits using equation (4.4.5).

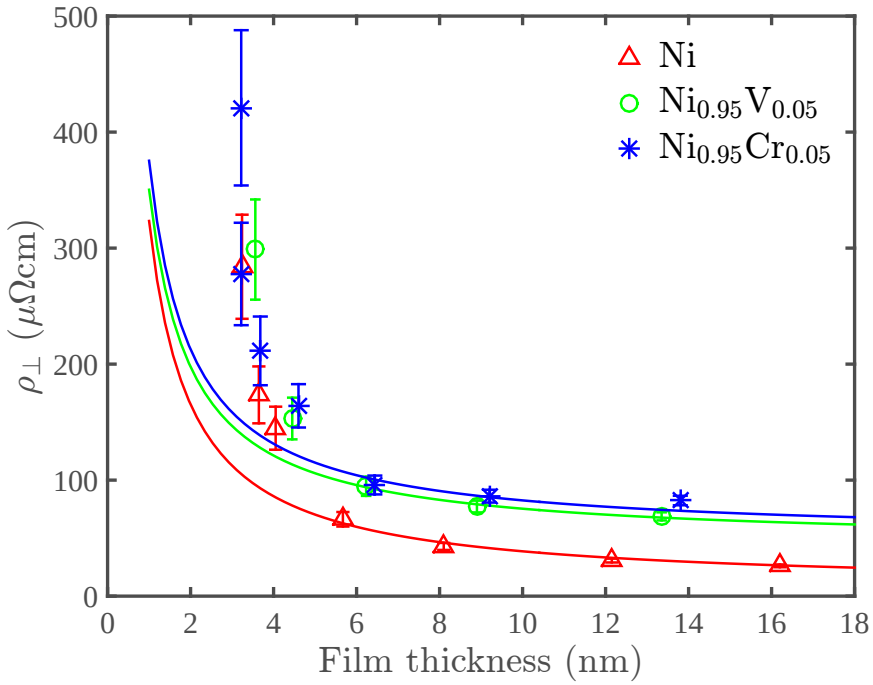

Figure 4.12: The film resistivity when magnetised transverse to the current flow ($\rho_\perp$) as a function of film thickness for sputtered Ni, $Ni_{95}V_5$ and $Ni_{95}Cr_5$ films. Solid lines show the best fits using equation (4.4.5).

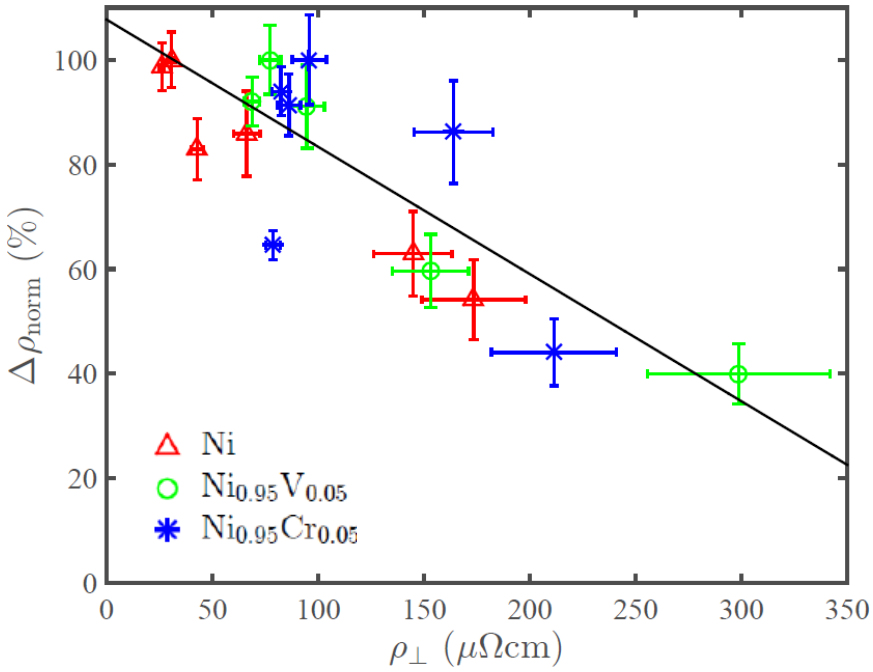

Figure 4.13: $\Delta\rho_{norm}$ plotted as a function of the resistivity, $\rho_\perp$, for Ni, $Ni_{95}V_5$ and $Ni_{95}Cr_5$ films. The solid line shows a linear fit made to the data.

4.4.1 Interfaces and the CFJ model

In this section the CFJ model, which was discussed in detail in chapter 2, is applied to explain the difference in saturation $\Delta\rho$ between the Ni, $Ni_{95}V_5$ and $Ni_{95}Cr_5$ films. The CFJ model is then discussed in the context of the loss of $\Delta\rho$ and the effect of the increased contribution from the interfaces and sample morphology.

4.4.2 Principle expressions from the CFJ model

The CFJ model [58] can be used to make quantitative predictions of the AMR ratio in Ni-based alloys. Crucially the following expressions were obtained:

$$\Delta\rho = \frac{\gamma(\rho_\downarrow - \rho_\uparrow)\rho_\downarrow}{\rho_\uparrow + \rho_\downarrow + 4\rho_{\downarrow\uparrow}} \tag{4.4.6}$$

$$\frac{\Delta\rho}{\rho} = \frac{\gamma(\rho_\downarrow - \rho_\uparrow)\rho_\downarrow}{\rho_\uparrow\rho_\downarrow + \rho_{\downarrow\uparrow}(\rho_\uparrow + \rho_\downarrow)} \tag{4.4.7}$$

where γ is a constant that is related to the strength of the spin-orbit interaction in the material, $\rho_\uparrow$ and $\rho_\downarrow$ are the spin channel resistivities from the Mott two-current model and $\rho_{\downarrow\uparrow}$ is the spin-mixing resistivity that allows for some spin-flip scattering of electrons. The terms ρ_σ where $\sigma =\uparrow$ or $\downarrow$, can be separated into $\rho_\sigma = \rho^i_\sigma(T) + \rho^0_\sigma$, where $\rho^i_\sigma(T)$ is an intrinsic temperature dependent resistivity characteristic of the host ferromagnetic and ρ^0_σ is a resistivity that depends on how the dopant modifies the ferromagnet density of states. At low temperature, assuming $\rho_{\downarrow\uparrow} << \rho_\sigma$ this simplifies to,

$$\frac{\Delta\rho}{\rho} = (\alpha - 1)\gamma \tag{4.4.8}$$

demonstrating the linear dependence of $\Delta\rho/\rho$ with $\alpha = \rho^0_\downarrow/\rho^0_\uparrow$, i.e the ratio of spin-channel resistivities.

Referring back to the difference in saturation values of $\Delta\rho$ for the Ni, $Ni_{95}V_5$ and $Ni_{95}Cr_5$ series shown in Fig 4.10 a), this can now be understood using the CFJ model with quantitative predictions.

4.4.3 Explanation of the difference in saturation $\Delta\rho$ with Cr and V dopants

The resistivity for each spin-channel is given by, $\rho_\sigma = \rho^i_\sigma(T) + \rho^0_\sigma$. However, for the pure Ni film, the ρ^0_σ terms are zero by definition since the purpose of this term is to characterise how the introduction of transition metal impurities modify the band structure. Note that this is separate to the zero temperature resistivity which would be present in all the films and is incorporated within the $\rho^i_\sigma(T)$ terms. For the Ni films, the resistivity of the spin-channels are therefore determined by the intrinsic resistivity, $\rho_\sigma = \rho^i_\sigma(T)$ only. All measurements in this chapter are at room temperature so for simplicity, from here on ρ^i_σ refers to the room temperature value.

For the Ni thickness dependence, $\Delta\rho$ saturated at $\Delta\rho = 0.3\ \mu\Omega$cm. From this, all pairs of values for $\rho^i_\uparrow$ and $\rho^i_\downarrow$ which yield a value of $\Delta\rho = 0.3\ \mu\Omega$cm when substituted into equation (4.4.6) can be found computationally. After this, each of these pairs of $\rho^i_\uparrow$ and $\rho^i_\downarrow$ can then be tested with the $Ni_{95}V_5$ saturation $\Delta\rho$ and $Ni_{95}Cr_5$ saturation $\Delta\rho$ data, this time with the complete terms $\rho_\sigma = \rho^0_\sigma + \rho^i_\sigma$, where ρ^0_σ are known values determined from the values of α in references [58, 60] and are shown in Table 4.4. The pair of ρ^i_σ values which were found to give the closest solution to the observed saturation values of $\Delta\rho$ for all three sample series were found to be $\rho^i_\uparrow = 9.8\ \mu\Omega$cm and $\rho^i_\downarrow = 57.4\ \mu\Omega$cm. The results are summarised in Table 4.4. Values of $\rho_{\downarrow\uparrow} = 1\ \mu\Omega$cm and $\gamma = 0.0075$ were used for all calculations which are similar to those originally used in the CFJ model [58] for Ni based alloys.

There is some disagreement between $\Delta\rho_{\text{pred}}$ and $\Delta\rho_{\text{meas}}$, but the model does reproduce the ordering of the data series. The disagreement between the absolute values may be due to the chosen values of ρ^0_σ, which have been assumed to be independent of concentration,

	$\rho^0_\uparrow$ ($\mu\Omega cm$)	$\rho^0_\downarrow$ ($\mu\Omega cm$)	$\Delta\rho_{\text{pred}}$ ($\mu\Omega cm$)	$\Delta\rho_{\text{meas}}$ ($\mu\Omega cm$)
Ni	0	0	0.30	0.30±0.02
$Ni_{95}V_5$	11.8	7.7	0.24	0.18±0.01
$Ni_{95}Cr_5$	17.0	7.7	0.20	0.10±0.01

Table 4.4: Saturation values of $\Delta\rho$ predicted ($\Delta\rho_{\text{pred}}$) using equation (4.4.6) for $Ni_{95}Cr_5$ and $Ni_{95}V_5$ films. Values of ρ^0_σ used are those from the original CFJ model publication [58]. The measured values of $\Delta\rho$ termed $\Delta\rho_{\text{meas}}$ is shown for comparison.

an assumption which strictly speaking is only valid at low temperature.

Following this, the investigation now moves to discuss the effects of reduced dimensionality in the context of the CFJ model regarding the universal thickness dependence of $\Delta\rho$ observed between the Ni, $Ni_{95}V_5$ and $Ni_{95}Cr_5$ films.

4.5 Discussion of the impact of encroaching interfaces on the CFJ model

By doping the films and observing the thickness dependence, the same universal scaling was observed. In the CFJ model, the dopant would modify the $\rho_\uparrow$ and $\rho_\downarrow$ terms. Since the thickness dependence of $\Delta\rho$ was independent of the dopant, this suggests that these terms do not contribute to the thickness dependence. Furthermore, $\rho_\uparrow$ and $\rho_\downarrow$ are determined from the spin-density of states at E_F, which is relatively unchanged over the thickness range investigated in this study [143]. Consequently the thickness dependence could be associated with either γ or $\rho_{\downarrow\uparrow}$.

For the length-scales at which the critical behaviour occurs, in these samples 6 nm, it can be expected that $\rho_{\downarrow\uparrow}$ would show the most significant thickness dependence. The argument for this is that the exchange length of Ni is ≈ 8.3 nm [144]. This is the length-scale over which the exchange interaction is the dominating energy contribution, hence it can be expected that there would be significant modifications to spin-spin interactions for thicknesses below this.

Since the main contribution to the term $\rho_{\downarrow\uparrow}$ is electron-magnon scattering [143], it was hypothesised that this term would change most significantly with reducing film thickness.

4.6 Contribution of electron-magnon scattering with reducing film thickness

In order to investigate the hypothesis that the origin for the loss of $\Delta\rho$ is due to an enhancement in $\rho_{\downarrow\uparrow}$, it is necessary to understand how the magnon population changes with film thickness.

To interpret this, measurements of the spin-wave stiffness were made. The spin-wave stiffness is associated with the energy cost to produce a low energy magnon excitation, hence it is representative of the number of magnons available at fixed temperature.

4.6.1 Spin-wave stiffness and enhanced electron-magnon scattering

The spin-wave stiffness can be extracted from temperature dependent magnetisation measurements. These measurements were made on the Ni films with the assistance of Dr O. Céspedes at the University of Leeds using a Quantum design SQUID-VSM.

The temperature dependent magnetisation can be fitted with the Bloch-$T^{3/2}$ law,

$$M(T) = M(0)\left(1 - \beta T^{3/2}\right) \tag{4.6.9}$$

where $M(T)$ is the temperature dependent magnetisation, β is a constant, with a dependence on the spin-wave stiffness, and T is the temperature. The data for all the Ni films is shown in Fig. 4.14 with fits made using equation (4.6.9). The temperature range of the fits was restricted, since the Bloch-$T^{3/2}$ law only applies in the low temperature spin-wave dominated region of the magnetisation temperature dependence.

The extrapolated magnetisation at 0 K as well as the extracted β parameter are plotted in Fig. 4.15 as a function of Ni film thickness. The drop in magnetisation with thickness is associated with the increased contribution from the Ni interfaces [145]. It can be shown that,

$$M(t_{\mathrm{Ni}}) = M_{\mathrm{Ni}}\left(1 - \frac{N_{\mathrm{int,Ni}}}{N_{\mathrm{Tot,Ni}}}\right) = M_{\mathrm{Ni}}\left(1 - \frac{2\Delta}{t_{\mathrm{Ni}}}\right) \tag{4.6.10}$$

where $M_{\mathrm{Ni}} = 487$ emu/cm^{-3} is the bulk magnetisation of Ni, $N_{\mathrm{int,Ni}}$ and $N_{\mathrm{Tot,Ni}}$ are the number of interfacial Ni atoms and total Ni atoms respectively, Δ are the widths of the top and bottom Ni interfaces and t_{Ni} is the Ni thickness. This has been fitted to the magnetisation data in Fig. 4.15, yielding $\Delta = 0.90 \pm 0.05$ nm which is consistent with the Ni and SiO_2 interface widths extracted from the XRR.

Using the values of $M(0)$ and β, the spin-wave stiffness, D, can then be extracted using

$$D = \frac{k_{\mathrm{B}}}{4\pi}\left(\frac{\zeta(3/2)g\mu_{\mathrm{B}}}{M(0)\beta}\right) \tag{4.6.11}$$

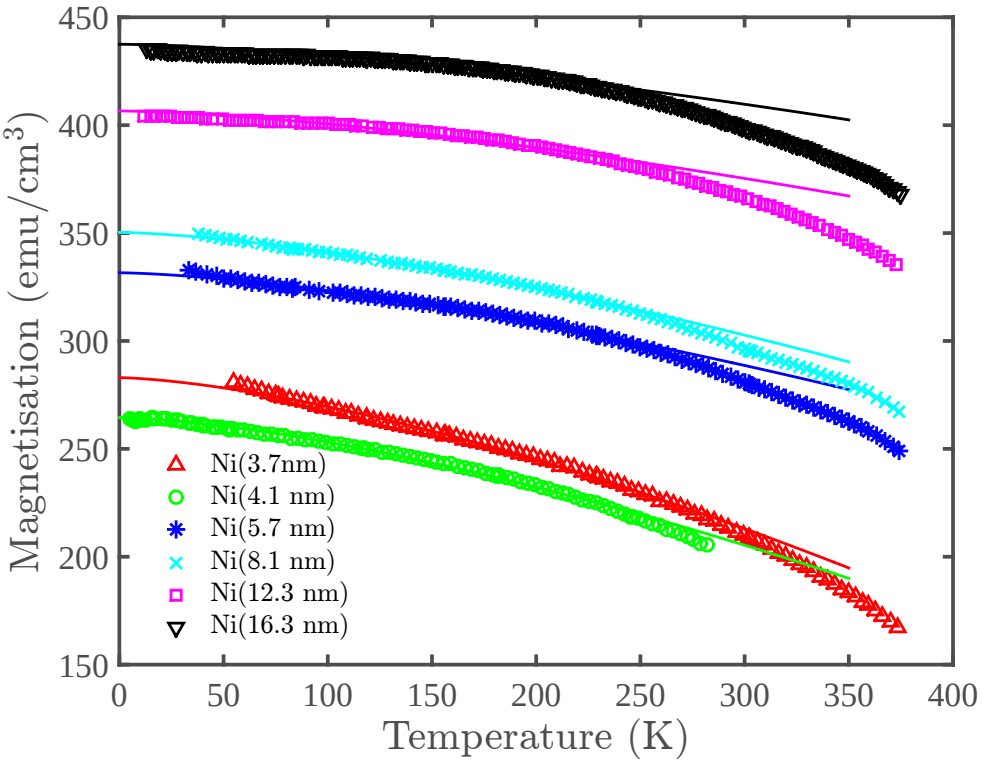

Figure 4.14: Magnetisation as a function of temperature for Ni films of different thickness. The solid lines denote best fits using equation (4.6.9) in the spin-wave region.

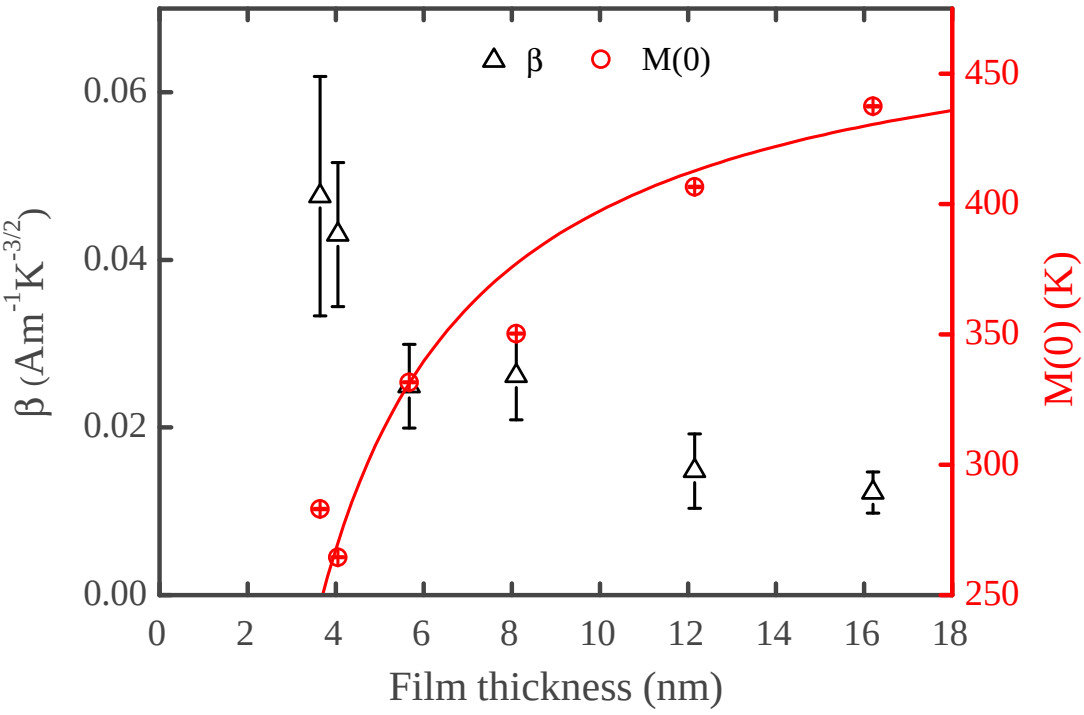

Figure 4.15: Values of $M(0)$ and β as extracted from the fits in Fig. 4.14 and plotted as a function of Ni film thickness. The solid line shows a fit to the $M(0)$ data using equation (4.6.10).

where k_B is the Boltzmann constant, $\zeta(3/2) = 2.612$ is the Riemann zeta function, $g = 2.20$ is the g factor [146], and μ_B is the Bohr magneton.

The spin-wave stiffness is plotted against the film thickness in Fig. 4.16 and reduces dramatically with film thickness on a similar lengthscale as $\Delta\rho$. The drop in spin-wave stiffness can be understood phenomenologically in terms of nearest neighbour interactions between the Ni atoms. Atoms at the interface have fewer nearest neighbours to enforce the exchange interaction, consequently the ferromagnetism is less stable at the interfaces. As the film thickness is reduced, the interface makes up a greater contribution of the film thickness. This surface contribution is particularly enhanced when the film becomes discontinuous, in fact it is known that Ni nanoparticles have a reduced spin-wave stiffness compared to thin films [147].

In Fig. 4.17, $\Delta\rho$ is plotted as a function of D and shows a linear dependence. The fit has been forced to pass through the origin, since a spin-wave stiffness of zero would imply no magnetisation and hence no AMR. This demonstrates that the rapid loss of $\Delta\rho$ with reducing thickness is in fact a result of the rapidly falling D due to the increased contribution from the interfaces.

This can be understood in terms of the CFJ model in that the reduced value of D and

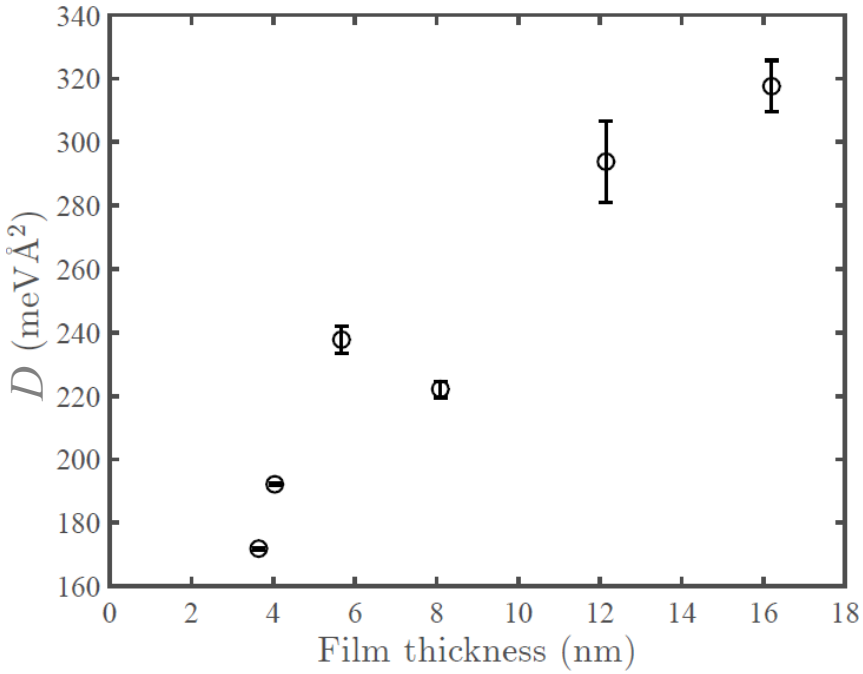

Figure 4.16: The spin wave stiffness, D, extracted from temperature dependent magnetisation measurements and plotted as a function of Ni film thickness.

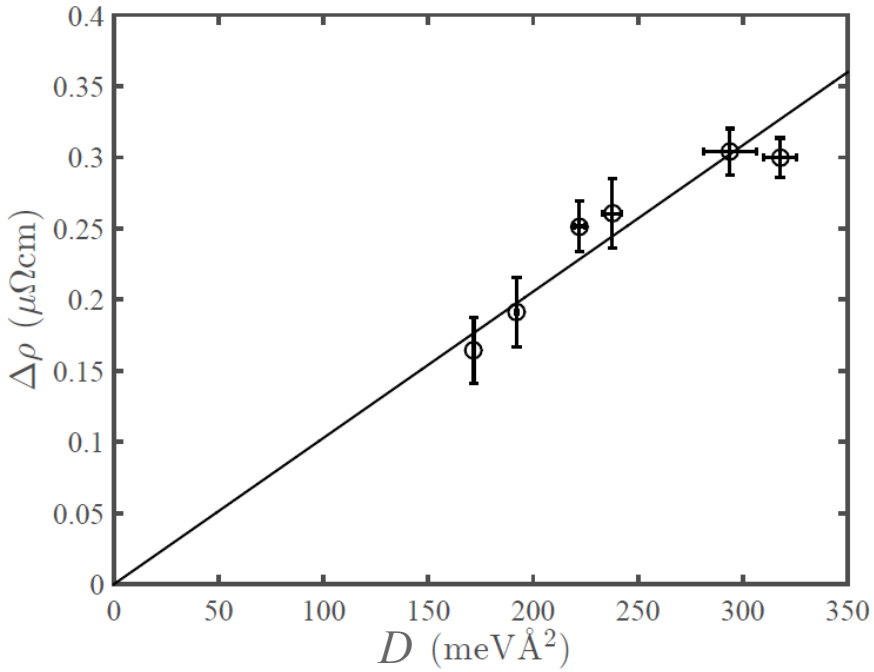

Figure 4.17: $\Delta\rho$ plotted as a function of D. A linear fit has been made to the data which passes through the origin.

the reduced magnetisation suggests a greater presence of magnons. This would result in enhanced electron-magnon scattering, which is a spin-flip scattering mechanism. This weakens the validity of the fundamental assumption of the Mott-two-current model, by which spin ↑ and spin ↓ electrons conduct independently and is crucial to AMR. Within the CFJ model, this manifests itself as an enhancement of the $\rho_{\downarrow\uparrow}$ term, which is isotropic with respect to the magnetisation direction. Hence an isotropic scattering mechanism is superimposed onto the anisotropic scattering responsible for AMR and as the film thickness is reduced the isotropic electron-magnon scattering begins to dominate and $\Delta\rho$ begins to vanish. With this knowledge, the next section discusses how a generalised thickness dependence can be incorporated into the CFJ model.

4.6.2 Inclusion of thickness dependence into the CFJ model

Fundamentally, $\Delta\rho$ falls with reducing thickness because of the increased contribution from the interfaces and sample morphology causes a reduction in D which causes an enhancement in electron-magnon scattering. Previously it was shown that the film resistivity scales with $\Delta\rho$, which can now be understood in terms of the onset of these discontinuities which are responsible for the rapid rise in resistivity as well as the rapid drop in D. The film re-

sistivity can therefore be used as a measure of the presence of electron-magnon scattering and can be used to apply thickness dependence to the CFJ model.

Although the Fuchs-Sondheimer model could not reproduce the film resistivity, an exponential captures the form of the data well and is demonstrated in the inset of Fig. 4.18. This exponential was therefore applied to $\rho_{\downarrow\uparrow}$ with the functional form,

$$\rho_{\downarrow\uparrow}(t) = \rho_{\downarrow\uparrow,\text{bulk}} + \rho_{\downarrow\uparrow}(0)\exp(-t/t_0) \tag{4.6.12}$$

where $\rho_{\downarrow\uparrow,\text{bulk}}$ is the spin-mixing resistivity for bulk Ni, $\rho_{\downarrow\uparrow}(0)$ is a hypothetical value for the spin-mixing resistivity at zero thickness and t_0 is the characteristic lengthscale of the process. The value for t_0 was obtained from the exponential fit to the $\rho_\perp$ data, shown in the inset of Fig. 4.18 and was found to be 1.36 nm.

In this way thickness dependence could be incorporated into the CFJ model using the functional form of the resistivity thickness dependence. This functional form is in qualitative agreement with that found theoretically by Ren and Dow using a Boltzmann analysis to study the spin-flip scattering rate in thin films, predicting an enhancement with reducing thickness [148]. Equation (4.6.12) is then substituted for $\rho_{\downarrow\uparrow}(t)$ in

$$\frac{\Delta\rho(t)}{\rho} = \frac{\gamma(\rho_\downarrow - \rho_\uparrow)\rho_\downarrow}{\rho_\uparrow\rho_\downarrow + \rho_{\downarrow\uparrow}(t)(\rho_\uparrow + \rho_\downarrow)}. \tag{4.6.13}$$

The resulting fits to the AMR ratio, with equation (4.6.13) are shown in Fig. 4.18. In order to reduce the number of variables, the following procedure was used to fit equation (4.6.13) to the AMR ratio data, which applied constraints to the fits. As before, $\rho_\sigma = \rho_\sigma^i + \rho_\sigma^0$. For all samples, $\rho_\downarrow^i = 57.4\ \mu\Omega$cm and $\rho_\uparrow^i = 9.8\ \mu\Omega$cm as was found from the calculation of $\Delta\rho$ for Ni in section 4.4.3.

This leaves the values of $\rho_{\downarrow\uparrow,\text{bulk}}$, $\rho_{\downarrow\uparrow}(0)$ and ρ_σ^0 to be determined. To further simplify the problem, the Ni AMR ratio data was fitted first. As was discussed in section 1.4.3, $\rho_\sigma^0 = 0$ for the pure Ni films and hence only the parameters $\rho_{\downarrow\uparrow}(0)$ and ρ_σ^0 needed to be fitted.

These were found to be $\rho_{\downarrow\uparrow,\text{bulk}} = 20\ \mu\Omega$cm and $\rho_{\downarrow\uparrow}(0) = 5000\ \mu\Omega$cm. The value of $\rho_{\downarrow\uparrow,\text{bulk}}$ is larger than expected, but not entirely unreasonable. These were then fixed in the subsequent fits for the $Ni_{95}V_5$ and $Ni_{95}Cr_5$ data since the universal scaling demonstrated that the thickness dependence of $\Delta\rho$ should be the same independent of the dopant.

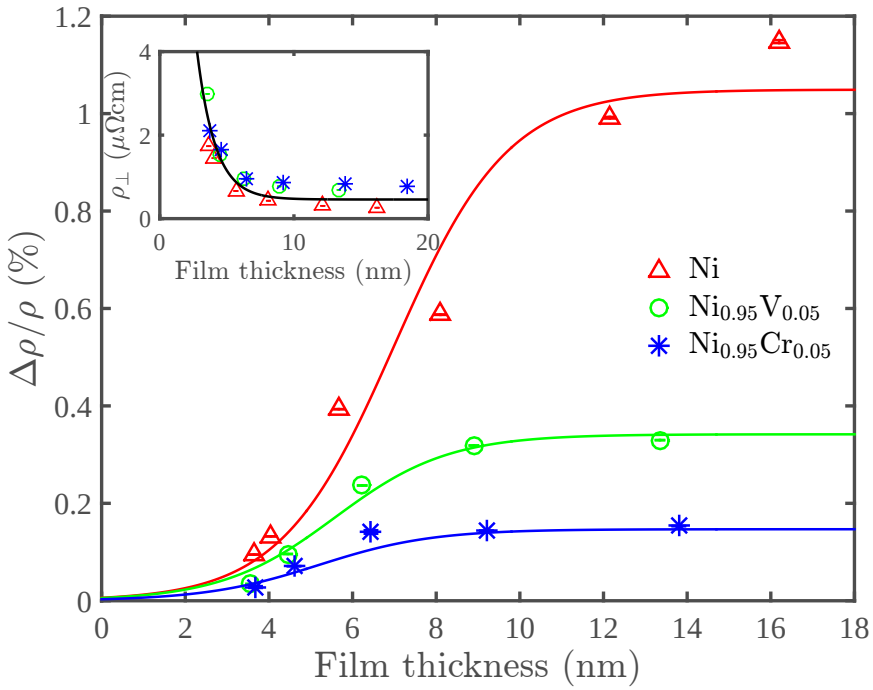

Figure 4.18: The thickness dependence of the AMR ratio for the Ni, $Ni_{95}V_5$ and $Ni_{95}Cr_5$ films and fits made using the CFJ model with thickness dependence incorporated into the $\rho_{\downarrow\uparrow}$ term. Inset: thickness dependence of $\rho_\perp$, demonstrating how an exponential fit can be used to capture the functional form of the data which can then be used to include thickness dependence within the CFJ model.

Therefore, fixing the parameters, t_0, $\rho_{\downarrow\uparrow,\text{bulk}}$ and $\rho_{\downarrow\uparrow}(0)$ ensures that equation (4.6.12) yields the same thickness dependence for the AMR ratio when fitted to the $Ni_{95}V_5$ and $Ni_{95}Cr_5$ datasets. The resulting values for ρ_σ^0 and the calculated $\alpha = \rho_\downarrow/\rho_\uparrow$ are shown in Table 4.5. The values of ρ_σ^0 are large but not unreasonable. Importantly, α undergoes a reduction when doping with V and a further reduction when doping with Cr.

The agreement of the fits with the data demonstrates that the sample resistivity is indeed representative of the film morphology which in turn reflects the contribution from $\rho_{\downarrow\uparrow}$.

It follows that in any system, if the functional form of the thickness dependence of

	$\rho_\downarrow^0$ ($\mu\Omega cm$)	$\rho_\uparrow^0$ ($\mu\Omega cm$)	α
Ni	0	0	–
$Ni_{95}V_5$	104	91	1.15
$Ni_{95}Cr_5$	143	151	0.94

Table 4.5: Extracted parameters from the best fits to the $\Delta\rho/\rho$ data shown in Fig. 4.18 using equation (4.6.13).

the resistivity is known, then $\Delta\rho$ can be calculated from this. This is because the thickness dependence of the resistivity reflects the contribution of the interfaces and sample morphology to electron scattering, and since we have shown here that the electron-magnon spin-flip scattering is influenced by the same changes in morphology, the thickness dependence of resistivity can be used to calculate the thickness dependence of $\Delta\rho$ in any system.

4.7 Chapter conclusions

In this chapter Ni, $Ni_{95}V_5$ and $Ni_{95}Cr_5$ films of various thickness were investigated. Structural analysis of the Ni films was made using XRR and it was found that there was an oxide of approximately constant thickness of 1 nm present on the surface of all the samples which was independent of ferromagnetic film thickness. TEM was also used from which it was also established that the onset of discontinuities occurred for Ni films thinner than 6 nm.

Measurement of the AMR in these films established that the loss of $\Delta\rho$ occurred at the same thickness independent of the dopant, highlighting that the drop in $\Delta\rho$ was likely associated with the effect of the encroaching interfaces as the film thickness reduced. The drop in $\Delta\rho$ occurred for films with thickness less than 6 nm, which coincided with the onset of film discontinuities. The role of interfaces and sample morphology was further evidenced by the linear scaling between $\Delta\rho$ and the film resistivity.

The spin-wave stiffness D was extracted from temperature dependent magnetisation measurements. From this it was observed that D also dropped dramatically in the region that $\Delta\rho$ did. It was interpreted that as the film thickness reduced, the surface contribution increased, and in particular when the film became discontinuous, this resulted in a reduction of nearest neighbour atomic interactions and an enhancement of magnonic excitations.

From this is was suggested that the increase in magnon density leads to enhanced electron-magnon scattering, which is a spin-flip scattering process. This mixes the spin-channels within the Mott-two-current model and therefore causes the loss of $\Delta\rho$ with reducing thickness since spin $\uparrow$ and spin $\downarrow$ electrons can no longer be considered to conduct independently. In the context of the CFJ model, this modifies the $\rho_{\downarrow\uparrow}$ term, which is isotropic with respect to the magnetisation direction, resulting in a reducing $\Delta\rho$ with decreasing film thickness.

Since the effect depends dramatically on the film morphology, $\Delta\rho$ is subject to many extrinsic factors such as film roughness and grain size which are dependent to an extent on the deposition environment. This explains why $\Delta\rho$ vanishes at different thickness between the sputtered samples used in this study and the evaporated samples used by L. Bogart [115]. However, it was shown from the structural analysis of the films that the functional form of the film resistivity inherently incorporates these extrinsic factors and can therefore be used to include a generalised thickness dependence into the CFJ model. This successfully reproduced the $\Delta\rho/\rho$ data with reasonable parameters and in principle could be applied to any system to determine the thickness dependence of $\Delta\rho$, as long as the functional form of the thickness dependence of the film resistivity is known.

5

Spin-orbit torques: damping-like and field-like torques in systems with different anisotropies

5.1 Introduction

Spin-orbit torques (SOTs) offer an alternative approach for electrical manipulation of magnetisation to conventional spin-transfer torque [7, 149]. Using a heavy metal/ferromagnet bilayer system, requiring just a single ferromagnetic element, it has been shown that an in-plane current can be used to manipulate magnetisation direction [24, 72, 150, 151]. There exists two torques, both act in directions orthogonal to each other. A "field-like torque" which can be represented as an effective magnetic field of the form $\vec{\boldsymbol{H}}_{\mathrm{FL}} \sim \hat{\boldsymbol{z}} \times \vec{\boldsymbol{j}}_{\mathbf{e}}$, and a "damping-like torque" which takes on the effective magnetic field form of $\vec{\boldsymbol{H}}_{\mathrm{DL}} \sim \vec{\boldsymbol{m}} \times (\hat{\boldsymbol{z}} \times \vec{\boldsymbol{j}}_{\mathbf{e}})$, where $\hat{\boldsymbol{z}}$ is a unit vector normal to the film surface, $\boldsymbol{j}_{\mathbf{e}}$ is the charge current density and $\vec{\boldsymbol{m}}$ is the magnetisation.

It is generally believed that the driving phenomena behind these torques are the spin Hall effect [19, 152] and the Rashba effect [20, 22]. A detailed discussion on the origin of these phenomena can be found in chapter 2. The experimental situation has been somewhat controversial, with some works favouring the Rashba effect [22] and others strong advocates of the spin Hall effect as the main driving force [24]. However, a theoretical study by Haney *et al.* [66], who employed a Boltzmann analysis, found that both the Rashba and spin-Hall effects can contribute to both the field-like and damping-like torques, but they differ in magnitude, with the spin-Hall effect giving rise to a larger damping-like torque and the Rashba effect a larger field-like torque.

In an attempt to resolve the contributions of the spin-Hall and Rashba effect there followed a body of experimental work which has investigated the SOTs in a variety of systems [14, 67, 153, 154]. This consequently demonstrated that the sign and magnitude of the SOTs can depend dramatically upon a variety of factors including ferromagnetic layer thickness [68, 69, 155], heavy metal layer thickness [68] and in particular the choice of heavy metal [14, 156, 157]. The ease by which SOTs can be engineered is positive in one regard, but it has been difficult to pin down the underlying physics.

SOTs have been studied in systems with in-plane [155, 158] and out-of-plane magnetic anisotropies [74, 159]. Of particular interest here was the work of Emori *et al.* [160], who demonstrated that oxygen migration at the ferromagnetic interface and a reduction in perpendicular magnetic anisotropy can result in an order of magnitude increase in the SOT with the $\vec{\boldsymbol{H}}_{\mathrm{DL}}$ contribution rising from 4.2 Oe to 46.8 Oe per 10^{10} Am^{-2}. This result demonstrated the sensitivity of the SOT to the magnetic anisotropy and the interfacial structure.

This is further developed in this chapter, where SOTs were studied in systems with strong in-plane anisotropy as well as systems with weak out-of-plane magnetic anisotropy. Furthermore, the sample structures were devised in order to separate and clarify the role of the Rashba and spin-Hall effects.

The chapter is split into two sections. The first focuses on measurements of SOTs, using the planar Hall effect (PHE) and longitudinal magneto-optical Kerr effect (MOKE), made on a $\mathrm{Ni_{81}Fe_{19}}$ (4 nm)/Pt (4.5 nm) bilayer with magnetic anisotropy in-the-plane of the film. The second section builds on the work of Emori *et al.* [160] and presents results where the SOTs were investigated in systems with weak perpendicular magnetic anisotropy (PMA). Here, a polar MOKE measurement with a lock-in detection method was used to measure a symmetric Pt (1 nm)/Co (0.6 nm)/Pt (5 nm) sample with weak PMA. Following this, the same experimental method was used to measure an asymmetric Pt (3 nm)/Co (0.6 nm)/MgO (2 nm)/Pt (1.5 nm) sample, which also had weak PMA, to study the Rashba contribution.

5.2 Definitions of parameters and measurement configurations

In this chapter there are a large number of experiment configurations as the measurements require magnetic fields applied at different angles with respect to the current flow. In order to simplify the descriptions it is worthwhile defining some angles. These are summarised in Fig. 5.1. The azimuthal angle, θ, defines vectors in the plane of the film. It is the azimuthal angle between the current flow and the applied magnetic field. The direction of current flow, $\vec{j_e}$ is defined as $\theta = 0°$. The polar angle, ϕ, defines vectors out of the plane of the film. It is the polar angle between the current flow and the applied magnetic field. It is defined such that the film normal, $\hat{z}$, is at $\phi = 90°$. Consequently, a magnetic field applied along the current flow is at angles $(\theta = 0°, \phi = 0°)$ and a magnetic field applied in-plane but transverse to the current flow is at angles $(\theta = 90°, \phi = 0°)$.

Three magnetic field directions are used regularly throughout this chapter. They are referred to as the longitudinal magnetic field $(\theta = 0°, \phi = 0°)$, the transverse magnetic field $(\theta = 90°, \phi = 0°)$ and the perpendicular magnetic field $\phi = 90°$. With these definitions in place the first section investigates SOTs in a $Ni_{81}Fe_{19}$/Pt bilayer with in-plane magnetic anisotropy.

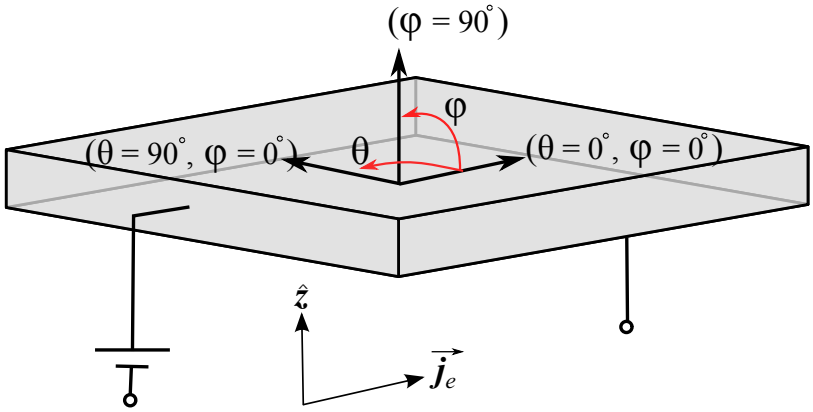

Figure 5.1: Definitions of the azimuthal (θ) and polar angles (ϕ) with respect to the current ($\vec{j_e}$) and film normal ($\hat{z}$) directions.

5.3 Spin-orbit torques in films with in-plane magnetisation

Since $\vec{H}_{\mathrm{FL}} \sim \hat{z} \times \vec{j}_{\mathrm{e}}$ and $\vec{H}_{\mathrm{DL}} \sim \vec{m} \times (\hat{z} \times \vec{j}_{\mathrm{e}})$, for samples where the magnetisation lies in the plane of the film, the resulting directions of the SOTs are those summarised in Fig 5.2. $\vec{H}_{\mathrm{FL}}$ causes magnetisation rotation in the plane of the film, hence the PHE and longitudinal MOKE are suitable choices to measure this rotation. Conversely, $\vec{H}_{\mathrm{DL}}$ causes the moment to cant out of the plane, hence in principle both the AHE and polar MOKE are appropriate choices for these measurements.

First, attempts at measuring magnetisation rotation due to $\vec{H}_{\mathrm{FL}}$ using the PHE are shown. The PHE has been used to characterise $\vec{H}_{\mathrm{FL}}$ by Fan *et al.* [69, 155] for in-plane magnetised systems, but in this measurement a unique approach was used, in which it was measured simultaneously with longitudinal MOKE so that any changes in the switching field reversal due to the $\vec{H}_{\mathrm{FL}}$ would be observable in the hysteresis loops.

A schematic of the setup is shown in Fig. 5.3. The longitudinal MOKE and PHE measurement setups are as described in chapter 3, whereby the magnetic field was driven by a Kepco BOP 50-5M power supply which oscillated the field polarity at 23 Hz. The samples were made by sputter deposition through a shadow mask resulting in tracks that were 0.5 mm wide and a schematic of the samples surface is also shown in Fig. 5.3.

For the PHE, a constant DC current was applied through the central bar of the sam-

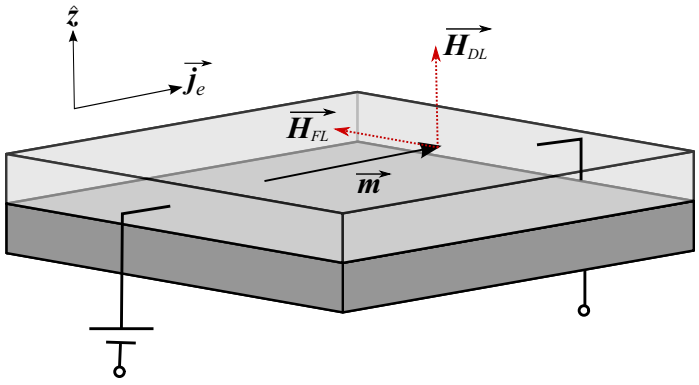

Figure 5.2: Schematic of a $Ni_{81}Fe_{19}$/Pt bilayer with magnetisation $\vec{m}$ and current density $\vec{j}_{\mathrm{e}}$ in the plane of the film and the resulting directions of $\vec{H}_{\mathrm{FL}}$ and $\vec{H}_{\mathrm{DL}}$. The unit vector $\hat{z}$ is defined as the normal to the film surface. Although the Pt is on the top, for clarity the magnetisation and effective field vectors associated with the ferromagnetic layer have been drawn on the surface.

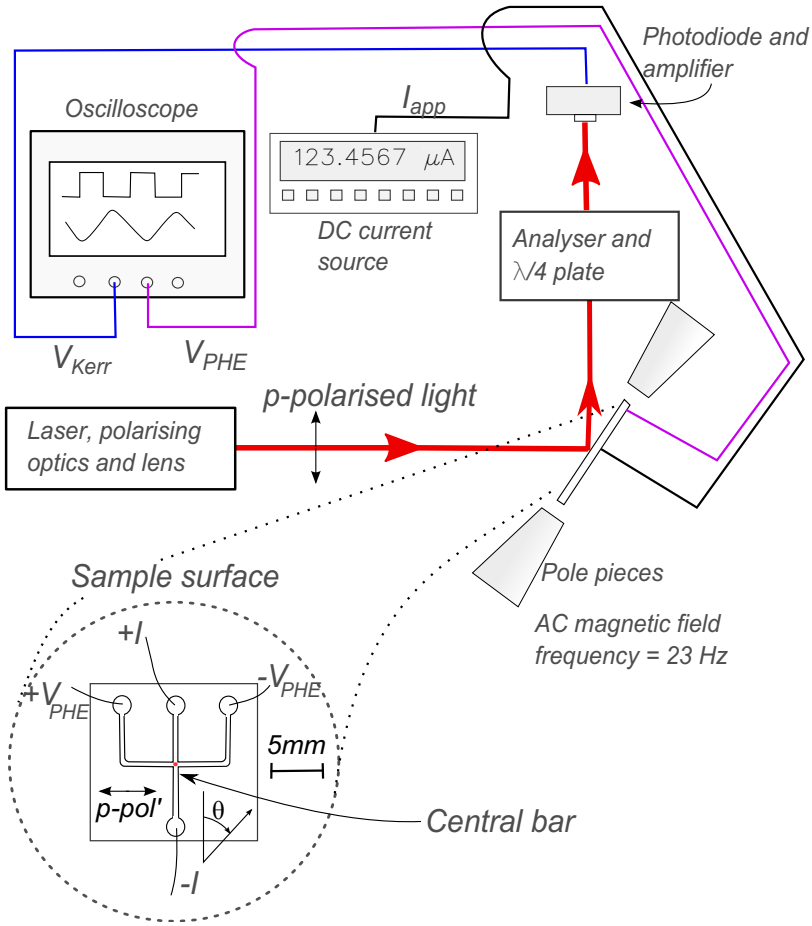

Figure 5.3: Schematic showing the experimental setup for measuring magnetisation rotation due to $\vec{H}_{\mathrm{FL}}$. A sourcemeter was used to apply a DC current to the sample and the resulting current induced field modifies the magnetisation reversal. The magnetisation reversal was measured using both longitudinal MOKE and the PHE simultaneously. The Kerr voltage and V_{PHE} were passed to the oscilloscope and averaged over multiple field cycles.

ple between $+I$ and $-I$ contacts and the PHE voltage was measured across the contacts $+V_{\mathrm{PHE}}$ and $-V_{\mathrm{PHE}}$ as a function of the in-plane field (which oscillated at 23 Hz) using the oscilloscope. Due to the oscillating magnetic field, the Kerr voltage and PHE showed time dependence and the oscilloscope was used to measure both the PHE and Kerr voltages simultaneously and was triggered to the in-plane AC magnetic field modulation frequency, allowing both signals to be averaged over multiple field cycles.

For the longitudinal MOKE measurement, the focused p-polarised laser spot hit the sample at the midpoint of the central bar, and after passing through a quarter-wave plate and analyser was directed into the photodiode. The resulting laser intensity due to the Kerr rotation was measured by the photodiode as a function of the in-plane field and measured with the oscilloscope as a Kerr voltage. The in-plane field was applied at different angles θ

with respect to the DC current.

5.3.1 Planar Hall effect and hysteresis loops as a function of applied magnetic field angle

The PHE has an angular dependence that follows $\sim \sin 2\theta_m$ [161], where θ_m is the azimuthal angle between the current and magnetisation directions. Consequently, the Hall voltage changes sign as θ_m passes through 0° and has a maximum magnitude at $\theta_m = 45°$. Furthermore, the $\sin 2\theta_m$ curve is steepest at $\theta_m = 0°$ hence the PHE is most sensitive to magnetisation changes about the current flow direction, making it very useful for measuring SOTs.

In Fig 5.4, measurements of the PHE as a function of magnetic field are shown, where the field was applied at different angles, θ, to the current flow. The PHE field sweeps have been centred about zero volts. The shape of the PHE peak is determined by the magnetisation reversal of the sample. This is not a single domain sample and neither does it have a strong uniaxial anisotropy, so the interpretation of the peak shape is complex and related to the net magnetisation direction of the domains at each point under the reversal process. However, in this qualitative analysis, it can be seen that the PHE peak is closely correlated to the magnetisation reversal, which is indicated by the switching in the hysteresis loop.

The PHE peak is smallest at $\theta = 0°, 90°$ and 180° and changes sign as the angle goes through $\theta = 90°$, as expected from the $\sin 2\theta_m$ dependence of the PHE.

The positive PHE peaks are smaller than their negative counterparts. This could be related to the small anisotropy exhibited by the sample since it can be seen that the hysteresis loop is hard-axis-like for magnetic field sweeps applied at $\theta = 130°$, whereas it is squarer with high remanence at $\theta = 60°$. The sample was rotated throughout the sputter deposition period, but small deposition induced anisotropies like this can still arise particularly if there is oblique incidence [109]. For field sweep angles between $\theta = 0° - 90°$ the PHE peak is positive. In the saturated state for these field sweeps there is a larger component of the magnetisation aligned along the easy axis at $\theta_m = 60°$ than there is orthogonal to it. It could then be expected that upon reversal, the magnetisation would first rotate along the easy axis then rotate around to align with the field. For field sweep angles between $\theta = 90° - 180°$, where the PHE is negative, in the saturated state the opposite it true, in

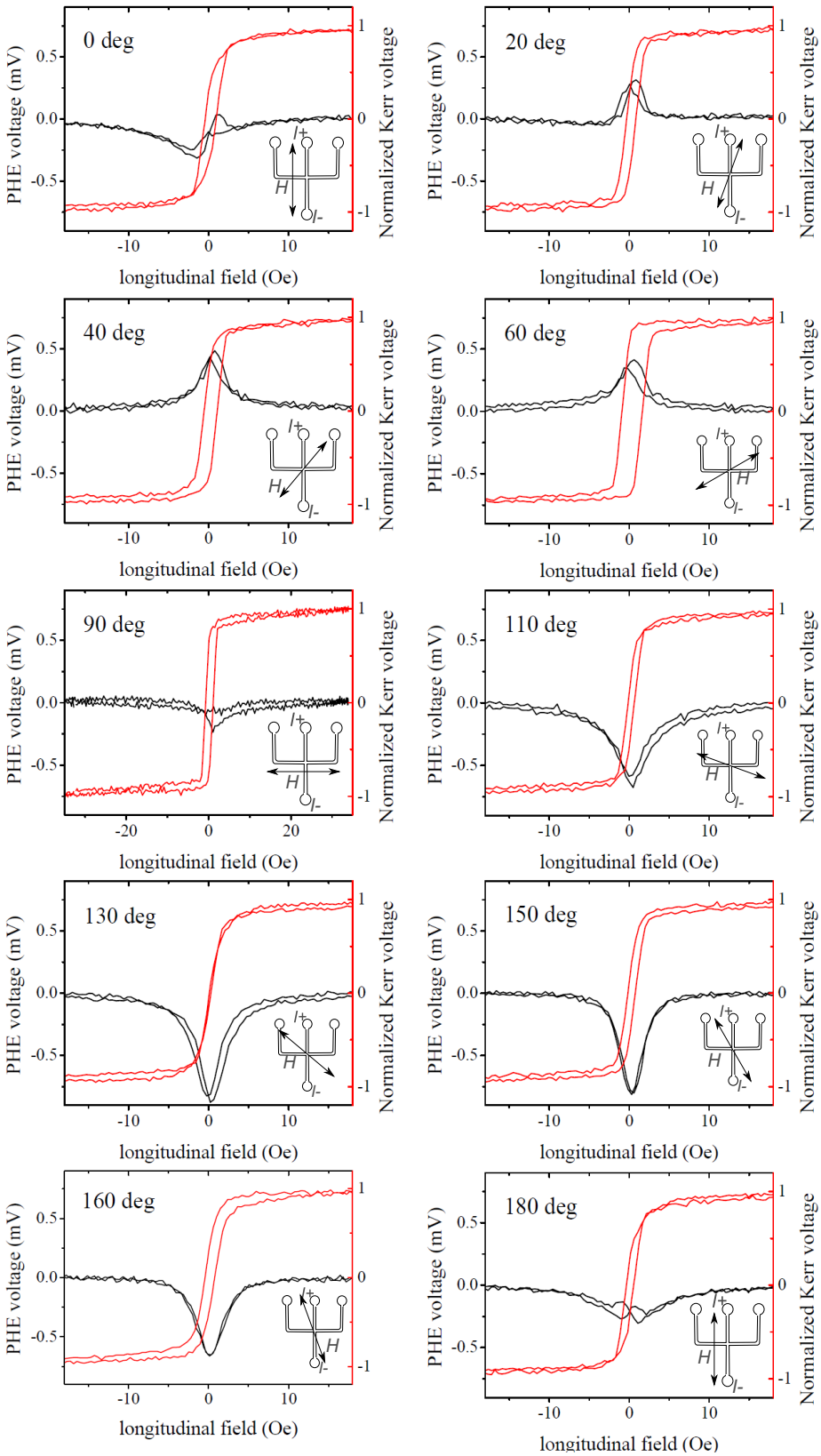

Figure 5.4: Example curves demonstrating the PHE voltage (black) and normalised longitudinal MOKE hysteresis loops (red) measured simultaneously from a $Ni_{81}Fe_{19}$ (4 nm)/Pt (4.5 nm) bilayer at various angles θ, the azimuthal angle between the current flow and applied in-plane magnetic field. A DC current density of 0.24×10^{10} Am^{-2} was applied for all measurements.

that a larger component of magnetisation is aligned orthogonal to the easy axis. Therefore upon reversal, the magnetisation has to undergo a larger rotation which results in a larger peak in the PHE.

The coercive field has been plotted as a function of magnetic field angle θ in Fig. 5.5. Given the very small coercive field inherent to $Ni_{81}Fe_{19}$ (due to its minimal magnetocrystalline anisotropy) and the limited field resolution of the measurement, it is difficult to draw definite conclusions from this data. However, there is evidence to suggest a small amount of anisotropy within the sample, with maximum H_c at 60°. The dashed line shows a fitted $H_0 + A\sin^2(\theta - \theta_0)$ distribution, where H_0 and θ_0 are vertical and lateral offset and A is the oscillation amplitude. The fit suggests the easy and hard axes are at $\theta_m = (62 \pm 4)°$ and $(152 \pm 4)°$ respectively.

5.3.2 Current-assisted magnetisation reversal in a NiFe/Pt bilayer

A simple way to probe the current-induced effective fields, including both the Oersted field and SOTs, is to measure how the PHE changes as a function of current. Fig. 5.6 shows a series of PHE field sweeps under different applied DC currents, all taken with the field parallel to the current flow, i.e. $\theta = 0°$. The PHE voltage increases as the current density increases with a distinctive change in the shape of the peak for applied current densities

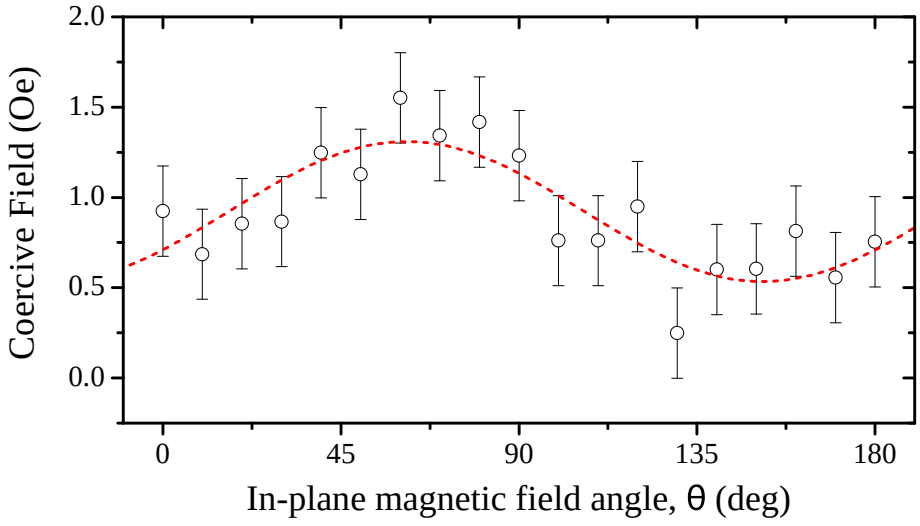

Figure 5.5: Variation of coercive field of $Ni_{81}Fe_{19}$(4nm)/Pt(4.5nm) bilayer as a function of the magnetic field angle θ, with a constant DC current density of 0.24×10^{10} Am^{-2} through the sample. The dashed line shows the best fit using the uniaxial anisotropy distribution, $H_0 + A\sin^2(\theta - \theta_0)$.

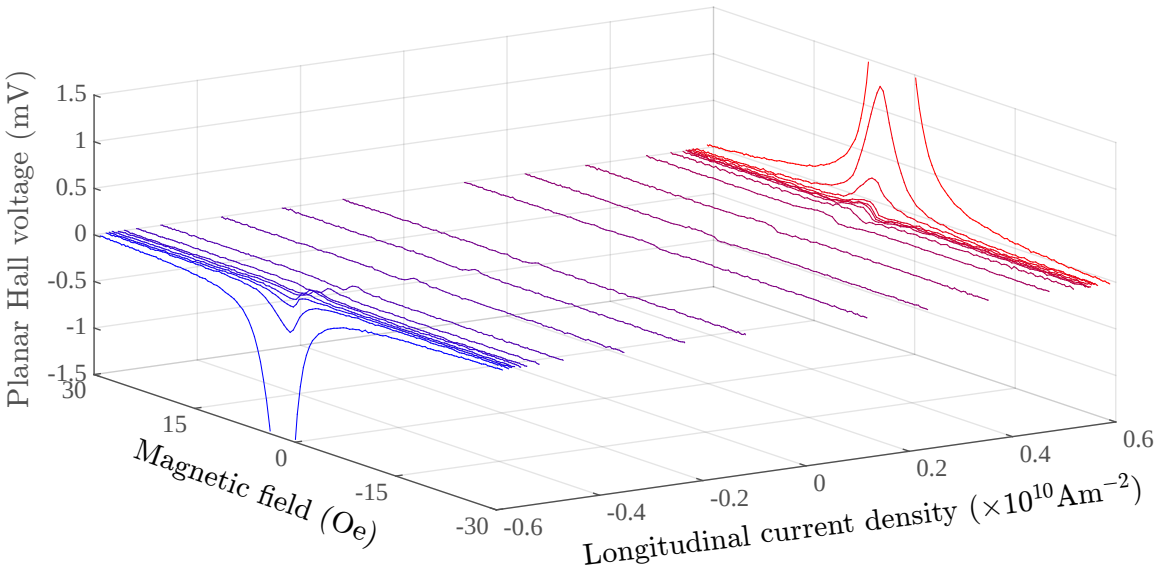

Figure 5.6: Variation of the PHE voltage with magnetic field sweeps taken at $\theta = 0°$ at different current densities.

greater than $\pm 0.5 \times 10^{10}$ Am^{-2}. The peak shape changes to resemble more closely that observed in Fig. 5.4 at $\theta = 40°$ and 130° for positive and negative currents respectively.

The combination of the current-induced Oersted field and $\vec{\boldsymbol{H}}_{\mathrm{FL}}$ act to rotate the magnetisation away from the applied magnetic field direction. The competition between these current-induced fields and the externally applied magnetic field is such that as the applied field is reduced the magnetisation can begin to rotate away from $\theta_{\mathrm{m}} = 0°$. With larger current densities, the Oersted field and $\vec{\boldsymbol{H}}_{\mathrm{FL}}$ become effective at rotating the magnetisation away from the applied field direction θ at larger applied fields, hence the PHE peaks get broader along the field direction. At small applied field, the magnetisation is still acted on by the current-induced fields, which now dominate, so the peak itself changes shape, because when the Oersted field and $\vec{\boldsymbol{H}}_{\mathrm{FL}}$ are effective, the magnetisation reversal does not occur along the direction θ set by the applied field at saturation since the current-induced fields act to rotate the magnetisation away from the magnetic field axis. The PHE peak therefore becomes more symmetrical like those taken at $\theta = 40°$ and 130° for positive and negative currents respectively as the current-induced fields rotate the magnetisation towards these directions.

As the current density is increased, there would also be an increase in voltage across the sample due the incorporation of a longitudinal voltage component along the current direction. This is a particular problem in these relatively wide structures where there is

likely to be a significant longitudinal voltage contribution from the lateral offset between the voltage probes caused by the non-uniform current distribution and imperfections in the mask. This increase in voltage with current should be linear. The peak PHE voltage from the magnetic field sweeps is plotted in Fig. 5.7 a) as a function of current density. The inset in Fig. 5.7 a) shows a zoomed in version of the graph between $\pm 0.52\times10^{10}$ Am^{-2}. In this region the rise in V_{PHE} is approximately linear and may be attributed to this longitudinal voltage component. However, the dramatic rise in V_{PHE} above $\pm 0.5\times10^{10}$ Am^{-2}, as shown in the main figure, must be due to an additional component and is most likely due to the magnetisation rotation by the combined current induced fields. The PHE resistance $R_{\mathrm{PHE}} = V_{\mathrm{PHE}}/I$ is shown on a logarithmic scale in Fig. 5.7 b). Calculating R_{PHE} removes the linear voltage increase with the current and the data becomes approximately flat for current densities below $\pm 0.5\times10^{10}$ Am^{-2}. Above this, the data rises dramatically demonstrating an enhancement of R_{PHE} due to magnetisation rotation assisted by the combined action of $\vec{\boldsymbol{H}}_{\mathrm{FL}}$ and the Oersted field.

It has been shown that the application of an in-plane current density of order 0.5×10^{10} Am^{-2} in a $Ni_{81}Fe_{19}$ (4nm)/Pt (4.5nm) can have a dramatic effect on the magnetisation reversal as measured through the PHE and longitudinal MOKE. Using longitudinal MOKE, the PHE magnetic field sweeps at different θ could be characterised with respect to the weak anisotropy present in the sample. From this it was inferred from the depen-

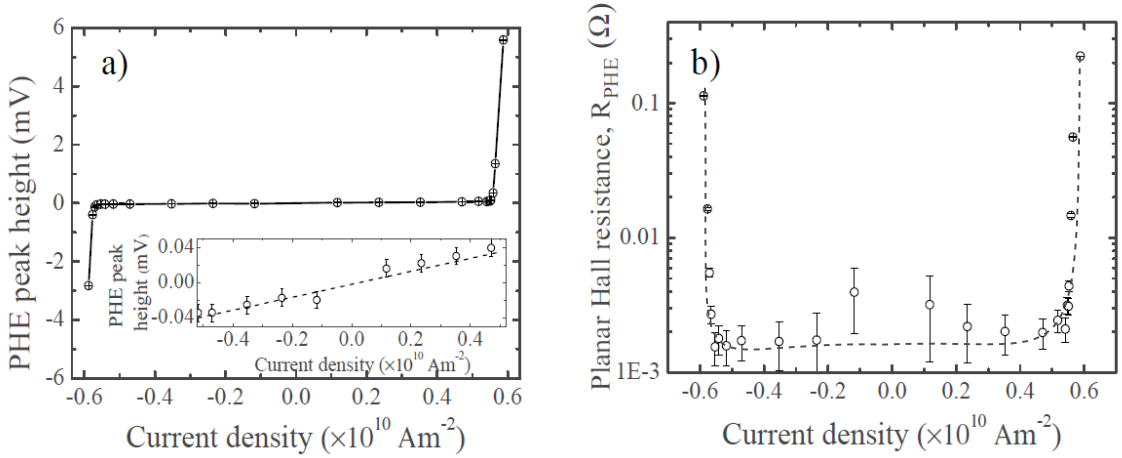

Figure 5.7: a) PHE peak voltage found from the field sweeps at 0° for different applied currents. The inset shows the same data zoomed in the region of $\pm 0.52\times10^{10}$ Am^{-2}. The dashed line shows a linear fit to the data. b) R_{PHE} calculated for each PHE peak voltage as a function of applied current and plotted on a logarithmic scale. The dashed line is a guide for the eye.

dence on current density for the PHE field sweeps at fixed $\theta = 0°$ that the current-induced effective field was causing magnetisation rotation and modifying the reversal process.

In a similar study, Fan *et al.* [155] were able to determine a field-like torque $\vec{H}_{\mathrm{FL}}$ of 1.3 Oe per 10^{10} Am^{-2} in a $\mathrm{Ni_{80}Fe_{20}}$(2 nm)/Pt(5 nm) bilayer. Considering the low ($\approx$ 1 Oe) coercive field of our sample, an effective field on this scale would have a dramatic effect on the PHE magnetic field sweeps. Here, significant modification of the PHE signal as a function of applied current was observed, and this has been attributed to the same field-like torque. However, it is important to note that in this study, the contribution of the Oersted field was not measured, although other studies on similar systems with in-plane magnetisation have demonstrated the SOT to be dominant current-induced field [24, 69, 155]. This chapter now progresses by turning to samples with perpendicular magnetic anisotropy (PMA).

5.4 Spin-orbit torques in films with perpendicular magnetic anisotropy

From a technological point of view SOTs in perpendicular materials are of great interest and have been demonstrated to be highly effective for magnetic reversal of perpendicularly magnetised structures [23, 162, 163]. First, a description of how SOTs can be measured using polar MOKE is presented.

5.4.1 Measurements of spin-orbit torques using polar MOKE with lock-in detection

The effective fields due to the SOTs in a sample with PMA are shown in Fig. 5.8 a). The SOTs act to move the magnetisation away from the perpendicular axis. This can be measured using the anomalous Hall effect or the polar Kerr effect. The electrical approach using the Hall effect is well established in the literature [14, 157]. However, the polar Kerr effect has the advantage that the signal does not contain artefacts from the anomalous Nernst effect [160]. Furthermore, unlike the Hall effect, for the polar MOKE measurement the SOT arises in the first harmonic of the lock-in detection, which is much stronger than

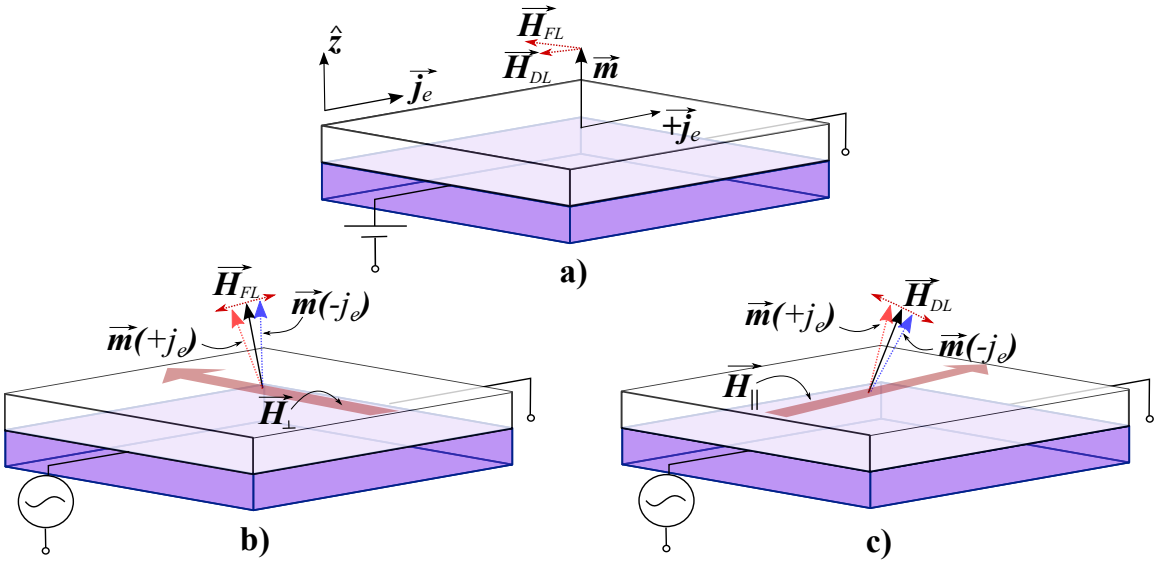

Figure 5.8: a) Schematic showing heavy metal/ferromagnetic bilayer film with magnetisation $\vec{m}$ out-of-plane and current density $\vec{j}_e$ in the plane of the film with the resulting directions of $\vec{H}_{\mathrm{FL}}$ and $\vec{H}_{\mathrm{DL}}$. b) When a constant transverse bias field, $\vec{H}_{\perp}$ ($\theta = 90°, \phi = 0°$) is applied perpendicular to the AC current flow, the resulting magnetisation oscillation is due to $\vec{H}_{\mathrm{FL}}$. c) When a constant longitudinal bias field, $\vec{H}_{\parallel}$ ($\theta = 0°, \phi = 0°$) is applied along the AC current flow, the resulting magnetisation oscillation is due to $\vec{H}_{\mathrm{DL}}$.

the second harmonic signal required for the Hall effect measurement.

A schematic of the experimental setup using the polar Kerr effect is shown in Fig. 5.9. The optics of the polar MOKE setup are the same as that described in chapter 3, the primary difference being that an AC current is passed through the sample. When passing an AC current through the sample, the SOTs cause the magnetisation to oscillate about the polar axis. This oscillation in magnetisation results in an oscillation of the light intensity due to the MOKE which was measured by the photodiode. This signal was sent to the lock-in amplifier input which used the AC current frequency as its reference and measured the amplitude of the oscillation as a function of the applied in-plane magnetic field. In all of the measurements presented in this chapter, the AC current frequency was 492 Hz.

Magnetic fields were applied in the plane of the film between the pole pieces and a small Helmholtz coil behind the sample was used to produce perpendicular fields ($\phi = 90°$) of up to ±30 Oe.

As well as this, DC currents were applied, and the anomalous Hall effect was measured this way by measuring the resulting V_{AHE} with the oscilloscope as the in-plane magnetic field was cycled. The transverse voltage contacts were pointed in order to minimise the

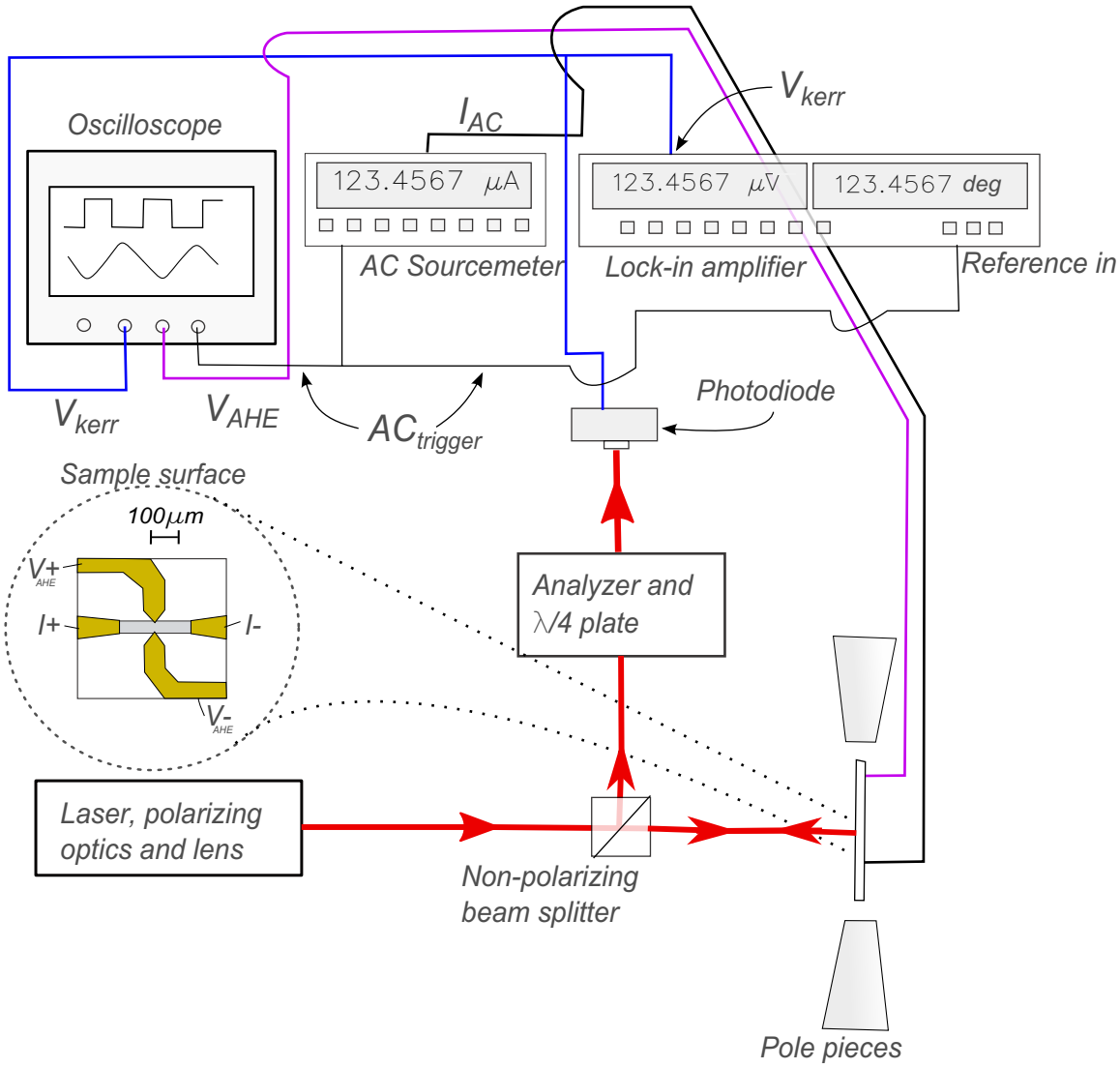

Figure 5.9: Experimental setup for measuring SOTs in samples with PMA using polar MOKE and lock-in detection. The laser beam was *p*-polarised and a beam splitter was required to gather the signal reflected from polar incidence. The polar MOKE modifies the laser intensity at the photodiode in a way that is proportional to the polar component of magnetisation. The magnitude of the voltage oscillation measured by the photodiode due to the SOT was measured using a lock-in amplifier. The inset shows a schematic of the sample surface with a 50 μm wire and Ti/Au contacts patterned using optical lithography.

contribution of longitudinal voltage to the Hall voltage due to lateral offsets.

The MOKE signal was also passed to the oscilloscope so that the oscillation itself could be investigated and as required, averaged over many AC current cycles. This was used for measuring the current-induced magnetisation reversal (CIMR) hysteresis loops.

As shown previously in Fig 5.8 b), by applying a constant in-plane magnetic bias field transverse to the AC current flow $\vec{H}_{\perp}(\theta = 90°, \phi = 0°)$, the axis of the magnetisation os-

cillation can be restricted such that only $\vec{H}_{\mathrm{FL}}$ is effective. Likewise, in Fig 5.8 c), applying the magnetic field along the AC current flow, $\vec{H}_{\parallel}$ ($\theta = 0°, \phi = 0°$), means that only $\vec{H}_{\mathrm{DL}}$ will be effective. This method of separating the components of SOTs has been shown to be effective in numerous studies in the literature [14, 67, 68, 150, 160, 164].

Sweeping either $\vec{H}_{\parallel}$ or $\vec{H}_{\perp}$ whilst measuring the magnitude of the MOKE magnetisation oscillation with the lock-in amplifier yields a linear trend in oscillation amplitude that passes through zero and for which the gradient is proportional to the magnitude of the current-induced effective field. This is demonstrated schematically in Figs. 5.10 a) and b) and occurs, since when an in-plane field is applied, the oscillation is offset away from the polar axis and consequently positive and negative applied currents yield different components of polar magnetisation. This results in a difference between the respective Kerr

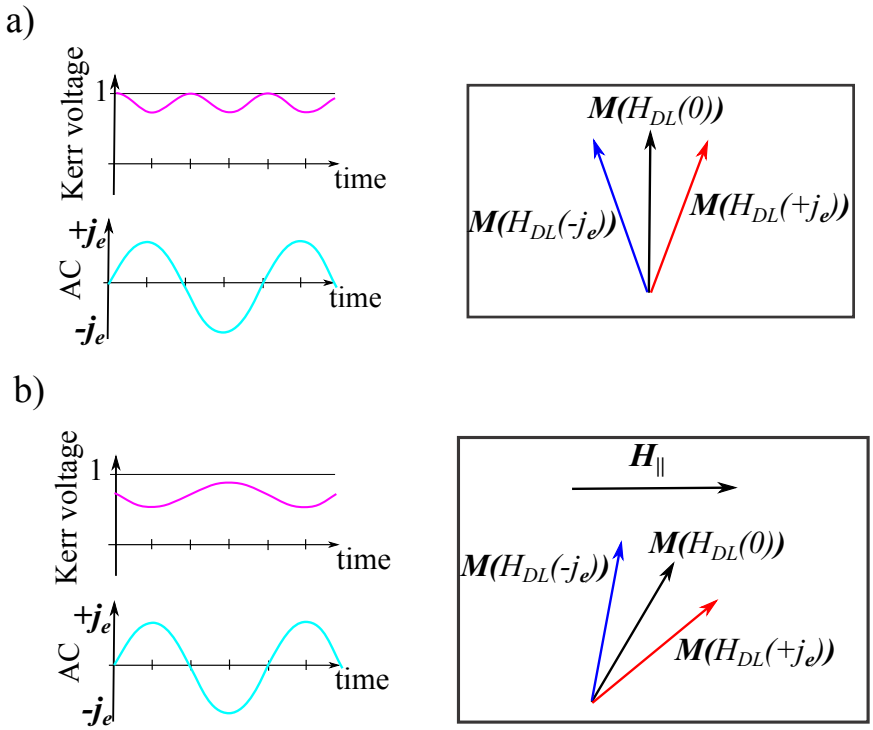

Figure 5.10: Schematics demonstrating the origin of the lock-in signal due to the SOT. For simplicity only $\vec{H}_{\mathrm{DL}}$ has been considered but the same arguments would apply to $\vec{H}_{\mathrm{FL}}$ if a transverse bias field was used ($\vec{H}_{\perp}$). a) With no $\vec{H}_{\parallel}$ applied, the effective field $\vec{H}_{\mathrm{DL}}$ under positive and negative currents both yield the same polar magnetisation component and hence have the same polar Kerr voltage. This results in a signal that oscillates at double the AC frequency. Consequently the lock-in does not register a signal oscillating at the reference frequency. b) With the application of $\vec{H}_{\parallel}$, the symmetry is broken. Positive and negative currents result in different polar Kerr voltages and a signal oscillating at the reference frequency is obtained. Note in this example the magnetisation oscillation is in anti-phase with the current, in this case the sign of the spin-Hall angle can be determined to be negative.

voltages which then registers as an oscillation at the frequency of the AC current sweep. The phase of this oscillation also contains the sign of the spin Hall angle of the material, since positive and negative spin Hall angles would cause the magnetisation to oscillate in opposite directions with respect to positive and negative current directions, which would result in a 180° difference in phase. 70

The functional form for the dependence of the magnetisation oscillation on the in-plane bias field is given by [165];

$$\frac{C_\omega}{C_0} = \frac{|\vec{\boldsymbol{H}}_{\mathrm{DL(FL)}}|}{H_\mathrm{k}^2}|\vec{\boldsymbol{H}}_{\parallel\,(\perp)}|. \tag{5.4.1}$$

Here, C_ω is the first harmonic lock-in voltage, which is the magnitude of the polar Kerr voltage oscillation due to the SOT. C_0 is the magnitude of the Kerr voltage when the magnetisation is orientated along the polar axis. The ratio of these parameters therefore represents the fraction of polar magnetisation lost due to the magnetisation oscillation at $\pm\vec{\boldsymbol{j}}_\mathbf{e}$. Finally, H_k is the effective anisotropy field, which in this case is the applied field required to rotate the magnetisation in-plane.

In addition to sweeping the in-plane field, the SOTs can be measured as a function of the amplitude of the AC current oscillation, the magnitude of the DC offset applied to the AC current, as well as perpendicular magnetic fields ($\phi = 90°$), giving further insight into the mechanism of the SOTs. In the next section, the polar MOKE method for measuring SOTs is applied to a system with weak PMA.

5.5 Spin-orbit torques in a structurally symmetric system with weak PMA

In general, samples with strong uniaxial anisotropy have large coercive fields. By weakening the anisotropy, the energy barrier for magnetisation reversal can be reduced and it becomes easier to reverse the magnetisation. Therefore, in a weak PMA system, the effects of SOTs can be more dramatic. From equation (5.4.1) it can be seen that the magnetisation oscillation will be increased in a system with weak perpendicular anisotropy. With sufficiently weak PMA, the SOT is ultimately capable of reversing the magnetisation [74, 162].

Throughout this section the same sample was used, which has the nominal structure

Pt (1 nm)/Co (0.6 nm)/Pt (5 nm). This was patterned using two stages of optical lithography. In the first stage an array of micro-wires with length 400 μm and widths of 16 μm, 20 μm, 30 μm and 50 μm were patterned. The Pt/Co/Pt stack was then sputter deposited through this onto a Si/SiO_2 substrate under base pressures of order 5×10^{-8} Torr. The second lithography stage was used to pattern Ti/Au contacts. A schematic of the sample structure can be seen inset in Fig. 5.9.

The hysteresis loop shown in Fig. 5.11 a) shows PMA with a small coercive field of 30±2 Oe. The anisotropy field, H_k, required for equation (5.4.1) was obtained by fitting a Stoner-Wohlfarth model,

$$\frac{M_z}{M_s} = \cos(\arcsin(H_{||}/H_k)), \tag{5.5.2}$$

to the longitudinal field sweep data in Fig. 5.11 b). Here, M_z is the perpendicular component of magnetisation, M_s is the saturation magnetisation and $H_{||}$ is the longitudinal field. A value of $H_k = (1340 \pm 20)$ Oe was obtained from fitting equation (5.5.2) to the longitudinal field sweep data. The weak anisotropy was achieved by varying the Co and Pt thicknesses over many samples until a structure with the required magnetic anisotropy was found.

Alongside the weak PMA, the symmetric Pt (1 nm)/Co (0.6 nm)/Pt (5 nm) sample structure should minimise the contribution from the Rashba effect and therefore minimise $\vec{H}_{FL}$. Furthermore, the buffer Pt layer is comparable to spin-diffusion length of Pt, $\lambda_{sd} \approx 1-2$ nm [93]. This means that the spin-current at the top Co/Pt interface due to the SHE in the top Pt(5 nm) layer would be larger than at the buffer Pt/Co interface due to the Pt (1 nm) layer. This therefore prevents the cancellation of spin-currents from the

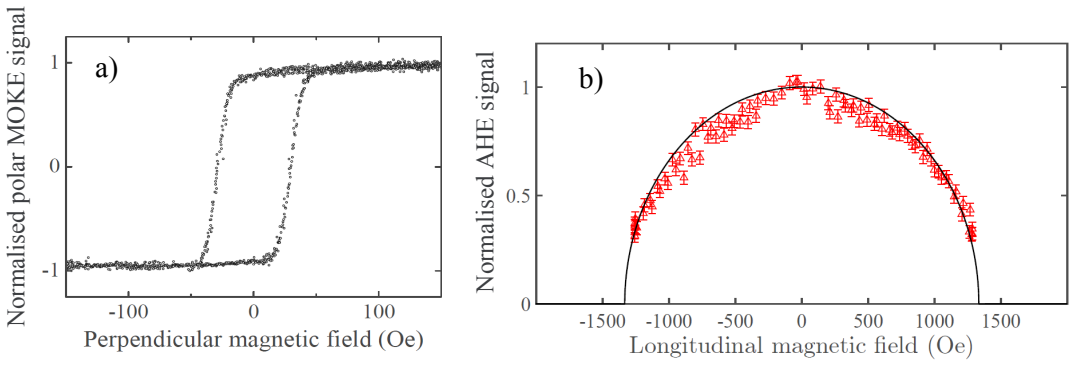

Figure 5.11: a) Polar MOKE hysteresis loop for the Pt(1nm)/Co(0.6nm)/Pt(5nm) trilayer. b) The polar magnetisation component as a function of longitudinal applied field obtained using the anomalous Hall effect. Solid line denotes the best fit using equation (5.5.2).

symmetrical interfaces, leading to a net spin-current originating at the top Co/Pt interface and an appreciable $\vec{H}_{\mathrm{DL}}$.

5.5.1 Applying DC current to modify magnetisation switching

The magnetisation reversal of the Pt/Co/Pt sample was investigated with the application of a DC current, and is shown in Fig. 5.12 a), where the polar Kerr voltage was measured with an in-plane field and different DC current densities. With no DC current there is no magnetisation reversal when the in-plane field is swept, noting the smaller magnetic field range than in Fig. 5.11 b). However, when a constant DC current density of 2.5×10^{10} Am^{-2} is applied, the in-plane field is capable of inducing magnetisation reversal. This is also ob-

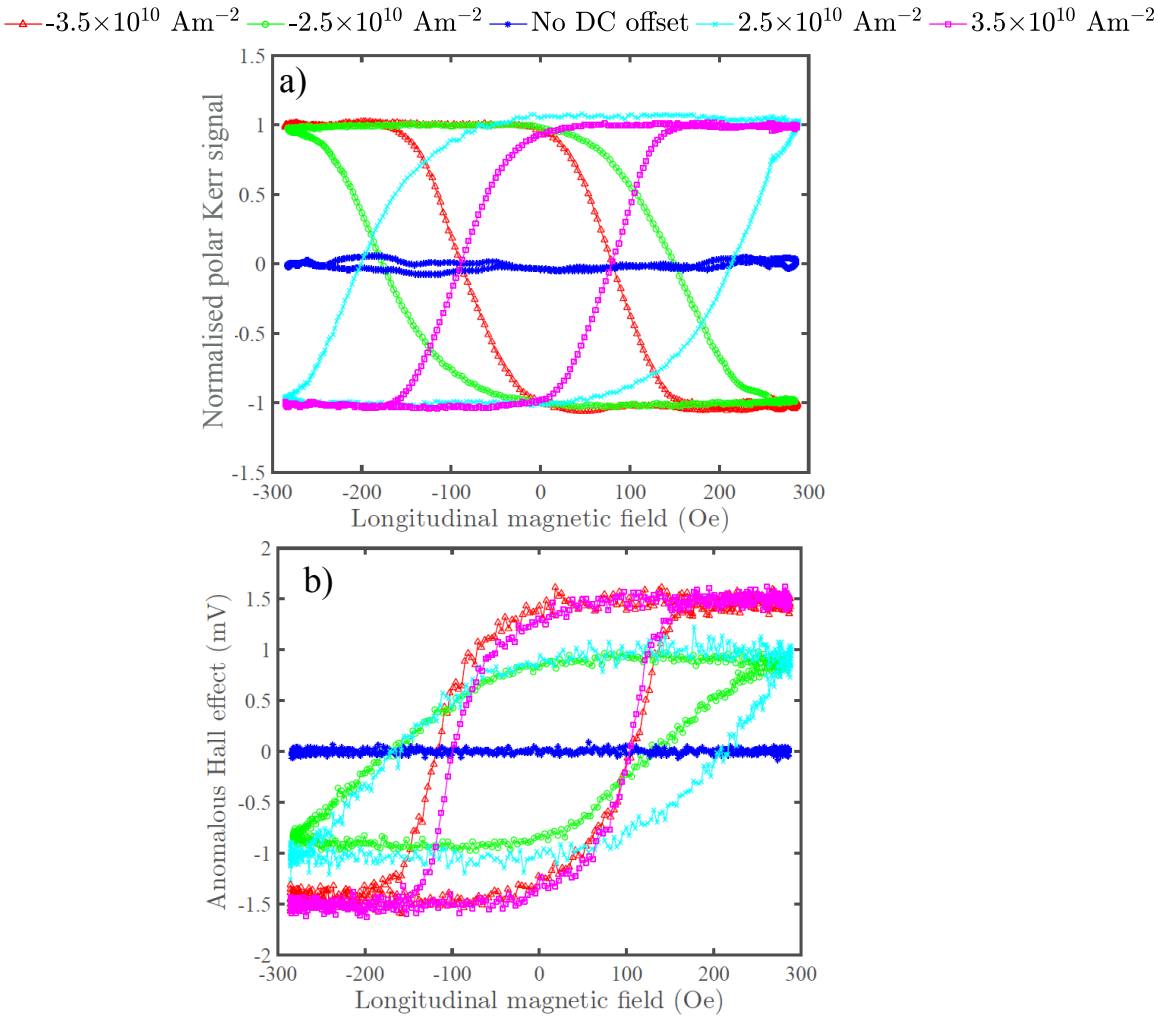

Figure 5.12: Hysteresis loops measured as a function of the in-plane longitudinal magnetic field with different DC current densities using a) polar MOKE and b) anomalous Hall effect. The polar MOKE loops have been normalised to the saturation Kerr voltage.

served in the anomalous Hall effect in Fig. 5.12 b). Since the SOT scales with current, the effective longitudinal coercive field gets smaller as the DC current is increased.

The Oersted field and the field-like torque, $\vec{H}_{\mathrm{FL}}$ are independent of magnetisation direction so would favour switching for one field polarity and hamper it for the other, which would cause the loop to be displaced along the field axis. There is some evidence for this, in that when the DC current is reversed there is a small difference in the longitudinal coercive field, particularly for the $\pm$ 2.5×10^{10} Am^{-2} measurements. Unlike the field-like torque and the Oersted field, the damping-like torque depends on the magnetisation direction, $\vec{H}_{\mathrm{DL}} \sim \vec{m} \times \hat{z} \times \vec{j}_{\mathrm{e}}$, it therefore aids magnetisation reversal equally for both field polarities since it changes direction once the magnetisation has reversed.

When the DC current is reversed, the sign of the polar Kerr voltage with positive/negative longitudinal field reverses. Reversing the current changes the sign for $\vec{H}_{\mathrm{DL}}$ for up/down magnetisation directions. Consequently, the longitudinal field polarities which favour up/down magnetisation states are reversed as well, which causes the loop to invert. This also occurs in the anomalous Hall effect (AHE) measurements, but since the AHE voltage itself depends on the sign of the current, the loop is reversed a second time, cancelling the effect.

5.5.2 Investigating the damping-like torque

In this section the damping-like torque is investigated in detail in the Pt/Co/Pt system with weak PMA. In Fig. 5.13 lock-in measurements of the magnitude of the first harmonic voltage (C_ω), normalised to the polar Kerr voltage magnitude (C_0) are shown as a function of the longitudinal magnetic field. The sign of the voltage magnitude has been reversed when the phase of C_ω changed by 180°, in order to demonstrate the change in sign with field polarity. Since a longitudinal field, $\vec{H}_{\parallel}$ ($\theta = 0°, \phi = 0°$) was used, this measurement is sensitive only to the effects of $\vec{H}_{\mathrm{DL}}$, the damping-like torque.

There is linear behaviour in the low current and low field regimes and the straight lines correspond to linear fits within this region which are used for the extraction of $\vec{H}_{\mathrm{DL}}$ from equation (5.4.1). As the AC current density amplitude is increased the gradient of C_ω with $\vec{H}_{\parallel}$ increases, consistent with a $\vec{H}_{\mathrm{DL}}$ of increasing magnitude. However, saturation is observed for some of the higher AC current density amplitude measurements, which is a

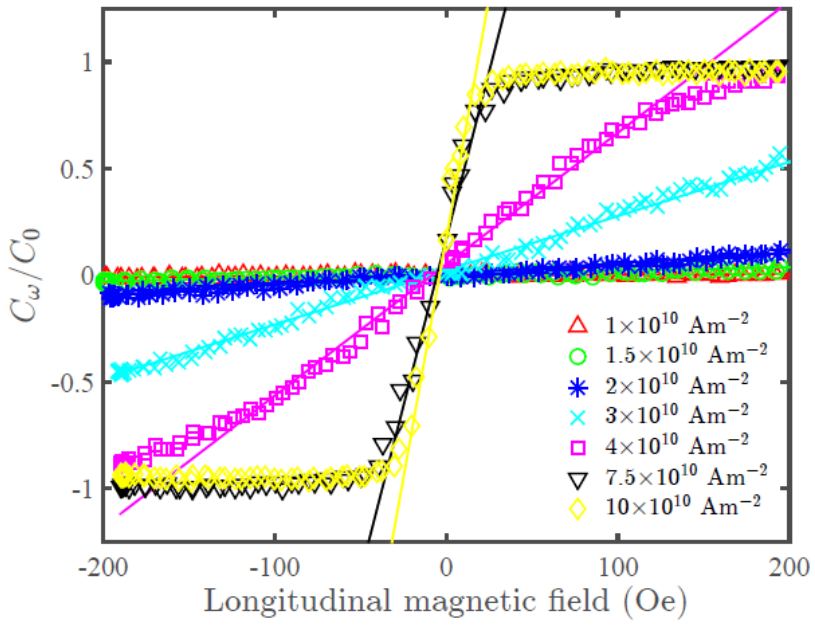

Figure 5.13: Normalised first harmonic lock-in polar Kerr voltage, C_ω/C_0, measured as a function of longitudinal magnetic field ($\theta = 0°, \phi = 0°$) with different AC current density amplitudes.

result of current induced magnetisation reversal (CIMR).

Fig. 5.14 shows the phase of the first harmonic lock-in voltage with respect to the applied AC current, as a function of the longitudinal magnetic field. There is a 180° phase shift when the field polarity changes. This occurs because the field polarity determines the magnetisation offset from the out-of-plane axis. This then determines whether the torques increase of decreases the projection of the magnetisation on the out-of-plane axis. This is demonstrated in the schematic shown in the inset of Fig. 5.14. With positive longitudinal fields a positive current causes an increase in the projection of $\boldsymbol{m}$ along the out-of-plane axis whereas a negative current causes a drop in the projection of $\boldsymbol{m}$ on the out-of-plane axis, this results in a polar MOKE voltage oscillation that is in-phase with the AC current. With negative fields the effects of positive and negative current on the polar component of $\boldsymbol{m}$ are reversed, and the polar MOKE voltage oscillation is in anti-phase with the AC current resulting in a 180° phase shift. The phase data becomes noisier for low $\vec{\boldsymbol{H}}_{\parallel}$ and low AC current density amplitudes because in these regions the polar MOKE oscillation is small, and hence the phase is difficult to determine reliably.

Using equation (5.4.1), $\vec{\boldsymbol{H}}_{\mathrm{DL}}$ was extracted from the linear fits in Fig. 5.13. The results are plotted in Fig. 5.15. Contrary to reports in the literature [159, 160, 164, 166], the depen-

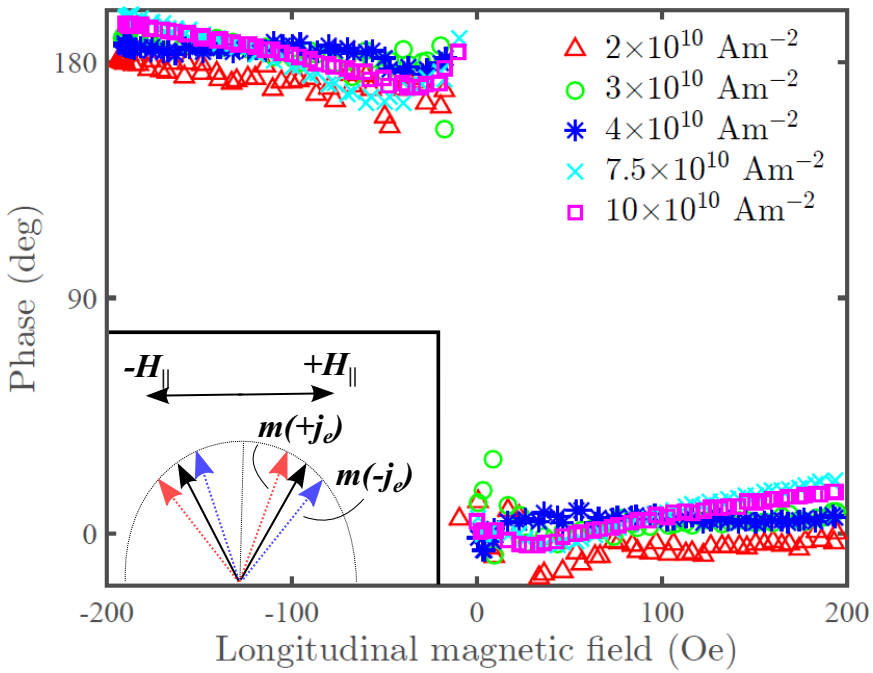

Figure 5.14: The phase of the first harmonic relative to the AC current as a function of the longitudinal magnetic field. Inset: Schematic demonstrating the origin of the 180° phase shift when the field polarity is reversed.

dence of $\vec{H}_{\mathrm{DL}}$ on the current density is consistently non-linear. The inset shows that this continues even at low current density. Furthermore, the magnitude of $\vec{H}_{\mathrm{DL}}$ is enormous compared to those found in similar multilayer structures in the literature [67, 159, 160], which typically range between 50-100 Oe with an 10^{11} Am^{-2} current density. This suggests that the simple model employed by equation (5.4.1) is not valid in this system. This could be because the model assumes coherent magnetisation rotation which does not account for domain nucleation and magnetisation reversal. Reverse domain nucleation would result in larger changes in C_{ω} than would be accounted for by coherent magnetisation rotation under the same SOT, consequently this would enhance the effective value of $\vec{H}_{\mathrm{DL}}$ extracted. This could help explain the very large values of $\vec{H}_{\mathrm{DL}}$ obtained using this methodology.

It is thought that the microscopic origin of $\vec{H}_{\mathrm{DL}}$ is predominantly due to the SHE. Furthermore, in this symmetric system the Rashba effect should be minimised. The sign of the effective field is a consequence of the sign convention for positive and negative fields directions and current as well as the sign of the SOT. For this Pt (1 nm)/Co (0.6 nm)/Pt (5 nm) multilayer, the thickness of the buffer Pt layer is comparable the spin-diffusion length of Pt, [93], hence most spin-current due to the SHE will originate from the top

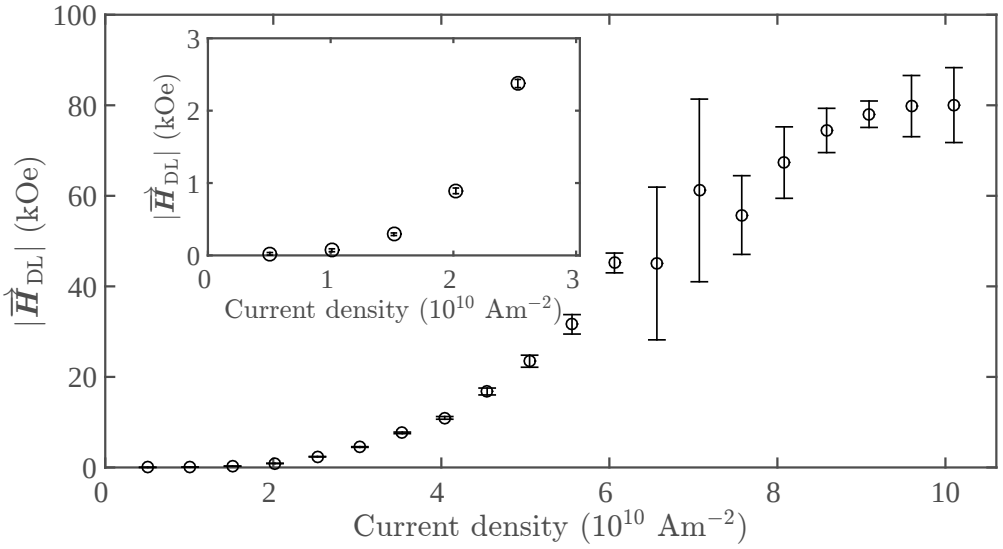

Figure 5.15: Magnitude of $\vec{H}_{DL}$ extracted from the longitudinal field sweeps as a function of AC current density amplitude assuming coherent magnetisation reversal. The inset shows a magnified version of the low current density data, demonstrating that the non-linear behaviour exists over all measured AC current density amplitudes. The error bars are calculated from the 95% confidence intervals from the linear fits to the longitudinal field sweep data.

Pt layer. Consequently, it is found here that $\vec{H}_{DL}$ originating from a Co/Pt interface is positive. Likewise, this means measurements of $\vec{H}_{DL}$ originating from a Pt/Co interface should result in a negative value if the sign convention for positive current and positive field directions are maintained.

In Fig. 5.16 a) the switching map is shown. Here, the magnitude of the lock-in signal is plotted as a function of both the applied longitudinal field and the AC current density magnitude. After each longitudinal field sweep measurement the AC current density amplitude was increased and the field sweep was repeated. The yellow regions mark the areas where CIMR occurs. Since the coercive field in this sample is so small, it is particularly sensitive to small offsets in ϕ to the applied in-plane magnetic field. This gives rise to a small asymmetry between positive and negative fields in Fig. 5.16 a). This asymmetry is responsible for the large errors in the extracted $\vec{H}_{DL}$ from AC current density amplitudes between 6 - 8×10^{10} Am^{-2} in Fig. 5.15. For similar switching maps shown in the literature, this asymmetry is not discussed, as only one field polarity was investigated when making the parameter maps [67]. The switching map was also measured in reverse, starting at an AC current density amplitude of 10^{11} Am^{-2} and reducing to 0.5×10^{10} Am^{-2}, which reproduced an identical map demonstrating that the large current densities used were not

damaging the sample.

Using the oscilloscope, it is possible to measure the signal that is passed to the lock-in amplifier at specific points on the switching map. Some examples are shown in Fig. 5.16 b) which correspond to the points 1-4 on the switching map. All of the loops use an AC current density magnitude of $9\times10^{10}\mathrm{Am}^{-2}$, but different values of the applied longitudinal field. It can be seen that without a constant longitudinal field, no switching occurs. However, application of a small field of 35 Oe induces magnetisation reversal. As this field is

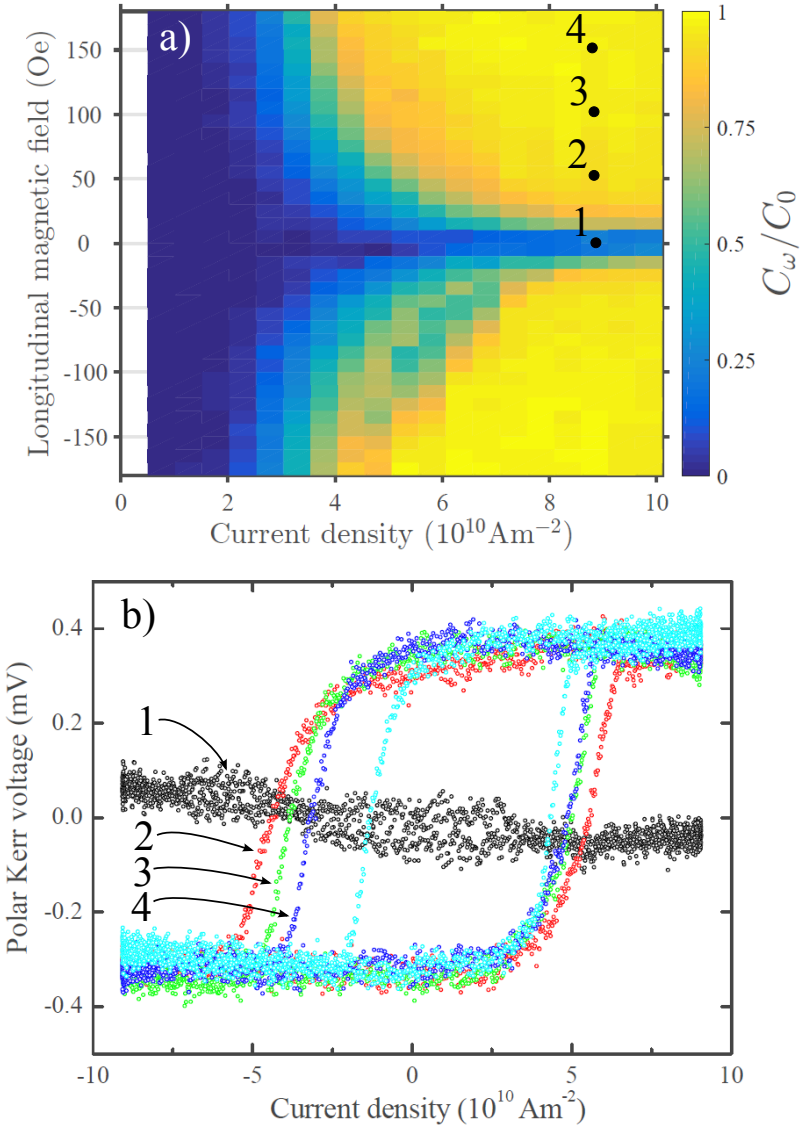

Figure 5.16: a) Switching map demonstrating the interdependence of the magnetisation reversal on AC current density amplitude and longitudinal field. Points 1-4 correspond in respective order to the points in parameter space with 0 Oe, 54 Oe, 105 Oe and 154 Oe longitudinal field and a $9\times10^{10}\mathrm{Am}^{-2}$ AC current density amplitude. b) CIMR loops measured with the oscilloscope at positions 1-4 in parameter space shown in a).

further increased, it is also clear from Fig. 5.16 b) that the shape of the loop changes. The critical current density, defined as the current density at which the magnetisation passes through zero on reversal, decreases as the longitudinal field is increased. Interestingly, the process is asymmetric, whereby the positive critical current density reduces at a slower rate than the negative critical current density. This may be due to the Oersted field, which, since it does not change direction when the magnetisation is reversed, would aid CIMR in one direction and hamper it in the other. Likewise, the half-loop width, which is half the difference between these values, analogous to the coercive magnetic field, decreases with increasing field. This is summarised in Fig. 5.17 where the half-loop width and the positive and negative critical current densities can all be seen to decrease linearly with increasing longitudinal field.

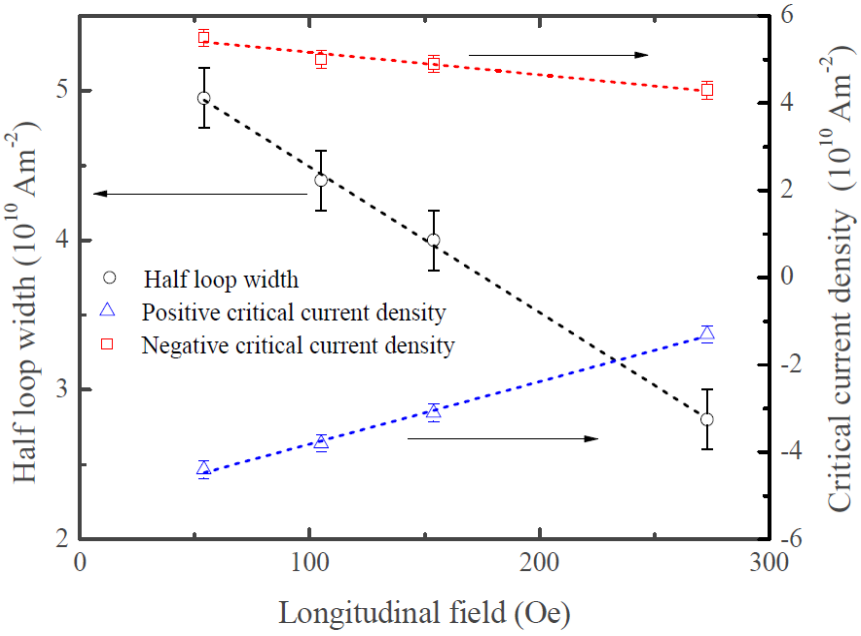

Figure 5.17: The variation of the half loop width for CIMR as well as the positive and negative critical currents for magnetisation reversal under different static longitudinal fields. The dashed lines are linear fits.

5.5.3 Discussion of the origin of the current induced magnetisation reversal

For CIMR, the critical current density j_c for magnetisation reversal as a result of the spin-Hall effect is proportional to [166];

$$j_c \propto \frac{\alpha M_s H_{eff}}{\theta_{SH}} \tag{5.5.3}$$

where α is the magnetic damping, M_s is the saturation magnetisation, $H_{eff} = H_k - 4\pi M_s$ where H_k is the anisotropy field and θ_{SH} is the spin Hall angle.

The magnetic damping counter-acts the damping-like torque and therefore increase j_c. A difficulty with PMA systems is that typically the magnetic damping is dramatically enhanced due to the combination of ultrathin ferromagnetic layers and heavy metal layers. A study by Mizukami *et al.* [167] on Pt/Co/Pt multilayers found α could be as large as 0.4 for similar Co thickness as used in this study.

In this system, this issue is overcome by engineering the sample structure such that H_k and therefore H_{eff} are small, which acts to reduce j_c. Furthermore, it is likely the saturation magnetisation is dramatically reduced as the Co layer is reduced to sub-monolayer thickness, which further acts to reduce j_c. A reduced M_s reduces the anisotropy energy and therefore reduces the energy barrier for magnetisation reversal. A study by P. F. Carcia [168] found that in Pt/Co/Pt super-lattices, for Co thickness between 3 - 10 Å, M_s was between 50 - 300 emu/cm^3. This is significantly less than the bulk M_s of Co, which is 1400 emu/cm^3. Hence the CIMR is a consequence of the reduced H_k and M_s as well as the large spin Hall angle of Pt, which is of the order 0.1 [81, 93, 94].

5.5.4 Measurements of the damping-like torque with perpendicular magnetic fields

By applying a perpendicular magnetic field ($\phi = 90°$) the perpendicular anisotropy can be effectively enhanced along one direction. The effect of a small constant perpendicular field of 10 Oe on the longitudinal field sweeps at different AC current density amplitudes can be seen in Fig. 5.18 a). The perpendicular field increases the longitudinal magnetisation

switching field in both directions. The SOT is competing with the perpendicular field, hence the effect becomes more pronounced as the AC current density amplitude is reduced, since the SOT becomes weaker.

The effect of sweeping the perpendicular field ($\phi = 90°$) with a constant longitudinal field ($\theta = 0°, \phi = 0°$) of 200 Oe is shown in Fig. 5.18 b). With no perpendicular field the CIMR occurs. This is suppressed by the application of the perpendicular field. The effect is symmetrical with respect to positive and negative perpendicular fields because the phase of the oscillation C_ω is unchanged with respect to the AC current for positive and negative

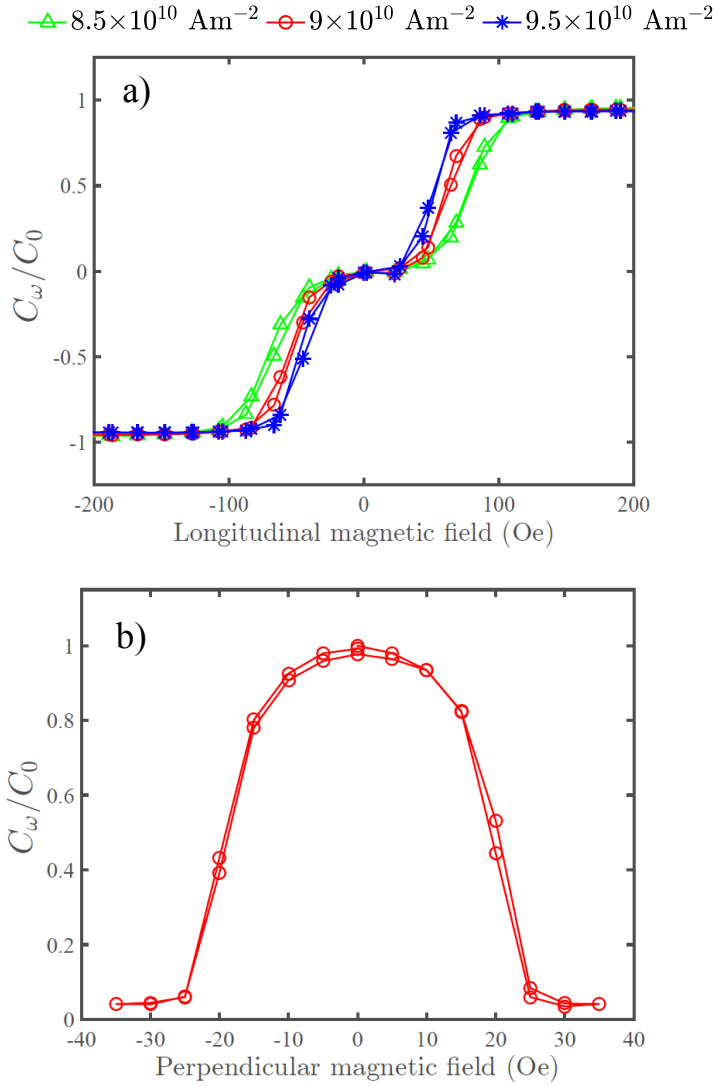

Figure 5.18: a) Polar MOKE measurement of C_ω/C_0 as a function of longitudinal field ($\theta = 0°, \phi = 0°$), measured with a constant 10 Oe polar field ($\phi = 90°$) for three different AC current density amplitudes. b) Polar MOKE measurement of C_ω/C_0 as a function of perpendicular field ($\phi = 90°$), measured with a constant longitudinal field of 200 Oe ($\theta = 0°, \phi = 0°$) and AC current density amplitude of $9{\times}10^{10}$ Am^{-2} .

perpendicular fields.

In the next section, the study turns to investigate whether the field-like torque is present in this Pt/Co/Pt system by measuring the angular dependence of the SOTs.

5.5.5 Investigating the contribution of the field-like torque

Since the Pt/Co/Pt multilayer lacks SIA it would not be expected to have a significant $\vec{H}_{\mathrm{FL}}$. As explained in Fig. 5.8, by applying a magnetic field at $\theta = 0°$ and 90°, $\vec{H}_{\mathrm{DL}}$ and $\vec{H}_{\mathrm{FL}}$ can be effectively separated. Initial measurements made using a transverse in-plane field $\vec{H}_{\perp}$ ($\theta = 90°, \phi = 0°$) showed little evidence of a significant field-like term, $\vec{H}_{\mathrm{FL}}$. Within the intervening angles both $\vec{H}_{\mathrm{DL}}$ and $\vec{H}_{\mathrm{FL}}$ would be expected to contribute as a function of θ, in the form $|\vec{H}_{\mathrm{DL}}| \cos\theta + |\vec{H}_{\mathrm{FL}}| \sin\theta$. By measuring the dependence of this combined effective SOT on the angle between the in-plane field and the current, θ, further insight can be gained into the SOT strength and the presence of a $\vec{H}_{\mathrm{FL}}$ in this sample.

From Fig. 5.19 a), it can be seen that the SOT is strongest for magnetic field sweeps measured parallel to the current flow ($\theta = 0°, \phi = 0°$), i.e the longitudinal geometry and sensitive to $\vec{H}_{\mathrm{DL}}$. When the field angle θ is increased, the saturation (which indicates CIMR) occurs at larger in-plane field values, suggesting the effective SOT is less effective along the given field orientation. For values of θ above 70°, the effective SOT is not capable of inducing CIMR within the range of longitudinal magnetic fields applied. There is a change in sign above 90°. When θ is greater than 90° the polarity of the positive and negative current flow is reversed with respect to positive and negative longitudinal field directions, and hence the change in sign.

The field sweep measured at ($\theta = 90°, \phi = 0°$) with respect to the current flow, i.e. the transverse geometry which is sensitive only to $\vec{H}_{\mathrm{FL}}$, shows the smallest signal. There are some features in this sweep, and it is suggested that these are measurement artifacts due to the extreme sensitivity of this sample to the in-plane field alignment, which needs to be precisely confined to the plane of the film when the PMA is weak and H_c is small. For this Pt/Co/Pt multilayer structure, with weak PMA, a small perpendicular component of field due to an offset in ϕ can have significant effects when the SOT is weak. This is the case for the measurements of $\vec{H}_{\mathrm{FL}}$, and also the case for the measurements of $\vec{H}_{\mathrm{DL}}$ at low AC current density, as was demonstrated by the asymmetry of the switching map in

Fig. 5.16 a).

Although the magnitudes of $\vec{H}_{\mathrm{DL}}$ obtained using equation (5.4.1) may not be strictly valid for a sample that exhibits domain formation due to a SOT, the methodology can be used to compare the relative changes in net combined effective SOT from $\vec{H}_{\mathrm{DL}}$ and

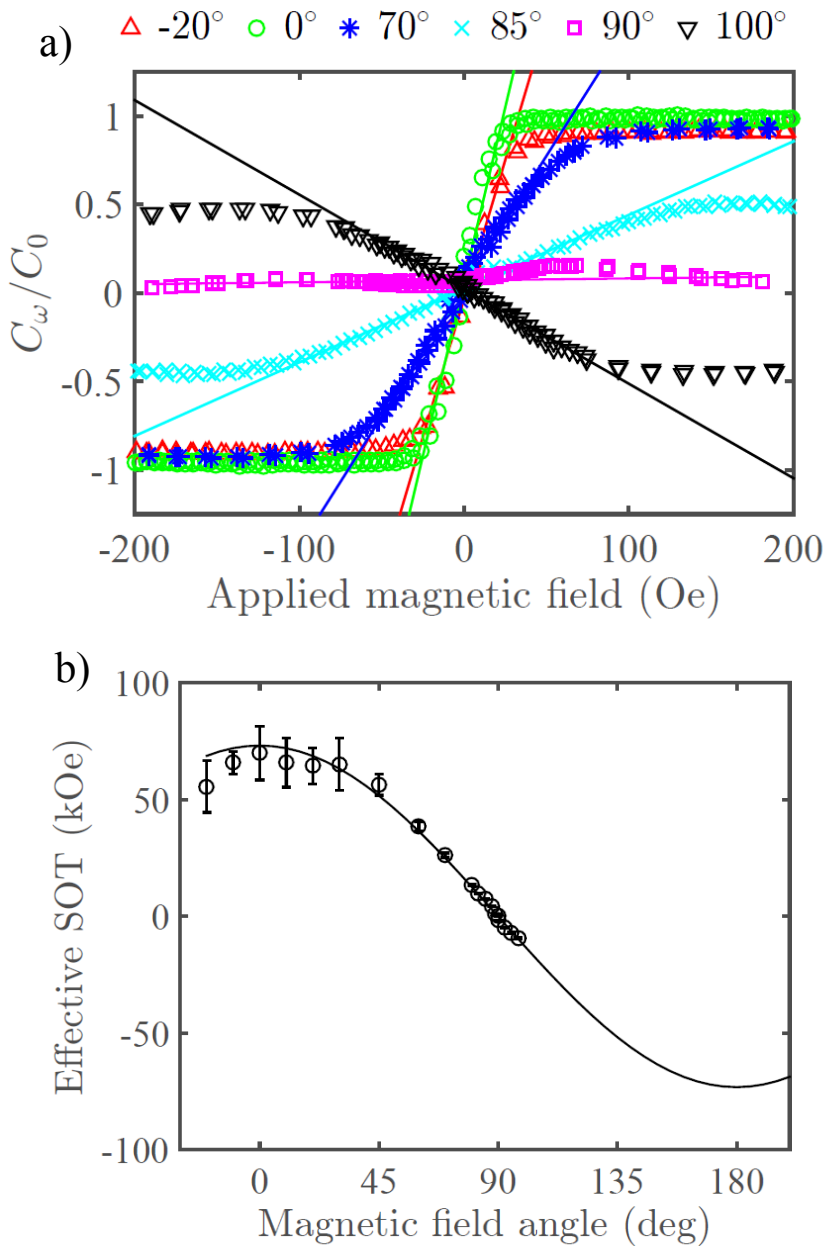

Figure 5.19: a) Polar MOKE measurements of C_ω/C_0 as a function of the magnetic field applied in the plane ($\phi = 0°$) and at different angles of θ relative to the AC current. The AC current density amplitude was $10^{11}\,\mathrm{Am}^{-2}$ for all measurements. No perpendicular field ($\phi = 90°$) was applied. The straight lines are linear fits in the region of ± 70% of the saturated signal. b) Values of effective SOT extracted from the field sweep measurements. The solid line shows the fit made using effective SOT = $|\vec{H}_{\mathrm{DL}}|\cos\theta + |\vec{H}_{\mathrm{FL}}|\sin\theta$.

$\vec{H}_{\mathrm{FL}}$ as a function of the angle θ. This effective SOT extracted from the linear fits shown in Fig. 5.19 a) is plotted as a function the magnetic field angle with respect to the current flow (θ) in Fig. 5.19 b). The functional form, effective SOT = $|\vec{H}_{\mathrm{FL}}|\cos\theta + |\vec{H}_{\mathrm{FL}}|\sin\theta$ has been fitted to the data. The values for $|\vec{H}_{\mathrm{DL}}|$ and $|\vec{H}_{\mathrm{FL}}|$ extracted from the fit are (73 ± 4) kOe and (0 ± 0.6) kOe respectively, for an AC current density amplitude of $10^{11}\mathrm{Am}^{-2}$. The available data fits the distribution, passing through zero at $\theta = 90°$ within the error margins. Therefore the dominating contribution to the CIMR is $\vec{H}_{\mathrm{DL}}$ for this Pt/Co/Pt multilayer structure with weak PMA. This is consistent with the Rashba effect being the primary contribution to $\vec{H}_{\mathrm{FL}}$ and that the Rashba effect requires SIA and is minimised in systems with symmetric interfaces above and below the ferromagnetic layer.

$\vec{H}_{\mathrm{FL}}$ has been measured in a variety of perpendicular magnetised systems in the literature, where SIA has been introduced with the use of dissimilar heavy metal and oxide layers on either side of the ferromagnetic layer [22, 162, 164, 169]. There have been fewer studies in which $\vec{H}_{\mathrm{FL}}$ and $\vec{H}_{\mathrm{DL}}$ have been measured independently without the presence of an oxide [67, 153]. However, recent work by Yang *et al.* [166] using a symmetrical Pt/NiCoNi/Pt structure also found, in agreement with this work, no evidence for $\vec{H}_{\mathrm{FL}}$ but measured a sizeable $\vec{H}_{\mathrm{DL}}$. In their experiment the current distribution was different between the two Pt layers, therefore preventing the cancellation of the spin-Hall currents. These results suggest that the SIA is crucial for $\vec{H}_{\mathrm{FL}}$ which is consistent with the Rashba effect.

Within this setup, there is also the capability to sweep the AC current density amplitude or the out-of-plane magnetic field. As before, an in-plane field was used to define the axis of the magnetisation oscillation, and was applied at an in-plane angle θ. However, for these measurements the magnitude of the in-plane field was kept constant and instead the AC current density amplitude or perpendicular field were varied.

Fig. 5.20 a) shows perpendicular field sweeps ($\phi = 90°$), as was shown in Fig. 5.18 b), but measured with the constant in-plane field applied at different azimuthal angles θ relative to the constant AC current density amplitude. As was shown in Fig. 5.18 b), the polar field acts to suppress the current induced magnetisation reversal.

As θ increases, the polar field reduces C_ω more dramatically, which is consistent with the effective SOT getting weaker. The downward slopes on either side of the data progress

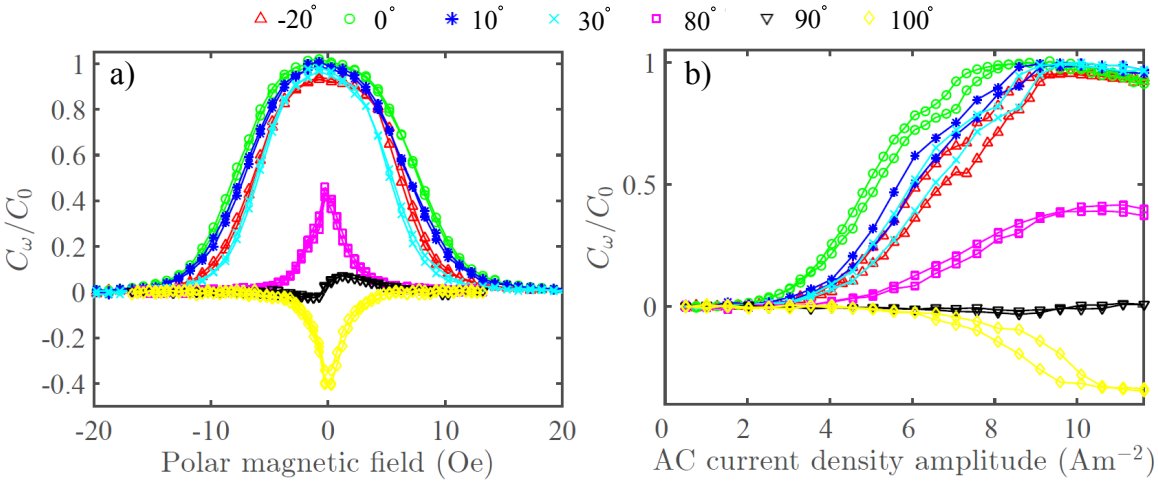

Figure 5.20: a) Polar field sweeps where a constant field of 50 Oe was applied in-the-plane of the film and at different angles θ. The AC current density amplitude was $10^{11}\mathrm{Am}^{-2}$ for all measurements. b) AC current density amplitude sweeps measured with the in-plane field applied at different angles θ relative to the current. No polar field was applied.

to lower fields as θ is increased. In the case of the constant in-plane field applied along $\theta = 80°$, 90° and 100° sweeps, even with no polar field, CIMR does not take place. At this point the slopes overlap and the shape of the data changes. Again, as expected with $\vec{\boldsymbol{H}}_{\mathrm{DL}}$ being the dominant mechanism, there is a sign change above $\theta = 90°$.

Likewise, the AC current density amplitude was swept with a constant in-plane field applied at different azimuthal angles θ, but with no out-of-plane field. This is shown in Fig. 5.20 b). The signal rises with AC current density amplitude until it reaches saturation where full CIMR occurs. The rate of this rise decreases as θ increases from zero. There is some hysteresis in the current sweeps, this could be due to Joule heating, which is evidenced by the downward turn of the saturated region at the highest AC current density amplitudes.

The $\theta = 90°$ AC current density amplitude sweep is a flat line. $\vec{\boldsymbol{H}}_{\mathrm{FL}}$ should have a dependence on the current amplitude, so this is strong evidence that the features in the perpendicular ($\phi = 90°$) and transverse in-plane field sweeps ($\theta = 90°, \phi = 0°$) shown in Fig. 5.19 a) and Fig. 5.20 a) are in fact measurement artefacts associated with the swept field. This provides further evidence that $\vec{\boldsymbol{H}}_{\mathrm{FL}}$ is not present in this sample. For current density amplitude sweeps above 90° the sign is reversed because the component of the constant in-plane field parallel to the current flow (and therefore probing $\vec{\boldsymbol{H}}_{\mathrm{DL}}$) reverses

when θ passes through 90°. In the final part of this section, the contribution from the Oersted field is discussed in the context of the previous measurements, which so far has been disregarded.

5.5.6 The contribution from the current induced Oersted field

When a current is passed through a wire, a magnetic field is created around that wire which is referred to as the Oersted field. Here, this field would be present alongside the SOTs. The Oersted field can be calculated using the Biot-Savart law, and by assuming the length and width are infinite, as well as a uniform current distribution, the simplified form [170]

$$H_{\mathrm{Oe}} = \frac{2\pi j_{\mathrm{e}}}{10^3}\left(\left|z - \frac{l_z}{2}\right| - \left|z + \frac{l_z}{2}\right|\right) \tag{5.5.4}$$

can be used to calculate the in-plane Oersted field, H_{Oe}, at some position z through a film with a thickness l_z.

Using equation (5.5.4), a H_{Oe} = 6 Oe was calculated for the sample geometry using a current density of $14{\times}10^{10}\mathrm{Am}^{-2}$. This is significantly smaller than the values found for $|\vec{\boldsymbol{H}}_{\mathrm{DL}}|$ and is significantly smaller than H_{c} = 30 Oe. Furthermore, the symmetry of the H_{Oe} is the same as that for $\vec{\boldsymbol{H}}_{\mathrm{FL}}$ and hence would have an angular dependence that is maximum at 90° to the current flow. The Oersted field therefore cannot explain the CIMR observed in the Pt/Co/Pt sample.

In summary, CIMR has been observed in a symmetric Pt/Co/Pt structure due to $\vec{\boldsymbol{H}}_{\mathrm{DL}}$. This was achieved by engineering the sample structure to ensure it had a small H_{k} as well as having dissimilar thickness of Pt above and below the Co. No measurable $\vec{\boldsymbol{H}}_{\mathrm{FL}}$ was observed consistent with the requirement of SIA for the Rashba effect.

5.6 Spin-orbit torques in a weak PMA system with inversion asymmetry

As an extension to this study, a Pt (3 nm)/Co (0.6 nm)/MgO (2 nm)/Pt (1.5 nm) multilayer was fabricated. Here it was expected that the MgO layer would isolate the top Pt layer from the Co. Consequently the SOT would arise from the buffer Pt layer. The MgO layer also

introduces the SIA required for the Rashba effect. However, after measuring this sample it became apparent that the applied currents used to induce the SOTs modified the sample causing the PMA to be weakened.

In Fig. 5.21 a) the change in hysteresis after the application of an AC current density amplitude of 5×10^{10} Am^{-2} is shown. The PMA is dramatically weakened by the application of the current, after which the remanence is significantly reduced. This is further demonstrated in Fig. 5.21 b) where the AHE was measured for magnetic fields applied predominantly in-plane with a small out-of-plane component ϕ. Here, the Hall resistance increases with ϕ, demonstrating that the magnetisation must be orienting with a component in-plane. It is still easiest to orient the magnetisation out-of-plane, as demonstrated by the $\phi = 90°$ measurement. However, when the field is removed the sample does not maintain the perpendicular magnetisation.

In Fig. 5.22, the magnetisation as a function of an in-plane applied magnetic field is shown. The data has been fitted with a Langevin function which assumes zero remanence and hence also that the in-plane field direction is a magnetic hard axis. From the best fit with a Langevin function, it was found that 95% of the magnetisation is oriented in-plane with an in-plane field of 1700 Oe. The extracted magnetisation from the SQUID-VSM measurement was (184 ± 8) emu/cm^3, which is substantially smaller than the bulk value for Co of 1400 emu/cm^3.

Since the sample does not have a clearly defined anisotropy, the interpretation of the

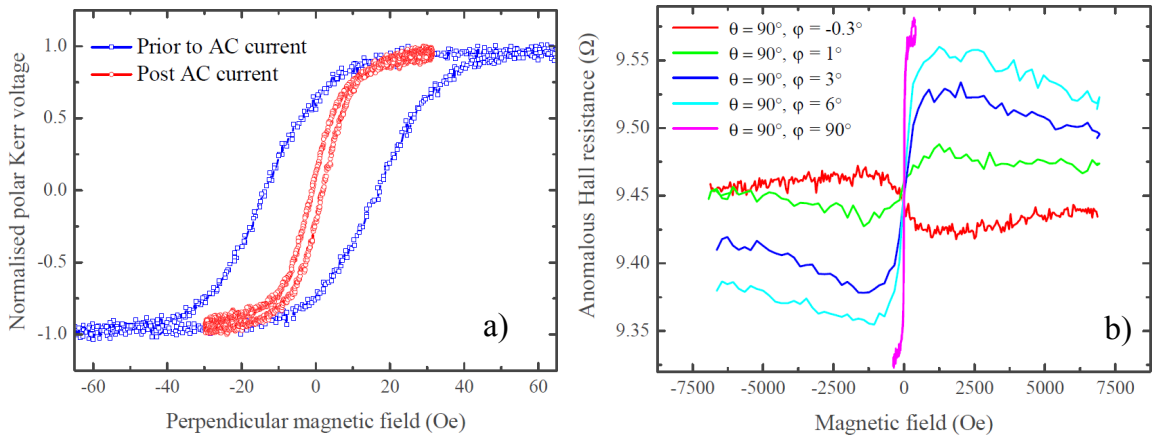

Figure 5.21: a) Normalised polar MOKE hysteresis loops measured prior to and post application of an AC current of 5×10^{10} Am^{-2} . b) Anomalous Hall resistance measured as a function of magnetic fields applied predominantly in-plane but with small offsets in the polar angle ϕ. AHE measurements were made at the University of Leeds with the assistance of Dr. P. M. Shepley.

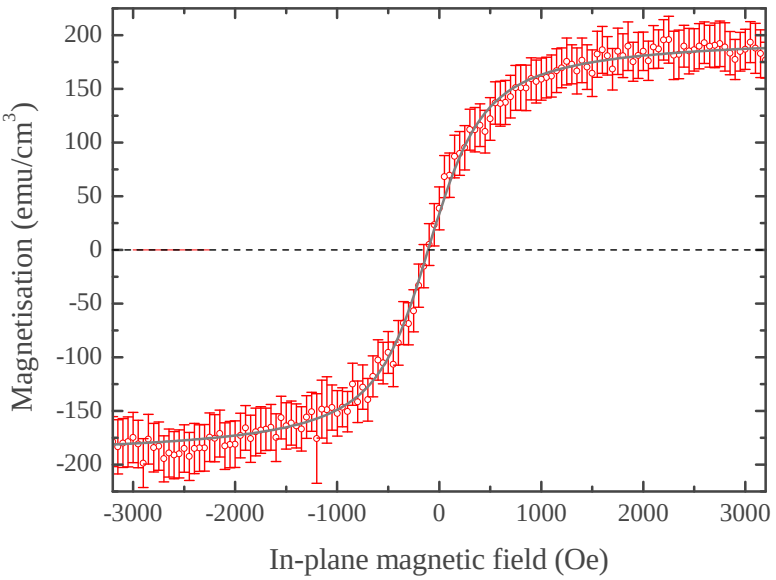

Figure 5.22: Magnetisation as a function of an in-plane magnetic field measured using the SQUID-VSM at the University of Leeds with the assistance of Dr. P. M. Shepley. The solid line shows a fit made using a Langevin function.

SOT measurements is challenging. However, it is still useful to discuss the following measurements since they demonstrate some interesting features.

5.6.1 Contribution of damping-like and field-like SOTs

It would be expected that the MgO will introduce SIA and result in a measurable contribution from $\vec{H}_{\mathrm{FL}}$. To investigate this, the angular dependence of C_ω/C_0 was measured for in-plane magnetic fields applied at increasing angle θ.

Consider first the $\theta = 0°$ measurement shown in Fig. 5.23 a), which probes $\vec{H}_{\mathrm{DL}}$ only. Contrary to the Pt/Co/Pt sample, the dependence is linear with longitudinal magnetic field. This indicates that there is no CIMR, but instead a linearly increasing magnitude of magnetisation oscillation with field. Furthermore, at $\theta = 0°$ the slope has the opposite gradient to the Pt/Co/Pt sample, which indicates that $\vec{H}_{\mathrm{DL}}$ acts in the opposite direction for this Pt/Co/MgO/Pt sample. In the Pt/Co/Pt the dominant source of spin-current was from the top Co/Pt interface, hence this suggests that the MgO is reducing the spin-pumping from the top Pt layer and the dominant source of spin-current from this sample is from the buffer Pt/Co interface.

As was the case for the Pt/Co/Pt sample, the slope of the C_ω/C_0 data decreases as the field sweeps were measured at increasing angle θ. This continues as far as $\theta = 90°$, above

which the SOT recovers but the slope has the opposite sign. As before, the change in sign occurs because the polarity of the positive and negative current flow is reversed with respect to positive and negative longitudinal field directions when θ passes through 90°.

Again, using equation (5.4.1) the effective SOT was extracted from the slope of the field sweeps as a function of angle θ and is plotted in Fig. 5.23 b), and fitted with effective

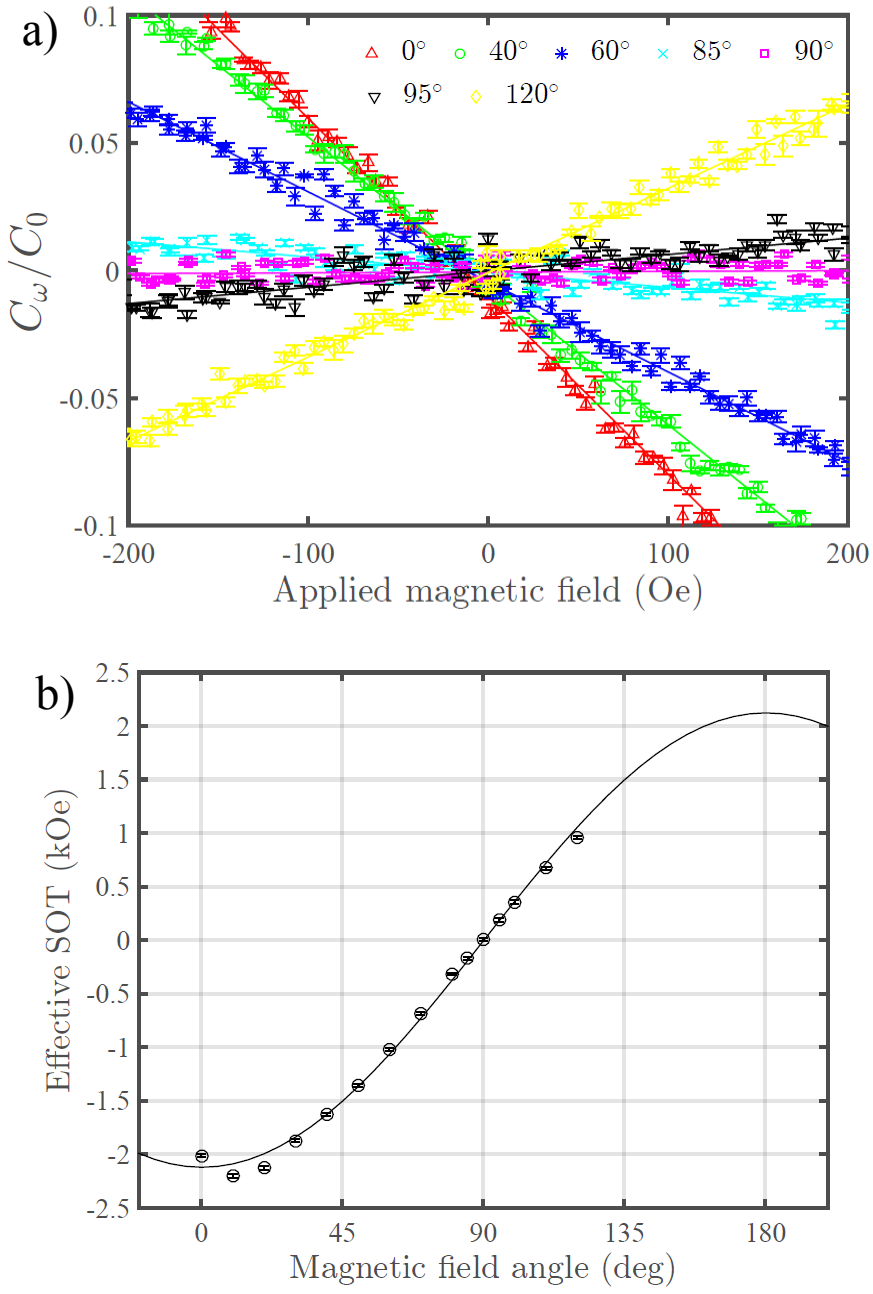

Figure 5.23: a) First harmonic measured as a function of applied in-plane magnetic field at different angles θ. An AC current density amplitude of 10^{11} Am^2 was used for all magnetic field sweeps. b) Effective SOT as a function of the angle being the applied field and current. The solid line denotes a best fit using effective SOT = $|\vec{H}_{\mathrm{DL}}|\cos\theta + |\vec{H}_{\mathrm{FL}}|\sin\theta$

SOT = $|\vec{H}_{\mathrm{DL}}|\cos\theta + |\vec{H}_{\mathrm{FL}}|\sin\theta$. It was found from the SQUID-VSM measurement (see Fig. 5.22) that 95% of the magnetisation was oriented in-plane with a field of 1700 Oe and here this has been used as a rough estimate of H_{k}. However, since this sample lacks a well defined anisotropy, the actual values of the effective SOT have limited meaning, but are shown only for the comparison of the relative magnitudes of $\vec{H}_{\mathrm{DL}}$ and $\vec{H}_{\mathrm{FL}}$.

There is reasonable agreement between the best fit and the experimental data and the fit gives values of $\vec{H}_{\mathrm{DL}} = (2.12 \pm 0.07)$ kOe and $\vec{H}_{\mathrm{FL}} = (0 \pm 0.05)$ kOe at 10^{11} Am^{-2}. The data passes smoothly through zero at $\theta = 90°$ indicating that the magnitude of $\vec{H}_{\mathrm{FL}}$ is at least smaller than the resolution of the experiment, which for this sample, is a current-induced field of 0.15 kOe. This is the current-induced field that produces a 1% increase in C_ω/C_0 with the application of a 200 Oe in-plane external magnetic field. Thus these measurements suggest that the field-like torque is not present in this system.

In this system the MgO layer should introduce SIA and allow for a measurable $\vec{H}_{\mathrm{FL}}$ arising from the Rashba effect [22,162,164,169]. This was not observed, which may imply that the damage to the sample from the applied current has modified the MgO layer and disrupted the SIA. However, the sizeable $\vec{H}_{\mathrm{DL}}$ would suggest that the MgO is capable of disrupting the spin-pumping from the top Pt layer and should therefore be inducing some degree of asymmetry to the structure. However, since the buffer and top Pt thickness are different in this sample, the situation is further complicated as the contribution from the SHE from each Pt layer is therefore not necessarily symmetric.

5.6.2 Extraction of the damping-like field by applying DC offsets

For this sample, when the longitudinal magnetic field was swept C_ω/C_0 demonstrated a linear dependence on the field. Interestingly, it was also found that by sweeping a DC offset applied to the AC current, a similar linear dependence of C_ω/C_0 was observed without the use of any external magnetic fields, rather by sweeping the effective field due to the SOT. This linear dependence of C_ω/C_0 on the DC offset is shown in Fig. 5.24 a). Furthermore, a single conversion factor can be used, which maps the DC offset data onto the longitudinal field sweep data. This factor was found by taking the ratio of the gradient of the DC offset sweep data to the gradient of the longitudinal field sweep data. This gave a conversion factor of $(-39 \pm 1)\times10^{-10}$ Oe/Am^{-2}. In Fig. 5.24 b) the DC offset sweep data shown

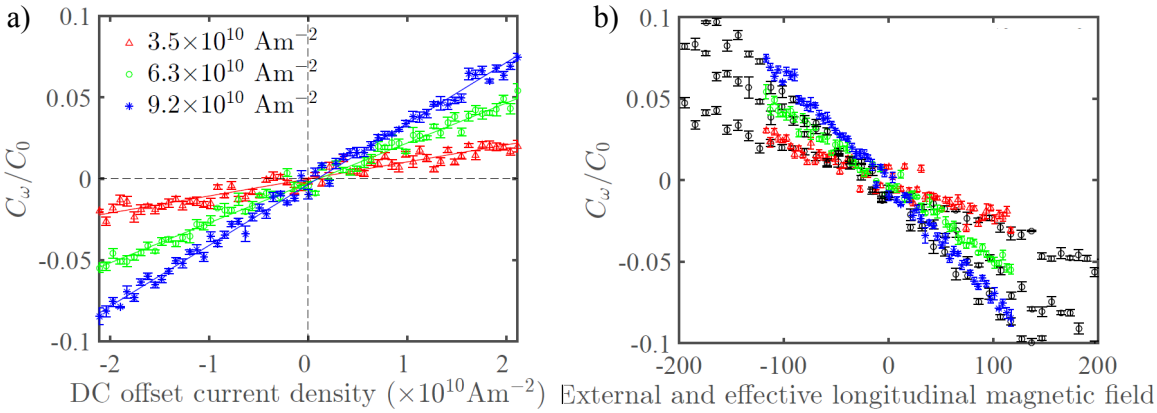

Figure 5.24: a) First harmonic lock-in voltage measured as a function of the DC offset applied to three different AC current density amplitudes. b) The DC offset sweeps converted into effective fields using the SOT efficiency of -39×10^{-10} Oe/Am^{-2}. The longitudinal field sweep data performed at the corresponding AC current density amplitude are shown underneath in black. The same legend for AC current density amplitude applies.

in Fig. 5.24 a) has been multiplied by this factor to convert the DC current density into effective longitudinal fields and demonstrates how a single conversion factor is sufficient to map all DC offset datasets onto the respective longitudinal field sweep data.

It is important to note that sweeping the DC offset does not allow for the measurement to single out $\vec{\boldsymbol{H}}_{\mathrm{DL}}$ or $\vec{\boldsymbol{H}}_{\mathrm{FL}}$. However, since the angular dependence demonstrated that $\vec{\boldsymbol{H}}_{\mathrm{FL}}$ is much smaller than the experimental resolution it can be assumed that in this particular system these DC offset sweeps represent $\vec{\boldsymbol{H}}_{\mathrm{DL}}$ only.

The conversion factor represents the term, $|\vec{\boldsymbol{H}}_{\mathrm{DL}}|/j_{\mathrm{e}}$. If it is assumed that $\vec{\boldsymbol{H}}_{\mathrm{DL}}$ arises from the spin Hall effect, using $|\vec{\boldsymbol{H}}_{\mathrm{DL}}|/j_{\mathrm{e}} = 39\times10^{-10}$ Oe/Am^{-2}, it is possible to calculate the spin-Hall angle from [160];

$$\frac{|\vec{\boldsymbol{H}}_{\mathrm{DL}}|}{j_{\mathrm{e}}} = \frac{\hbar\theta_{\mathrm{SH}}}{2|e|M_{\mathrm{s}}t_{\mathrm{FM}}}\,. \tag{5.6.5}$$

For $M_{\mathrm{s}} = 184$ emu/cm^3 and $t_{\mathrm{FM}} = 0.6$ nm, we obtain $\theta_{\mathrm{SH}} = 0.13 \pm 0.06$, which is comparable to those found elsewhere in the literature [13, 74, 81, 160]. This demonstrates that through this self calibration method, whereby the DC offset sweeps were matched to the longitudinal magnetic field sweeps, provides a method by which the spin-Hall angle can be extracted. Since it is self calibrated from the magnetic field sweeps, it does not require the values of M_{s} or H_{k}. However, it relies on two underlying assumptions: that there is one dominant SOT, since the method can not separate $\vec{\boldsymbol{H}}_{\mathrm{DL}}$ and $\vec{\boldsymbol{H}}_{\mathrm{FL}}$, and also that in the region

of the DC offsets used, the SOT behaves in a manner comparable to the external magnetic field i.e. it does not rotate with the magnetisation. This second assumption is invalid for $\vec{H}_{\mathrm{DL}}$ when CIMR is observed, since $\vec{H}_{\mathrm{DL}}$ rotates with the magnetisation, but is reasonable for small magnetisation oscillations as observed with the Pt/Co/MgO/Pt sample.

5.7 Chapter conclusions

In this chapter SOTs have been investigated in systems with in-plane magnetic anisotropy and out-of-plane magnetic anisotropy. For the NiFe/Pt bilayer system with in-plane magnetic anisotropy, the SOTs were studied through the simultaneous measurement of the longitudinal MOKE and PHE. The key result from this was the observation of current-assisted in-plane magnetisation reversal as measured through the PHE.

The investigation into systems with PMA employed the polar Kerr effect, which provides an all optical approach to characterising SOTs. SOTs were studied as a function of in-plane magnetic fields. The contributions of $\vec{H}_{\mathrm{DL}}$ and $\vec{H}_{\mathrm{FL}}$ could be separated by applying the in-plane field longitudinal or transverse to the current flow respectively.

A Pt/Co/Pt multilayer which had weak PMA was fabricated in order to investigate how magnetic anisotropy influenced the response of the magnetisation to the SOTs. With the much weaker H_{k} in this sample, it was possible to obtain CIMR and the dependence of the switching current was analysed as a function of in-plane magnetic fields, perpendicular magnetic fields and AC current density amplitude. It was found that the CIMR was more effective at higher AC current density amplitudes, consistent with the increasing SOT. A longitudinal magnetic field was always required to induce CIMR and increasing the magnitude of this reduced the critical switching current. The angular dependence of the in-plane field was also investigated, and there was no evidence for the existence of $\vec{H}_{\mathrm{FL}}$. Since this multilayer lacks SIA, this result is consistent with the Rashba effect as the origin of $\vec{H}_{\mathrm{FL}}$.

A Pt/Co/MgO/Pt multilayer with weak PMA was also fabricated in order to compare a sample with SIA. However, the sample showed evidence of degradation after the application of current. Again, $\vec{H}_{\mathrm{FL}}$ could not be measured, but this result is treated with some caution since it is possible the sample degradation was due to damage to the MgO barrier after the application of current. However, an appreciable $\vec{H}_{\mathrm{DL}}$ could be measured in this

sample. Interestingly, the longitudinal field sweep measurements of C_ω/C_0, which probe $\vec{H}_{\mathrm{DL}}$, could be reproduced by sweeping a DC offset that was applied to the AC current, without the need for an external magnetic field. From these measurements a conversion factor of $|\vec{H}_{\mathrm{DL}}|/j_{\mathrm{e}} = -39 \times 10^{-10}$ Oe/Am^2 was found which gave a $\theta_{\mathrm{SH}} = 0.13 \pm 0.06$.

6 Investigating the lengthscale of the induced moment in Pt through the addition of Au and Ir spacer layers

6.1 Introduction

When Pt is deposited adjacent to a ferromagnet, a spontaneous magnetic polarisation of the Pt arises at the interface that persists through the first few atomic layers of Pt [40,171–175]. This proximity induced magnetism (PIM) in Pt is associated with the large Stoner factor associated with higher-*d* transition elements, similarly, Pd has also been shown to exhibit a large induced moment when placed in proximity to a ferromagnet [41, 176].

Some of the earliest indications of PIM came from the enormous moments measured in FePd alloys [46,47]. Here the moment was too large to be accounted for by the itinerant ferromagnetism of Fe alone and the ferromagnetism persisted down to Fe concentrations as low as 1.25 at.% [46].

With the observations of perpendicular magnetic anisotropy in Pd/Co [37, 177] and Pt/Co multilayers [178,179] the role of interfacial PIM became of great interest with regard to these phenomena [180, 181].

Furthermore, the development of x-ray magnetic circular dichroism (XMCD) [117] opened up a method by which PIM could be measured directly. One of the first uses of XMCD was to study PIM in Pt/Co multilayers, which showed that there existed undoubtedly a significant induced moment in Pt [182, 183]. Subsequently numerous other studies using XMCD confirmed the existence of some degree of PIM across the entirety of the 5*d* transition elements, either in thin film multilayers or impurities in a ferromagnetic ma-

trix [40, 53, 174, 184–188].

These higher-*d* transition metals such as Ta, Ir, Pd and in particular Pt also have a history of use in magnetic heterostructures due to their large spin-orbit interaction. Recently, they have found considerable use in investigating the spin-Hall effect [189], Rashba effect [22, 164] and the Dzyaloshinskii-Morriya interaction (DMI) [44, 190].

Clearly the role of PIM must be considered with respect to these spin-orbit phenomenon. A recent study which measured the temperature dependence of $Ni_{80}Fe_{20}$/Pd and $Ni_{80}Fe_{20}$/Pt bilayers, as well as first principle calculations, suggested that PIM was detrimental to the spin-Hall effect [98].

Studies into the DMI by Ryu *et al.* [21, 55], within the group of S. S. P. Parkin, have provided compelling evidence for a strong association of PIM with DMI. However, *ab-initio* calculations conflict with this, suggesting that the role of PIM is negligible with regard to DMI [56].

Fundamental to the experiments of Ryu *et al.* [55] was the use of interface engineering in which ultrathin Au spacer layers were used to modify the PIM. However, there was no direct measurement of the PIM in these experiments only an inferred relationship with DMI from domain wall velocity measurements and spacer layer thickness.

In the literature, spacer layers have been used to separate the ferromagnetic layer from Pt when attempting to rule out PIM [55, 98, 191]. However, the lengthscale of this is based on existing measurements of the PIM lengthscale within the Pt, with a value of approximately the order of 10 Å [40]. To the best of one's knowledge, no studies exist where the Pt PIM was characterised as a function of spacer layers, where the contributions of interface morphology, alloying and the choice of spacer layer could potentially change the lengthscale of the interaction. There is therefore a need for a study by which the evolution of the PIM is measured directly and as a function of spacer layers. In particular a technique capable of measuring the PIM whilst simultaneously characterising the morphology.

X-ray resonant magnetic reflectivity (XRMR) offers this functionality since it combines the element specificity of XMCD with the depth sensitivity of the x-ray reflectivity technique, allowing depth resolved PIM profiles to be determined [40, 41]. The element specificity allows the measurement of the Pt PIM without the signal being dominated by the ferromagnetic layer. Further details of the technique can be found in chapter 3 and a

review article on XRMR can be found at Ref. [192].

In overview, this chapter concerns the evolution of the PIM as a function of Au and Ir spacer layers inserted between the upper Co/Pt interface in Pt/Co/Pt trilayers with in-plane magnetic anisotropy. The aim was to investigate the lengthscale of the interaction and dependence on sample morphology with respect to each spacer to develop a general understanding of how the Pt couples to the ferromagnetic layer. In chapter 9 this information is used to search for correlations between the PIM and the DMI with reference to the experiments of Ryu *et al.* [21, 55].

6.2 The induced moment in Pt as a function of heavy metal spacer layers

6.2.1 Description of samples and measurements

To investigate the modification of PIM as a function spacer layer (SL) material and thickness, a series of multilayered samples consisting of Pt (54 Å)/Co (25 Å)/SL (1-20 Å)/ Pt (26 Å) were deposited onto thermally oxidized Si (111) substrates by DC and RF magnetron sputtering from a base pressure of order 10^{-8} Torr. For this study the SL was either Au or Ir. There are three reasons for the choice of SL: Au and Ir are positioned on either side of Pt in the periodic table, Ir is fully miscible with Pt [193] whereas Au is not [194], and Ir is expected to take on a moderate PIM itself [184] whereas Au is expected to have a minimal PIM [53]. A basis sample was also made which had no spacer layer.

XRMR was used to measure the depth dependent PIM in these samples as a function of the Au and Ir spacer layer (SL) thickness. Further detail on the experimental technique can be found in chapter 3, but in summary XRMR is measured at grazing incidence using circularly polarised x-rays, whereby the reflected intensity throughout the angular range depends on the sample magnetisation direction. It is a resonant reflectivity technique which combines depth sensitivity obtained from reflectivity with magnetic sensitivity obtained since the x-ray energy is tuned to the resonant edge of Pt. The measurements in this chapter were made at the Pt-L_3 edge to probe the PIM of the Pt.

A limitation of XRMR, which relates to the multilayer sample design, is that it is not

possible to extract absolute magnitudes for induced moments using the sum rules, because the magnetic scattering is correlated with both the resonant scattering factors and the size of the induced interfacial moment. Resonant scattering factors can be obtained from neutron scattering or XMCD and inserted as a constant in the fitting procedure. However, in this investigation an alternative approach was used. Here, it was assumed that the PIM in the buffer Pt layer would be the same for all spacer layers (SLs). Hence, this could be used as a normalisation layer in the analysis, thus dividing the PIM in top Pt layer by that in the buffer Pt layer allowed comparison between samples as a function of the SL thickness. The buffer Pt layer acts as a control in each sample, measuring the change in PIM in the top Pt layer relative to it.

The XRMR measurements for the Au and Ir SLs were performed on the XMaS beamline at the ESRF over two separate beam-time experiments. The Pt-L_3 resonance was found at 11.564 keV in the first beam-time run and 11.562 keV in the second series. The sample with no SL was measured in both runs for comparison.

Crucially from the XRMR measurement, the spin-asymmetry ratio was calculated and is discussed in the next section.

6.2.2 X-ray resonant magnetic reflectivity measurements

The spin-asymmetry ratio, R_a, contains all the structural and magnetic depth dependent information for the sample. It is defined as

$$R_\mathrm{a} = \frac{I^+ - I^-}{I^+ + I^-} \tag{6.2.1}$$

where I^+ is the scattered intensity of circularly polarised light whilst the sample is saturated under an in-plane positive magnetic field and I^- is the equivalent under negative magnetic field. The helicity of the light could be reversed instead of the magnetic field, but in practice it is faster to switch the magnetisation, and this was done in these measurements. The spin-asymmetry ratio, R_a, is calculated at every point along the specular reflectivity curve by reversing the sample magnetisation repeatedly throughout the measurement.

The specular reflectivity and spin-asymmetry, both measured at the Pt-L_3 edge for the basis Pt/Co/Pt sample are shown in Fig. 6.1. The spin-asymmetry was measured with both light helicities as a function of the scattering angle, 2θ. It can be seen that by reversing the helicity of the polarised light, the spin asymmetry switches sign. This occurs because reversing the helicity changes the sign of the momentum for the incoming photon.

Both specular reflectivity and spin asymmetry were fitted simultaneously in order to obtain the best fitting solution that represents the structure and Pt moment of the sample. The fits were made using the GenX software [116], which employs a Parratt recursive method to simulate the data, described in chapter 3, and both fits are shown in Fig. 6.1.

For this sample the resonant scattering factors were allowed to vary in the fitting procedure. The factors extracted from this fit were then used as fixed values in the subsequent

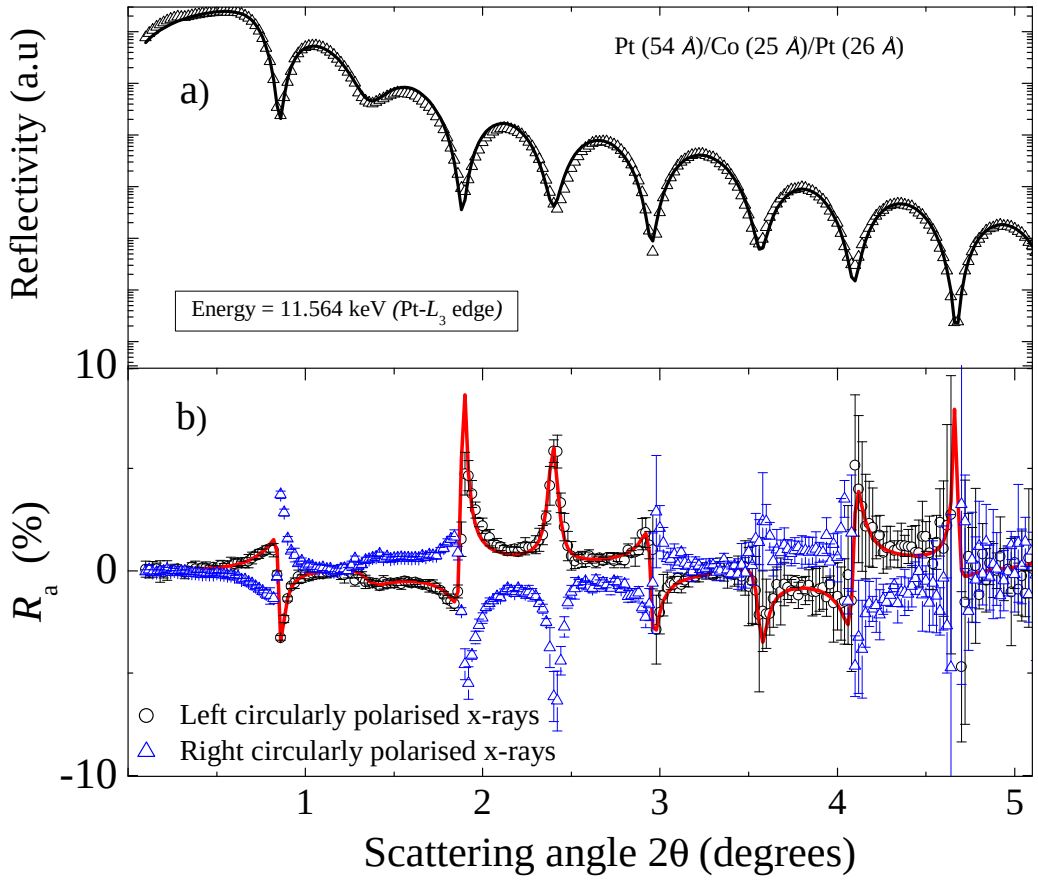

Figure 6.1: a) Specular reflectivity measured at the Pt-L_3 edge for the basis sample Pt (54 Å)/Co (25 Å)/Pt (26 Å). The solid line denotes the best fit. b) The spin asymmetry ratio, R_a, as the function of the specular scattering angle using left circularly polarised x-rays and using right circularly polarised x-rays. The solid red line denotes the best fit.

fits where a SL existed.

Both specular reflectivity, spin asymmetry and the best fitting models for all of the samples with Au and Ir spacer layers are shown in Fig. 6.2. It can be seen that the simulations agree well with the data. From the R_a measurements of both datasets there is evidence that the magnitude of the asymmetry peaks are decreasing with increasing SL thickness. This indicates that the total signal of polarised Pt is decreasing with increasing SL thickness.

The layer thickness, t, and interface width, σ, extracted from the best fitting simulations are shown in Table 6.1 for the Au SL samples and Table 6.2 for the Ir SL samples. Note that σ contains both topological roughness and chemical intermixing. In all cases the error has been rounded up to 1 Å since a sub-angstrom layer thickness variation would be non-

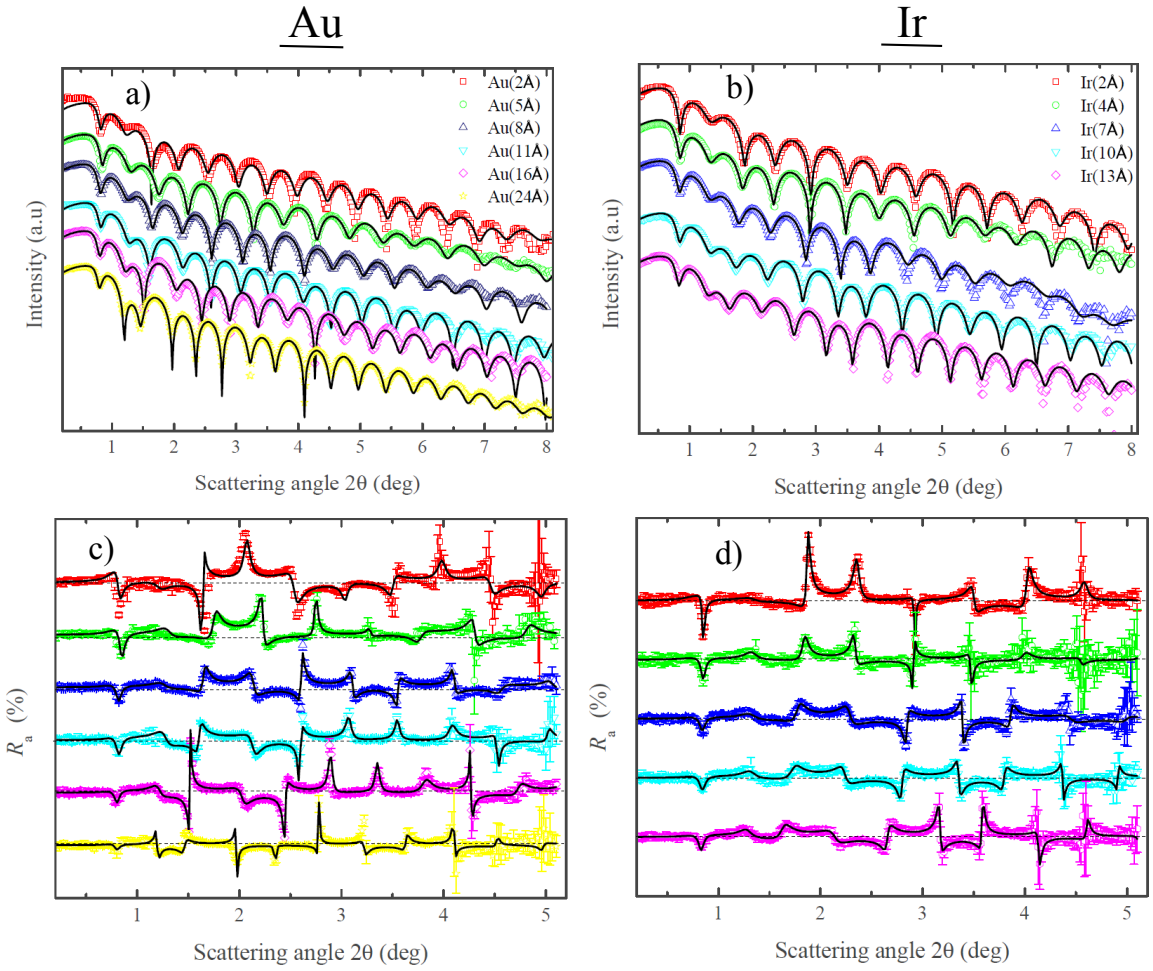

Figure 6.2: Specular reflectivity for Pt/Co/SL/Pt samples with different thickness of a) Au SLs and b) Ir SLs. Spin asymmetry for Pt/Co/SL/Pt samples with different thickness of c) Au SLs and d) Ir SLs. All datasets have been offset vertically in order to allow them to be plotted on the same figure. The solid lines show the best fits to the data. For the samples with Au SLs the Pt-L_3 edge found at 11.564 keV, whereas for the Ir SL samples the Pt-L_3 edge found at 11.562 keV.

Sample	Pt		Co		Au		Pt	
	t (Å)	σ (Å)	t (Å)	σ (Å)	t (Å)	σ (Å)	t (Å)	σ (Å)
No SL	52 ± 1	4 ± 1	24 ± 1	4 ± 1	0 ± 1	0 ± 1	25 ± 1	5 ± 1
Au (2 Å)	58 ± 1	7 ± 1	28 ± 1	6 ± 1	2 ± 1	5 ± 1	27 ± 1	6 ± 1
Au (5 Å)	57 ± 1	5 ± 1	20 ± 1	5 ± 1	3 ± 1	6 ± 1	27 ± 1	8 ± 1
Au (8 Å)	57 ± 1	5 ± 1	25 ± 1	5 ± 1	6 ± 1	8 ± 1	24 ± 1	9 ± 1
Au (11 Å)	57 ± 1	4 ± 1	25 ± 1	5 ± 1	16 ± 1	6 ± 1	22 ± 1	9 ± 1
Au (24 Å)	56 ± 1	6 ± 1	25 ± 1	6 ± 1	24 ± 1	5 ± 1	24 ± 1	7 ± 1

Table 6.1: Extracted layer thickness, t, and interface widths, σ from the best fitting simulations to the specular reflectivity shown in Fig. 6.2 a).

Sample	Pt		Co		Ir		Pt	
	t (Å)	σ (Å)	t (Å)	σ (Å)	t (Å)	σ (Å)	t (Å)	σ (Å)
No SL	51 ± 1	4 ± 1	24 ± 1	4 ± 1	0 ± 1	0 ± 1	22 ± 1	5 ± 1
Ir (2 Å)	54 ± 1	4 ± 1	21 ± 1	3 ± 1	5 ± 1	6 ± 1	22 ± 1	7 ± 1
Ir (4 Å)	53 ± 1	6 ± 1	23 ± 1	6 ± 1	5 ± 1	6 ± 1	24 ± 1	7 ± 1
Ir (7 Å)	54 ± 1	5 ± 1	23 ± 1	6 ± 1	7 ± 1	6 ± 1	23 ± 1	7 ± 1
Ir (10 Å)	54 ± 1	5 ± 1	24 ± 1	6 ± 1	10 ± 1	5 ± 1	21 ± 1	9 ± 1
Ir (13 Å)	57 ± 1	4 ± 1	23 ± 1	6 ± 1	13 ± 1	5 ± 1	24 ± 1	7 ± 1

Table 6.2: Extracted layer thickness, t, and interface widths, σ from the best fitting simulations to the specular reflectivity shown in Fig. 6.2 b).

physical.

The values of σ and t of the Pt and Co layers are comparable between samples. Generally the top Pt layer has a slightly larger σ as a result of the SL. The two measurements of the sample with no SL give consistent structural parameters from both beam-time experiments.

For the SLs, the similarity between the scattering lengths for Pt, Au and Ir make it very difficult to distinguish reliably between these layers when the SL is below 10 Å in thickness. Above this thickness the measured SL thickness converges to the nominal SL thickness shown in the far left column. From this it can be concluded that the sputtering growth rate calibrations are correct, and form a more reliable measure of the SL thickness. The interface width is approximately 6 Å for all SLs, demonstrating that the two thinnest SL samples from the Au and Ir sample series can be considered as discontinuous layers.

Magnetic roughness, magnetic thickness, and magnetic moment parameters were also included in the model. These, alongside the structural parameters, characterise the interfa-

cial Pt moment and were used to produce the best fits to the spin asymmetry data. However, these parameters are strongly correlated, so various combinations of values can produce the same fit. The values of magnetic roughness, thickness and moment are therefore not unique and may be unreliable.

In the simulations the purpose of these parameters is to produce the scattering length density profiles. These are described in detail in chapter 3, but they can be considered as cross-sections through the samples. The structural scattering length density (sSLD) profiles represent the physical structure of the samples, and reflect the values of the interface widths and the layer thicknesses. The magnetic scattering length density (mSLD) profiles represent the depth dependent PIM in Pt throughout the samples. Although the magnetic fitting parameters themselves were variable, they produced a consistent mSLD for the best fits, and hence describe the same distribution of Pt induced moment throughout the sample.

6.2.3 Scattering length density profiles with variable spacer layer thickness

Both sSLD and mSLD profiles extracted from the Au SL samples as well as that for the basis sample with no SL are shown in Fig. 6.3. The SLDs for the Ir SL samples are shown in Fig. 6.4.

Looking first at the sSLD for the sample with no SL, see Fig. 6.3 a), the plateaux correspond to each layer and how far they extend is dictated by the layer thickness. Schematic shading of the layers has been superimposed onto all of the sSLD profiles as colour coded blocks to make this clearer. Increased interface width, σ, causes the slopes between the layers to become shallower, extending further into the adjacent layer. The height of each plateau is representative of the material in the layer, since it depends on the electron density and scattering factors unique to the material.

The magnetic scattering length density (mSLD) shows the distribution of polarised Pt throughout the sample. The mSLD is coupled to the sSLD, since the physical roughness as well as the magnetic roughness influence the shape of the mSLD going from one layer into the next. The mSLD profiles have been normalised, such that the height of the buffer Pt mSLD peak is the same for all mSLD profiles. This is a reasonable assumption for the PIM in the buffer Pt, and allows comparison between samples as it excludes variations in

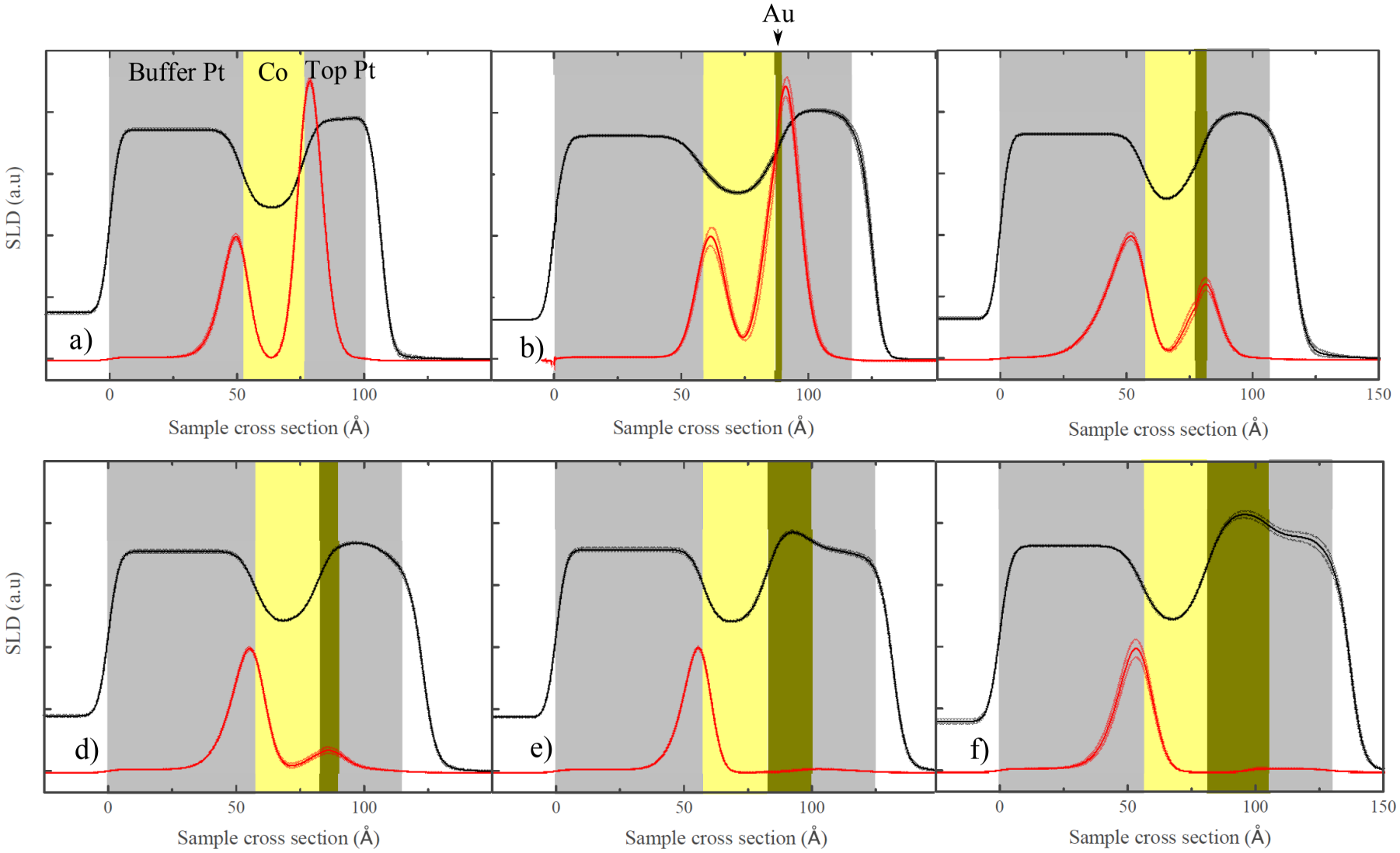

Figure 6.3: The extracted sSLD (black) and mSLD (red) profiles for a) no SL, b) Au (2 Å), c) Au (5 Å), d) Au (8 Å), e) Au (11 Å) and f) Au (24 Å). The lighter black and red curve above and below the SLD profiles show the ± one standard deviation SLD profiles used in the error analysis. The SLD profiles have been normalised such that the buffer Pt layer mSLD peak is always the same height between samples. These samples were measured at the first beam-time, at an energy of 11.564 keV.

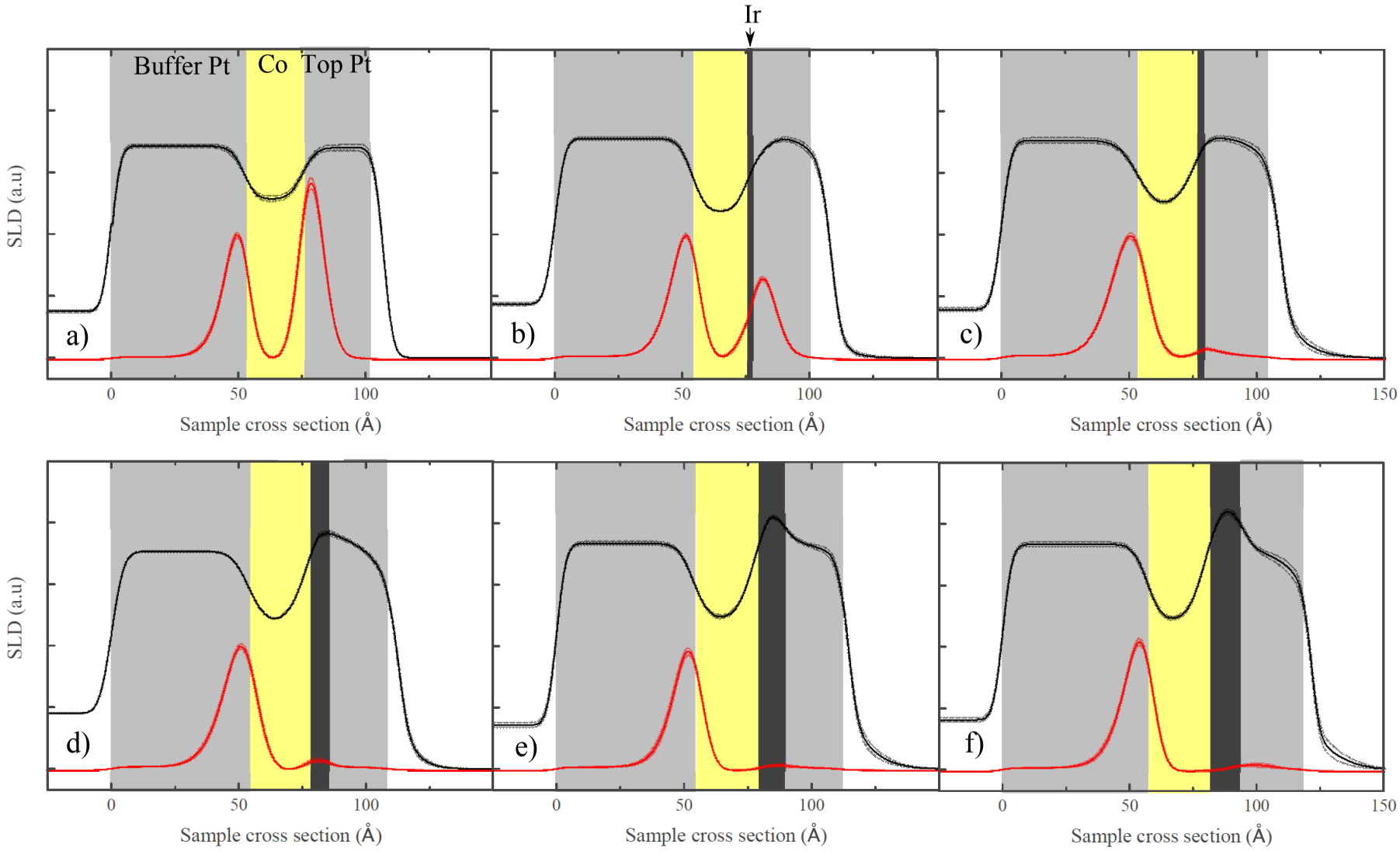

Figure 6.4: The extracted sSLD (black) and mSLD (red) profiles for a) no SL, b) Ir (2 Å), c) Ir (4 Å), d) Ir (7 Å), e) Ir (10 Å) and f) Ir (13 Å). The lighter black and red curve above and below the SLD profiles show the ± one standard deviation SLD profiles used in the error analysis. The SLD profiles have been normalised such that the buffer Pt layer mSLD peak is always the same height between samples. Samples measured at second beam-time, at an energy of 11.562 keV.

experimental measurement.

For the sample with no SL, the total moment of the polarised Pt above the Co is larger than for the buffer Pt layer. This was measured on both beam-time experiments and this difference in the PIM is reproduced in both Fig.6.3 a) and Fig.6.4 a) from the first and second beam-time experiments respectively. PIM is intimately linked to interface morphology [195, 196], hence it is possible that the observed difference in Pt moment could be attributed to different interfacial structures for the Pt/Co and the Co/Pt interfaces, which arise due to the differences between depositing Co onto Pt and vice versa [197]. However, the interface widths for the Pt/Co and Co/Pt interfaces extracted from the fits, shown in Table 6.1, are both 4 Å. In a tomographic atomic probe study of Pt/Co multilayers it was found that a greater degree of intermixing occurred at the top Co/Pt interface compared to the bottom Pt/Co interface [197]. It is possible that this is present within this sample also, since the contribution of chemical intermixing and topological roughness cannot be separated from the interface width using XRR alone. A greater degree of intermixing at the Co/Pt interface would agree with the observed mSLD profiles, since it is known that intermixing at the ferromagnet interface can give rise to enhanced proximity induced moments [196].

Comparing the two extracted mSLD profiles for the sample with no SL, there is disagreement in the magnitude of the top Pt PIM relative to the buffer Pt PIM. The origin of this discrepancy is not clear, it may be a result of the slight difference in energy used, though this seems unlikely, or possibly a variation in the degree of circular polarisation between the experiments. Alternatively the sample may have deteriorated between the two beam-time experiments. However, it is shown later that this discrepancy is not important for the overall SL thickness dependence of the PIM.

The effect of adding the Au spacer layers is shown in Fig. 6.3 b)-f) and Ir spacer layers in Fig. 6.4 b)-f). Looking first at the effect of the addition of Au SLs on the sSLD. This causes a rounding of the top of the Pt sSLD plateau due to increased interfacial width between Co, Au and Pt. As the Au SL becomes thicker than 10 Å (Figs. 6.4 e),f)), a pronounced peak in the sSLD is observed and the Au thickness can be resolved more definitively.

It can be seen in Fig. 6.3 b) that a Au (2 Å) SL has little effect on the induced moment.

Contrary to this, Fig. 6.4 b) shows that the Pt PIM was greatly modified by the insertion of an Ir (2 Å) SL. Pt-Au phase diagrams show a large miscibility gap for alloys composed primarily of Pt [194], whereas Pt-Ir alloys are entirely miscible [193]. This may explain why the moment may be sustained under the Au (2 Å) SL, which would result in island growth of the Au and a slower coverage of the Co/Pt interface. Conversely, Ir would immediately alloy with the Pt, pushing it further from the Stoner criterion. However, Tables 6.1 and 6.2 show that for the Au (2 Å) and Ir (2 Å) SL samples, the interfacial widths of the Co layers and SLs are very similar. As was suggested previously for Co/Pt and Pt/Co interfaces, there may exist a difference in topological roughness and intermixing between the Au and Ir SLs which is not separable in the XRR measurement.

With the addition of thicker Au spacer layers the PIM at the top Pt interface drops dramatically. It can be seen in Fig. 6.3 d) that for the Au (8 Å) sample, the majority of the Pt that is polarised resides inside the Au/Pt interfacial region, which may indicate the presence of polarised islands of Pt in a Au matrix.

Focusing now on the Ir SL samples, the sSLD are similar to those observed with Au, with a pronounced peak forming for Ir SL thicknesses above 10 Å, where the Ir layer begins to be resolved as continuous from the Co and Pt. The mSLD shows a dramatic change with the addition of Ir SLs. A discontinuous Ir (2 Å) SL reduces the top Pt mSLD peak amplitude to below that of the buffer Pt. Further increases in SL thickness then causes the rapid loss of the PIM from the top Pt interface.

In summary, from the difference between the Au (2 Å) and Ir (2 Å) SL samples, the results suggest that the loss of PIM cannot be described as the result of the SL separating the Pt further from the ferromagnetic layer alone, but in fact the morphology and alloying of the interface is crucial to the process. This is further evidenced by the differences in PIM at the Pt/Co and Co/Pt interfaces in the sample with no SL.

In the next section the Pt moment ratio is calculated and the Pt PIM lengthscale is characterised as a function of the SL thickness.

6.3 Investigating the lengthscale of the induced Pt moment

The area under each mSLD peak can be thought of as proportional to the total induced moment at that interface. However, it is not possible to obtain the absolute moments without having measured the resonant scattering factors. The Pt moment ratio was defined to resolve this. This is the ratio of areas under the mSLD peaks for the top Co/Pt interface to the area under the control buffer Pt/Co interface mSLD peak. This does not allow for absolute moments to be extracted, but it does allow comparison between samples measured in the same way since the buffer Pt should be the same irrespective of SL behaviour. The Pt moment ratio as a function of SL thickness is shown in Fig. 6.5 a).

The ratio obtained for the sample with no SL was (1.9 ± 0.2) for the first beam-time experiment with x-ray energy of 11.564 keV and (1.3 ± 0.2) for the second beam-time experiment with x-ray energy of 11.562 keV. These are shown as the two blue triangular data points in Fig. 6.5 a). It is assumed that this discrepancy is due to differences in the experimental conditions, in particular the slight difference between the energies that these measurements were taken at. An attempt to account for this is discussed later.

It appears that the Ir causes the PIM at the top Co/Pt interface to be reduced more rapidly, eradicating the top Pt moment within the error margins for a Ir (4 Å) SL. The Au thickness dependence appears more gradual, with the PIM persisting for a Au (11 Å) SL. Interestingly these lengthscales are much smaller than that observed in a study of $[Pd/Cu/Ni_{81}Fe_{19}/Cu]_{20}$ super-lattices, which measured a Pd polarisation across a Cu (30 Å) spacer layer [187]. This may indicate that in the $Pd/Cu/Ni_{81}Fe_{19}$ system a different mechanism induces the PIM, namely the RKKY interaction mediated by the *s*-electrons of Cu, whereas in this study the PIM is induced by short-ranged interfacial *d*-orbital hybridisation.

The dashed lines are exponential decays fitted to quantitatively characterise the lengthscale of the PIM interaction. For the Au SLs, an exponential decay constant of (2.3 ± 0.4) was found and for the Ir SLs a value of (1.9 ± 0.4) was obtained. These results overlap within the errors, hence it cannot be shown conclusively that Ir causes a more rapid loss of PIM. Both the lengthscales are extremely short, with the PIM vanishing on the order of one lattice constant for Ir and three lattice constants for Au. Correspondence between

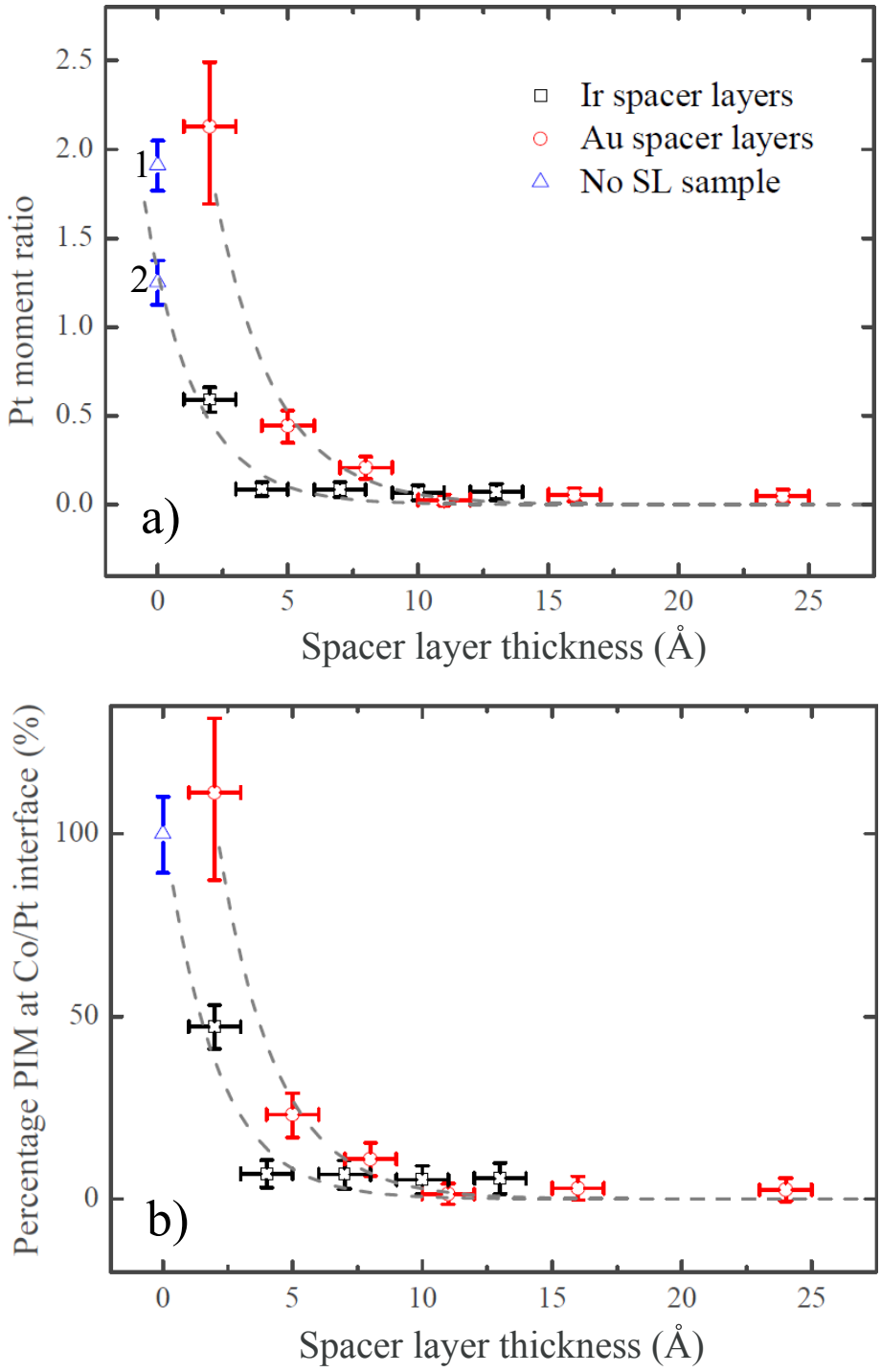

Figure 6.5: a) Pt moment ratio as a function of Au and Ir SL thickness. The blue triangles labelled 1 and 2 show the measurements at 11.564 keV and 11.562 keV of the sample with no SL respectively. These correspond to the Pt moment ratio from the mSLD in Fig. 6.3 a) and Fig. 6.4 a) respectively. b) The Pt moment ratio normalised to data point 1 for the Au SL series and data point 2 for the Ir SL series. This is interpreted as the percentage PIM at the top Co/Pt interface relative to the no SL sample measurement. The dashed lines in both figures show fitted exponential decays to quantify the lengthscale over which the PIM vanishes.

these lengthscales and those measured in the same samples for the Dzyaloshinskii-Moriya interaction as well as the Gilbert damping are discussed in chapter 8.

In an attempt to allow better comparison between the two datasets taken on the separate beam-time runs, a second normalisation was made. Here, the Pt moment ratio for the SL samples measured on each run were divided by the value for the Pt moment ratio found for the sample with no SL for that respective beam-time (which assuming no sample degradation, should be the same). This converts the Pt moment ratio into the percentage PIM remaining at the top Co/Pt interface relative to what was measured originally with no SL and is shown as a function of SL thickness in Fig. 6.5 b).

The main effect of mapping the two datasets onto each other in this way is that it increases the relative size of the Ir (2 Å) SL data point compared to the Au (2 Å) data point. However, within this region the PIM is falling so rapidly with SL that it does little to change the trend of the SL thickness dependence. Again, exponential decays have been fitted to this data, yielding a decay constant of (2.2 ± 0.3) for the Au spacer layers and (2.0 ± 0.4) for the Ir spacer layers, which are consistent with the fits from Fig 6.5 a). Therefore, the discrepancy between the Pt moment ratio between beam-time experiments for the sample with no SL does not influence the extracted lengthscale of the PIM interaction.

These measurements confirm conclusively that the PIM in Pt is rapidly lost with the insertion of SLs. For both Au and Ir SLs the PIM is lost for SL thicknesses greater than 10 Å, and the evidence suggests Ir causes the PIM to vanish on a shorter lengthscale, with a SL of just 4 Å thickness.

The sSLD and mSLD profiles showed that the interface morphology influences the PIM and the evidence for a difference in lengthscale for the Pt PIM for Au and Ir spacer layers suggests that the contributions of topological roughness and alloying at the interface may be important. The next section combines the information gained from the specular reflectivity in order to gain some insight into this.

6.3.1 Interpretation of the induced Pt moment with regard to interface morphology

The measurements of the Pt PIM as a function of the SL thickness indicated that Ir causes the PIM to vanish more rapidly than Au. The role of interface morphology is potentially

important in understanding this difference.

At the Co/Pt interface, the PIM in Pt arises due to the enhanced density of states of the Pt at E_F as a result of the d-orbital hybridisation with the Co atoms [51]. This subsequently leads to the satisfaction of the Stoner criterion for Pt in the vicinity of Co.

With the insertion of ultrathin discontinuous spacer layers, first a Co-Ir-Pt or Co-Au-Pt alloy or matrix is formed in the interfacial region. It may be surmised that Pt atoms in Pt-Ir and Pt-Au alloys are less likely to proximity polarise since the alloy would have a lower Stoner enhanced paramagnetic susceptibility relative to the pure Pt.

Structurally, the difference between Au and Ir is their ability to wet with Co and Pt, where Au is almost entirely immiscible [194] and Ir is fully miscible [193] with Pt. It would be expected that Au would develop island-like growth, thus allowing a significant amount of direct contact between the Co and Pt at the interface, whereas for Ir mixing would be more homogeneous and direct Co/Pt contact less common.

From the specular reflectivity fits, the parameter, σ/t, the ratio of the interface width, σ, to the thickness of the SL, t, has been calculated. A ratio greater than one indicates a discontinuous spacer layer. It is important to note that this does not distinguish between a discontinuous barrier formed by roughness greater than the spacer layer thickness and a discontinuous barrier formed by an intermixed region greater than the spacer layer thickness. The percentage of PIM remaining has been plotted as a function of σ/t in Fig. 6.6.

Viewing Fig. 6.6 from right to left, in this crude analysis the samples transition from discontinuous SLs to continuous SLs where the vertical dashed line indicates the onset of a continuous SL. It is interesting to note that for Ir SLs, it can be conclusively stated that the moment is completely lost before a continuous film has been formed. This must be related to the alloying of Ir with Pt, which modifies the density of states, since for a discontinuous Ir SL a proportion of the Pt atoms would continue be in contact with the Co.

For the Au SLs, the moment persists until a complete continuous layer is formed, which occurs for a Au thickness between 8-10 Å. The island-like growth of Au may give rise to greater topological roughness but less intermixing compared to more homogeneous alloying of Ir, which would give rise to a greater amount of intermixing but smaller roughness. Unfortunately these two components cannot be resolved using reflectivity alone and additional transverse diffuse scans are required to separate these components. Transverse dif-

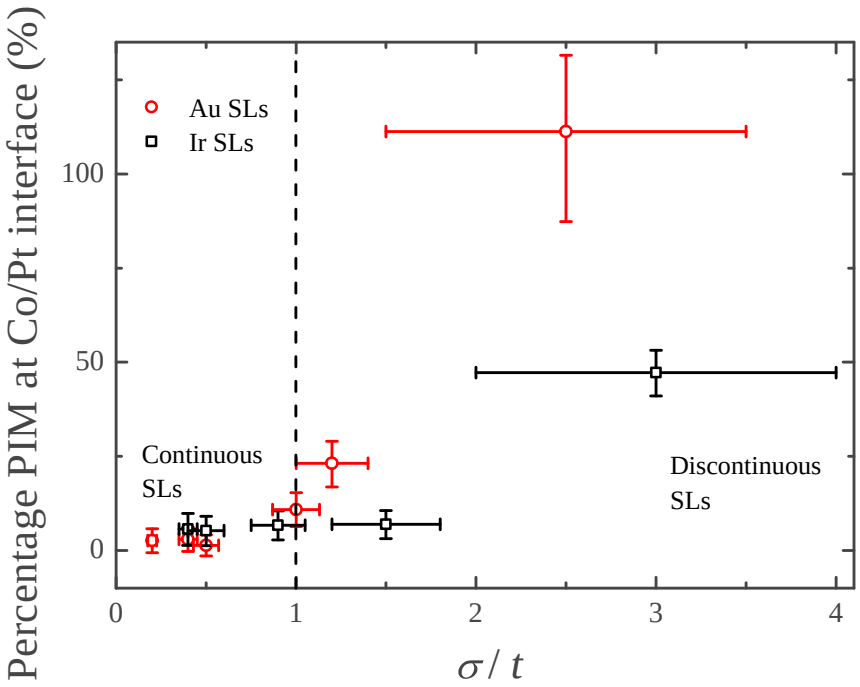

Figure 6.6: The percentage PIM at the top Co/Pt interface (calculated relative to the sample with no SL) plotted as a function of the ratio of interface width to spacer layer thickness (σ/t) as extracted from the specular reflectivity measurements.

fuse scans were measured using the Bede D1 x-ray reflectometer, which has a monochromated Cu-K_α laboratory source, and is described in chapter 3. However, the intensity of the source was too low to measure the diffuse scatter in sufficient detail to reliably determine whether the topological roughness is greater at the Au/Pt interface and the intermixing is greater at the Ir/Pt interface.

However, based on the miscibilities of Au and Ir with Pt [193, 194], then it would not be entirely unreasonable to assume this is the case. These results would then suggest that the Pt PIM is more sensitive to intermixing than topological roughness, as would be expected since homogeneous alloying would result in modifications to the Pt band structure and therefore push Pt further from the Stoner criterion. Similarly, measurements of $FePt_{1-x}Ir_x$ alloys demonstrate that the ferromagnetism vanishes for Ir concentrations of $x > 0.2$ [198]. These results demonstrate the extreme sensitivity of PIM to the micro-structure of the interface.

6.4 Chapter conclusions

This investigation studied the modification of PIM within Pt in Pt/Co/SL/Pt structures as a function of Au and Ir SL thicknesses between 2-20 Å. XRMR was used to obtain the depth resolved PIM throughout the sample cross-section. Particular attention was given to establishing the SL thickness over which the PIM existed and the role of the interface morphology.

The spin asymmetry was measured at the Pt-L_3 edge and was fitted alongside the specular reflectivity. From the fits to each sample the respective sSLD profiles and mSLD profiles were extracted. The insertion of the SL resulted in a rise in the interface width for the top Pt layer, as extracted from the specular reflectivity fits, compared to the sample with no SL. The mSLD for the sample with no SL showed a larger induced moment at the top Co/Pt interface compared to the buffer Pt/Co interface. It was suggested that this was due a greater degree of intermixing at the Co/Pt interface [197] which then enhanced the orbital hybridisation between the Co and Pt.

The insertion of a Au (2 Å) SL made little difference to the mSLD profile. However, the insertion of an Ir (2 Å) SL resulted in a dramatic loss of PIM at the top Co/Pt interface. Further addition of Au and Ir SLs of increasing thickness resulted in the dramatic reduction of PIM in the top Pt layer. In particular, for the Au (8 Å) SL sample the majority of the remaining Pt moment resided within the Au/Pt interfacial region.

The PIM within the top Pt was eradicated for SLs of Au and Ir thicker than 11 Å and 4 Å respectively. The percentage PIM at the Co/Pt interface relative to the Pt/Co interface was found as a function of SL thickness and was fitted with exponentials. From these fits, decay lengths of (2.2 ± 0.3) Å and (2.0 ± 0.4) Å were obtained for the Au and Ir SLs respectively. The large errors are due to the shortage of data-points in the ultrathin SL region.

To gain more insight into the role of the interface morphology, the ratio σ/t was calculated for each SL using parameters extracted from the specular reflectivity fits, and the percentage PIM at the Co/Pt interface was plotted as a function of this. Here, it was shown that the Ir (4 Å) SL eradicated the PIM before forming a complete layer. Since this Ir SL was discontinuous, Pt atoms would continue to be in contact with Co atoms, hence this

loss of PIM must be a result of the alloying of Ir with Pt and the resulting change in the density of states. The Au SLs showed that the PIM was only lost once a continuous SL was formed. This difference in behaviour was attributed to the miscibility gap in Pt-Au alloys [194] which is expected to result in island-like growth and a topologically rough interface. In contrast, Ir is expected to mix well with Pt, even at low concentrations [193] producing an interface with a greater degree of alloying and therefore a greater degree of orbital hybridisation between the Ir and Pt.

7 The effect of changing Co thickness and magnetic anisotropy on the induced moment in Pt

7.1 Introduction

Continuing with the interface modification of proximity induced magnetism (PIM) demonstrated in the previous chapter, this short chapter focuses on the effect of the Co thickness in the Pt/Co/Pt structure and thereby proportionately increases the interfacial contribution to the magnetic anisotropy in the Co. The focus is on comparison of the element specific hysteresis loops from x-ray resonant magnetic reflectivity (XRMR), with the loops obtained using the magneto-optical Kerr effect (MOKE).

The previous chapter demonstrated the important role of interface morphology in the PIM on Pt, whereby the Co/Pt interface was modified by the insertion of ultra thin spacer layers of Au and Ir. An important aim of this work was to attempt to resolve the conflict in the literature between the role of PIM in the Dzyaloshinskii-Moryia interaction (DMI).

Most experimental studies into the DMI used samples with perpendicular magnetic anisotropy (PMA) [44, 55, 55]. Therefore in order to consider the results from the previous chapter regarding in-plane magnetised Co in the context of the DMI it is also useful to understand how the PIM in Pt changes as the Co thickness is reduced and the magnetic anisotropy is changed.

In the literature, there have been various XMCD and XRMR studies of Pt/ferromagnetic structures with both in-plane and out-of-plane magnetic anisotropy [40, 174, 181, 195, 199]. In particular, a study by Figueroa *et al.* [200] demonstrated that in a perpendicularly mag-

netised Co-Pt multilayer, the hysteresis loops obtained at the Co-K edge, Pt-L_3 edge and using SQUID magnetometery were identical. This result demonstrated that proximity polarised Pt takes on the same magnetic anisotropy as that of the Co. However, these measurements were only made on a single perpendicularly magnetised sample and at 14 K, but this demonstrated that the PIM continues to exist when the ferromagnetic layer is thin enough to be perpendicularly magnetised.

In this investigation the evolution of the element specific hysteresis loops were studied over a range of Co thicknesses and at room temperature to investigate any changes of the PIM in comparison to the total magnetisation loop measurements obtained using longitudinal and polar MOKE.

7.2 Sample structure and characterisation using XRR

A series of samples with Pt (50 Å)/Co (t)/Pt (50 Å) structure were sputter deposited onto Si/SiO_2 substrates, with base pressures of order 1×10^{-8} Torr. The Co thickness, t, varied from 4-20 Å between the samples. The XRR and best fits for all the samples are shown in Fig. 7.1. The XRR measurements were made using circularly polarised x-rays at the Pt-L_3 edge, with x-ray energy 11.564 keV.

The structural parameters extracted from the best fits are shown in Table 7.1. The values of the interface width, σ, extracted for the Co layer, decrease as the layer gets thicker. This is perhaps associated with a greater degree of film continuity for the thicker Co layers, and therefore a reduction in alloying. Likewise, σ for the top Pt layer generally reduces in accordance with the Co σ, suggesting that the Co structure has some influence on the Pt structure. In chapter 6, there was difficulty resolving the ultrathin Au and Ir spacer layers with thickness below 10 Å, likewise, there is difficultly in resolving the Co thickness when below 10 Å in thickness. However, this analysis indicates that the growth rate calibration was reliable, obtaining within 1 Å of the expected thickness of the Co, hence these nominal Co thickness are used for the Co thickness throughout this chapter.

Sample	Buffer Pt		Co		Top Pt	
	t (Å)	σ (Å)	t (Å)	σ (Å)	t (Å)	σ (Å)
Co (4 Å)	54 ± 1	7 ± 1	5 ± 1	17 ± 3	45 ± 1	2 ± 1
Co (6 Å)	48 ± 1	10 ± 1	7 ± 1	10 ± 1	46 ± 1	10 ± 1
Co (8 Å)	52 ± 1	6 ± 1	7 ± 1	8 ± 1	48 ± 1	7 ± 1
Co (10 Å)	52 ± 1	7 ± 1	10 ± 1	7 ± 1	47 ± 1	7 ± 1
Co (15 Å)	52 ± 1	7 ± 1	15 ± 1	7 ± 1	47 ± 1	4 ± 1
Co (20 Å)	53 ± 1	5 ± 1	20 ± 1	6 ± 1	48 ± 1	4 ± 1

Table 7.1: Structural parameters extracted from the best fits to the specular reflectivity shown in Fig. 7.1. Nominal Co thicknesses are shown in the far left column. The Co thicknesses extracted from best fits to the XRR data are within the error margins of ±1 Å of the nominal Co thickness.

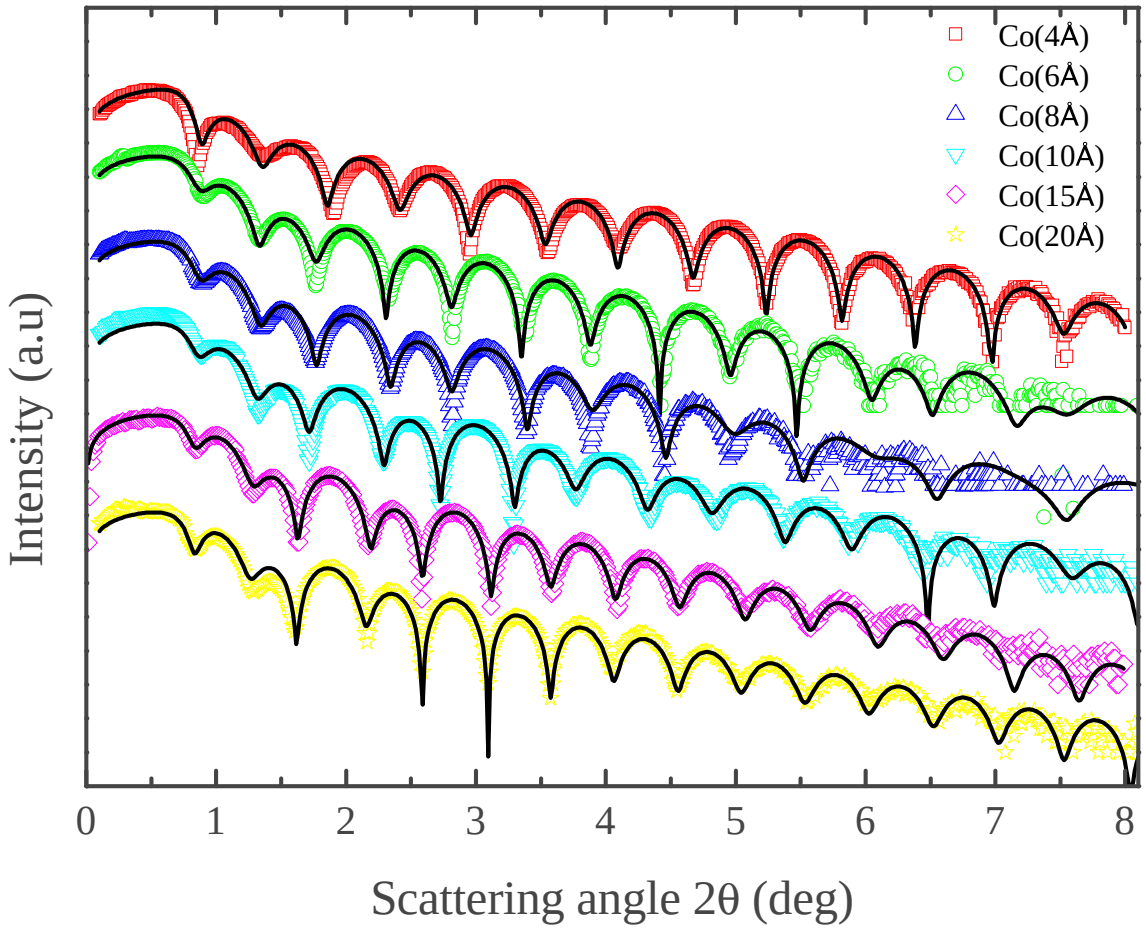

Figure 7.1: Specular reflectivity measured at the Pt-L_3 edge for Pt (50 Å)/Co (t)/Pt (50 Å) samples. All datasets have been offset vertically in order to allow them to be plotted on the same figure. The solid lines represent the best fitting simulations.

7.3 Magnetic measurements using longitudinal and polar MOKE

The samples were studied using longitudinal and polar MOKE. Longitudinal and polar hysteresis loops obtained for the samples with different Co thickness are shown in Fig. 7.2. The changing shape of the loops reflects the changing magnetic anisotropy as the Co thickness is varied.

The polar MOKE hysteresis loops obtained for the Co (4 Å), Co (6 Å) and Co (8 Å) samples indicates perpendicular anisotropy. Furthermore, when the field is applied in-plane for the longitudinal measurements, a hard axis is observed with no remanence for the Co (4 Å) and Co (6 Å) samples. As the Co thickness is further increased the polar MOKE loops have reduced magnetic remanence, M_r and an increased coercive field, H_c. In contrast, the longitudinal MOKE loops show an increasing M_r and decreasing H_c with increasing Co thickness, which reflects the changing magnetic anisotropy.

For the samples where it was possible to saturate the magnetisation, the magnetic remanence is plotted as a function of Co thickness in Fig. 7.3 a) for both in-plane magnetic fields and out-of-plane magnetic fields. The perpendicular loops are square, showing near 100% remanence for the thinnest three samples and a slight dip for the Co (10 Å) sample measurement. For thicker Co layers, it was not possible to saturate the magnetisation out-of-plane with the magnetic field available. The in-plane field remanence shows a reverse trend where the thickest Co samples have the highest remanence.

The coercive fields of the samples that could be saturated in the MOKE measurements are shown in Fig.7.3 b). H_c has a complex dependence on anisotropy, in-plane grain size, defects, and surface roughness [201]. For the polar Kerr loops, the magnitude of H_c should decrease with increasing Co thickness, since the PMA reduces with increasing Co thickness. This trend is observed for Co thicknesses between 6-10 Å. The reduction in H_c for the thinnest Co (4 Å) film may suggest a reduced PMA which could occur due to significant discontinuity within the film and alloying with the Pt [178]. In contrast, the reducing grain size and increasing contribution of defects as the Co thickness is reduced would increase the number of domain wall pinning sites and act to increase H_c. The interpretation of H_c is therefore extremely complex. For the in-plane magnetised films, the decrease in

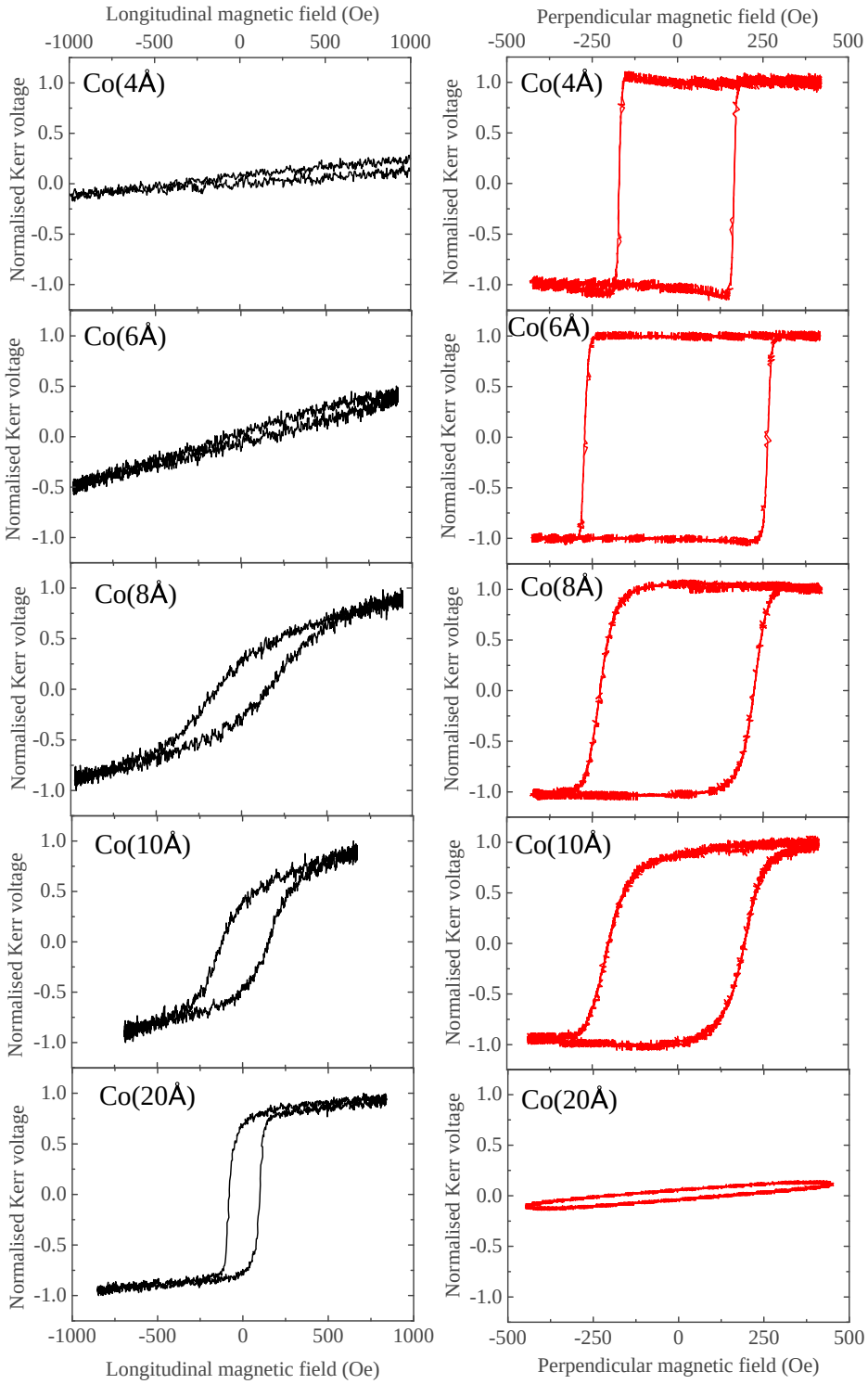

Figure 7.2: Longitudinal (black) and polar (red) MOKE loops for Pt/Co/Pt films with increasing Co thickness. Note that since the longitudinal MOKE loops for the Co (4 Å) and Co (6 Å) samples could not be saturated, for comparison they have been normalised to the extrapolated saturation from the Co (8 Å) sample, which is a good approximation of the saturation Kerr voltage. Likewise, the polar MOKE loops for the Co (20 Å) and Co (15 Å) samples have been normalised to the Co (10 Å) saturation polar Kerr voltage.

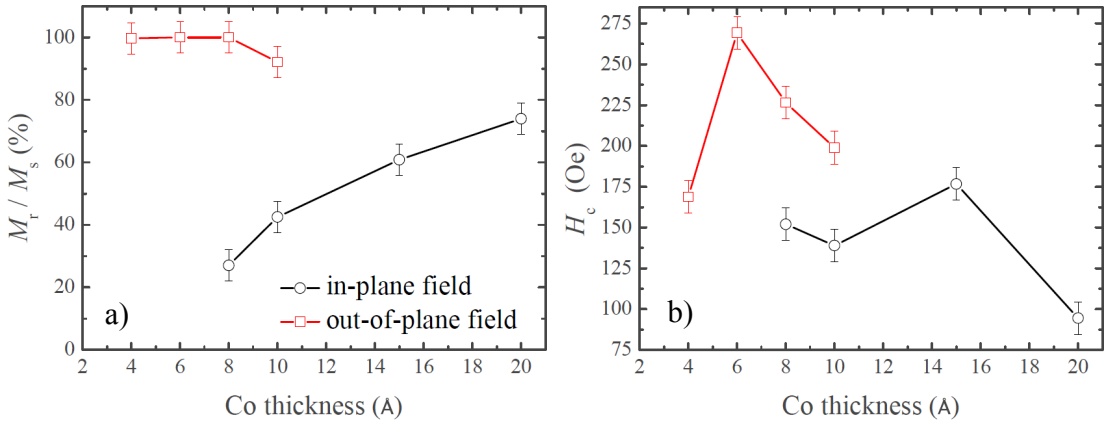

Figure 7.3: a) Percentage remanence as a function of Co thickness after saturation with a magnetic field in the plane of the film or out of the plane of the film. b) The coercive field as a function of Co thickness and saturation field applied in-plane and out of the plane of the film.

H_c with increasing Co thickness in the longitudinal MOKE measurements is likely due to the increased grain size in the thicker films resulting in less domain wall pinning.

This chapter now continues by comparing these hysteresis loops with the element specific loops obtained at the Pt-L_3 edge.

7.4 Element specific hysteresis loops obtained at the Pt-L_3 edge for varying Co thickness

Before the element specific hysteresis loops were measured, the angular dependence of the spin asymmetry ratio, R_a, was measured in order to find the optimum position in the reflectivity to measure the hysteresis loop.

7.4.1 Spin-asymmetry ratio measurements

The spin-asymmetry ratio was extracted from the XRMR as a function of scattering angle, 2θ, for all the Co samples and is shown in Fig 7.4. The x-rays were circularly polarised and the energy was 11.564 keV. A 1 kOe in-plane magnetic field was applied along the x-ray scattering axis and was used to switch the magnetisation of the samples in the plane of the film to calculate R_a. From the MOKE loops in Fig. 7.2, and assuming the PIM in the Pt takes on the same anisotropy as the Co, the samples with Co thickness greater than 6 Å would be saturated in-plane by the 1 kOe field.

The significant noise for the measurement of the Co (10 Å) sample at high angle occurred because the synchrotron beam was lost partway through this measurement, which resulted in a loss of alignment when the beam returned. The sample was realigned before measuring the element specific hysteresis loop.

The height of the peaks in the magnetic reflectivity are proportional to the size of the total induced moment. For the samples with Co layers of thickness between 8-20 Å the magnitude of the R_a peaks are fairly comparable, approximately 2-3%. For the Co (6 Å) samples there is a significant drop in the magnitude of the R_a peaks, with only one statistically significant peak, occurring at 1.8°. This was where the element specific hysteresis loop was measured. For the Co (4 Å) sample, no statistically significant peaks could be resolved. This indicates that either the Pt was not polarised or the 1 kOe in-plane field was insufficient to rotate a measurable component of the PIM into the plane and along the scattering direction. The periodic spikes in noise in R_a are associated with the Keissig minima in the XRR which result in low count statistics.

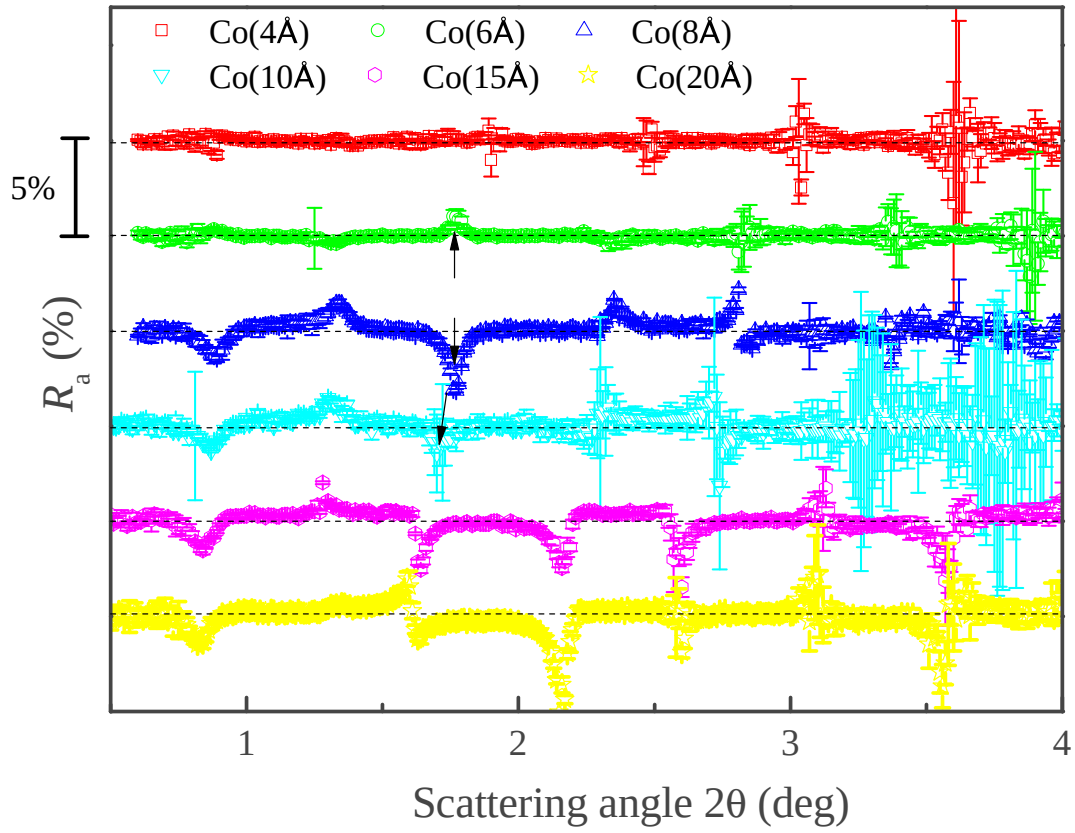

Figure 7.4: Magnetic reflectivity measured for Pt (50 Å)/Co (t)/Pt (50 Å) multilayers with different Co thickness, t. Constant offsets were applied to the data to allow it to be plotted on the same figure.

7.4.2 Element specific hysteresis loops

The Pt-L_3 edge hysteresis loops were measured in four of the six samples. The experimental method for the element specific hysteresis loop measurement was discussed in detail in chapter 3, but in summary, R_a was measured by switching the light helicity, and as a function of the in-plane magnetic field at a fixed scattering angle 2θ.

XRMR is sensitive to the magnetisation components along the scattering vector, hence for the grazing incidence reflectivity configuration used here, this corresponds to magnetisation components in the plane of the film and along the beam direction. The magnetic field was swept along the scattering vector, hence this provides the x-ray equivalent to longitudinal MOKE. Perpendicular components of magnetisation can be measured using an x-ray transmission configuration and measuring the spin dependent absorption, this was not done here.

The element specific hysteresis loops are shown in Fig. 7.5. The orientation of the magnetic field in the plane of the film was the same as that in the longitudinal MOKE measurements, in case of any uniaxial in-plane anisotropy present in the thickest Co samples. The loops have been fitted with Langevin functions to extract M_r and H_c.

Clearly the anisotropy of the polarised Pt changes as the Co thickness is varied. The hard-axis observed for the Co (6 Å) sample suggests that the reason no magnetic signal was observed for the Co (4 Å) sample was that the 1 kOe in-plane magnetic field was not sufficient to reorientate a measurable component of the polarised Pt into the plane of the film. Based on the longitudinal MOKE measurement for this sample, shown in Fig. 7.2 a), a 1 kOe in-plane field would result in an in-plane component of magnetisation equal to approximately 10-15% of the saturation magnetisation. This is comparable to the error bars on the R_a measurements which would explain why no statistically significant spin-asymmetry could be measured for the Co (4 Å) sample.

The extracted values of M_r and H_c from the fits using Langevin functions are shown in Fig 7.6 and compared to those found from the longitudinal MOKE measurements. There is convincing similarity between the extracted values for M_r and H_c from the element specific hysteresis loops and those from the longitudinal MOKE measurements. Consistent with the changing Co anisotropy, the M_r of the proximity polarised Pt increases with Co thickness.

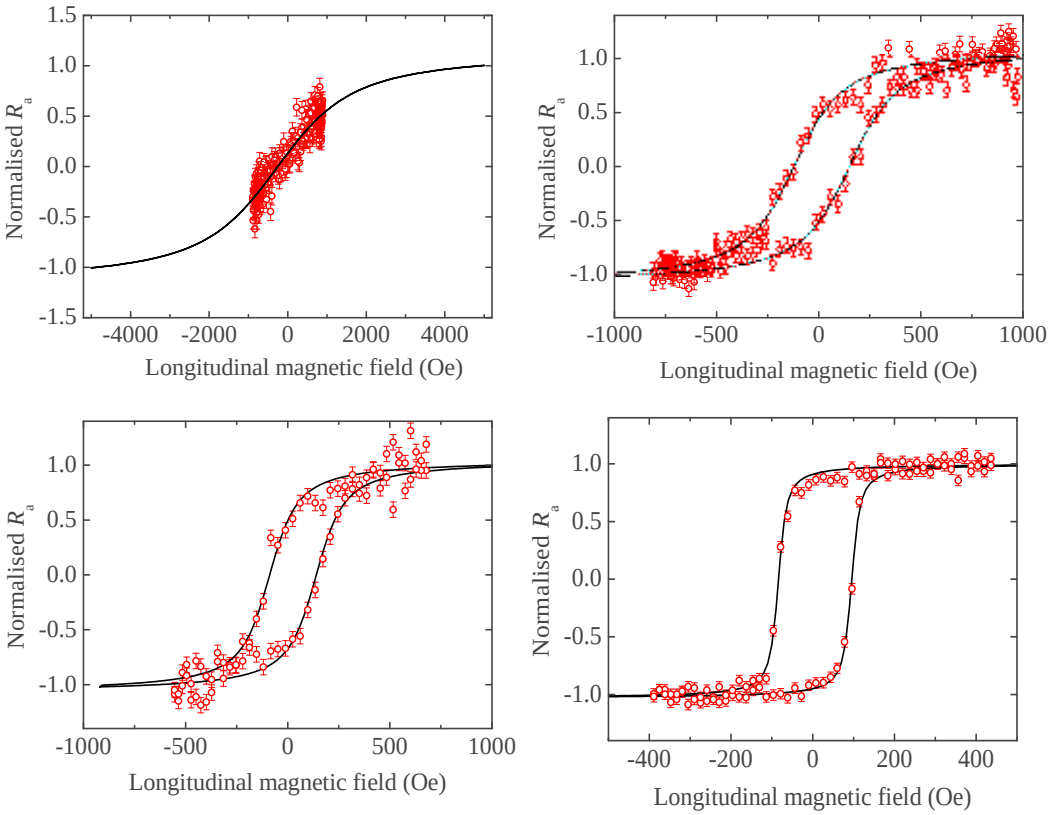

Figure 7.5: Element specific hysteresis loops measured at the Pt-L_3 edge for Pt (50 Å)/Co (t)/Pt (50 Å) with a) t = 6 Å, b) t = 8 Å, c) t = 10 Å and d) t = 20 Å. Langevin functions have been fitted and are shown as the solid lines. The datasets have been normalised to the saturation R_a found from the Langevin fit to aid comparison.

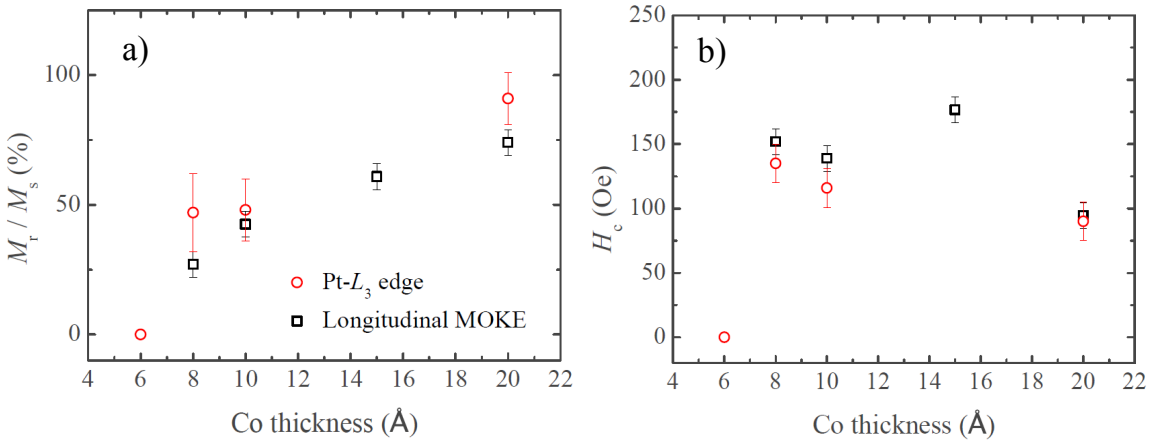

Figure 7.6: Comparison of extracted a) M_r/M_s and b) H_c from longitudinal MOKE and XRMR hysteresis loops.

Likewise, the H_c of the Pt decreases with increasing Co thickness. The similarity of H_c between the measurements is particularly interesting since the polarised region of the

Pt would not necessarily have the same extrinsic contributions to H_c, i.e defects and grain boundaries, as that of the Co.

To further emphasise the consistency between the longitudinal MOKE hysteresis loops and those measured at the Pt-L_3 edge, both measurements are plotted together in Fig. 7.7. Since the MOKE is dominated by the Co signal and the Pt-L_3 edge hysteresis loops are sensitive only to the Pt moment, the comparable evolution of the hysteresis loops with changing Co thickness gives strong evidence that the magnetic anisotropy of the polarised Pt is directly linked to the orientation of the Co, such that when the Co anisotropy changes the Pt PIM follows it.

Since the polarised Pt has only one defined interface, that which occurs with the Co, the other magnetic interface instead decays exponentially into the Pt itself, it is interesting that the polarised Pt points out-of-plane when the Co thickness is reduced. This suggests

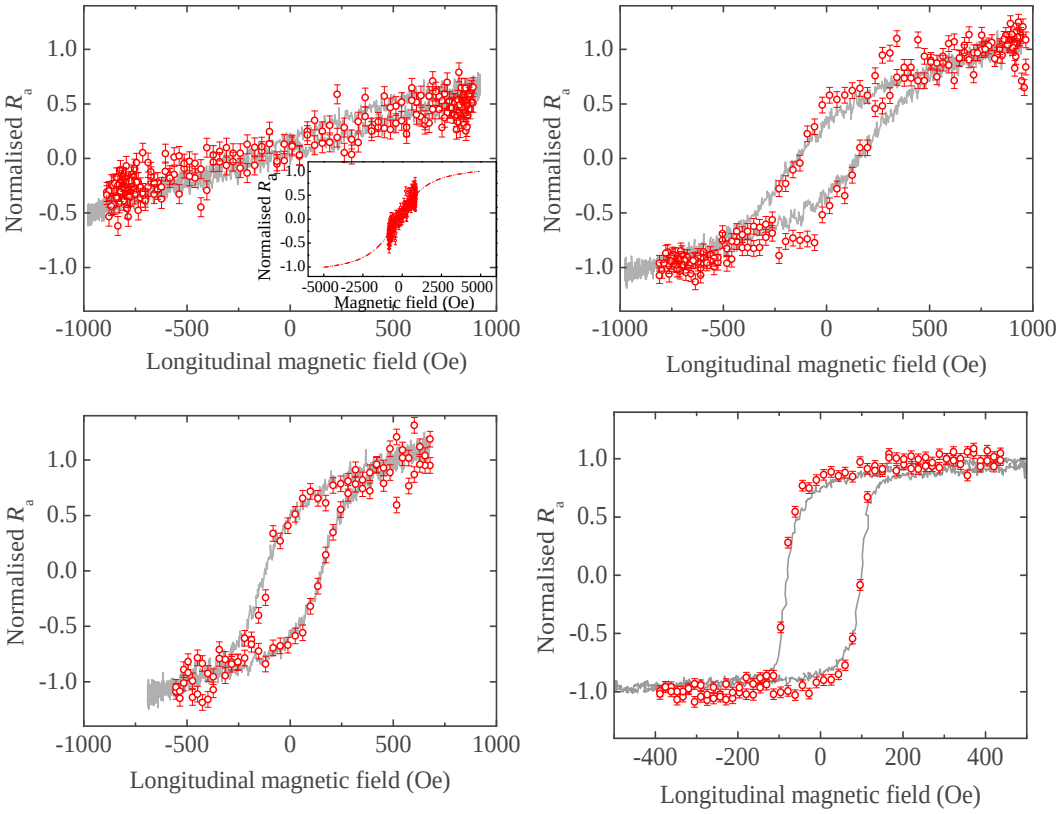

Figure 7.7: Element specific hysteresis loops measured at the Pt-L_3 edge for Pt(50 Å)/Co (t)/Pt (50 Å) with a) t = 6 Å, b) t = 8 Å, c) t = 10 Å and d) t = 20 Å. The longitudinal MOKE loops are shown in grey. In a) the normalisation has been made to the saturation R_a estimated by the Langevin fit which is shown in the inset of the figure.

that the Pt PIM must be strongly coupled to the Co, in order to overcome the large energy cost of the demagnetisation field.

7.5 Chapter conclusions

The purpose of this investigation was to study the change in PIM with decreasing Co thickness, in particular the transition from in-plane magnetic anisotropy to out-of-plane magnetic anisotropy. Samples with the structure Pt (50 Å)/Co (t)/Pt (50 Å), where the Co thickness was varied between t = 4-20 Å, were structurally characterised using x-ray specular reflectivity and measured magnetically using polar and longitudinal MOKE and element specific XRMR. Over the range of Co thicknesses, the magnetic anisotropy transitioned from a strong out-of-plane magnetic anisotropy to in-plane magnetic anisotropy with increasing Co thickness.

Element specific hysteresis loops were measured at the Pt-L_3 edge and therefore only sensitive to the Pt polarisation. These were compared to the MOKE longitudinal hysteresis loops and good agreement was found between the shapes of these loops. Importantly the consistency between the loops was found for all four Co thicknesses measured, independent of the Co anisotropy and morphology. This demonstrated that the polarised Pt magnetic orientation closely followed the Co magnetic anisotropy, and both polarised Pt and Co moments must therefore be strongly coupled.

This study also demonstrated the existence of PIM over a range of Co thicknesses and as indicated in these results and demonstrated by the XMCD measurements of perpendicular Pt/Co multilayers by Figueroa *et al.* [200], it can be expected that the PIM is still in existence in the perpendicularly magnetised samples used in recent high profile studies of the DMI [44, 55].

8 Role of interfacial proximity induced magnetism in magnetic damping and the Dzyaloshinskii-Moriya interaction

8.1 Introduction

The previous two chapters focused heavily on the proximity induced magnetism that arises in Pt and how it can be modified in response to changing ferromagnetic anisotropy and interface engineering with heavy metal spacer layers at the Co/Pt interface.

Due to the large spin-orbit interaction (SOI) of Pt, it is now established as a standard component for inducing a variety of spin-orbit phenomena [12, 22, 79, 160]. However, the proximity induced magnetism (PIM) in Pt clearly gives rise to questions regarding the role of PIM in these phenomena.

For example, for the recently observed spin-Hall magnetoresistance in YIG/Pt bilayers [94, 191], there is an ongoing debate concerning whether the effect is in fact a consequence of an interfacial AMR within a proximity polarised Pt layer [202]. Alongside this, a similar discussion has surrounded the spin-Seebeck effect [6,203], in which it was proposed that the transverse voltage in YIG/Pt is actually a result of the anomalous Nernst effect from a proximity polarised Pt layer [173,204]. Consequently there followed a number of XMCD studies of various ferromagnetic insulator/Pt bilayer systems to address this [174,205,206].

The XRMR data obtained here, on the Pt/Co/Pt samples which were extensively analysed in chapter 6, is presented with measurements and analysis of the large magnetic damping [207] and the Dzyaloshinksii-Moriya interaction [10, 208] (DMI) associated with the Pt/ferromagnet interface.

The reason for focusing on these two effects is that they are both intrinsic to ferromagnets. Unlike for example the spin-Hall effect, which requires only a large SOI, magnetic damping and DMI both require an exchange interaction, by which the spin-spin interactions are modified in the presence of the SOI. In this regard, it may be considered that the induced exchange through PIM within a material with a strong SOI, such as Pt, may yield a significant modification to either or both the total damping or the DMI.

The chapter is split into two sections, the first discusses the role of PIM in magnetic damping and the second regarding PIM with respect to the DMI. The PIM characterised as a function of Au and Ir spacer layers (SLs) at the top Co/Pt interface is compared with measurements of magnetic damping and DMI made on the same samples using time-resolved MOKE and Brillouin light scattering respectively.

8.2 Magnetic damping

Magnetic damping describes the dissipation of energy away from the magnetisation as it precesses around an applied magnetic field. The effect was described in chapter 2. The microscopic mechanisms by which the energy is dissipated are poorly understood, but is known to have a dependence on the SOI [15]. The presence of heavy met al layers alongside ferromagnetic layers would enhance the SOI and theoretical studies have predicted intrinsic components of damping due to spin-pumping that arise due to this [75]. There have consequently been a variety of experimental investigations in the literature by which the dependence of damping on heavy metal capping layers is investigated. Some results relevant to the motivation of this study with regard to PIM, where Pt and Pd capping layers are used, are discussed below.

8.2.1 Studies in the literature

An important study by Mizukami *et al.* [209] investigated the variation of the damping parameter, α, on $Ni_{80}Fe_{20}$ film thickness when sandwiched between non-magnetic layers of Pt, Pd, Ta and Cu. The results are reproduced in Fig. 8.1 a). The damping rapidly rises as $Ni_{80}Fe_{20}$ thickness is reduced and the rate of rise is highest for the Stoner enhanced paramagnets Pt and Pd. This work inspired the pioneering theoretical study by Tserkovnyak *et*

al. [75] who ascribed the enhancement to a new form of energy dissipation, by which angular momentum is spin-pumped away from the magnetisation as it precesses. Due to the strong SOI in the heavy metals Pt, Pd and Ta, the spin diffusion length is short and hence they are good spin sinks by which no spin-accumulation occurs. Conversely, the large spin diffusion length of Cu, λ_{sd} ~300 nm at room temperature [210], leads to spin-accumulation in the Cu and limits the effectiveness of spin pumping.

The spin-flip relaxation time, τ_{sf}, should scale as Z^4 in accordance with the SOI [75] and consequently Pd has a longer spin diffusion length λ_{sd} ~7 nm at room temperature [211] compared to the λ_{sd} ~2 nm measured for Ta [91]. It would therefore seem inconsistent that Pd has such a large damping associated with it, which suggests that perhaps the PIM of Pd enhances the damping.

Another theoretical study by Barati *et al.* [76] demonstrated the importance of orbital hybridisation at the interface, in particular *d*-orbital hybridisation of bands at the Fermi energy (E_F). Pd has a large density of *d*-states at E_F, which is why it is a Stoner enhanced paramagnet, and explains why these materials result in an enormous enhancement of damping. In this study, the PIM associated with Pt and Pd was not considered. However, the question is: is the damping enhancement brought about by the *d*-*d* hybridisation alone, or is the fact the Pt is magnetically polarised an important consideration?

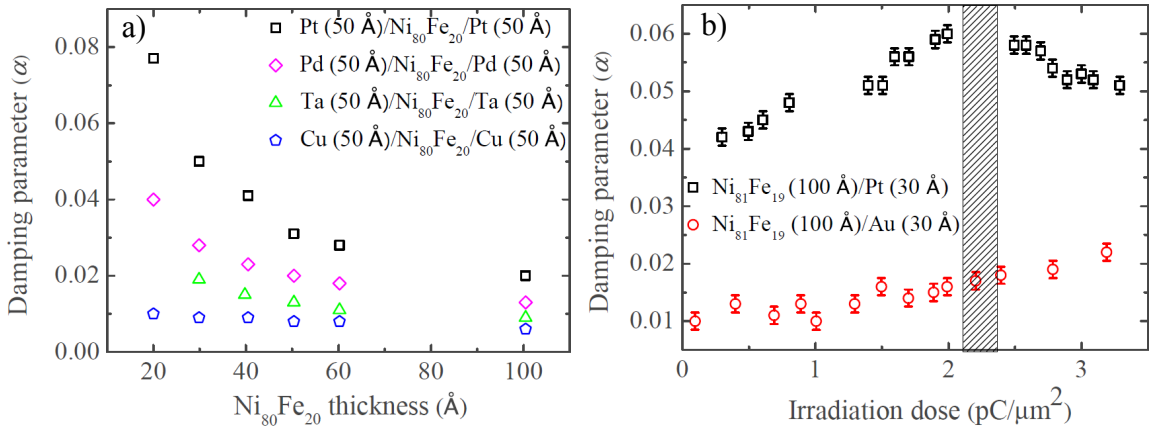

Figure 8.1: a) The damping parameter as a function of $Ni_{80}Fe_{20}$ thickness in transition metal multilayer sandwiches. A significant enhancement in damping is associated with the Stoner enhanced paramagnets Pt and Pd. Data reproduced from Ref. [209]. b) The damping parameter as a function of FIB irradiation dose for $Ni_{81}Fe_{19}$ films capped with Au and Pt, reproduced from Refs. [38] and [79] for the Au and Pt datasets respectively. The hashed region denotes where the peak in damping for $Ni_{81}Fe_{19}$/Pt films would be expected to occur based on the trend of the data.

In a separate later study, Mizukami *et al.* [212] investigated a Cu/$Ni_{80}Fe_{20}$/Pt structure and the effect of inserting Cu SLs between the top $Ni_{80}Fe_{20}$/Pt interface. They observed an initial sharp drop in damping with a Cu (30 Å) SL followed by a gradual reduction in damping over a Cu thickness of 300 nm. The latter effect is explained by spin-pumping through the Cu with λ_{sd} ~300 nm, whereas this initial interfacial reduction was unexplained.

A study by Sun *et al.* [213] used YIG/Pt bilayers and claimed that the PIM in Pt was directly responsible for an observed step-like enhancement of damping with a 3 nm Pt cap. They then inserted Cu SLs between the YIG/Pt interface to disrupt the PIM and observed the same interfacial reduction in damping as Mizukami *et al.* [212]. However, the significant roughness of their nanoscale YIG, σ ~1.4 nm would result in large extrinsic contributions as the continuous Pt layer is formed [78] over the thickness range of 3 nm, which would require detailed analysis of the precession frequency to rule out.

Shown in Fig. 8.1 b) is the combined works of King *et al.* [38] and Ganguly *et al.* [79], who studied the modification of damping through controlled intermixing of $Ni_{81}Fe_{19}$/Au and $Ni_{81}Fe_{19}$/Pt bilayers respectively using focused ion beam irradiation. Both datasets rise with dose which can be understood through an enhancement of the two-magnon scattering mechanism [77]. However, even though Au and Pt have similar atomic weights, the enhancement in damping for Pt is much more significant, which possibly suggests an additional component, which could perhaps be an enhancement in total moment due to the polarisation of the intermixed Pt at low doses. Further increasing the dose would eventually result in the loss of M_s from the $Ni_{81}Fe_{19}$ and a loss of PIM in the Pt [39], which could explain the peak in damping. Alongside this, increasing dose would result in sputtering away of the Pt cap which would also contribute to the reduction in damping. Contrary to the Pt, the Au would be expected to exhibit a minimal PIM [188] and shows a uniform increase in damping over the full range of FIB dose.

Hence there is much evidence to motivate a study into the role of PIM and magnetic damping. In the next section the measurements of the magnetic damping parameter in Pt/Co/SL/Pt structures is presented.

8.2.2 Magnetic damping as a function of spacer layer thickness

In this section, measurements of the Pt (54 Å)/Co (25 Å)/Au (1-25 Å)/Pt (26 Å) multilayers made using the time-resolved MOKE (TR-MOKE) technique are presented. TR-MOKE measurements for the Ir SL samples were not available to allow comparison of the PIM and damping between two SL series. However, samples with a Pt (54 Å)/Co (25 Å)/Cu (1-25 Å)/Pt (26 Å) structure, where the Cu thickness was varied, were also measured using TR-MOKE. Even though the PIM data on the Cu spacer samples is not available, the comparison of Cu and Au is useful because Cu has a significantly larger spin diffusion length, $\lambda_{sd} \sim 300$ nm [212]. This means that within the thickness range investigated, all the Cu spacer layers may be expected to be essentially spin-transparent and not disrupt spin-pumping into the top Pt layer. The spin diffusion length of Au is $\lambda_{sd} = 32$ nm [214] so could be expected to show some differing behaviour in this regard. Although Au and Cu can be expected to disrupt the spin-pumping differently, they will both at some thickness cause the PIM to vanish.

TR-MOKE can be used to measure the precessional motion of the magnetisation about an external applied field. It is a pump-probe technique by which a delay stage is used to sample the magnetisation state at different time intervals throughout a repeated magnetisation precession process. The laser beam hits the sample at normal incidence, hence the polar component of magnetisation normal to the film plane was measured. The technique is presented in more detail in chapter 3.

Examples of the measured magnetisation precession for the Pt/Co/Au (1-25 Å)/Pt samples are shown in Fig. 8.2. The Kerr voltage V_{Kerr} has been normalised to the amplitude of the first oscillation to allow comparison. To extract the damping parameter, the Kerr voltage, V_{Kerr}, was fitted with the damped sinusoid expression;

$$V_{\text{Kerr}} = Ae^{(-t/\tau)} \sin(2\pi f(t - t_0)) \tag{8.2.1}$$

where A is the oscillation amplitude, τ is the decay time constant, f is the precession frequency and t_0 a constant lateral offset. The damping constant was extracted using

$$\alpha = \frac{1}{2\pi f \tau} \tag{8.2.2}$$

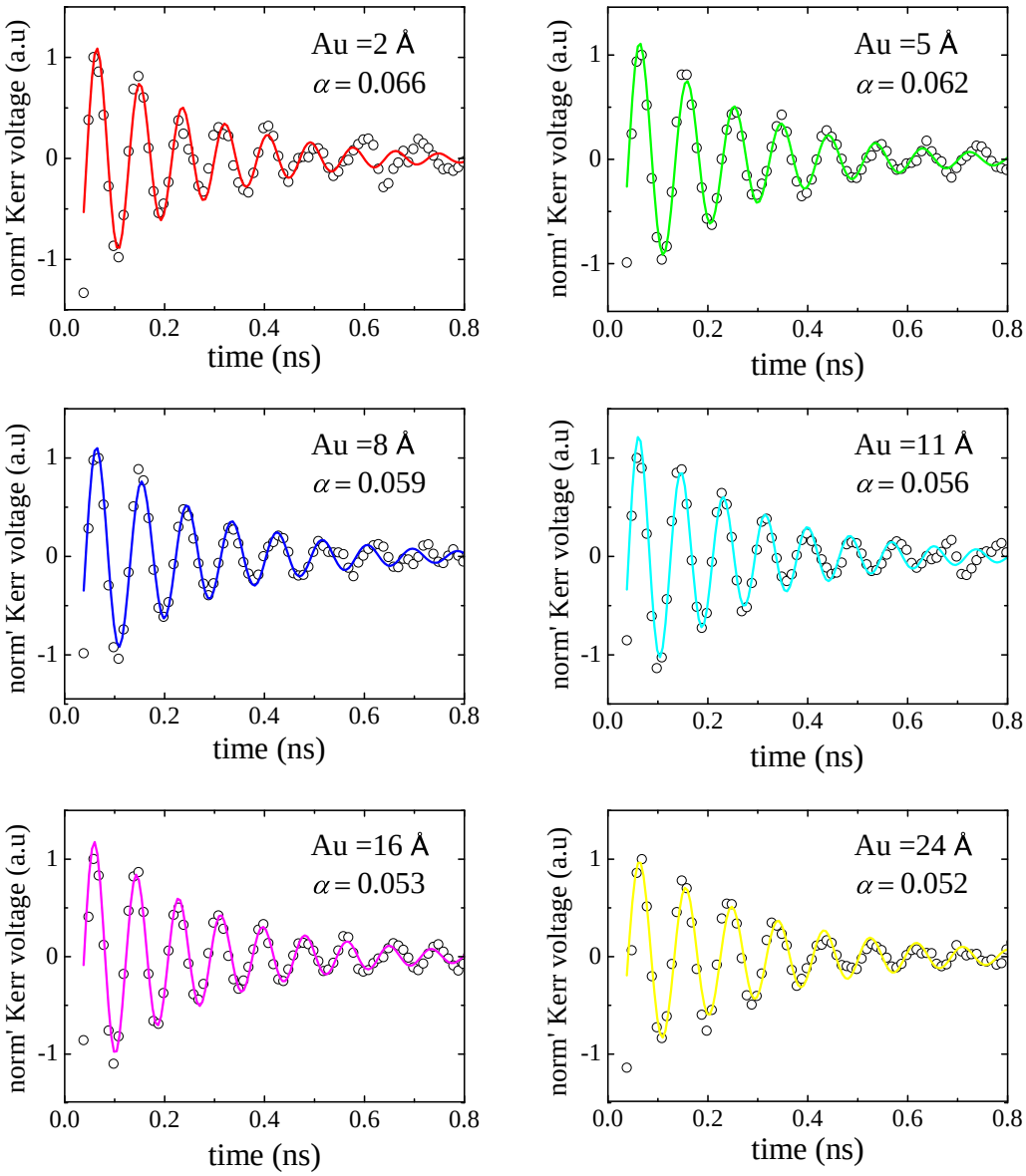

Figure 8.2: Example magnetisation precession data measured using TR-MOKE for Pt (54 Å)/Co (25 Å)/Au (1-24 Å)/Pt (26 Å) samples with different thicknesses of Au SLs. Solid lines show best fits made by A. Ganguly using equation (8.2.1), from which the precession frequency, f and damping parameter, α were extracted.

The precession is clearly apparent in all the samples and the fits are generally a good representation of the data. The calculated values of α from the fits show that the damping is reducing with increasing Au SL thickness.

The values of α for both the Au and Cu spacer series are shown in Fig. 8.3 a). The damping shows a significant reduction compared to the pure Pt/Co/Pt sample as the thickness of the SL is increased. Four contributions that could result in this decrease were

considered. Firstly the loss of PIM at the Co/Pt interface. Secondly, a reduction in *d*-*d* hybridisation, which in itself would be intimately coupled to the PIM [51, 54]. Thirdly, a reduction in two-magnon scattering as the SL thickness is increased and develops into a continuous film [78]. However, this two-magnon contribution would be primarily associated with an initial increase in magnetic damping since the initial dusting of the SL would introduce numerous scattering centres. Finally, spin-pumping through Au and Cu spacer layers into the Pt spin-sink.

Considering the two-magnon scattering contribution, insight can be gained from the precession frequency as a function of the SL thickness, as is shown in Fig 8.3 b). A drop in precession frequency is indicative of an enhanced extrinsic two-magnon scattering contribution due to island-like growth of the SL [78] and the presence of scattering centres due to the discontinuous SL. This is observed for both Au and Cu SLs. The frequency recovery for Cu SLs is more rapid and is perhaps representative of the high miscibility of Cu-Pt [215] resulting in the formation of a continuous layer of Cu more rapidly than for Au.

It is interesting that no enhancement of damping is observed for the thinnest Cu (2 Å), Au (2 Å) and Au (5 Å) SLs, where there is a dip in the precession frequency. The total damping is always reduced by the addition of the ultra-thin SL which suggests that any enhancement in damping brought about by two-magnon scattering is more than compen-

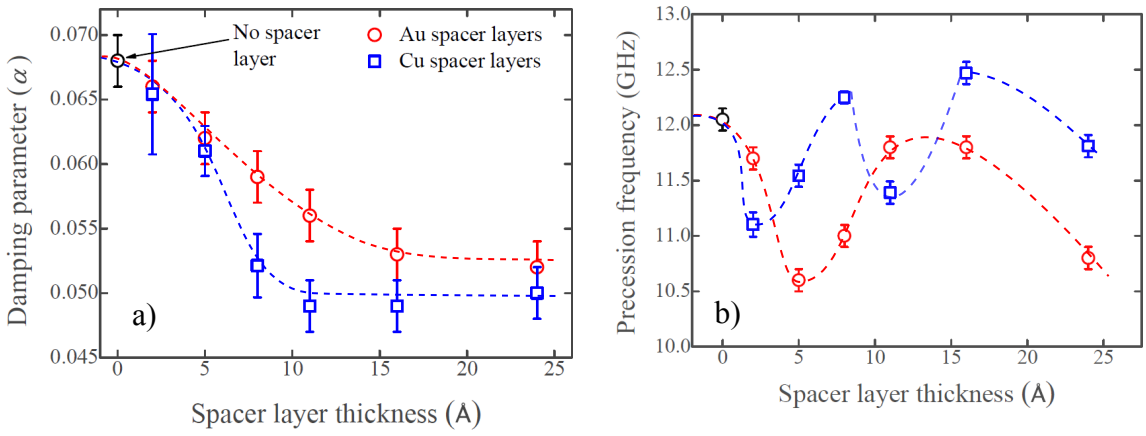

Figure 8.3: a) Extracted total damping parameter, α as a function of Au and Cu SL thickness. b) Change in precession frequency as a function of Au and Cu SLs. The same legend applies as in a). In both figures, the dashed lines are guides to the eye. All fits to the TR-MOKE data from which these parameters were extracted were made by A. Ganguly, except for the Cu (2 Å), Cu (5 Å) and Cu (7 Å) SLs which were made by the author.

sated for by the reduction in *d*-*d* hybridisation and PIM as a result of the SL. This suggests that for these samples, two-magnon scattering is not the dominant mechanism. There is a second dip in the precession frequency associated with the Cu (11 Å) SL. The origin of this is unknown and may be an outlier datapoint.

To address the contribution of spin-pumping we consider the Cu series. Here, λ_{sd} is so large in Cu that this would not be expected to have a significant effect until much greater SL thicknesses, between 50-300 nm [212]. The dramatic change in damping corresponds to a thickness comparable to that for forming a continuous layer, dropping over a thickness of just 11 Å which suggests that this is a purely interfacial effect not associated with spin-pumping. The damping parameter falls to (0.049 ± 0.002) with a Cu (11 Å) SL where the effect flattens off. However, it is likely that for thicker Cu spacer layers, between 50-300 nm, the damping would continue to fall where the spin-flip scattering within the Cu layer will contribute as the thickness approaches λ_{sd} of Cu. This weak thickness dependence has been confirmed by Mizukami *et al.* [212].

When the normal metal layer thickness is significantly below λ_{sd}, as is the case for Cu (24 Å) SL, the contribution to damping from spin-pumping, α_{SP} is governed by the spin-mixing conductivity, $g_{\uparrow\downarrow}$ of the interface and it is reasonable to approximate it as [216];

$$\alpha_{SP} = \frac{g\mu_B}{3\pi M_s} g_{\uparrow\downarrow} \frac{1}{t_{FM}} \tag{8.2.3}$$

with $\mu_B = 9.274\times10^{-21}$ erg/G is the Bohr magneton, $g = 2.17$ the bulk Landé g-factor [12], $M_s = 1400$ emu/cm^{-3} the saturation magnetisation and $t_{FM} = 25$ Å is the Co film thickness. From ref [217], the spin mixing conductivity of a Co/Cu interface was found to be $g_{\uparrow\downarrow} = 1.8\times10^{14}$ cm^{-2}. This yields a contribution of $\alpha_{SP} = 8.2\times10^{-5}$ which clearly is significantly smaller than the observed drop in damping due to the Cu SL thickness. Therefore the change in spin-mixing conductance associated with the new Co/Cu interface is not sufficient to explain the large drop in damping in terms of spin-pumping over such a small lengthscale .

The dependence on the Au SL also shows a drop in the damping parameter with increasing SL thickness. However, the rate of reduction is less dramatic, falling to (0.052 ± 0.002) over a SL thickness of 16 Å. Again, this is not a consequence of spin-pumping, since the

Au SLs with the shorter λ_{sd} would be more effective at isolating the Pt spin-sink and therefore would be expected to modify the damping parameter more rapidly than the Cu SLs. The difference in the rate of modification of the damping is likely associated with the interface structure, by which Au would be associated with island like growth and would likely require a greater thickness to form a continuous film.

The larger damping with a Au (24 Å) SL compared to that with a Cu (24 Å) SL reflects the difference in contributions from the SLs themselves, where the Au over-layer with the larger SOI would be expected to contribute more to the total damping.

In summary, the drop in magnetic damping with SL thickness cannot be explained by changes in two-magnon scattering or spin-pumping, hence it is a consequence of the changes in *d-d* hybridisation or PIM or both. We now discuss the damping parameter in the context of the PIM as a function of SL.

8.2.3 Discussion of the magnetic damping with regard to the proximity induced magnetism

As was shown in chapter 6, the PIM is extremely sensitive to the interface structure. Cu is fully miscible within Pt [215] and therefore in a similar manner to Ir, would be expected to cause the PIM to vanish more rapidly than Au with increasing Cu thickness. This is in agreement with the observed behaviour in Fig. 8.3 a).

For the Au SL series, the PIM can be plotted against the damping parameter directly and is shown in Fig. 8.4. It is clear from this figure that any potential correlation between PIM and magnetic damping with increasing Au SL thickness is not a simple linear relationship. The magnetic damping and PIM fall on similar lengthscales. However, the damping parameter continues to drop once the PIM at the top Co/Pt interface can be considered to have been entirely eradicated. As stated before, there are multiple contributions to the damping parameter as the SL thickness is increased, so this does not rule out the importance of PIM.

As the SL thickness is increased past 11 Å and the PIM has vanished, continued improvements in interfacial structure with SL would be expected to further reduce the contributions from two-magnon scattering. However, this would manifest itself as a continuous increase in precession frequency which is not observed. It may be that the *d-d* hybridisation

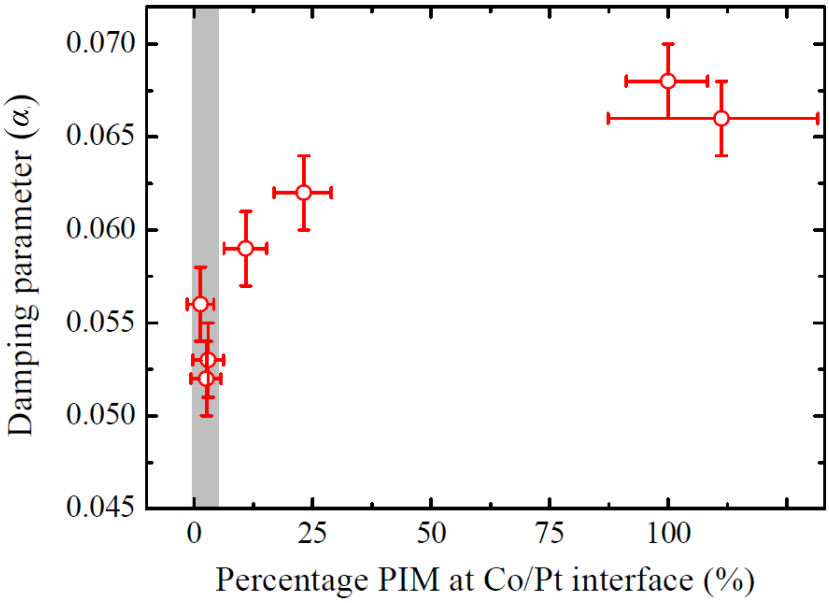

Figure 8.4: Damping parameter plotted against the percentage PIM at the top Co/Pt interface as Au SLs of increasing thickness are inserted to disrupt the PIM. The percentage is relative to the PIM at the Co/Pt interface prior to the addition of Au. The grey area denotes the region where the PIM can be considered to have vanished based on the sensitivity of the XRMR measurement.

continues to have a significant effect on the electronic structure of the Co, but not enough on the Pt to manifest itself as a magnetic polarisation. The continued addition of Au in this case would reduce the hybridisation and continue to reduce the intrinsic contribution to damping.

It would seem then that the change in damping is dominated by the changing electronic structure in the interfacial region through the orbital hybridisation. This is in agreement with theoretical study of Barati *et al.*, who concluded that the *d*-*d* hybridisation of bands crossing the Fermi energy results in an enormous enhancement of magnetic damping [76]. However, the PIM is intimately linked with orbital hybridisation [51, 54]. With this respect it is fundamentally difficult to decouple the contributions of hybridisation and PIM because without the hybridisation the Pt would not be magnetic.

8.2.4 Conclusion: Proximity induced magnetism and magnetic damping

The magnetic damping in Pt/Co/Au/Pt and Pt/Co/Cu/Pt samples has been measured with varying thickness of Au and Cu SLs. With both SLs there was a dramatic reduction in

damping as SL thickness was increased. For Au SLs the reduction occurred over a larger lengthscale than Cu and it is expected that this is because Au may exhibit island like growth and consequently require a greater thicknesses to form a continuous film relative to Cu.

The rapid drop in damping cannot be explained by spin-pumping since the drop in damping occurred over a lengthscale that is comparable to one atomic layer and the values of λ_{sd} are too large for both Au and Cu to account for this. Two-magnon scattering would be expected to enhance the damping and there is an indicative drop in the precession frequency for the thinnest SLs. However, this was not expressed in the damping parameter which showed a reduction in damping for all SL thicknesses. Therefore the dominant mechanism for the damping is associated with the reduction in *d*-*d* hybridisation that arises due the large density of *d*-states at the Fermi energy for Pt and is disrupted by the increasing thickness of SLs used. However, it is known that this hybridisation is also intimately linked to the PIM.

Plotting the PIM at the Co/Pt interface for the Au SLs against the magnetic damping parameter showed non-linear behaviour and that the damping parameter continued to fall after the PIM could be confirmed to have vanished. This suggested that the main contribution to the enhanced damping in the Pt/Co/Pt structures was the *d*-*d* hybridisation at the interface. Any dependence on the PIM is non-trivial, with the effects of the orbital hybridisation contribution continuing after the induced moment has vanished. It is therefore clear that the enhanced magnetic damping observed in Pt/$Ni_{80}Fe_{20}$/Pt and Pd/$Ni_{80}Fe_{20}$/Pd by Mizukami *et al.* [209] had a significant contribution from the large density of *d*-states at E_F in Pt and Pd. However, since this is a property inherent to PIM, the induced magnetism cannot be disregarded in the context of the enhanced damping, and fundamentally it is challenging to decouple this from the *d*-*d* hybridisation.

8.3 Dzyaloshinskii-Moriya interaction

In the second part of this chapter, the role of PIM in the DMI is considered. This work was motivated by the results of Ryu *et al.* [55] in the group of S.S.P. Parkin which are discussed in the following section.

8.3.1 Link between proximity induced magnetism and Dzyaloshinskii-Moriya interaction from domain wall velocity measurements

As was discussed in chapter 2, the DMI is an antisymmetric exchange interaction that favours orthogonal alignment of spins and the Hamiltonian takes the form;

$$\hat{\mathcal{H}}_{\mathrm{DM}} = \boldsymbol{D}_{\mathrm{ij}} \cdot \boldsymbol{S}_{\mathrm{i}} \times \boldsymbol{S}_{\mathrm{j}} \tag{8.3.4}$$

where $\boldsymbol{D}_{\mathrm{ij}}$ is the Dzyaloshinskii-Moriya vector, which is non-zero only in the presence of inversion asymmetry and couples the spins $\boldsymbol{S}_{\mathrm{i}}$ and $\boldsymbol{S}_{\mathrm{j}}$. The DMI stabilises Néel magnetic domain walls by acting as an effective internal magnetic field and also induces a specific chirality which depends on the sign of this effective DMI field [13, 21, 45].

Using Kerr microscopy, Ryu *et al.* [55] made a series of measurements of domain wall velocities in perpendicularly magnetised nanowires driven by the spin Hall effect. Each nanowire had a different heavy metal underlayer (UL), which was either Au, Pt, Pd or Ir in an UL/Co/Ni/Co/TaN structure and is shown schematically in Fig. 8.5 a). They found that the domain wall velocity was very sensitive to magnetic fields applied longitudinally along the length of the nanowires for Pt, Pd and Ir underlayers, which all exhibit at least a moderate PIM [40, 41, 184].

By applying a longitudinal magnetic field, H_{long} which acts along the domain wall width, the effective field due to the DMI can be cancelled and the current-induced domain wall motion stopped. This occurs because the spin-Hall effect can only drive Néel type magnetic domain walls [13]. The magnitude of this magnetic field was referred to as the crossing field and it is proportional to the strength of the DMI. If the Pt underlayer was replaced with Au, which has a minimal PIM, no dependence on the longitudinal magnetic field was observed. Furthermore, as shown in Fig. 8.5 a), the crossing field reduced dramatically as ultrathin Au spacer layers were inserted at the lower Pt/Co interface, on a lengthscale similar to that expected for the PIM to vanish. Likewise, the domain wall velocity reduced on a similar length scale. From this it was concluded that the PIM was critical to obtain a significant DMI.

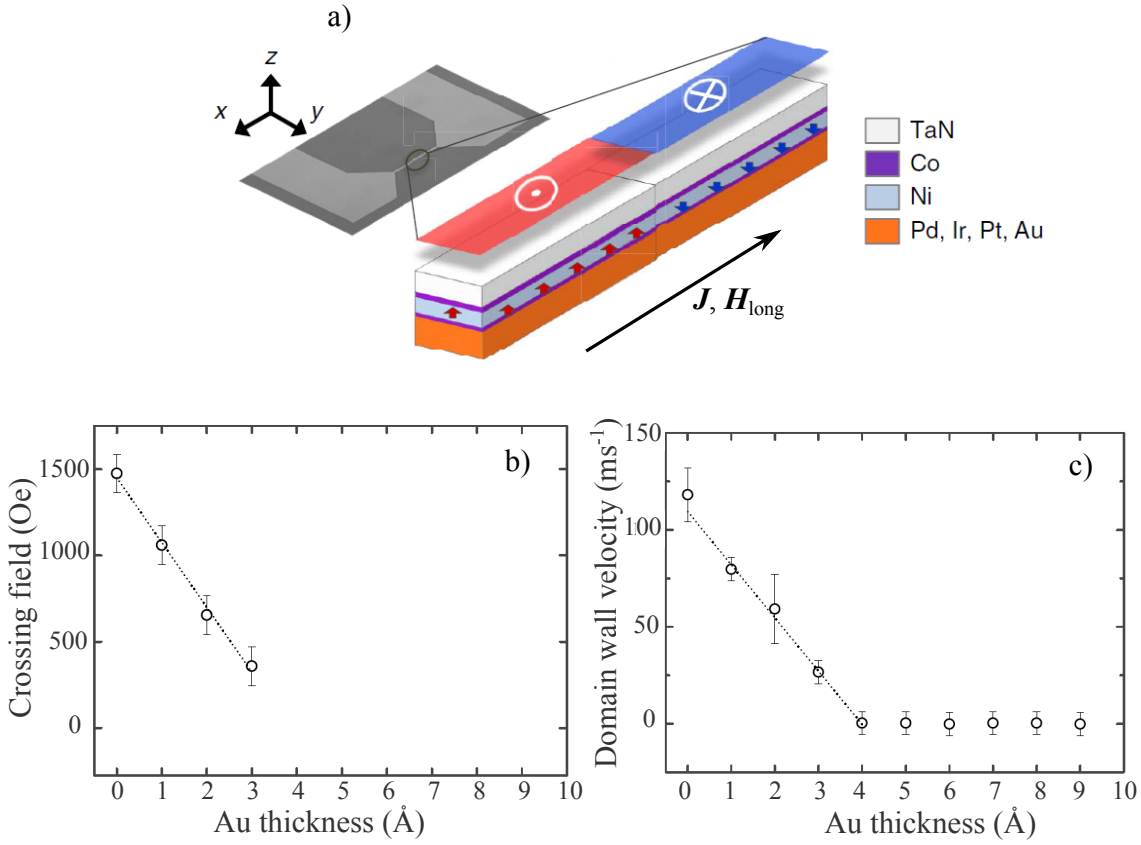

Figure 8.5: a) Schematic of sample structure used by Ryu *et al.* [55]. The longitudinal field, H_{long}, was applied along the length of the nanowire and current density, J, used to drive domain wall motion through the spin-Hall effect. b) Crossing field as a function of Au SL inserted between the Pt/Ni underlayer interface. Crossing fields were only shown up to Au (3 Å) in the manuscript. The Pt underlayer was 15 Å thick. c) Domain wall velocity as a function of Au SL thickness inserted between the Pt/Ni underlayer.

8.3.2 Dzyaloshinskii-Moriya interaction as a function of heavy metal spacer layer thickness

Following the results of Ryu *et al.* [55], in order to test whether the PIM is crucial to the DMI, the effective DMI constant D_{eff} was extracted from the Pt/Co/Au,Ir/Pt samples.

The effective DMI constant D_{eff} was determined using Brillouin light scattering (BLS) as a function of Au and Ir SL thickness in the Pt/Co/SL/Pt sample series. The DMI introduces non-reciprocity for spin-wave propagation dependent on the sign of the spin-wave number. This manifests itself as a frequency shift for spin-wave modes travelling in opposite directions. The BLS technique was discussed in more detail in chapter 3.

The measurement geometry was such that the Damon-Eshbach surface spin-wave mode

was probed. The frequency of the stokes and anti-stokes inelastic magnon lines were compared, where any shift in frequency was due to the interfacial DMI.

Two examples of BLS spectra for SLs of Au (2 Å) and Au (16 Å) are shown in Fig. 8.6 a) and b) respectively. The black curves show the spectra reflected in the y-axis in order to emphasise the frequency shift between stokes and anti-stokes lines ($\Delta f = f_s - f_{as}$). For the Au (2 Å) SL a small frequency shift of $\Delta f = 0.14$ GHz is just resolvable. The frequency shift for the Au (16 Å) SL sample is much larger with $\Delta f = 0.88$ GHz and can be clearly observed as a difference in peak position between the stokes and anti-stokes lines.

If the DMI is purely an interfacial effect, then the expected thickness dependence would follow $D_{\text{eff}} = D_s/t$ where D_s is the interfacial DMI constant, which is the more fundamental parameter. The frequency shift, Δf, can be converted to the interfacial DMI term using [12];

$$D_s = D_{\text{eff}} t_{\text{FM}} = \frac{\pi}{2\gamma} \frac{M_s t_{\text{FM}} \Delta f}{k_{\text{sw}}} \tag{8.3.5}$$

where γ is the gyromagnetic ratio $\gamma = g\mu_B/\hbar = g \times 8.794 \times 10^6$ Hz/G, $t_{\text{FM}} = 25$ Å is the ferromagnetic layer thickness and k_{sw} is the spin-wave number given by;

$$k_{\text{sw}} = \frac{4\pi}{\lambda_{\text{opt}}} \sin\theta \tag{8.3.6}$$

where $\lambda_{\text{opt}} = 0.532$ μm is the laser wavelength and $\theta = 50°$ is the angle of incidence with respect to the surface normal. These were kept constant between measurements, hence

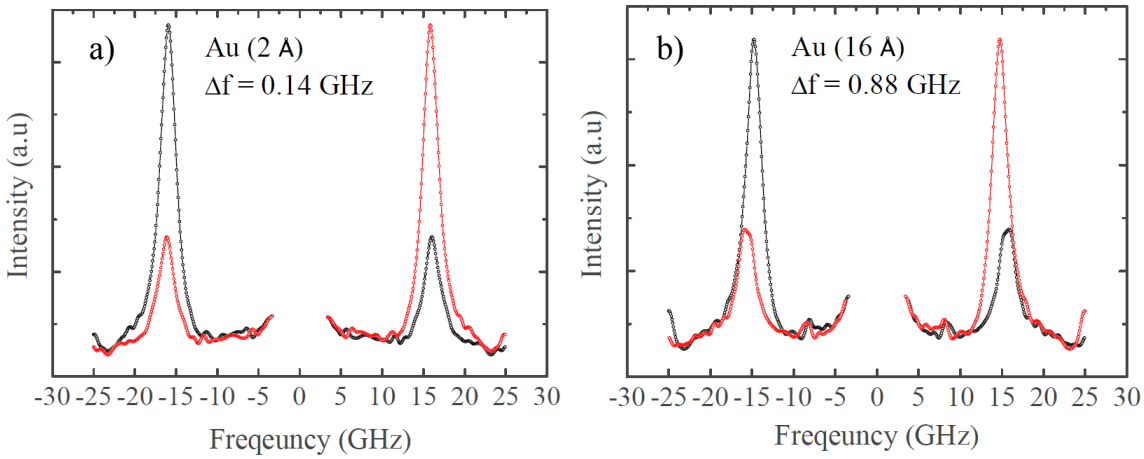

Figure 8.6: Stokes and anti-stokes magnon lines for the a) Pt/Co/Au (2 Å)/Pt and b) Pt/Co/Au (16 Å)/Pt samples under a +4 kOe magnetic field. The red spectrum shows the distribution reflected in the y-axis in order to show the frequency shifts more clearly.

scattering with spin-waves with wave numbers $k_{sw} = 18.095\ \mu m^{-1}$ were measured.

The bulk saturation magnetisation of Co, $M_s = 1400$ emu/cm^3 was used for all samples. This is justified since typical values of PIM for Pt are $\mu_{Pt} = 0.21\ \mu_B$/atom [40] compared to $\mu_{Co} = 1.4\ \mu_B$/atom for Co. Therefore one can calculate the increase in Co thickness, Δt_{Co}, which would be equivalent to a 10 Å wide Pt polarised interface t_{PIM}, which is a reasonable approximation for the thickness of the polarised interface based on the results in chapter 6. Comparing the μ_{Pt} and μ_{Co} moments, the expression;

$$\Delta t_{Co} = \frac{\mu_{Pt}}{\mu_{Co}} \frac{M_{Co}\rho_{Pt}}{\rho_{Co}M_{Pt}} t_{PIM} = 1\ \text{Å} \tag{8.3.7}$$

is obtained, where $\rho_{Pt}, \rho_{Co}, M_{Pt}, M_{Co}$ are the mass density and molar masses of Pt and Co respectively. The value of Δt_{Co} obtained is equal to the error in the Co thickness, hence any magnetisation measurement would be dominated by the Co contribution and the Pt polarisation would be lost in the error associated with the sample volume.

The D_s calculated from equation (8.3.5) for the different SL thicknesses is shown in Fig. 8.7. The first thing to note is that with no SL no net D_s is observed. This is in contrast to the measurements of D_s made through domain bubble expansion experiments by Hrabec *et al.* [44], which found that unless the structure was epitaxial, the asymmetry of the microstructure between the buffer Pt/Co and top Co/Pt interface can still give rise to a finite net D_s in symmetric Pt/Co/Pt multilayers with perpendicular magnetic anisotropy. The interfacial nature of DMI requires that it is larger for thinner Co films [12], hence this difference could be related to the comparatively thick polycrystalline Co used here meaning that we are not sensitive to the microstructure of the interfaces.

The rise in D_s with SL thickness is on a lengthscale consistent with the interface width determined by XRR, which was approximately 6 Å, and was the same for both Au or Ir SLs. This rapid rise in D_s with Ir SL thickness is consistent with the 7 Å found for perpendicular Pt/Co/Ir/Pt structures elsewhere [44].

Since the PIM decay length is governed by an exponential [40], here the D_s for the Au and Ir SL series have been fitted with the function

$$D_s = D_0(1 - \exp(-t/t_0)) \tag{8.3.8}$$

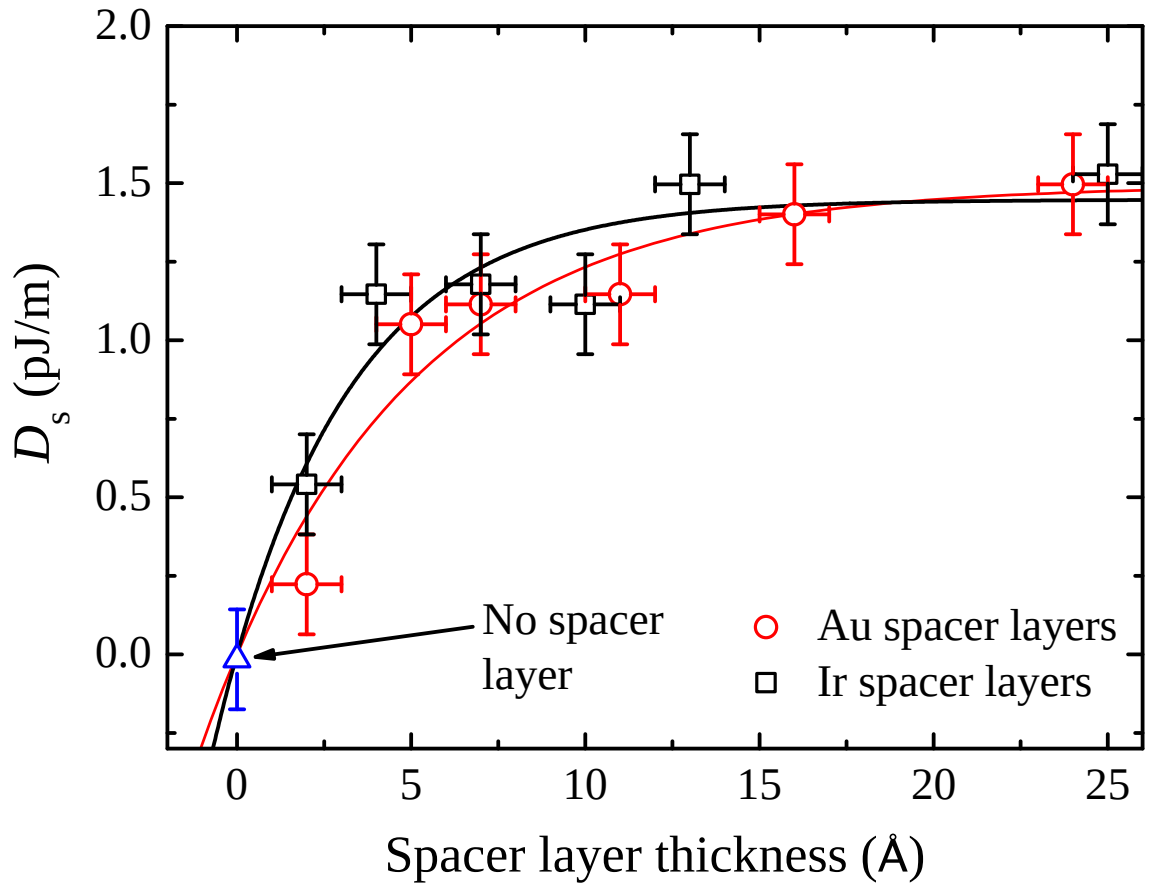

Figure 8.7: The change in interfacial DMI constant, D_s, with the addition of Au and Ir SLs of increasing thickness at the Co/Pt interface. The distributions have been fitted with equation (8.3.8).

where t_0 is the decay length of the exponential and D_0 is the saturation value of the interfacial DMI constant once a complete Au or Ir interface has formed. The values of t_0 extracted for the Ir SLs was (4 ± 1) Å and for Au SLs was (4.0 ± 0.6) Å. These are both larger than the values extracted in chapter 6 from the exponential decays fitted to the PIM as a function of SL thickness, which were (2.0 ± 0.4) Å and (2.2 ± 0.3) Å for Ir and Au SLs respectively.

Interestingly D_s saturates to very similar values for the Au and Ir SLs, with D_0 = (1.49 ± 0.13) pJ/m and (1.45 ± 0.12) pJ/m for Au and Ir SLs respectively. These values are comparable with previous work for Pt/Co/AlOx [12] with perpendicular magnetic anisotropy which gave a slightly higher D_s of 1.7 pJ/m. As would be expected, the sign is also the same ($f_{as} > f_s$), since Pt is at the bottom in both cases. This would suggest that in both cases the dominant contribution to D_s is from the buffer Pt/Co interface.

The *ab initio* calculations of H. Yang *et al.* [56] predicted a D_s of -0.39 pJ/m for Au/Co

and -0.24 pJ/m for Ir/Co, compared to +1.95 pJ/m for Pt/Co interfaces. From this it would be expected that the total D_s would saturate at 2.34 pJ/m for Au, and 2.19 pJ/m for Ir SLs. These predicted values are all above the maximum D_s observed, which was (1.53 $\pm$ 0.15) pJ/m. Structural imperfections reduce D_s which would explain why the measured value is lower than that predicted for an ideal structure by Yang *et al.* [56]. The difference in D_s predicted between the Au and Ir SLs is 0.15 pJ/m, which is the same as the error and therefore below the resolution of the measurement, particularly when structural imperfections are taken into account.

In the next section the results are discussed with reference to the PIM characterised in these samples.

8.3.3 Proximity induced magnetism and Dzyaloshinskii-Moriya interaction

We now turn to focus directly on correlations between the DMI and PIM data. Firstly, no net D_s was detected for the symmetrical Pt/Co/Pt sample, even though the PIM at the Co/Pt and Pt/Co interfaces was substantially different. This suggests that the DMI requires inversion asymmetry over the whole ferromagnet and that differences in PIM at each interface do not contribute. However, it must be noted that the sensitivity to D_s reduces as the ferromagnet thickness increases and it may be that the difference is below the resolution of the measurement for the 25 Å Co films used in this study.

The rise of the D_s in Fig. 8.7 with SL thickness is due to the SL preventing the complete cancellation of the DMI contributions from the top Co/Pt and bottom Pt/Co interfaces. However, if there exists a contribution from the PIM, this would change the way in which the net DMI emerges for the different SLs. Since the XRMR measurements suggested that the Ir SLs reduce the moment at the top Pt interface more rapidly than the Au SLs, then it would therefore cause the DMI at that Co/Pt interface to vanish more rapidly as well, which in turn would result in a more rapid rise in total DMI from the sole contribution of the buffer Pt/Co interface.

The fits of equation (8.3.8) in Fig. 8.7 suggest this is the case, but it would be wrong to take this as conclusive since the difference is comparable to the error bars on the SL thickness.

Regarding the differences between the DMI contributions from the Co/Ir and Co/Au interfaces themselves, it would be expected that the induced moment on Ir [184,188] would be greater than that for Au [53]. This forms part of the argument for the importance of PIM by Ryu *et al.* [55] for which Ir exhibited a crossing field and Au did not. Assuming that both Co/Ir and Co/Au produce positive DMI contributions (since the Au and Ir layers are now on the top) [44,56,218], hence if PIM is critical to DMI then it would be expected that after the formation of a complete SL then the Pt/Co/Ir/Pt samples would have the largest total D_s. However, the maximum values, which correspond to the thickest Au and Ir SLs, show that the D_s is the same. This is in agreement with Yang *et al.* [56] who predicted only a small difference between Au and Ir, even though the PIM would be different.

To gain further insight into any potential correlations between the DMI and PIM, the percentage moment lost at the top Pt interface is plotted against D_s in Fig. 8.8. The dashed line represents a 1:1 correspondence. The trend initially seems linear in the ultrathin SL

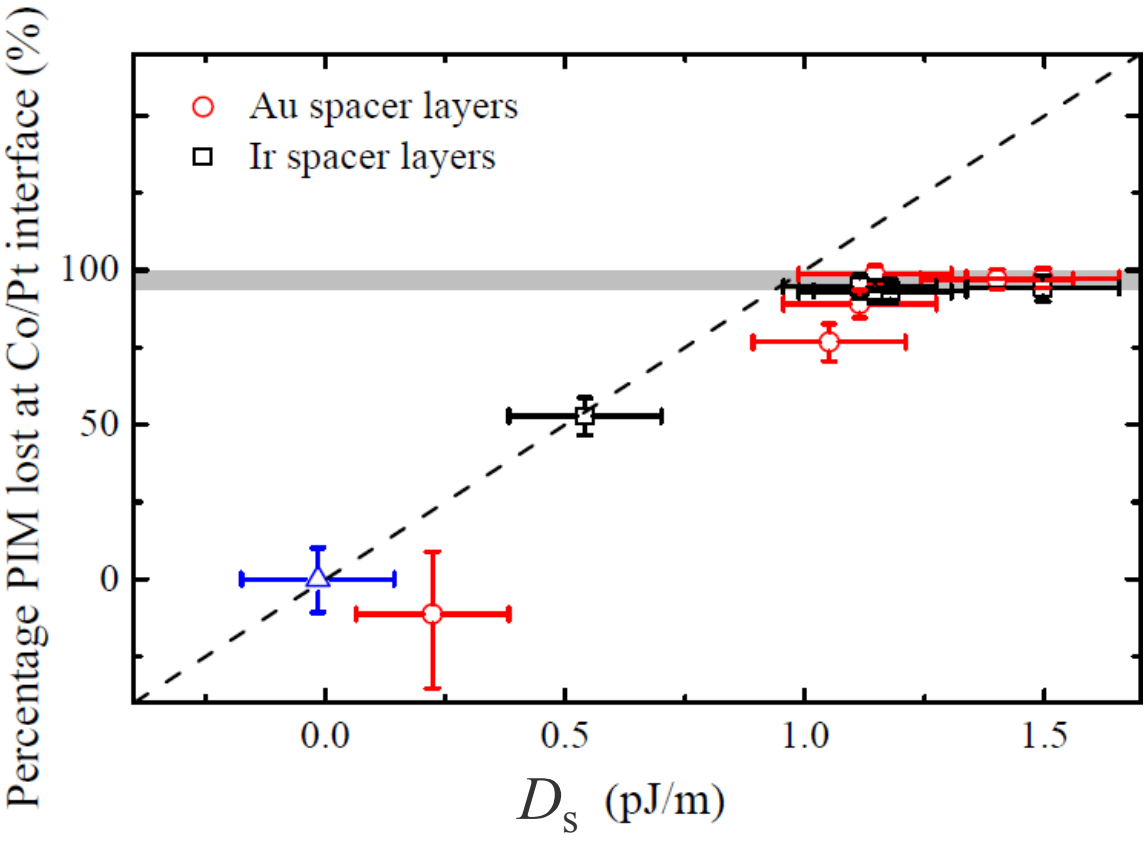

Figure 8.8: The percentage moment at top Co/Pt interfaces plotted against the D_s for Au and Ir SLs. The dashed line denotes a 1:1 correlation. It can be seen that more datapoints lie to the right of the line. The grey area denotes the region where the PIM can be considered to have vanished based on the sensitivity of the XRMR measurement.

regime, although the shortage of datapoints in the lower frequency DMI shift region makes this difficult to say conclusively. Most data points fall on the right hand side of the line, suggesting that D_s is rising more rapidly than the PIM is vanishing. The lateral placement of datapoints where the PIM is entirely lost reflects that the DMI continues to rise after the induced moment has vanished. The D_s associated with the Co/Ir and Co/Au interfaces must be small in comparison to that from the Pt/Co interface since they both converged to approximately the same D_s with the thickest SLs. Therefore this continued rise after the PIM has gone must be associated with the continued change in the top Co interface, notably the reduction in Pt atoms at the alloyed top Co interface as the SL is made thicker.

8.3.4 Conclusion: Dependence of the Dzyaloshinskii-Moriya interaction on proximity induced magnetism

The interfacial DMI constant, D_s, was measured in Pt/Co/SL/Pt samples where the PIM at the top Co/Pt interface with respect to the addition of Au and Ir SLs was known. The change in D_s with increasing SL thickness was discussed in context of the PIM at the top Co/Pt interface.

No net D_s was observed in the symmetric Pt/Co/Pt sample even though the induced moments at the Pt/Co and Co/Pt interfaces were different. With the addition of SLs at the top Co/Pt interface, the net D_s emerged due to the prevention of the cancellation of the identical DMI contributions from the bottom Pt/Co and top Co/Pt interfaces. Fits to the datasets suggested that the rise in D_s occurred at the same rate with both Au and Ir SLs, even though the XRMR data indicated that Ir destroyed the PIM on a shorter lengthscale. However, the error in the decay lengths for Au and Ir were relatively large due to the shortage of datapoints in the ultrathin SL region.

The saturation values of D_s were very similar for both Au and Ir, which is consistent with the predictions of Yang *et al.* [56] and disagrees with the difference expected based on the difference in PIM that would be associated with Au and Ir. This is in contradiction with the conclusions of Ryu *et al.* [55] who emphasised the importance of PIM within DMI .

Plotting the Co/Pt interfacial PIM against D_s demonstrated that the D_s continues to rise after the PIM had vanished. These results demonstrate that the dominant contribution to the DMI is not the PIM but the presence of Pt atoms at the top Co interface.

9 Conclusions and further work

In this thesis, phenomena relating to the spin-orbit interaction have been studied, namely, the anisotropic magnetoresistance, the spin Hall effect, the Rashba effect, the Dzyaloshinskii-Moriya interaction and magnetic damping. When investigating these phenomena, particular attention was given to the role of the interfaces and how these can modify the behaviour. In particular the proximity induced magnetism in Pt was characterised in detail, and the consequences of this interfacial polarisation were investigated with regard to the DMI and magnetic damping.

9.1 Thesis conclusions

In chapter 4, AMR was measured in Ni, $Ni_{95}V_5$ and $Ni_{95}Cr_5$ films of various thickness and analysed theoretically using the Campbell, Fert and Jaoul (CFJ) model. The films were structurally characterised using XRR and TEM, from which it was established that the onset of discontinuities occurred for Ni films thinner than 6 nm. From the AMR measurements in these films it was found that a rapid loss of the absolute resistivity change due to AMR ($\Delta\rho$) occurred for films thinner than 6 nm irrespective of the dopant. Prior to this investigation, this thickness dependence of $\Delta\rho$ was unexplained. This loss of $\Delta\rho$ coincided with the onset of discontinuities in the Ni films. The relationship between sample morphology and AMR was further evidenced by the linear scaling between $\Delta\rho$ and the film resistivity. The spin-wave stiffness, D, was measured in the Ni films and a linear correlation between $\Delta\rho$ and D was observed. From the reduction in D with reducing film thickness, it was inferred that the magnon density of states was enhanced as film thickness reduced. In turn, this would lead to enhanced electron-magnon scattering, which is a spin-flip scattering process, which then results in mixing of the spin-channels within the Mott-two-current model, effectively preventing spin-dependent conduction and coupling the spin-channels

leading to the loss of AMR.

Within the CFJ model, this spin-flip scattering leads to an enhancement of the spin-mixing resistivity, $\rho_{\downarrow\uparrow}$, which is isotropic with respect to the magnetisation orientation. It was shown that the functional form of the film resistivity can be used to include a generalised thickness dependence to $\rho_{\downarrow\uparrow}$. This successfully reproduced the AMR data and provides a generalised explanation and a method by which the thickness dependence of $\Delta\rho$ can be found in any system, so long as the functional form of the thickness dependence of the film resistivity is known.

In chapter 5, SOTs were studied in systems with in-plane magnetic anisotropy as well as systems with weak out-of-plane magnetic anisotropy. First a $Ni_{81}Fe_{19}$ (4 nm)/Pt (4.5 nm) bilayer system with in-plane magnetic anisotropy was investigated, whereby the field-like torque was studied using the simultaneous measurement of the longitudinal MOKE and the planar Hall effect (PHE). Here, it was shown that on the application of current densities greater than 0.5×10^{10} Am^{-2} the shape of the PHE magnetic field sweeps were dramatically modified. Comparison of these PHE measurements at high current density with those measured at different in-plane field angles with respect to the current suggested that the SOT was altering the magnetisation reversal.

Following this, a Pt (1 nm)/Co (0.6 nm)/Pt (5 nm) multilayer which had weak PMA was investigated using polar MOKE with a lock-in detection method. Using this method the contributions of damping-like and field-like torques could be separated by applying the in-plane magnetic field longitudinal or transverse to the current flow respectively. With this sample, current-induced magnetisation reversal (CIMR) was observed using current densities as low as 4×10^{10} Am^{-2} . This was considered to be the result of the weak PMA. To induce CIMR, an in-plane magnetic field along the current direction was required, and increasing the magnitude of this reduced the critical switching current. Since the field was applied longitudinal to the current flow, the magnetisation switching was due to the damping-like torque. Applying the field transverse to the current flow investigated the field-like torque, for which no evidence for the existence of this was found in this sample. Since the Pt/Co/Pt multilayer was symmetric and lacking structural inversion asymmetry (SIA), this result was consistent with the Rashba effect as the origin of the field-like torque.

Alongside this, a Pt (3 nm)/Co (0.6 nm)/MgO (2 nm)/Pt (1.5 nm) multilayer, which

also had weak PMA, was investigated using the same polar MOKE with lock-in detection method. However, the sample showed signs of degradation following the SOT measurements, so these results were treated with caution. It was shown that the magnetisation oscillation due to the SOT measured by sweeping the longitudinal field could be replicated by sweeping the DC offset applied to the AC current used to excite the SOTs. A single conversion factor of $(-39 \pm 1) \times 10^{-10}$ Oe/Am^{-2} was found that mapped the DC offset sweep data onto the longitudinal field sweep data. From this a spin Hall angle of (0.13 ± 0.06) was calculated, which is consistent with values found elsewhere in the literature [81, 160]. Again no field-like torque was observed, even though this sample had SIA. However, it is possible the sample degradation was associated with a loss of integrity to the MgO layer, and therefore disrupted the SIA.

In chapter 6, the PIM in Pt was studied in Pt (54 Å)/Co (25 Å)/Pt (26 Å) multilayers with in-plane magnetic anisotropy as a function of Au and Ir spacer layers inserted at the top Co/Pt interface with thicknesses between 2-20 Å. XRMR was used to obtain the depth resolved PIM throughout the sample cross-section in order to establish the spacer layer thickness over which the PIM existed.

The spin asymmetry ratio was measured at the Pt-L_3 edge and was therefore sensitive only to the Pt induced moment. The structural scattering length density (sSLD) and magnetic scattering length density (mSLD) profiles for each sample were extracted from the best fits to the spin asymmetry. From the mSLD for the Pt/Co/Pt sample with no spacer, it was shown that a larger induced moment existed at the top Co/Pt interface compared to the buffer Pt/Co interface. Enhanced intermixing at the top Co/Pt interface compared with the buffer Pt/Co interface has been observed in Co/Pt multilayers in the literature [197]. However, here no difference was observed in the interface widths of the Pt/Co and Co/Pt interfaces extracted from best fits to the specular reflectivity. However, XRR is not capable of separating the contributions from intermixing and topographical roughness, so this similarity in interface width extracted for the Pt/Co and Co/Pt interfaces does not exclude the possibility of different degrees of intermixing between the interfaces.

The insertion of an Ir (2 Å) spacer layer resulted in a significant reduction in PIM at the top Co/Pt interface. In contrast a Au (2 Å) spacer layer made little difference to the PIM. Further increasing the thickness of the Au and Ir spacer layers resulted in a dramatic loss of

PIM. The PIM at the Co/Pt interface could be considered to have vanished for a Au spacer layer thicker than 11 Å and for an Ir spacer layer thicker than 4 Å. The percentage PIM remaining at the Co/Pt interface was plotted as a function of spacer layer thickness and fitted with exponentials, from which decay lengths of (2.2 ± 0.3) Å and (2.0 ± 0.4) Å were obtained for the Au and Ir SLs respectively. This is referred to later when comparing the characteristic lengthscale of the PIM with that observed in the same samples for the DMI.

In an attempt to consider the role of interface morphology on the PIM, the ratio of spacer layer interface width to spacer layer thickness was calculated using the parameters extracted from the specular reflectivity fits. By comparing this with the percentage PIM remaining at the Co/Pt interface it was shown that for the Ir (4 Å) spacer layer, the PIM was eradicated before a continuous layer had formed. In contrast, the Au spacer layers showed that the PIM was only lost after the formation of a continuous film. This further emphasised the importance of intermixing and alloying at the interface with regard to the PIM. Interfacial alloying of Pt with the spacer layer modifies the density of states and prevents Pt from satisfying the Stoner criterion [198]. This therefore demonstrates the importance of electronic hybridisation and the influence the interface structure has on this. The difference in behaviour between Au and Ir was therefore attributed to the difference in miscibilities between Pt-Au [194] and Pt-Ir alloys [193], resulting in a greater degree of alloying for Ir spacer layers and a greater degree of hybridisation between the Pt and Ir.

In chapter 7 XRMR was used to investigate Pt (50 Å)/Co (t)/Pt (50 Å) multilayers with different Co thickness, t. The range of Co thicknesses were between 4-20 Å such that the magnetic anisotropy of the Co transitioned from out-of-plane to in-plane with increasing Co thickness. Longitudinal and polar MOKE measurement were used to characterise the in-plane and out-of-plane magnetisation reversal for the whole Pt/Co/Pt multilayer respectively. The longitudinal MOKE loops showed a decreasing remanence with decreasing Co thickness, consistent with the changing magnetic anisotropy of the film. Following this, element specific hysteresis loops were measured at the Pt L_3 edge which were sensitive to the in-plane magnetisation orientation of the polarised Pt only. The extracted remanence and coercive fields from the longitudinal MOKE and element specific hysteresis loops were very similar. The element specific hysteresis loops reproduced the longitudinal MOKE loops and reflected the changing magnetic anisotropy of the Co with decreasing thickness,

therefore confirming that the polarised Pt obtained the same magnetic anisotropy as the Co.

In chapter 8, the same samples for which the Pt PIM had been characterised in chapter 6 were used to investigate potential correlations between the PIM, magnetic damping and the DMI. Time-resolved MOKE was used to measure the Pt/Co/Au (t)/Pt samples to extract the magnetic damping parameter as a function of Au spacer layer thickness. Furthermore, a series of Pt/Co/Cu (t)/Pt samples were also measured in order to compare the contribution to damping from spin-pumping. A rapid drop in magnetic damping was observed for both spacer layers, where for Au the damping parameter fell to a value of (0.052 ± 0.002) over a Au spacer thickness of 16Å, whereas for Cu the damping parameter fell to (0.049 ± 0.002) over a Cu spacer thickness of 11 Å.

The change in damping could not be explained by spin-pumping due the short lengthscale that it occurred over and the magnitude of the change. It was concluded the that primary contribution was the reduction in *d-d* hybridisation at the interface, and also consequently the PIM, as the spacer layer thickness increased. By comparing the change in damping with the change in PIM for the Pt/Co/Au (t)/Pt samples, it was demonstrated that the damping continued to fall after the PIM in the top Pt layer had vanished. This showed that any dependence of the magnetic damping on the polarisation of the Pt is non-trivial, and that the dominant contribution is due to the *d-d* hybridisation. However, it is fundamentally challenging to decouple the *d-d* hybridisation from the PIM, since this in itself is the origin of the PIM.

In the final study, the DMI was investigated in the Pt/Co/Au (t)/Pt and Pt/Co/Ir (t)/Pt samples in order to investigate the correlation between DMI and PIM observed by Ryu *et al.* [55]. The interfacial DMI constant, D_s was extracted using Brillouin light scattering. No measurable D_s was found for the Pt/Co/Pt sample with no spacer layer, even though the induced moments at the top and bottom interfaces were different.

Introducing the Au and Ir spacer layers resulted in a rapid rise in D_s, since the spacer layer prevented the cancellation of the equal and opposite D_s contributions from the buffer Pt/Co and top Co/Pt interfaces. The rise in D_s was fitted with exponentials, which yielded characteristic lengths of (4 ± 0.6) Å and (4 ± 1) Å for the Au and Ir spacer layers respectively. This was longer than the characteristic lengthscale extracted for the Pt PIM, which was (2.2 ± 0.3) Å and (2.0 ± 0.4) Å for the Au and Ir spacer layers respectively. This pro-

vided evidence to suggest that the PIM and DMI are not correlated. Furthermore, for the thickest spacer layers, D_s saturated to the same value irrespective of the spacer layers. This demonstrated that the DMI contributions of Co/Au and Co/Ir interfaces were similar, even though the Ir was expected to exhibit a moderate induced moment [184]. This behaviour is consistent with the *ab initio* calculations of Yang *et al.* [166], who found no dependence of the DMI on PIM.

When the PIM was plotted with D_s, it was shown that the DMI continued to rise after the PIM had vanished, which demonstrated that the lengthscale of the rise in D_s was different to the lengthscale over which the PIM vanished. This demonstrated that the dominant contribution to the DMI was not the PIM but the presence of Pt atoms at the Co interface.

9.2 Further work

Almost all the work in this thesis can be extended for further studies of the spin-orbit phenomena investigated. Although much of the work presented has reached a suitable conclusion, where there are still questions to be answered, in this section, some possible routes to further this work are highlighted.

It would seem that the work presented in chapter 4 reached a satisfactory conclusion, where an explanation for the thickness dependence of AMR was presented and justified by experiment. However, this work has further emphasised the sensitivity of AMR to film morphology and structure. It would be interesting to study whether the same loss of $\Delta\rho$ could be observed at fixed thickness, instead using structural modification of the film by adjusting the working gas pressure used for the sputter deposition. AMR could then be used as a characterisation tool, sensitive to the film quality and used to optimise deposition parameters. The dramatic change in $\Delta\rho$ observed would make this a very sensitive technique for optimising film structure.

With regard to the investigation of SOTs, recent studies in the literature have demonstrated that the application of a gate voltage can be used to obtain reversible control of PMA through interface ion migration [219] or strain-induced control [220], and offer exciting methods by which the PMA can be functionalised. It would be interesting with regard to applications to demonstrate magnetisation reversal using the SOTs, whereby the

reversal is either switched "on" or "off" by enhancing or weakening the PMA dependent on the gate voltage polarity.

There is still much to learn with regard to the microscopic origin of the SOTs. In order to attempt to separate the contributions of the Rashba and spin-Hall effects, it would be useful to investigate a structure by which SIA could be introduced gradually. This could be achieved in a Pt/Co/MgO (t)/Pt structure, by which the SOTs could be characterised as a function MgO thickness, t, ranging from 0-50 Å.

In chapter 6, it was suggested that Ir spacer layers caused a more rapid loss of PIM in comparison to Au spacer layers due to the difference in intermixing and topological roughness of the respective interfaces. These components of intermixing and topological roughness could in principle be separated using high resolution cross-sectional TEM measurements of the Co/Au/Pt and Co/Ir/Pt interfaces.

The work of chapter 7 showed that as the magnetic anisotropy of the Co changed with reducing thickness, the anisotropy of the polarised Pt evolved alongside it. The element specific hysteresis loops were sensitive to the in-plane component of magnetisation. It would be insightful to repeat the measurements in the transmission scattering geometry, sensitive to the out-of-plane component of magnetisation to confirm that they reflect the polar MOKE loops. In the literature this has been demonstrated for a single Co-Pt film with strong PMA [200], but to the best of one's knowledge the transition from the in-plane to out-of-plane anisotropy has not been measured.

In chapter 8, where the magnetic damping within the Pt/Co/Au (t)/Pt and Pt/Co/Cu (t)/Pt multilayers was investigated, there was difficulty in establishing whether the PIM was necessary for the enhancement in damping associated with the Co/Pt interface, or whether it was a result of d-d hybridisation at the Co/Pt interfaces alone. It has been shown in Pd/Fe/Pd multilayers that the proximity induced magnetism in the Pd layers has a different temperature dependence to that of the magnetism in the Fe layer [41]. This may well be the case in the Pt/Co/Pt structures also, and in principle, by measuring the temperature dependence of the magnetic damping, the contribution from d-d hybridisation could be separated from any contribution to magnetic damping from the PIM.

With regard to the investigation of PIM and DMI, as a further investigation, it would be insightful to measure D_s in a Pt/Co/Pd (t)/Pt structure whereby the increasing Pd thickness,

t, would be expected to disrupt the PIM at the top Co/Pt interface but unlike Au would take on a substantial moment itself. Furthermore, the Pd is expected to have a D_s of similar magnitude but opposite sign to Au [56] and would therefore make an interesting comparison. However, this would require further XRMR measurements, since the substantial induced moment on the Pd could significantly modify the lengthscale over which the PIM in the Pt layer persists.

Bibliography

[1] Baibich, M. N., Broto, J. M., Fert, A., Van Dau, F. N., Petroff, F., Etienne, P., Creuzet, G., Friederich, A. and Chazelas, J. Giant Magnetoresistance of (001)Fe/(001)Cr Magnetic Superlattices. *Phys. Rev. Lett.* **61**, 2472 (1988).

[2] Binasch, G., Grünberg, P., Saurenbach, F. and Zinn, W. Enhanced magnetoresistance in layered magnetic structures with antiferromagnetic interlayer exchange. *Phys. Rev. B* **39**, 4828 (1989).

[3] Kent, A. D. and Worledge, D. C. A new spin on magnetic memories. *Nat. Nano.* **10**, 187 (2015).

[4] Sbiaa, R., Meng, H. and Piramanayagam, S. N. Materials with perpendicular magnetic anisotropy for magnetic random access memory. *Phys. Status. Solidi RRL* **5**, 413 (2011).

[5] Parkin, S. S. P., Hayashi, M. and Thomas, L. Magnetic Domain-Wall Racetrack Memory. *Science* **320**, 190 (2008).

[6] Uchida, K., Adachi, H., An, T., Ota, T., Toda, M., Hillebrands, B., Maekawa, S. and Saitoh, E. Long-range spin Seebeck effect and acoustic spin-pumping. *Nat. Mater.* **10**, 737 (2011).

[7] Ralph, D. C. and Stiles, M. D. Spin transfer torques. *J. Magn. Magn. Mater.* **320**, 1190 (2008).

[8] Gambardella, P. and Miron, I. M. Current-induced spin–orbit torques. *Phil.Trans. R. Soc. London A* **369**, 3175 (2011).

[9] Gilbert, T. A Lagrangian formulation of the gyromagnetic equation of the magnetic field. *Phys. Rev.* **100**, 1243 (1955).

[10] Moriya, T. New Mechanism of Anisotropic Superexchange Interaction. *Phys. Rev. Lett.* **4**, 228 (1960).

[11] Dzyaloshinskii, I. E. A Thermodynamic Theory of Weak Ferromagnetism of Antiferromagnetics. *J. Phys. Chem. Sol.* **4**, 4, 241 (1958).

[12] Belmeguenai, M., Adam, J.-P., Roussigné, Y., Eimer, S., Devolder, T., Kim, J.-V., Cherif, S. M., Stashkevich, A. and Thiaville, A. Interfacial Dzyaloshinskii-Moriya interaction in perpendicularly magnetized Pt/Co/AlO_x ultrathin films measured by Brillouin light spectroscopy. *Phys. Rev. B* **91**, 180405 (2015).

[13] Emori, S., Bauer, U., Ahn, S.-M., Martinez, E. and Beach, G. S. D. Current-driven dynamics of chiral ferromagnetic domain walls. *Nat. Mater.* **12**, 611 (2013).

[14] Garello, K., Miron, I. M., Avci, C. O., Freimuth, F., Mokrousov, Y., Blugel, S., Auffret, S., Boulle, O., Gaudin, G. and Gambardella, P. Symmetry and magnitude of spin-orbit torques in ferromagnetic heterostructures. *Nat. Nano.* **8**, 587 (2013).

[15] Hickey, M. C. and Moodera, J. S. Origin of Intrinsic Gilbert Damping. *Phys. Rev. Lett.* **102**, 137601 (2009).

[16] McGuire, T. R. and Potter, R. I. Anisotropic magnetoresistance in ferromagnetic 3*d* alloys. *IEEE. Trans. Mag.* **11**, 1018 (1975).

[17] Smit, J. Magnetoresistance of ferromagnetic metals and alloys at low temperatures. *Physica* **17**, 612 (1951).

[18] Smit, J. The spontaneous hall effect in ferromagnetics II. *Physica* **24**, 39 (1958).

[19] Hirsch, J. E. Spin Hall Effect. *Phys. Rev. Lett.* **83**, 1834 (1999).

[20] Bychkov, Y. A. and Rashba, E. I. Properties of a 2D electron gas with lifted spectral degeneracy. *J. Exp. Theor. Phys. Lett.* **39**, 78 (1984).

[21] Ryu, K.-S., Thomas, L., Yang, S.-H. and Parkin, S. Chiral spin torque at magnetic domain walls. *Nat. Nano.* **8**, 527 (2013).

[22] Miron, I. M., Gaudin, G., Auffret, S., Rodmacq, B., Schuhl, A., Pizzini, S., Vogel, J. and Gambardella, P. Current-driven spin torque induced by the Rashba effect in a ferromagnetic metal layer. *Nat. mat.* **9**, 230 (2010).

[23] Cubukcu, M., Boulle, O., Drouard, M., Garello, K., Onur Avci, C., Mihai Miron, I., Langer, J., Ocker, B., Gambardella, P. and Gaudin, G. Spin-orbit torque magnetization switching of a three-terminal perpendicular magnetic tunnel junction. *Appl. Phys. Lett.* **104**, 042406 (2014).

[24] Liu, L., Pai, C.-F., Li, Y., Tseng, H. W., Ralph, D. C. and Buhrman, R. A. Spin-Torque Switching with the Giant Spin Hall Effect of Tantalum. *Science* **336**, 555 (2012).

[25] Thompson, W. On the electro-dynamic qualities of metals: Effects of the magnetization on the electrical conductivity of Nickel and Iron. *Proc. R. Soc.* **8**, 546 (1857).

[26] Velev, J., Sabirianov, R. F., Jaswal, S. S. and Tsymbal, E. Y. Ballistic Anisotropic Magnetoresistance. *Phys. Rev. Lett.* **94**, 127203 (2005).

[27] Wunderlich, J., Jungwirth, T., Kaestner, B., Irvine, A. C., Shick, A. B., Stone, N., Wang, K.-Y., Rana, U., Giddings, A. D., Foxon, C. T., Campion, R. P., Williams, D. A. and Gallagher, B. L. Coulomb Blockade Anisotropic Magnetoresistance Effect in a (Ga, Mn)As Single-Electron Transistor. *Phys. Rev. Lett.* **97**, 077201 (2006).

[28] Kobs, A. and Oepen, H. P. Disentangling interface and bulk contributions to the anisotropic magnetoresistance in Pt/Co/Pt sandwiches. *Phys. Rev. B* **93**, 014426 (2016).

[29] Yeh, T. and Witcraft, W. F. Effect of magnetic anisotropy on signal and noise of NiFe magnetoresistive sensor. *IEEE. Trans. Mag.* **31**, 3131 (1995).

[30] Hunt, R. A magnetoresistive readout transducer. *IEEE. Trans. Mag.* **7**, 150 (1971).

[31] Zhang, W., Han, W., Jiang, X., Yang, S.-H. and Parkin, S. S. P. Role of transparency of platinum-ferromagnet interfaces in determining the intrinsic magnitude of the spin Hall effect. *Nat. Phys.* **11**, 496 (2015).

[32] Fuchs, K. The conductivity of thin metallic films according to the electron theory of metals. *Math. Proc. Cambridge* **34**, 100 (1938).

[33] Sondheimer, E. The mean free path of electrons in metals. *Adv. Phys.* **1**, 1 (1952).

[34] Zhao, C.-J., Ding, L., HuangFu, J.-S., Zhang, J.-Y. and Yu, G.-H. Research progress in anisotropic magnetoresistance. *Rare Metals* **32**, 213 (2013).

[35] Ding, L., Teng, J., Zhan, Q., Feng, C., Li, M.-h., Han, G., Wang, L.-j., Yu, G.-h. and Wang, S.-y. Enhancement of the magnetic field sensitivity in Al_2O_3 encapsulated NiFe films with anisotropic magnetoresistance. *Appl. Phys. Lett.* **94**, 162506 (2009).

[36] Dieny, B., Li, M., Liao, S. H., Horng, C. and Ju, K. Effect of interfacial specular electron reflection on the anisotropic magnetoresistance of magnetic thin films. *J. Appl. Phys.* **88**, 4140 (2000).

[37] Draaisma, H., de Jonge, W. and den Broeder, F. Magnetic interface anisotropy in Pd/Co and Pd/Fe multilayers. *J. Magn. Magn. Mater.* **66**, 351 (1987).

[38] King, J. A., Ganguly, A., Burn, D. M., Pal, S., Sallabank, E. A., Hase, T. P. A., Hindmarch, A. T., Barman, A. and Atkinson, D. Local control of magnetic damping in ferromagnetic/non-magnetic bilayers by interfacial intermixing induced by focused ion-beam irradiation. *Appl. Phys. Lett.* **104**, 242410 (2014).

[39] Vieu, C., Gierak, J., Launois, H., Aign, T., Meyer, P., Jamet, J. P., Ferré, J., Chappert, C., Devolder, T., Mathet, V. and Bernas, H. Modifications of magnetic properties of Pt/Co/Pt thin layers by focused gallium ion beam irradiation. *J. Appl. Phys.* **91**, 3103 (2002).

[40] Geissler, J., Goering, E., Justen, M., Weigand, F., Schütz, G., Langer, J., Schmitz, D., Maletta, H. and Mattheis, R. Pt magnetization profile in a Pt/Co bilayer studied by resonant magnetic x-ray reflectometry. *Phys. Rev. B* **65**, 020405 (2001).

[41] Hase, T. P. A., Brewer, M. S., Arnalds, U. B., Ahlberg, M., Kapaklis, V., Björck, M., Bouchenoire, L., Thompson, P., Haskel, D., Choi, Y., Lang, J., Sánchez-Hanke, C. and Hjövarsson, B. Proximity effects on dimensionality and magnetic ordering in Pd/Fe/Pd trialyers. *Phys. Rev. B* **90**, 104403 (2014).

[42] Blundell, S. *Magnetism in condensed matter*. Oxford University Press (2009).

[43] Jiles, D. *Introduction to magnetism and magnetic materials*. Taylor & Francis (1998).

[44] Hrabec, A., Porter, N. A., Wells, A., Romero, M. J. B., Burnell, G., Mcvitie, S., Mcgrouther, D., Moore, T. A. and Marrows, C. H. Measuring and tailoring the Dzyaloshinskii-Moriya interaction in perpendicularly magnetized thin films. *Phys. Rev. B* **90**, 020402(R) (2014).

[45] Thiaville, A., Rohart, S., Jué, E., Cros, V. and Fert, A. Dynamics of Dzyaloshinskii domain walls in ultrathin magnetic films. *Europhys. Lett.* **100**, 57002 (2012).

[46] Clogston, A. M., Matthias, B. T., Peter, M., Williams, H. J., Corenzwit, E. and Sherwood, R. C. Local Magnetic Moment Associated with an Iron Atom Dissolved in Various Transition Metal Alloys. *Phys. Rev.* **125**, 541 (1962).

[47] Crangle, J. Ferromagnetism in Pd-rich palladium iron alloys. *Phil. Mag.* **5**, 335 (1960).

[48] Sakamoto, Y., Oba, Y., Maki, H., Suda, M., Einaga, Y., Sato, T., Mizumaki, M., Kawamura, N. and Suzuki, M. Ferromagnetism of Pt nanoparticles induced by surface chemisorption. *Phys. Rev. B* **83**, 104420 (2011).

[49] Zuckermann, M. The proximity effect for weak itinerant ferromagnets. *Solid State Commun.* **12**, 745 (1973).

[50] Kiwi, M. Origin of the Magnetic Proximity Effect. In *Symposia Q/R-Magnetoelectronics-Novel Magnetic Phenomena in Nanostructures-Advanced Characterization of Artificially Structured Magnetic Materials*, MRS Proceedings (2002).

[51] Cox, B. N., Tahir-Kheli, R. A. and Elliott, R. J. Thin films of itinerant-electron ferromagnets on a nonmagnetic metallic substrate. *Phys. Rev. B* **20**, 2864 (1979).

[52] Stoner, E. C. Collective Electron Ferromagnetism. *Proc. R. Soc. London, Ser. A* **165**, 372 (1938).

[53] Wienke, R., Schütz, G. and Ebert, H. Determination of local magnetic moments of 5*d* impurities in Fe detected via spin dependent absorption. *J. Appl. Phys.* **69**, 6147 (1991).

[54] Akai, H. Nuclear spin-lattice relaxation of impurities in ferromagnetic iron. *Hyperfine Interact.* **43**, 253 (1988).

[55] Ryu, K. S., Yang, S.-H., Thomas, L. and Parkin, S. S. P. Chiral spin torque arising from proximity-induced magnetization. *Nat. Commun.* **5** (2014).

[56] Yang, H., Thiaville, A., Rohart, S., Fert, A. and Chshiev, M. Anatomy of Dzyaloshinskii-Moriya Interaction at Co/Pt Interfaces. *Phys. Rev. Lett.* **115**, 267210 (2015).

[57] Bozorth, R. M. and Walker, J. G. Magnetic Crystal Anisotropy and Magnetostriction of Iron-Nickel Alloys. *Phys. Rev.* **89**, 624 (1953).

[58] Campbell, I. A., Fert, A. and Jaoul, O. The spontaneous resistivity in Ni-based alloys. *J. Phys. C: Solid State Phys.* **3**, 95 (1970).

[59] Mott, N. F. The electrical conductivity of transition metals. *Proc. R. Soc. Lond. A* **153**, 699 (1936).

[60] Fert, A. and Campbell, I. A. Two-Current Conduction in Nickel. *Phys. Rev. Lett.* **21**, 16, 1190 (1968).

[61] Fert, A. Two-current conduction in ferromagnetic metals and spin wave-electron collisions. *J. Phys. C: Solid State Phys.* **2**, 1784 (1969).

[62] Rowan-Robinson, R. M., Hindmarch, A. T. and Atkinson, D. Enhanced electron-magnon scattering in ferromagnetic thin films and the breakdown of the Mott two-current model. *Phys. Rev. B* **90**, 104401 (2014).

[63] Yang, F. J., Sakuraba, Y., Kokado, S., Kota, Y., Sakuma, A. and Takanashi, K. Anisotropic magnetoresistance in Co_2(Fe,Mn)Si Heusler epitaxial films: A fingerprint of half-metallicity. *Phys. Rev. B* **86**, 020409 (2012).

[64] Friedel, J. Metallic alloys. *Nuovo Cimento* **7**, 287 (1958).

[65] D'yakonov, M. I. and Perel, V. I. Possibility of orienting electron spins with current. *Zh. Eksp. Teor. Fiz* **13**, 657 (1971).

[66] Haney, P. M., Lee, H.-w., Lee, K.-j. and Stiles, M. D. Current induced torques and interfacial spin-orbit coupling : Semiclassical modeling. *Phys. Rev. B* **174411**, 1 (2013).

[67] Woo, S., Mann, M., Tan, A. J., Caretta, L. and Beach, G. S. D. Enhanced spin-orbit torques in Pt/Co/Ta heterostructures. *Appl. Phys. Lett.* **105**, 212404 (2014).

[68] Kim, J., Sinha, J., Hayashi, M., Yamanouchi, M., Fukami, S., Suzuki, T., Mitani, S. and Ohno, H. Layer thickness dependence of the current-induced effective field vector in Ta|CoFeB|MgO. *Nat. Mater.* **12**, 240 (2013).

[69] Fan, X., Celik, H., Wu, J., Ni, C., Lee, K.-J., Lorenz, V. O. and Xiao, J. Q. Quantifying interface and bulk contributions to spin-orbit torque in magnetic bilayers. *Nat. Commun.* **5**, 3042 (2014).

[70] Landau, L. D. and Lifshitz, E. M. On the theory of the dispersion of magnetic permeability in ferromagnetic bodies. *Phys. Z. Sowjet.* **8**, 153 (1935).

[71] Rantschler, J. O., McMichael, R. D., Castillo, A., Shapiro, A. J., Egelhoff, W. F., Maranville, B. B., Pulugurtha, D., Chen, A. P. and Connors, L. M. Effect of 3*d*, 4*d*, and 5*d* transition metal doping on damping in permalloy thin films. *J. Appl. Phys.* **101**, 033911 (2007).

[72] Garello, K., Avci, C. O., Miron, I. M., Baumgartner, M., Ghosh, A., Auffret, S., Boulle, O., Gaudin, G. and Gambardella, P. Ultrafast magnetization switching by spin-orbit torques. *Appl. Phys. Lett.* **105**, 212402 (2014).

[73] Beach, G. S. D., Nistor, C., Knutson, C., Tsoi, M. and Erskine, J. L. Dynamics of field-driven domain-wall propagation in ferromagnetic nanowires. *Nat. Mater.* **4**, 741 (2005).

[74] Liu, L., Lee, O. J., Gudmundsen, T. J., Ralph, D. C. and Buhrman, R. A. Current-Induced Switching of Perpendicularly Magnetized Magnetic Layers Using Spin Torque from the Spin Hall Effect. *Phys. Rev. Lett.* **109**, 096602 (2012).

[75] Tserkovnyak, Y., Brataas, A. and Bauer, G. E. W. Enhanced Gilbert Damping in Thin Ferromagnetic Films. *Phys. Rev. Lett.* **88**, 117601 (2002).

[76] Barati, E., Cinal, M., Edwards, D. M. and Umerski, A. Gilbert damping in magnetic layered systems. *Phys. Rev. B* **90**, 014420 (2014).

[77] Landeros, P., Arias, R. E. and Mills, D. L. Two magnon scattering in ultrathin ferromagnets: The case where the magnetization is out of plane. *Phys. Rev. B* **77**, 214405 (2008).

[78] Azzawi, S., Ganguly, A., Tokaç, M., Rowan-Robinson, R. M., Sinha, J., Hindmarch, A. T., Barman, A. and Atkinson, D. Evolution of damping in ferromagnetic/nonmagnetic thin film bilayers as a function of nonmagnetic layer thickness. *Phys. Rev. B* **93**, 054402 (2016).

[79] Ganguly, A., Azzawi, S., Saha, S., King, J. A., Rowan-Robinson, R. M., Hindmarch, A. T., Sinha, J., Atkinson, D. and Barman, A. Tunable Magnetization Dynamics in Interfacially Modified $Ni_{81}Fe_{19}$/Pt Bilayer Thin Film Microstructures. *Sci. Rep.* **5**, 17596 (2015).

[80] Avci, C. O. *Current-induced effects in ferromagnetic heterostructures due to spin-orbit coupling*. Ph.D. thesis (2015).

[81] Ganguly, A., Rowan-Robinson, R. M., Haldar, A., Jaiswal, S., Sinha, J., Hindmarch, A. T., Atkinson, D. A. and Barman, A. Time-domain detection of current controlled magnetization damping in Pt/Ni81Fe19 bilayer and determination of Pt spin Hall angle. *Appl. Phys. Lett.* **105**, 112409 (2014).

[82] Manchon, A. and Zhang, S. Theory of nonequilibrium intrinsic spin torque in a single nanomagnet. *Phys. Rev. B* **78**, 212405 (2008).

[83] Manchon, A. and Zhang, S. Theory of spin torque due to spin-orbit coupling. *Phys. Rev. B* **79**, 094422 (2009).

[84] Berger, L. Influence of spin-orbit interaction on the transport processes in ferromagnetic nickel alloys, in the presence of a degeneracy of the 3*d* band. *Physica* **30**, 1141 (1964).

[85] Karplus, R. and Luttinger, J. M. Hall Effect in Ferromagnetics. *Phys. Rev.* **95**, 1154 (1954).

[86] Murakami, S., Nagaosa, N. and Zhang, S.-C. Dissipationless Quantum Spin Current at Room Temperature. *Science* **301**, 1348 (2003).

[87] Kato, Y. K., Myers, R. C., Gossard, A. C. and Awschalom, D. D. Observation of the Spin Hall Effect in Semiconductors. *Science* **306**, 1910 (2004).

[88] Wunderlich, J., Kaestner, B., Sinova, J. and Jungwirth, T. Experimental Observation of the Spin-Hall Effect in a Two-Dimensional Spin-Orbit Coupled Semiconductor System. *Phys. Rev. Lett.* **94**, 047204 (2005).

[89] Valenzuela, S. O. and Tinkham, M. Direct electronic measurement of the spin Hall effect. *Nature* **442**, 176 (2006).

[90] Wang, H. L., Du, C. H., Pu, Y., Adur, R., Hammel, P. C. and Yang, F. Y. Scaling of Spin Hall Angle in 3*d*, 4*d*, and 5*d* Metals from $Y_3Fe_5O_{12}$/Metal Spin Pumping. *Phys. Rev. Lett.* **112**, 197201 (2014).

[91] Hahn, C., de Loubens, G., Klein, O., Viret, M., Naletov, V. V. and Ben Youssef, J. Comparative measurements of inverse spin Hall effects and magnetoresistance in YIG/Pt and YIG/Ta. *Phys. Rev. B* **87**, 174417 (2013).

[92] Vlaminck, V., Pearson, J. E., Bader, S. D. and Hoffmann, A. Dependence of spin-pumping spin Hall effect measurements on layer thicknesses and stacking order. *Phys. Rev. B* **88**, 064414 (2013).

[93] Zhang, W., Vlaminck, V., Pearson, J. E., Divan, R., Bader, S. D. and Hoffmann, A. Determination of the Pt spin diffusion length by spin-pumping and spin Hall effect. *Appl. Phys. Lett.* **103**, 242414 (2013).

[94] Althammer, M., Meyer, S., Nakayama, H., Schreier, M., Altmannshofer, S., Weiler, M., Huebl, H., Geprägs, S., Opel, M., Gross, R., Meier, D., Klewe, C., Kuschel, T., Schmalhorst, J.-M., Reiss, G., Shen, L., Gupta, A., Chen, Y.-T., Bauer, G. E. W., Saitoh, E. and Goennenwein, S. T. B. Quantitative study of the spin Hall magnetoresistance in ferromagnetic insulator/normal metal hybrids. *Phys. Rev. B* **87**, 224401 (2013).

[95] Gómez, J. E., Zerai Tedlla, B., Álvarez, N. R., Alejandro, G., Goovaerts, E. and Butera, A. Spin transport parameters in $Ni_{80}Fe_{20}$/Ru and $Ni_{80}Fe_{20}$/Ta bilayers. *Phys. Rev. B* **90**, 184401 (2014).

[96] Pai, C.-F., Liu, L., Li, Y., Tseng, H. W., Ralph, D. C. and Buhrman, R. A. Spin transfer torque devices utilizing the giant spin Hall effect of tungsten. *Appl. Phys. Lett.* **101**, 122404 (2012).

[97] Tanaka, T., Kontani, H., Naito, M., Naito, T., Hirashima, D. S., Yamada, K. and Inoue, J. Intrinsic spin Hall effect and orbital Hall effect in 4*d* and 5*d* transition metals. *Phys. Rev. B* **77**, 165117 (2008).

[98] Zhang, W., Jungfleisch, M. B., Jiang, W., Liu, Y., Pearson, J. E., Velthuis, S. G. E., Hoffmann, A. and Gr, P. Reduced spin-Hall effects from magnetic proximity. *Phys. Rev. B* **91**, 115316 (2015).

[99] Malterre, D., Kierren, B., Fagot-Revurat, Y., Pons, S., Tejeda, A., Didiot, C., Cercellier, H. and Bendounan, A. ARPES and STS investigation of Shockley states in thin metallic films and periodic nanostructures. *New J. Phys.* **9**, 391 (2007).

[100] Skinner, T. D. *Electrical control of spin dynamics in spin-orbit coupled ferromagnets*. Ph.D. thesis, University of Cambridge (2015).

[101] Skinner, T. D., Olejník, K., Cunningham, L. K., Kurebayashi, H., Campion, R. P., Gallagher, B. L., Jungwirth, T. and Ferguson, A. J. Complementary spin-Hall and inverse spin-galvanic effect torques in a ferromagnet/semiconductor bilayer. *Nat. Commun.* **6**, 6730 (2015).

[102] Sánchez, J. C. R., Vila, L., Desfonds, G., Gambarelli, S., Attané, J. P., De Teresa, J. M., Magén, C. and Fert, A. Spin-to-charge conversion using Rashba coupling at the interface between non-magnetic materials. *Nat Commun* **4**, 2944 (2013).

[103] Manchon, A., Koo, H. C., Nitta, J., Frolov, S. M. and Duine, R. A. New perspectives for Rashba spin-orbit coupling. *Nat. Mater.* **14**, 871 (2015).

[104] Worasukhkhung, S., Pudwat, S., Eiamchai, P., Horprathum, M., Dumrongrattana, S. and Aiempanakit, K. Hydrophilic Property of TiO2 Films Sputtered on Glass/ITO for Self Cleaning Glass and Heat Mirror Application. *Procedia Engineering* **32**, 780 (2012).

[105] Rossnagel, S. M. Sputter deposition for semiconductor manufacturing. *IBM J. Res. Develop.* **43**, 163 (1999).

[106] Kelly, P. and Arnell, R. Magnetron sputtering: a review of recent developments and applications. *Vacuum* **56**, 159 (2000).

[107] Hindmarch, A. T. *Spin transport in rare-earth magnetic heterostructures*. Ph.D. thesis, University of Leeds (2003).

[108] Mantis business webpage with general specifications of the Qprep500 sputtering system. `http://www.mantisdeposition.com/systems/view/product/info/qprep-series.html`.

[109] Chowdhury, N. and Bedanta, S. Controlling the anisotropy and domain structure with oblique deposition and substrate rotation. *AIP Advances* **4**, 027104 (2014).

[110] Als-Nielsen, J. and McMorrow, D. *Elements of Modern X-ray Physics*. John Wiley and Sons (2011).

[111] Gayen, S. A versatile simulator for specular reflectivity study of multi-layer thin films. *arXiv:1305.6149* (2013).

[112] Björck, M. *A structural viewpoint of magnetism in Fe and Co based superlattices*. Ph.D. thesis, Uppsala (2007).

[113] Burn, D. M. *Domain wall behaviour in ferromagnetic nanowires with interfacial and geometrical structuring*. Ph.D. thesis, Durham University (2013).

[114] Parratt, L. G. Surface Studies of Solids by Total Reflection of X-Rays. *Phys. Rev.* **95**, 359 (1954).

[115] Bogart, L. *An Investigation of the Structure, Pinning and Magnetoresistance of Domain Walls in Ni81Fe19 Planar Nanowires*. Ph.D. thesis, Durham University (2010).

[116] Björck, M. and Andersson, G. GenX: an extensible X-ray reflectivity refinement program utilizing differential evolution. *J. Appl. Crystallogr.* **40**, 1174 (2007).

[117] Schütz, G., Wagner, W., Wilhelm, W., Kienle, P., Zeller, R., Frahm, R. and Materlik, G. Absorption of circularly polarized x rays in iron. *Phys. Rev. Lett.* **58**, 737 (1987).

[118] Scattering length database maintained by NIST. `http://physics.nist.gov/PhysRefData/FFast/html/form.html`.

[119] Björck, M., Brewer, M. S., Arnalds, U. B., Östman, E., Ahlberg, M., Kapaklis, V., Papaioannou, E. T., Andersson, G., Hjörvarsson, B. and Hase, T. P. A. Reflectivity Studies of Magnetic Heterostructures. *J. Surf. Interfac. Mater.* **2**, 24 (2014).

[120] Dieter, L. *Magnetic X-ray Reflectivity*. Ph.D. thesis, Ludwig-Maximilians-Universität München (2001).

[121] Srajer, G., Lang, J. C. and Haskel, D. *Modern Techniques for Characterizing Magnetic Materials*, chapter Hard x-ray resonant techniques for studies of nanomagnetism, pages 201–227. Springer US, Boston, MA (2005).

[122] Giles, C., Malgrange, C., Goulon, J., de Bergevin, F., Vettier, C., Dartyge, E., Fontaine, A., Giorgetti, C. and Pizzini, S. Energy-dispersive phase plate for magnetic circular dichroism experiments in the X-ray range. *J. Appl. Crystallogr.* **27**, 232 (1994).

[123] Faraday, M. On the magnetization of light and the illumination of magnetic lines of force. *Philos. Trans. R. Soc. London, Ser. A* **136**, 1 (1846).

[124] Kerr, J. On the rotation of the plane of polarization by reflection from the pole of a magnet. *Phil. Mag.* **3**, 321 (1877).

[125] Zak, J., Moog, E. R., Liu, C. and Bader, S. D. Fundamental magneto-optics. *J. Appl. Phys.* **68**, 4203 (1990).

[126] Rana, B. *Quasistatic and ultrafast magnetization dynamics in magnetic nanostructures*. Ph.D. thesis, University of Calcutta (2013).

[127] Zhu, Y. *Modern Techniques for Characterizing Magnetic Materials*, chapter Brillouin light scattering spectroscopy, pages 543–578. Springer US, Boston, MA (2005).

[128] Stashkevich, A. A., Belmeguenai, M., Roussigné, Y., Cherif, S. M., Kostylev, M., Gabor, M., Lacour, D., Tiusan, C. and Hehn, M. Experimental study of spin-wave dispersion in Py/Pt film structures in the presence of an interface Dzyaloshinskii-Moriya interaction. *Phys. Rev. B* **91**, 214409 (2015).

[129] Sheng, S., Li, W., Li, M. and Yu, G. Investigation on interface of NiFeCr/NiFe/Ta films with high magnetic field sensitivity. *Rare Metals* **31**, 22 (2012).

[130] Krzyk, S., Schmidsfeld, a., Kläui, M. and Rüdiger, U. Magnetotransport effects of ultrathin Ni80Fe20 films probed in situ. *New J. Phys.* **12**, 013001 (2010).

[131] Liu, Y. F., Cai, J. W. and Sun, L. Large enhancement of anisotropic magnetoresistance and thermal stability in Ta/NiFe/Ta trilayers with interfacial Pt addition. *Appl. Phys. Lett.* **96**, 092509 (2010).

[132] Kokado, S. and Tsunoda, M. Anisotropic Magnetoresistance Effect: General Expression of AMR Ratio and Intuitive Explanation for Sign of AMR Ratio. *Adv. Mat. Res.* **750**, 978 (2013).

[133] Kokado, S. and Tsunoda, M. Anisotropic magnetoresistance effect of a strong ferromagnet: magnetization direction dependence in a model with crystal field. *Phys. Status Solidi C* **11**, 1026 (2014).

[134] Rushforth, A. W., Výborný, K., King, C. S., Edmonds, K. W., Campion, R. P., Foxon, C. T., Wunderlich, J., Irvine, A. C., Vašek, P., Novák, V., Olejník, K., Sinova, J., Jungwirth, T. and Gallagher, B. L. Anisotropic Magnetoresistance Components in (Ga,Mn)As. *Phys. Rev. Lett.* **99**, 147207 (2007).

[135] Moran, T. J. and Dahlberg, E. D. Magnetoresistive sensor for weak magnetic fields. *Appl. Phys. Lett.* **70**, 1894 (1997).

[136] Thanh, N. T., Tu, L. T., Ha, N. D., Kim, C. O. and Kim, C. Thickness dependence of parallel and perpendicular anisotropic resitivity in Ta/NiFe/IrMn/Ta multilayer studied by anisotropic Magnetoresistance and planar hall effect. *J. Appl. Phys.* **101**, 053702 (2007).

[137] Mitchell, E. N., Haukaas, H. B., Bale, H. D. and Streeper, J. B. Compositional and Thickness Dependence of the Ferromagnetic Anisotropy in Resistance of Iron-Nickel Films. *J. Appl. Phys.* **35**, 2604 (1964).

[138] Rijks, T. G. S. M., Coehoorn, R., de Jong, M. J. M. and de Jonge, W. J. M. Semi-classical calculations of the anisotropic magnetoresistance of NiFe-based thin films, wires, and multilayers. *Phys. Rev. B* **51**, 283 (1995).

[139] Lambers, E. S., Dykstal, C. N., Seo, J. M., Rowe, J. E. and Holloway, P. H. Room-tememerature oxidation of Ni(110) at low and atmospheric oxygen pressures. *Oxid. Met.* **45**, 301 (1996).

[140] Kaye, G. W. C. and Laby, T. H. *Tables of Physical & Chemical Constants. 4.2.1 X-ray absorption edges.* National Physical Laboratory (1995).

[141] Wang, D., Geyer, U., Schneider, S. and von Minnigerode, G. Grain sizes of Ni films measured by STM and X-ray methods. *Thin Solid Films* **292**, 184 (1997).

[142] Semenenko, E. E. and Sudovtsov, A. I. Effect of the domain structure on the electrical resistance of Iron, Nickel and Cobal at low temperatures. *J. Exp. Theor. Phys.* **47**, 486 (1964).

[143] Hoesch, M., Petrov, V. N., Muntwiler, M., Hengsberger, M., Checa, J. L., Greber, T. and Osterwalder, J. Two- and three-dimensional band structure of ultrathin Ni on Cu(001). *Phys. Rev. B* **79**, 155404 (2009).

[144] Abo, G., Hong, Y.-K., Park, J., Lee, J., Lee, W. and Choi, B.-C. Definition of Magnetic Exchange Length. *IEEE. Trans. Mag.* **49**, 4937 (Aug. 2013).

[145] Varnakov, S. N., Bartolomé, J., Sesé, J., Ovchinnikov, S. G., Komogortsev, S. V., Parshin, A. S. and Bondarenko, G. V. Size effects and magnetization of (Fe/Si) n multilayer film nanostructures. *Phys. Solid State* **49**, 1470 (2007).

[146] Bloembergen, N. On the Ferromagnetic Resonance in Nickel and Supermalloy. *Phys. Rev.* **78**, 572 (1950).

[147] Vitta, S. Nonlinear spin wave magnetization of solution synthesized Ni nanoparticles. *J. Appl. Phys.* **101**, 063901 (2007).

[148] Ren, S. Y. and Dow, J. D. Spin-flip transition rate due to electron-magnon scattering in ferromagnetic thin films. *Phys. Rev. B* **61**, 6934 (2000).

[149] Slonczewski, J. Current-driven excitation of magnetic multilayers. *J. Magn. Magn. Mater.* **159**, 1 (1996).

[150] Hin Sim, C., Cheng Huang, J., Tran, M. and Eason, K. Asymmetry in effective fields of spin-orbit torques in Pt/Co/Pt stacks. *Appl. Phys. Lett.* **104**, 012408 (2014).

[151] Yu, G., Upadhyaya, P., Fan, Y., Alzate, J. G., Jiang, W., Wong, K. L., Takei, S., Bender, S. A., Chang, L.-t., Jiang, Y., Lang, M., Tang, J., Wang, Y., Tserkovnyak, Y., Amiri, P. K. and Wang, K. L. Spin-orbit torques in the absence of external magnetic fields. *Nat. Nano.* **9**, 548 (2014).

[152] Van 't Erve, O. M. J., Hanbicki, A. T., McCreary, K. M., Li, C. H. and Jonker, B. T. Optical detection of spin Hall effect in metals. *Appl. Phys. Lett.* **104**, 172402 (2014).

[153] Huang, K.-f., Wang, D.-s., Lin, H.-h. and Lai, C.-h. Engineering spin-orbit torque in Co / Pt multilayers with perpendicular magnetic anisotropy Engineering spin-orbit torque in Co / Pt multilayers with perpendicular magnetic anisotropy. *Appl. Phys. Lett.* **107**, 232407 (2015).

[154] Skinner, T. D., Wang, M., Hindmarch, a. T., Rushforth, a. W., Irvine, a. C., Heiss, D., Kurebayashi, H. and Ferguson, a. J. Spin-orbit torque opposing the Oersted torque in ultrathin Co/Pt bilayers. *Appl. Phys. Lett.* **104**, 062401 (2014).

[155] Fan, X., Wu, J., Chen, Y., Jerry, M. J., Zhang, H. and Xiao, J. Q. Observation of the nonlocal spin-orbital effective field. *Nat. Commun.* **4**, 1799 (2013).

[156] Loong, L. M., Deorani, P., Qiu, X. and Yang, H. Investigating and engineering spin-orbit torques in heavy metal/$Co_2FeAl_{0.5}Si_{0.5}$/MgO thin film structures. *Appl. Phys. Lett.* **107**, 022405 (2015).

[157] Qiu, X., Deorani, P., Narayanapillai, K., Lee, K.-S., Lee, K.-J., Lee, H.-W. and Yang, H. Angular and temperature dependence of current induced spin-orbit effective fields in Ta/CoFeB/MgO nanowires. *Sci. Rep.* **4**, 4491 (2014).

[158] Rushforth, a. W. Domain wall motion driven by spin Hall effect-Tuning with in-plane magnetic anisotropy. *Appl. Phys. Lett.* **104**, 162408 (2014).

[159] Lee, H.-R., Lee, K., Cho, J., Choi, Y.-H., You, C.-Y., Jung, M.-H., Bonell, F., Shiota, Y., Miwa, S. and Suzuki, Y. Spin-orbit torque in a bulk perpendicular magnetic anisotropy Pd/FePd/MgO system. *Sci. Rep.* **4**, 6548 (2014).

[160] Emori, S., Bauer, U., Woo, S. and Beach, G. S. D. Large voltage-induced modification of spin-orbit torques in Pt/Co/GdOx. *Appl. Phys. Lett.* **105**, 222401 (2014).

[161] Seemann, K. M., Freimuth, F., Zhang, H., Blugel, S., Mokrousov, Y., Burgler, D. E. and Schneider, C. Origin of the Planar Hall Effect in Nanocrystalline $Co_{60}Fe_{20}B_{20}$. *Phys. Rev. Lett.* **107**, 086603 (2011).

[162] Miron, I. M., Garello, K., Gaudin, G., Zermatten, P.-J., Costache, M. V., Auffret, S., Bandiera, S., Rodmacq, B., Schuhl, A. and Gambardella, P. Perpendicular switching of a single ferromagnetic layer induced by in-plane current injection. *Nature* **476**, 189 (2011).

[163] Yu, G., Upadhyaya, P., Fan, Y., Alzate, J. G., Jiang, W., Wong, K. L., Takei, S., Bender, S. A., Chang, L.-T., Jiang, Y., Lang, M., Tang, J., Wang, Y., Tserkovnyak, Y., Amiri, P. K. and Wang, K. L. Switching of perpendicular magnetization by spin-orbit torques in the absence of external magnetic fields. *Nat. Nano.* **9**, 548 (2014).

[164] Pi, U. H., Won Kim, K., Bae, J. Y., Lee, S. C., Cho, Y. J., Kim, K. S. and Seo, S. Tilting of the spin orientation induced by Rashba effect in ferromagnetic metal layer. *Appl. Phys. Lett.* **97**, 162507 (2010).

[165] Emori, S., Bauer, U., Woo, S. and Beach, G. S. D. Supplementary Material - Derivation of SOT effective fields from polar MOKE data. *Appl. Phys. Lett.* **1** (2013).

[166] Yang, M., Cai, K., Ju, H., Edmonds, K. W., Yang, G., Liu, S., Li, B., Zhang, B., Sheng, Y., Wang, S., Ji, Y. and Wang, K. Spin-orbit torque in Pt/CoNiCo/Pt symmetric devices. *Sci. Rep.* **6**, 20778 (2016).

[167] Mizukami, S., Sajitha, E. P., Watanabe, D., Wu, F., Miyazaki, T., Naganuma, H., Oogane, M. and Ando, Y. Gilbert damping in perpendicularly magnetized Pt/Co/Pt films investigated by all-optical pump-probe technique. *Appl. Phys. Lett.* **96**, 152502 (2010).

[168] Carcia, P. F. Perpendicular magnetic anisotropy in Pd/Co and Pt/Co thin-film layered structures. *J. Appl. Phys.* **63**, 5066 (1988).

[169] Avci, C. O., Garello, K., Nistor, C., Godey, S., Ballesteros, B., Mugarza, A., Barla, A., Valvidares, M., Pellegrin, E., Ghosh, A., Miron, I. M., Boulle, O., Auffret, S., Gaudin, G. and Gambardella, P. Fieldlike and antidamping spin-orbit torques in as-grown and annealed Ta/CoFeB/MgO layers. *Phys. Rev. B* **89**, 214419 (2014).

[170] Krüger, B. *Current-Driven Magnetization Dynamics : Analytical Modeling and Numerical Simulation*. Ph.D. thesis, Universität Hamburg, Von-Melle-Park 3, 20146 Hamburg (2011).

[171] Wilhelm, F., Poulopoulos, P., Ceballos, G., Wende, H., Baberschke, K., Srivastava, P., Benea, D., Ebert, H., Angelakeris, M., Flevaris, N. K., Niarchos, D., Rogalev, A. and Brookes, N. B. Layer-Resolved Magnetic Moments in Ni/Pt Multilayers. *Phys. Rev. Lett.* **85**, 413 (2000).

[172] Lim, W. L., Ebrahim-Zadeh, N., Owens, J. C., Hentschel, H. G. E. and Urazhdin, S. Temperature-dependent proximity magnetism in Pt. *Appl. Phys. Lett.* **102**, 162404 (2013).

[173] Huang, S. Y., Fan, X., Qu, D., Chen, Y. P., Wang, W. G., Wu, J., Chen, T. Y., Xiao, J. Q. and Chien, C. L. Transport Magnetic Proximity Effects in Platinum. *Phys. Rev. Lett.* **109**, 107204 (2012).

[174] Geprags, S., Meyer, S., Altmannshofer, S., Opel, M., Wilhelm, F., Rogalev, A., Gross, R. and Goennenwein, S. T. B. Investigation of induced Pt magnetic polarization in Pt/$Y_3Fe_5O_{12}$ bilayers. *Appl. Phys. Lett.* **101**, 262407 (2012).

[175] Ferrer, S., Fajardo, P., de Bergevin F, Alvarez, J., Torrelles, X., van der Vegt HA and Etgens, V. Resonant Surface Magnetic X-Ray Diffraction from Co_3Pt(111). *Phys. Rev. Lett.* **77**, 747 (1996).

[176] Vogel, J., Fontaine, A., Cros, V., Petroff, F., Kappler, J.-P., Krill, G., Rogalev, A. and Goulon, J. Palladium magnetism in Pd/Fe multilayers studied by XMCD at the Pd-$L_{2,3}$ edges. *J. Magn. Magn. Mater.* **165**, 96 (1997).

[177] Lee, J.-B., An, G.-G., Yang, S.-M., Park, H.-S., Chung, W.-S. and Hong, J.-P. Thermally robust perpendicular Co/Pd-based synthetic antiferromagnetic coupling enabled by a W capping or buffer layer. *Sci. Rep.* **6**, 21324 (2016).

[178] Zeper, W. B., Greidanus, F. J. A. M., Carcia, P. F. and Fincher, C. R. Perpendicular magnetic anisotropy and magneto-optical Kerr effect of vapor deposited Co/Pt layered structures. *J. Appl. Phys.* **65**, 4971 (1989).

[179] He, P., McGahan, W. A., Woollam, J. A., Sequeda, F., McDaniel, T. and Do, H. Magneto-optical Kerr effect and perpendicular magnetic anisotropy of evaporated and sputtered Co/Pt multilayer structures. *J. Appl. Phys.* **69**, 4021 (1991).

[180] Lv, Q. L., Cai, J. W., He, S. L. and Sun, L. Perpendicular magnetic anisotropy and magnetic proximity effect in $Pt_{1-\delta}Fe_\delta$/Co multilayer films. *J. Magn. Magn. Mater.* **323**, 465 (2011).

[181] Ueno, T., Sinha, J., Inami, N., Takeichi, Y., Mitani, S., Ono, K. and Hayashi, M. Enhanced orbital magnetic moments in magnetic heterostructures with interface perpendicular magnetic anisotropy. *Sci. Rep.* **5**, 14858 (2015).

[182] Schütz, G., Wienke, R., Wilhelm, W., Zeper, W. B., Ebert, H. and Spörl, K. Spin dependent x-ray absorption in Co/Pt multilayers and $Co_{50}Pt_{50}$ alloy. *J. Appl. Phys.* **67**, 4456 (1990).

[183] Rüegg, S., Schütz, G., Fischer, P., Wienke, R., Zeper, W. B. and Ebert, H. Spin dependent x-ray absorption in Co/Pt multilayers. *J. Appl. Phys.* **69**, 5655 (1991).

[184] Schütz, G., Stähler, S., Knülle, M., Fischer, P., Parkin, S. and Ebert, H. Distribution of magnetic moments in Co/Pt and Co/Pt/Ir/Pt multilayers detected by magnetic x-ray absorption. *J. Appl. Phys.* **73**, 6430 (1993).

[185] Abes, M., Atkinson, D., Tanner, B. K., Charlton, T. R., Langridge, S., Hase, T. P. A., Ali, M., Marrows, C. H., Hickey, B. J., Neudert, A., Hicken, R. J., Arena, D., Wilkins, S. B., Mirone, A. and Lebègue, S. Spin polarization and exchange coupling of Cu and Mn atoms in paramagnetic CuMn diluted alloys induced by a Co layer. *Phys. Rev. B* **82**, 184412 (2010).

[186] Schütz, G., Wienke, R., Wilhelm, W., Wagner, W., Kienle, P., Zeller, R. and Frahm, R. Strong spin-dependent absorption at the L_2-edges of 5*d*-impurities in iron. *Z. Phys. B: Condens. Matter* **75**, 495 (1989).

[187] Bailey, W. E., Ghosh, a., Auffret, S., Gautier, E., Ebels, U., Wilhelm, F. and Rogalev, a. Pd magnetism induced by indirect interlayer exchange coupling. *Phys. Rev. B* **86**, 144403 (2012).

[188] Wilhelm, F., Poulopoulos, P., Wende, H., Scherz, a. and Baberschke, K. Systematics of the Induced Magnetic Moments in 5d Layers and the Violation of the Third Hund's Rule. *Phys. Rev. Lett.* **87**, 207202 (2001).

[189] Miao, B. F., Huang, S. Y., Qu, D. and Chien, C. L. Inverse Spin Hall Effect in a Ferromagnetic Metal. *Phys. Rev. Lett.* **111**, 066602 (2013).

[190] Nembach, H. T., Shaw, J. M., Weiler, M., Jué, E. and Silva, T. J. Linear relation between Heisenberg exchange and interfacial Dzyaloshinskii-Moriya interaction in metal films. *Nat. Phys.* **11**, 825 (2015).

[191] Nakayama, H., Althammer, M., Chen, Y.-T., Uchida, K., Kajiwara, Y., Kikuchi, D., Ohtani, T., Geprägs, S., Opel, M., Takahashi, S., Gross, R., Bauer, G. E. W., Goennenwein, S. T. B. and Saitoh, E. Spin Hall Magnetoresistance Induced by a Nonequilibrium Proximity Effect. *Phys. Rev. Lett.* **110**, 206601 (2013).

[192] Macke, S. and Goering, E. Magnetic reflectometry of heterostructures. *J. Phys.: Condens. Matter* **26**, 363201 (2014).

[193] Bharadwaj, S. R., Tripathi, S. N. and Chandrasekharaiah, M. S. The Ir-Pt (Iridium-Platinum) system. *J. Phase Equilib.* **16**, 460 (1995).

[194] Okamoto, H. and Massalski, T. B. The Au-Pt (Gold-Platinum) system. *Bull. Alloy Phase Diag.* **6**, 46 (1985).

[195] Geissler, J., Goering, E., Weigand, F. and Schütz, G. Interplay between chemical and magnetic roughness of Pt in a Pt/Co bilayer investigated with X-ray resonant magnetic reflectometry. *Z. Metallk.* **93**, 946 (2002).

[196] Scherz, A., Poulopoulos, P., Nünthel, R., Lindner, J., Wende, H., Wilhelm, F. and Baberschke, K. Direct probe of interdiffusion effects on the induced V spin polarization at Fe/V interfaces. *Phys. Rev. B* **68**, 140401 (2003).

[197] Lardé, R., Lechevallier, L., Zarefy, A., Bostel, A., Juraszek, J., Le Breton, J. M., Rodmacq, B. and Dieny, B. Structural analysis of a (Pt/Co)3/IrMn multilayer: Investigation of sub-nanometric layers by tomographic atom probe. *J. Appl. Phys.* **105**, 084307 (2009).

[198] Goto, T., Takahashi, J., Nakamura, M., Hirose, T., Watanabe, K. and Yoshida, H. Magnetic properties of FePt(1-x)Ir(x) alloys and applications of the thin films. *J. Magn. Magn. Mater.* **226**, 1656 (2001).

[199] Sakamaki, M., Amemiya, K., Liedke, M. O., Fassbender, J., Mazalski, P., Sveklo, I. and Maziewski, A. Perpendicular magnetic anisotropy in a Pt/Co/Pt ultrathin film arising from a lattice distortion induced by ion irradiation. *Phys. Rev. B* **86**, 024418 (2012).

[200] Figueroa, A. I., Bartolomé, J., García, L. M., Bartolomé, F., Bunău, O., Stankiewicz, J., Ruiz, L., González-Calbet, J. M., Petroff, F., Deranlot, C., Pascarelli, S., Bencok, P., Brookes, N. B., Wilhelm, F., Smekhova, A. and Rogalev, A. Structural and magnetic properties of granular Co-Pt multilayers with perpendicular magnetic anisotropy. *Phys. Rev. B* **90**, 174421 (2014).

[201] Mebarki, M., Layadi, A., Khelladi, M. R., Azizi, A., Tiercelin, N., Preobrazhensky, V. and Pernod, P. Structural and Magnetic Properties of Fe Films Electrodeposited on Al Substrates. *Metall. Mater. Trans. A* pages 1–7 (2016).

[202] Lu, Y. M., Cai, J. W., Huang, S. Y., Qu, D., Miao, B. F. and Chien, C. L. Hybrid magnetoresistance in the proximity of a ferromagnet. *Phys. Rev. B* **87**, 220409 (2013).

[203] Uchida, K., Xiao, J., Adachi, H., Ohe, J., Takahashi, S., Ieda, J., Ota, T., Kajiwara, Y., Umezawa, H., Kawai, H., Bauer, G. E. W., Maekawa, S. and Saitoh, E. Spin Seebeck insulator. *Nat. Mater.* **9**, 894 (2010).

[204] Kikkawa, T., Uchida, K., Shiomi, Y., Qiu, Z., Hou, D., Tian, D., Nakayama, H., Jin, X.-F. and Saitoh, E. Longitudinal Spin Seebeck Effect Free from the Proximity Nernst Effect. *Phys. Rev. Lett.* **110**, 067207 (2013).

[205] Geprags, S., Goennenwein, S. T. B., Schneider, M., Ollefs, K., Rogalev, A., Opel, M. and Gross, R. Comment on "Pt magnetic polarization on Y_3 Fe_5O_{12} and magnetotransport characteristics". *arXiv:1307.4869* (2013).

[206] Kuschel, T., Klewe, C., Schmalhorst, J.-M., Bertram, F., Kuschel, O., Schemme, T., Wollschläger, J., Francoual, S., Strempfer, J., Gupta, A., Meinert, M., Götz, G., Meier, D. and Reiss, G. Static Magnetic Proximity Effect in $Pt/NiFe_2O_4$ and Pt/Fe Bilayers Investigated by X-Ray Resonant Magnetic Reflectivity. *Phys. Rev. Lett.* **115**, 097401 (2015).

[207] Gilbert, T. L. A phenomenological theory of damping in ferromagnetic materials. *IEEE. Trans. Mag.* **40**, 3443 (2004).

[208] Dzyaloshinskii, I. E. Thermodynamic Theory of Weak Ferromagnetism In Antiferromagnetic Substances. *Soviet Physics JETP* **5**, 6, 1259 (1957).

[209] Mizukami, S., Ando, Y. and Miyazaki, T. Ferromagnetic resonance linewidth for NM/$Ni_{80}Fe_{20}$/NM films (NM=Cu, Ta, Pd and Pt). *Jpn. J. Appl. Phys.* **40**, 1640 (2001). Proceedings of the International Conference on Magnetism (ICM 2000).

[210] Yakata, S., Ando, Y., Miyazaki, T. and Mizukami, S. Temperature Dependences of Spin-Diffusion Lengths of Cu and Ru layers. *Jpn. J. Appl. Phys.* **45**, 3892 (2006).

[211] Tao, X. D., Feng, Z., Miao, B. F., Sun, L., You, B., Wu, D., Du, J., Zhang, W. and Ding, H. F. The spin Hall angle and spin diffusion length of Pd measured by spin pumping and microwave photoresistance. *J. Appl. Phys.* **115**, 17C504 (2014).

[212] Mizukami, S., Ando, Y. and Miyazaki, T. Effect of spin diffusion on Gilbert damping for a very thin permalloy layer in Cu/permalloy/Cu/Pt films. *Phys. Rev. B* **66**, 104413 (2002).

[213] Sun, Y., Chang, H., Kabatek, M., Song, Y.-Y., Wang, Z., Jantz, M., Schneider, W., Wu, M., Montoya, E., Kardasz, B., Heinrich, B., te Velthuis, S. G. E., Schultheiss, H. and Hoffmann, A. Damping in Yttrium Iron Garnet Nanoscale Films Capped by Platinum. *Phys. Rev. Lett.* **111**, 106601 (2013).

[214] Isasa, M., Villamor, E., Hueso, L. E., Gradhand, M. and Casanova, F. Temperature dependence of spin diffusion length and spin Hall angle in Au and Pt. *Phys. Rev. B* **91**, 024402 (2015).

[215] Li, J., Strane, J. W., Russell, S. W., Hong, S. Q., Mayer, J. W., Marais, T. K., Theron, C. C. and Pretorius, R. Observation and prediction of first phase formation in binary Cu-metal thin films. *J. Appl. Phys.* **72**, 2810 (1992).

[216] Heinrich, B., Burrowes, C., Montoya, E., Kardasz, B., Girt, E., Song, Y.-Y., Sun, Y. and Wu, M. Spin Pumping at the Magnetic Insulator (YIG)/Normal Metal (Au) Interfaces. *Phys. Rev. Lett.* **107**, 066604 (2011).

[217] Tokaç, M., Bunyaev, S. A., Kakazei, G. N., Schmool, D. S., Atkinson, D. and Hindmarch, A. T. Interfacial Structure Dependent Spin Mixing Conductance in Cobalt Thin Films. *Phys. Rev. Lett.* **115**, 056601 (2015).

[218] Chen, G., Ma, T., N'Diaye, A. T., Kwon, H., Won, C., Wu, Y. and Schmid, A. K. Tailoring the chirality of magnetic domain walls by interface engineering. *Nat. Commun.* **4**, 2671 (2013).

[219] Bauer, U., Yao, L., Tan, A. J., Agrawal, P., Emori, S., Tuller, H. L., van Dijken, S. and Beach, G. S. D. Magneto-ionic control of interfacial magnetism. *Nat. Mater.* **14**, 174 (2015).

[220] Shepley, P. M., Rushforth, A. W., Wang, M., Burnell, G. and Moore, T. A. Modification of perpendicular magnetic anisotropy and domain wall velocity in Pt / Co / Pt by voltage-induced strain. *Sci. Rep.* **5**, 1 (2015).